UNIVERSITÉ DE STRASBOURG

ÉCOLE DOCTORALE SCIENCES CHIMIQUES

[ICPEES]

THÈSE présentée par:

Jinming ZHANG

soutenue le : **12 Décembre 2024**

pour obtenir le grade de: **Docteur de l'université de Strasbourg**
Discipline/ Spécialité: Chimie / Chimie Physique

Étude de la chimie de surface des électrodes SOEC lors de l'électrolyse H_2O à haute température

Surface chemistry study on the SOEC Electrodes during high-temperature H_2O Electrolysis

THÈSE dirigée par :

M. ZAFEIRATOS Spyridon	Directeur de recherche CNRS, ICPEES

RAPPORTEURS :

M. Jerome LAURENCIN	Directeur de recherche au CEA
M. Nicolas BION	Directeur de recherche CNRS, IC2MP

AUTRES MEMBRES DU JURY :

Mme. Elena. SAVINOVA	Professeur, Université de Strasbourg
M. Mathias BARREAU	Maître de conférences, Université de Caen Normandy

To my family

Jinming ZHANG

Surface chemistry study on the SOEC Electrodes during high-temperature H_2O Electrolysis

Résumé

Cette thèse se concentre sur les performances électrochimiques et la chimie de surface des cellules d'électrolyse à oxyde solide avancées (SOEC), avec une attention particulière sur le comportement des électrodes Ni/YSZ lors de l'électrolyse de l'eau. Les SOEC présentent un potentiel considérable pour la production d'hydrogène par électrolyse de l'eau et le stockage d'énergie, tandis que les piles à combustible à oxyde solide (SOFC) utilisent l'hydrogène pour la production d'électricité. Compte tenu de l'efficacité économique, de la compatibilité thermique et de la haute conductivité des composites à base de nickel, largement utilisés dans les applications industrielles, cette recherche se concentre sur l'amélioration de ces matériaux grâce à la modification de surface.

À l'aide de la spectroscopie de photoélectrons par rayons X à pression quasi ambiante (NAP-XPS), l'interaction entre les électrodes Ni/YSZ et la vapeur d'eau a été étudiée dans des conditions de circuit ouvert et de polarisation. Des modifications ont été apportées aux cathodes poreuses traditionnelles en Ni/YSZ afin d'observer directement les zones fonctionnelles proches de l'électrolyte YSZ. Les résultats ont révélé des changements dynamiques dans les états d'oxydation et la composition du Ni/YSZ dans des atmosphères de H_2 et de H_2O. En outre, cette étude met en lumière l'impact de l'oxydation des électrodes sur la dégradation pendant l'électrolyse et souligne la relation entre l'état d'oxydation de la surface du nickel et les performances électrochimiques de la cellule.

Des nanoparticules (NP) à base de cérium ont été introduites pour modifier la surface des électrodes Ni/YSZ. Deux types de NP — le cérium dopé au nickel ($NiCeO_x$) et le cérium non dopé (CeO_y) — ont été synthétisés et utilisés pour imprégner des électrodes métalliques Ni/YSZ préfabriquées. L'étude comparative a montré que le $NiCeO_x$ présentait des performances supérieures en raison d'une meilleure dispersion et d'une taille de particules plus réduite. Les résultats obtenus par synchrotron ont également révélé que le dopage au nickel modifiait les propriétés rédox du cérium, conduisant à une réduction plus forte de Ni/YSZ par rapport à CeO_y, ce qui a augmenté le nombre de sites actifs et amélioré l'efficacité de l'électrolyse. De plus, des essais expérimentaux impliquant des nanoparticules de cérium dopé au vanadium et au cobalt ont été présentés, bien que les améliorations de performances aient été limitées.

Enfin, les surface des électrodes $La_{0.6}Sr_{0.4}Co_{0.2}Fe_{0.8}O_{3-\delta}$ (LSCF) ont été étudiés, en se concentrant sur la ségrégation du Sr. L'étude a également examiné le Pr_6O_{11} en tant que catalyseur électrochimique alternatif pour les applications SOEC, démontrant son potentiel.

En somme, cette recherche souligne l'impact significatif des modifications de surface des nanoparticules sur les performances électrochimiques des électrodes dans l'électrolyse de l'eau, révélant des améliorations notables en termes d'efficacité et de stabilité. La combinaison d'une conception innovante des matériaux et de techniques de caractérisation avancées offre des perspectives précieuses pour le développement de solutions énergétiques durables.

Résumé en anglais

This thesis focuses on the electrochemical performance and surface chemistry of advanced Solid Oxide Electrolysis Cells (SOECs), with particular emphasis on the behavior of Ni/YSZ electrodes in water electrolysis. SOECs hold significant potential for hydrogen production through water electrolysis and energy storage, while Solid Oxide Fuel Cells (SOFCs) use hydrogen for power generation. Given the cost-effectiveness, thermal compatibility, and high conductivity of nickel-based composites, widely used in industrial applications, this research concentrates on improving these materials through surface modification. Using Near Ambient Pressure X-ray Photoelectron Spectroscopy (NAP-XPS), the interaction between Ni/YSZ electrodes and water vapor under both open-circuit and polarization conditions was investigated. Modifications to traditional porous Ni/YSZ cathodes were made to directly observe the functional electrode areas near the YSZ electrolyte. Results revealed dynamic changes in the oxidation states and composition of Ni/YSZ in H_2 and H_2O atmospheres. Additionally, the study emphasizes the impact of electrode oxidation on degradation during electrolysis and highlights the relationship between the nickel surface oxidation state and the cell's electrochemical performance. Cerium-based nanoparticles (NPs) were introduced to modify the surface of Ni/YSZ electrodes. Two types of NPs—Ni-doped ceria ($NiCeO_x$) and undoped ceria (CeO_y)—were synthesized and used to impregnate pre-fabricated Ni/YSZ cermet electrodes. The comparative study demonstrated that $NiCeO_x$ exhibited superior performance due to enhanced dispersion and reduced particle size. Synchrotron results further showed that Ni doping altered the redox properties of ceria, leading to stronger reduction of Ni/YSZ compared to CeO_y, which increased the number of active sites and improved electrolysis efficiency. Additionally, the thesis presents experimental trials involving vanadium and cobalt-doped ceria nanoparticles, although their performance enhancements were limited. Finaly the surface state of $La_{0.6}Sr_{0.4}Co_{0.2}Fe_{0.8}O_{3-\delta}$ (LSCF) electrodes were explored, focusing on Sr segregation. The study also examined Pr_6O_{11} as a potential alternative electrocatalyst for SOEC applications.

Overall, the research highlights the significant impact of nanoparticle surface modifications on the electrochemical performance of electrodes in water electrolysis, revealing substantial improvements in both efficiency and stability. The combination of innovative material design and advanced characterization techniques offers valuable insights for the future of sustainable energy solutions.

Acknowledgements

I would like to express my heartfelt gratitude to everyone who supported me during my PhD journey at the Université de Strasbourg, within the ICPEES (Institut de Chimie et Procédés pour l'Énergie, l'Environnement et la Santé). I would particularly like to acknowledge the financial support provided by the **China Scholarship Council (CSC)**, which made this PhD possible.

I am deeply indebted to my PhD supervisor, **Dr. Spyridon Zafeiratos**, for his invaluable scientific guidance, unwavering trust, and constant support throughout my doctoral studies. His availability, kindness, and patience created a welcoming and motivating research environment, making my time in the lab truly enjoyable. His insightful advice and dedication to my development as a researcher were crucial in overcoming challenges and achieving milestones during my PhD.

A special thanks goes to my group colleagues, **Dr. Mathias Barreau**, **Dr. Dingkai Chen**, and **Dr. Vasiliki Papaefthimiou** and **Nermine Chihi** for their generous sharing of knowledge and experience. Their support, both technical and scientific, has been instrumental in my research. I am particularly grateful to **Dr. Liping Zhong** for recommending me for this PhD opportunity. I also want to extend my gratitude to **Dingkai**, **Mathias** and **Nermine** for their assistance with experiments, their feedback on my writing, and their help in navigating life in France.

I would like to express my sincere appreciation to **Dr. Detre Teschner** and **Dr. Michael Hävecker** at the ISISS beamline of HZB/BESSY II, **Prof. Jan Knudsen** at the HIPPE beamline of MAX IV, and **Dr. Olivier Mathon**, **Dr. Davide Salusso** and their colleagues at the BM23 beamline of ESRF. The synchrotron experiments presented in this thesis would not have been possible without their expertise and collaboration.

Furthermore, I am grateful to my thesis jury members, **Dr. Jerome Laurencin**, **Dr. Nicolas Bion**, **Prof. Elena Savinova**, and **Prof. Mathias Barreau**, for their valuable comments, constructive suggestions, and time spent reviewing my work.

My gratitude extends to the technical and administrative staff at ICPEES, including **Alain Rach**, **Sécou Sall**, **Michèle Thomas**, **Agnès Orb**, and **Julien Bertrand**, for their assistance in navigating the logistical aspects of my research. A special thank you to **Dr. Thierry Dintzer** for his support with the SEM experiments.

I would like to extend my deepest thanks to my fiancée **Dr. Jingjing Wang** for her unwavering support and companionship. Her patience, understanding, and encouragement were vital in helping me overcome the many obstacles I faced throughout this journey. Her wisdom and insightful advice provided inspiration and guidance on many research issues. Without her love and support, this work would not have been possible. She has been my source of inspiration and my most thoughtful critic.

Additionally, I am grateful to my Chinese friends in Strasbourg—**Senlin Dong**, **Yinlin Luo**, **Haijuan Liu**, **Han Peng**, **Xiong Zhang**, **Yu Zhang** and many others—for their companionship and support, both in my daily life and throughout my PhD studies.

Lastly, and most importantly, I would like to express my deepest gratitude to **my parents** for their unwavering support and encouragement throughout this entire journey. Their love has been a constant source of strength and motivation.

Table of Content

Résumé

a) Introduction

Les problèmes liés aux émissions de gaz à effet de serre, à l'approvisionnement en énergie et à leurs coûts, ainsi qu'aux questions de santé publique et aux changements climatiques, incitent fortement à se tourner vers des ressources énergétiques respectueuses de l'environnement et durables. L'hydrogène est considéré comme un vecteur énergétique attractif et un moyen de stockage pour les sources d'énergie intermittentes [1,2]. Les SOECs (cellules d'électrolyse à oxyde solide) à haute température sont vues comme une méthode efficace pour l'électrolyse de l'eau en raison de la cinétique et de la thermodynamique favorables à des températures élevées [3,4]. En plus de leur haute efficacité, les SOECs produisent également de l'oxygène pur, ce qui améliore considérablement la viabilité économique du processus. Ainsi, les SOECs offrent un moyen de stockage d'énergie chimique ou servent de vecteur en convertissant l'énergie renouvelable ou l'énergie excédentaire des centrales fossiles en hydrogène ou en gaz de synthèse. Dans les années 1960, la NASA a d'abord démontré l'électrolyse de H_2O, CO_2 et des mélanges H_2O/CO_2 dans des SOECs pour la production d'oxygène dans les sous-marins et les engins spatiaux [5,6].

Cependant, les SOECs ne sont pas encore viables commercialement, principalement en raison des défis liés au développement de matériaux capables de répondre aux exigences de performance et de durabilité à des températures de fonctionnement élevées. Un dispositif SOC est constitué d'un électrolyte céramique pris en sandwich entre deux électrodes poreuses, permettant la conduction ionique et les réactions électrochimiques nécessaires à la conversion d'énergie. L'efficacité des SOECs dépend largement des taux de réaction électrochimique aux électrodes ainsi que de la vitesse de transport de l'oxygène dans l'électrolyte. Bien que certaines recherches visent à réduire les températures de fonctionnement à des niveaux moyens ou bas pour diminuer les coûts et améliorer la durabilité, les recherches sur les matériaux clés et la conception des systèmes SOECs en sont encore à leurs débuts. Les composites céramique-métal optimisés pour les SOFCs (piles à combustible à oxyde solide) demeurent la référence pour les électrodes cathodiques des SOECs.

Les problèmes de dégradation se divisent en effets réversibles et irréversibles. Les effets irréversibles sont liés à la stabilité mécanique de l'appareil SOEC, mais l'accent de ce travail est mis sur la compréhension de l'oxydation des surfaces d'électrodes, identifiée comme l'une des principales causes de dégradation réversible. Cela implique d'abord l'étude de la chimie de surface des électrodes Ni/YSZ dans une atmosphère de SOEC, en utilisant principalement la spectroscopie de photoélectrons à rayons X en conditions de pression quasi-ambiantes (NAP-XPS) pour examiner l'impact des conditions de surface sur les performances électrocatalytiques. Ensuite, à partir de ces résultats, la surface du Ni/YSZ a été modifiée à l'aide de nanoparticules d'oxyde de cérium (CeO_2), et d'autres nanoparticules cérium dopées avec différents ions ont été explorées. De plus, cette étude analyse les caractéristiques chimiques de surface de deux électrodes de type pérovskite SOEC après une longue période de fonctionnement.

b) Résultats et discussions

I. Révélation des caractéristiques clés de l'interface des électrodes Ni/YSZ des cellules à oxyde solide dans l'électroréduction de H_2O grâce à la spectroscopie photoélectronique aux rayons X opérando

Nous avons utilisé des techniques de NAP-XPS et NAP-HAXPES basées sur des sources synchrotron pour étudier les caractéristiques de surface et sous-surface des électrodes Ni/YSZ dans des conditions de circuit ouvert et sous polarisation.

Pour l'étude de la réduction par H_2 et l'oxydation par H_2O en fonction de la température, des électrodes Ni/YSZ calcinées ont été exposées à 0,5 mbar de H_2 à 250 °C, puis la température a été augmentée progressivement. Les spectres NAP-XPS du Ni 2p et Zr 3d ont été acquis après 15 minutes à chaque température spécifique. L'évolution des spectres Ni $2p_{3/2}$ en atmosphère de H_2 puis de vapeur d'eau en fonction de la température est illustrée dans la Figure 1a, avec les résultats de l'ajustement présentés dans la Figure 1b. La Figure 1b montre qu'environ 90 % du Ni^{2+} subit une réduction dans une plage étroite de température comprise entre 325 et 375 °C, tandis que 10 % du nickel oxydé résiste à la réduction même à 400 °C. Ce comportement est conforme à la réduction attendue du NiO par H_2, caractérisée par une période d'incubation qui diminue avec l'augmentation de la température. Après la formation initiale de Ni métallique, le processus de réduction s'accélère en raison de l'influence catalytique du Ni sur la réactivité de H_2 [7]. Le rapport des aires de pics Ni 2p/Zr 3d ($R_{Ni/Zr}$) diminue avec l'augmentation de la température, reflétant la réduction du nickel en surface, ce qui pourrait être attribué à des changements volumétriques et/ou un transfert de masse des particules de nickel lors de la réduction.

Après ce processus de réduction, l'électrode Ni/YSZ a été refroidie à 250 °C et H_2 a été remplacé par de la vapeur d'H_2O, puis la température a de nouveau été augmentée pour l'acquisition des spectres en présence de H_2O. Comme illustré dans le panneau supérieur de la Figure 1a, au-delà de 425 °C, de nouvelles caractéristiques apparaissent dans les spectres Ni $2p_{3/2}$, indiquant une ré-oxydation du Ni^0 par H_2O. Contrairement à la réduction par H_2, l'oxydation par H_2O s'étend sur une large gamme de températures. À 600 °C, environ 40 % du nickel reste sous forme métallique, comme illustré dans la Figure 1b. Le rapport $R_{Ni/Zr}$ reste relativement stable jusqu'à 500 °C, mais montre une augmentation soudaine au-delà de cette température.

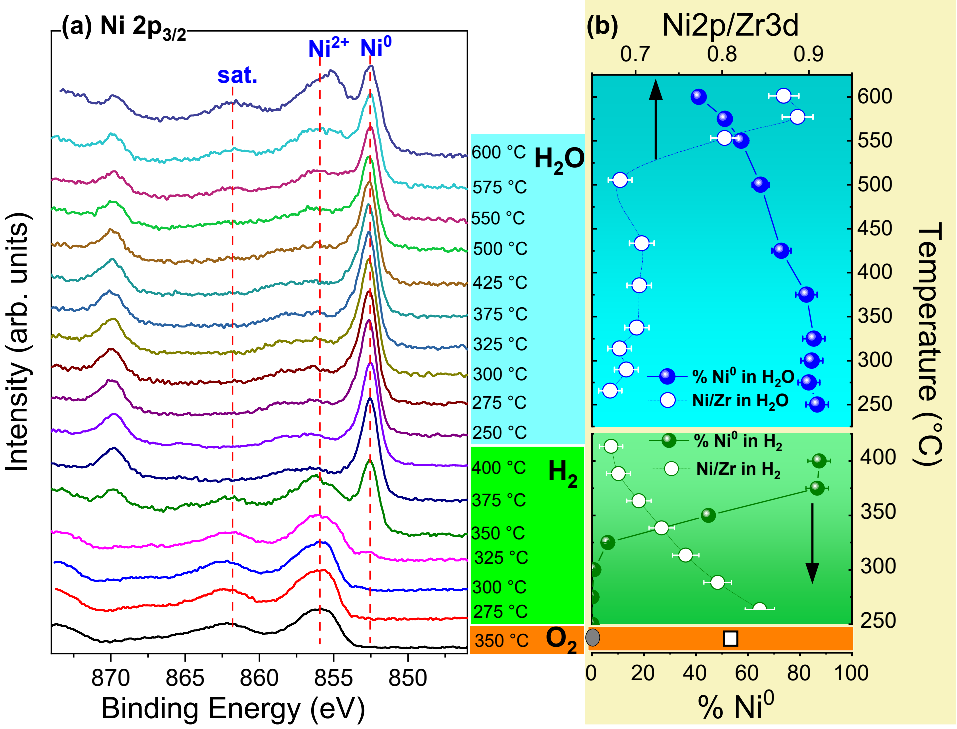

Figure 1. (a) présente les spectres NAP-XPS du Ni $2p_{3/2}$ des électrodes Ni/YSZ pré-calcinées en fonction de la température de recuit, mesurés avec une énergie photonique de 1065 eV sous une pression de 0,5 mbar d'O_2, de H_2 et de H_2O. **(b)** Le pourcentage atomique du composant métallique Ni (%Ni^0) par rapport à l'ensemble du spectre Ni $2p_{3/2}$, estimé par ajustement des pics, est montré à droite. Le rapport des aires des pics Ni 2p / Zr 3d, normalisé aux facteurs de sensibilité et au flux de photons, est également représenté. L'erreur sur les ratios $R_{Ni/Zr}$ et RNi/NiO est estimée à ±2 % et ±5 % respectivement.

Ensuite, les électrodes ont été soumises à des conditions d'électrolyse H_2O/H_2 afin d'examiner comment l'état d'oxydation de la surface du nickel influence les performances de la cellule. Il est essentiel de co-alimenter en H_2 avec H_2O pour éviter l'oxydation de l'électrode et sa désactivation rapide. Les résultats spectroscopiques ont été combinés avec l'analyse en ligne de la phase gazeuse et la caractérisation électrochimique de la cellule, permettant ainsi de corréler les états chimiques de surface avec les performances électrocatalytiques. L'électrode a d'abord subi un traitement sous pH_2O/pO_2 (9/1) à 750 °C pendant 15 minutes, puis l'atmosphère a été remplacée par du H_2 pour l'électrolyse H_2O/H_2 ($E_{W\text{-}C}$ = 2,5 V, pH_2O/pH_2 = 9/1 à 750 °C). Pour éclaircir l'effet de l'état de surface d'origine sur la performance de l'électrolyse, une seconde cellule a été prétraitée en enrichissant temporairement l'atmosphère en H_2 (le ratio pH_2O/pH_2 a été augmenté à 2/1 pendant moins d'une minute). Ainsi, deux électrodes ont été obtenues : l'une plus "oxydée" ($R_{Ni/NiO}$ d'environ 0,48) et l'autre plus "réduite" ($R_{Ni/NiO}$ d'environ 1,6). La densité de courant moyenne, la production d'O_2 et les diagrammes de Nyquist suggèrent que la cellule avec l'électrode "réduite" Ni/YSZ présente de meilleures performances que celle "oxydée". Ces résultats sont conformes aux attentes, à l'exception des spectres Ni 2p obtenus au début et à la fin du cycle d'électrolyse. L'estimation relative des quantités de Ni^0 et de NiO par ajustement des pics Ni 2p montre que les deux électrodes ont presque conservé leur état d'oxydation de surface initial, plutôt que de devenir toutes deux plus oxydées.

Afin de comprendre pourquoi le nickel de surface présente ce comportement « anti-oxydant », nous avons effectué des tests de profil en profondeur. La distribution en profondeur des phases oxydées et métalliques du nickel a été analysée à travers les spectres Ni 2p obtenus par les mesures NAP-XPS et NAP-HAXPES, en utilisant des photons incidents avec des énergies de 1065 eV et 4900 eV, permettant ainsi un profil de profondeur depuis la surface externe (1,6 nm) jusqu'aux couches sous-jacentes (12,1 nm). Comme le montrent les Figures 2, pendant les conditions d'électrolyse, les spectres Ni 2p présentent une similarité marquée aux deux profondeurs d'analyse, tandis qu'en circuit ouvert, ils diffèrent de manière significative. Le rapport $R_{Ni/NiO}$ a été approfondi à l'aide du logiciel SESSA, permettant de simuler la morphologie de la surface correspondante. Comme illustré, l'électrode "oxydée" Ni/YSZ présente une légère augmentation du $R_{Ni/NiO}$ à une profondeur d'analyse plus importante (Figure 2a), indiquant que le NiO se trouve principalement à la surface, avec un substrat de 45 % Ni^0 - 55 % NiO recouvert par des îlots de NiO de 17 % d'une épaisseur de 0,55 nm. Le $R_{Ni/NiO}$ reste pratiquement identique pour l'électrode plus « réduite » aux deux profondeurs d'analyse (Figure 2b), avec une composition de 63 % de nickel et 37 % de NiO. En circuit ouvert (Figure 2c), ils sont mieux simulés par une couche dense de NiO de 0,37 nm d'épaisseur couvrant un substrat composé de 40 % de Ni et de 60 % de NiO. Les résultats suggèrent une configuration inattendue entre le Ni0 et le NiO dans l'électrode partiellement oxydée Ni/YSZ, différente de l'oxydation classique des métaux de transition qui commence par la formation d'une fine couche d'oxyde en surface, comme observé en circuit ouvert. En tout cas, les expériences de photoémission operando apportent des preuves solides que pendant l'électrolyse, le NiO se forme principalement de manière horizontale ou latérale, plutôt que de progresser depuis la surface vers l'intérieur des particules de nickel comme cela se produit lors d'une oxydation conventionnelle en phase gazeuse.

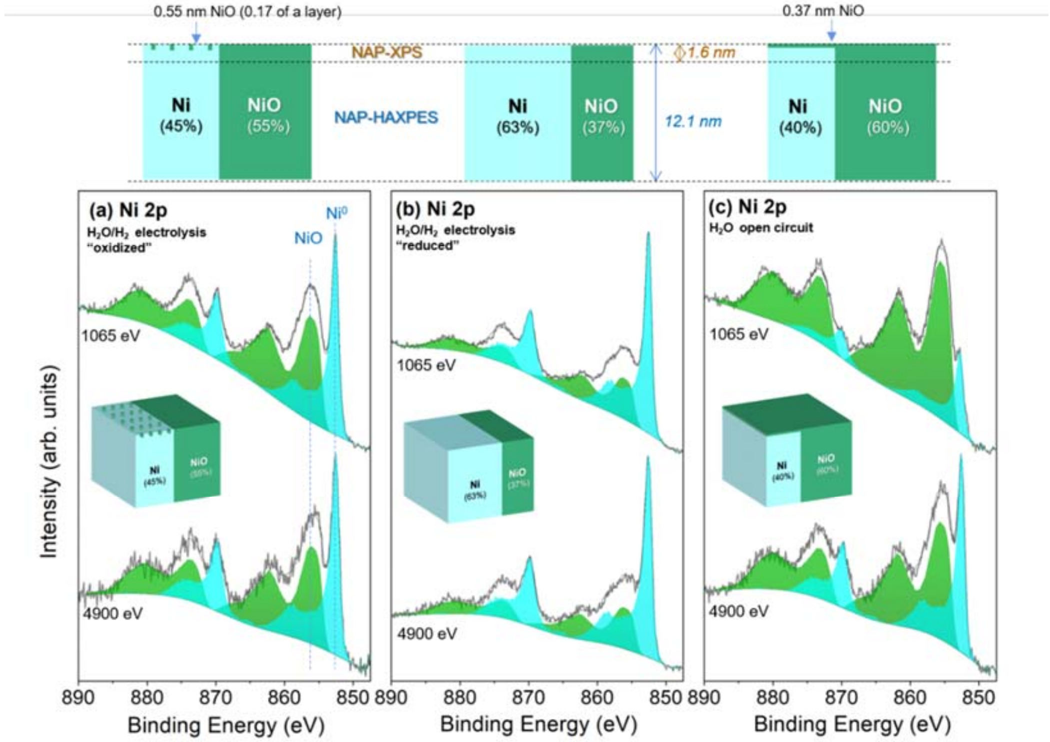

Figure 2. Les spectres de cœur Ni 2p ont été mesurés à l'aide de photons d'énergies de 1065 eV (NAP-XPS) et 4900 eV (NAP-HAXPES) sur l'électrode Ni/YSZ dans les conditions suivantes : **(a)** $E_{W\text{-}C}$ = 2,5 V, 1 mbar H_2O:H_2=9:1 à 750 °C (après un prétraitement de réduction modéré), **(b)** $E_{W\text{-}C}$ = 2,5 V, 1 mbar H_2O:H_2=9:1 à 750 °C (après un prétraitement de réduction sévère), et **(c)** circuit ouvert, 1 mbar H_2O à 750 °C (après réduction sous H_2). L'intervalle de temps entre les mesures NAP-XPS et NAP-HAXPES était d'environ 3 minutes. La morphologie de surface ayant permis d'obtenir l'ajustement optimal pour le $R_{Ni/NiO}$ expérimental dans la simulation SESSA est représentée en haut de la figure.

II. L'influence des nanoparticules de cérium dopées au nickel et non dopées sur les performances électrochimiques des cathodes Ni/YSZ lors de l'électrolyse de l'eau

Après avoir étudié l'état chimique de la surface des électrodes Ni/YSZ non modifiées (pristine), nous avons entrepris de rechercher l'amélioration des performances électrochimiques des électrodes Ni/YSZ par l'infiltration de deux types de nanoparticules d'oxyde de cérium ($Ni_{0.2}Ce_{0.8}O_{2-x}$ NPs et CeO_y NPs) sous forme de solutions organiques dans des électrodes cermet

Ni/YSZ pré-réduites. La technique utilisée par notre groupe permet d'éviter les étapes répétitives et lourdes d'infiltration et de co-frittage, tout en assurant une dispersion rapide et homogène des nanoparticules dans la structure de l'électrode, minimisant ainsi les risques d'agglomération et de blocage. Théoriquement, l'introduction de l'oxyde de cérium à la surface du Ni/YSZ pourrait offrir un grand nombre de sites d'interface d'oxyde de cérium, réduisant ainsi les pertes de surtension et augmentant la durabilité, tout en conservant les excellentes propriétés thermiques et la stabilité mécanique du Ni/YSZ. Parallèlement à la synthèse et à la caractérisation de ces nanoparticules, leur influence sur les performances électrochimiques des cathodes NiCe@NiYSZ a été évaluée.

Selon la méthode proposée, deux types de nanoparticules d'oxyde de cérium ont été préparées en solution organique : i) des nanoparticules de CeO_2 non dopées (CeO_y) et ii) des nanoparticules de CeO_2 dopées au Ni ($Ni_{0.2}Ce_{0.8}O_{2-x}$, abrégées en $NiCeO_x$) [8,9]. Tout d'abord, les propriétés physico-chimiques des nanoparticules à base de cérium en solution ont été étudiées à l'aide de plusieurs techniques de caractérisation. Les données de la thermogravimétrie (TGA) indiquent que le pourcentage de masse finale des $NiCeO_x$ est inférieur à celui des CeO_y, avec des valeurs moyennes de 23,0 ± 1,0 % et 33,2 ± 1,2 %, aboutissant à des concentrations massiques respectives de 4,9 mg/mL pour $NiCeO_x$ et 5,4 mg/mL pour CeO_y. La technique de diffusion dynamique de la lumière (DLS) a permis d'évaluer le profil de distribution de taille. Une proportion significative (77,9 %) des nanoparticules NiCeOx en solution dans l'hexane forme des agrégats d'une taille approximative de 0,75 µm, tandis que les nanoparticules de CeO_y forment des agrégats plus grands d'environ 1,32 µm, avec 79,9 % des particules atteignant cette taille. La diffraction des rayons X (XRD) a révélé la cristallinité des nanoparticules $NiCeO_x$ et CeO_y avant et après calcination. D'après l'équation de Debye-Scherrer, les tailles des cristallites des $NiCeO_x$ et CeO_y non calcinés ont été estimées à environ 3,8 ± 0,3 nm et 4,8 ± 0,5 nm, respectivement. Après calcination, les tailles des cristallites ont été calculées à 6,5 ± 0,2 nm et 7,4 ± 0,2 nm, respectivement.

Ensuite, nous avons procédé à l'infiltration des nanoparticules dans les électrodes Ni/YSZ (selon les étapes illustrées dans la Figure 3). Il y a eu des différences significatives dans les résultats et la quantité d'infiltration entre les deux types de nanoparticules. Nous supposons que ces variations sont principalement dues à l'effet d'agglomération des nanoparticules de CeO_y dans la phase liquide, ce qui rend leur imprégnation plus difficile. Les demi-cellules cermet Ni/YSZ supportées par électrolyte, produites par **Kerafol GmbH**, ont une épaisseur totale d'électrode de 40 à 45 µm. Nous avons découpé ces cellules en quarts d'une surface de 2 cm^2, soit une surface d'environ 0,785 cm^2. De simples calculs montrent que chaque 10 µL de nanoparticules de $NiCeO_x$ correspond à une charge de 18,06 mg/cm^3, tandis que pour CeO_y, chaque 10 µL permet une charge de 19,91 mg/cm^3.

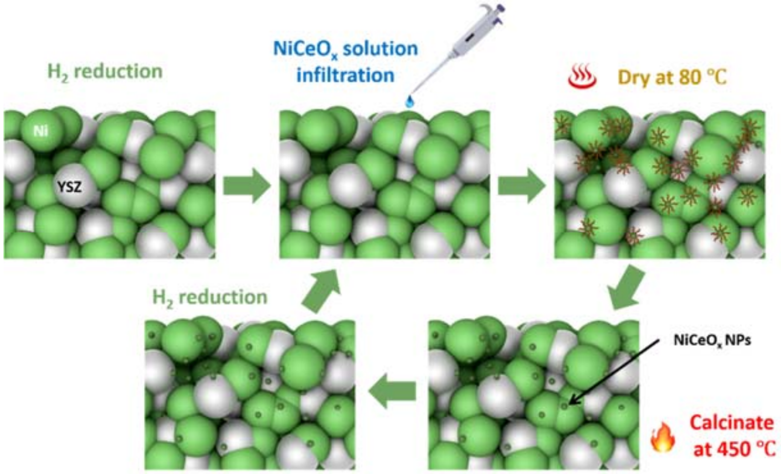

Figure 3. Représentation schématique du processus d'infiltration des nanoparticules $NiCeO_x$ et CeO_y sur des électrodes Ni/YSZ préfabriquées.

Pour élucider la performance électrochimique des échantillons infiltrés avec des nanoparticules $NiCeO_x$ et CeO_y, nous avons employé la chronoamperométrie, le balayage linéaire en escalier, les tests de stabilité à long terme et la spectroscopie d'impédance électrochimique (EIS). Pour l'infiltration de $NiCeO_x$, nous avons commencé avec une quantité de 10 µL, puis doublé à 20 µL, 40 µL, 80 µL, et enfin 160 µL. En ce qui concerne CeO_y, nous avons examiné des charges de 5 µL et 10 µL en raison de la taille des particules agrégées trop grande dans la phase liquide. Initialement, les cathodes Ni/YSZ ont subi une oxydation à 400 °C dans O_2, suivie d'une réduction à 700 °C dans H_2 afin d'éliminer le carbone organique. Ensuite, l'environnement gazeux a été changé pour une atmosphère d'électrolyse de 2 mbar de H_2O et H_2 (1:1), avec une température d'électrolyse maintenue de manière constante à 700 ± 5 °C. Au cours des expériences d'électrolyse, un spectromètre de masse à quadrupôle (QMS) a été utilisé pour analyser la composition des gaz d'échappement.

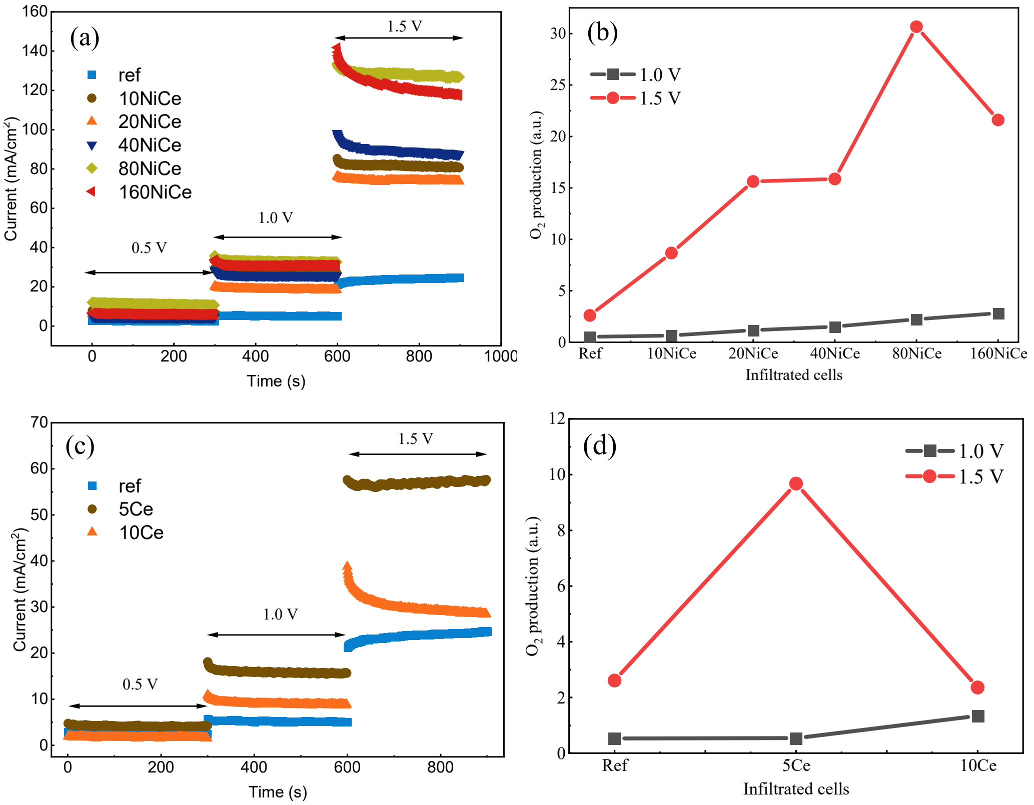

Figure 4. (a) Six groupes de résultats expérimentaux de chronoamperométrie (CA) pour le NiYSZ imprégné avec différentes quantités de nanoparticules $NiCeO_x$; **(b)** Signal QMS intégré correspondant pour le gaz O_2 (m/e 32) à chaque potentiel durant les expériences avec les nanoparticules $NiCeO_x$, enregistré dans la chambre de réaction par spectrométrie de masse en ligne ; **(c)** Trois groupes de résultats expérimentaux de CA pour le NiYSZ imprégné avec différentes quantités de nanoparticules CeO_y; **(d)** Signal QMS intégré correspondant pour le gaz O_2 à chaque potentiel durant les expériences avec les nanoparticules CeO_y. Conditions d'électrolyse : atmosphère de 2 mbar de H_2O et H_2 (1:1), avec la température d'électrolyse maintenue de manière constante à 700 ± 5 °C.

Le cellule infiltrée avec des nanoparticules $NiCeO_x$ montre des résultats d'électrolyse optimaux à une charge de 80 µL (voir Fig. 4a), où l'augmentation du courant d'électrolyse est d'environ quatre fois à 0,5 V, six fois à 1,0 V et cinq fois à 1,5 V, atteignant 130 mA/cm^2 par rapport à l'électrode non infiltrée. Les performances diminuent à une charge de 160 µL. Dans les expériences d'imprégnation avec des nanoparticules CeO_y (voir Fig. 4c), la performance optimale se produit à une charge de 5 µL, atteignant environ 57 mA/cm^2. Les signaux d'O_2 détectés par le QMS présentés dans les Fig. 4b et 4d correspondent bien aux mesures électriques, confirmant que l'amélioration des performances est attribuée à une plus grande activité électrocatalytique des électrodes après modification. Les résultats de l'EIS montrent également que la cellule infiltrée avec des nanoparticules $NiCeO_x$ présente une impédance totale plus faible, principalement avec une diminution de la résistance à la polarisation (R_p) à mesure que la quantité d'imprégnation augmente. Les comparaisons avec la méthode de balayage linéaire et la stabilité à moyen terme confirment également que les nanoparticules $NiCeO_x$ montrent des performances de modification supérieures.

Pour explorer davantage l'impact du dopage par le nickel sur les nanoparticules CeO_y, des expériences de photoélectronique à pression ambiante (NAP-XPS) ont été réalisées. Pour la préparation des échantillons, des suspensions de nanoparticules ont été déposées sur un mince film d'or. Les échantillons ont ensuite été soumis à un processus de séchage et de calcination à 450 °C pour oxyder complètement et volatiliser le solvant organique ainsi que le revêtement d'oléylamine. Pendant la caractérisation, 1 mbar de H_2 a été introduit dans la chambre NAP-XPS pour créer une atmosphère réductrice. Deux énergies de photon différentes (1065 eV et 1800 eV) ont été utilisées pour analyser chaque échantillon. Une comparaison des deux types de nanoparticules révèle des différences notables (voir Fig. 5). Le taux de réduction des nanoparticules CeO_y progresse progressivement avec l'augmentation des températures, suivant une tendance relativement lisse. En revanche, les nanoparticules $NiCeO_x$ subissent une réduction rapide à 450 °C, et de 450 °C à 550 °C, le taux de réduction ralentit. L'état de valence moyen final des nanoparticules $NiCeO_x$ est inférieur à celui des nanoparticules CeO_y, d'environ 0,32 (couche superficielle) et 0,2 (couche profonde). Cette découverte fournit un aperçu supplémentaire sur les raisons pour lesquelles les électrodes imprégnées de nanoparticules $NiCeO_x$ présentent une performance d'électrolyse supérieure par rapport à celles modifiées avec des nanoparticules CeO_y.

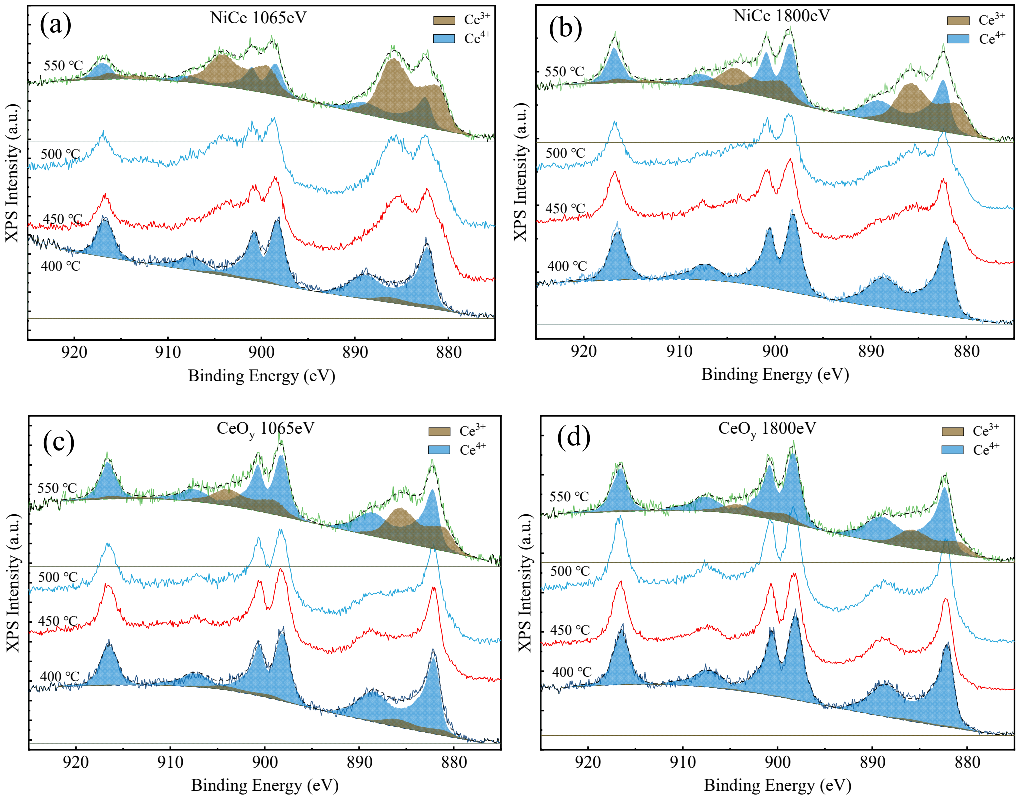

Figure 5. (a) Spectres de Ce dans les nanoparticules NiCe via une énergie de photon de 1065 eV à 400 °C, 450 °C, 500 °C et 550 °C lors de la mesure NAP-XPS sous une atmosphère de H_2 à 1 mbar ; **(b)** Spectres de Ce dans les nanoparticules NiCe via une énergie de photon de 1800 eV à 4 températures pendant la mesure NAP-XPS; **(c)** Spectres de Ce dans les nanoparticules CeOy via une énergie de photon de 1065 eV à 4 températures lors de la mesure NAP-XPS ; **(d)** Spectres de Ce dans les nanoparticules CeO_y via une énergie de photon de 1800 eV à 4 températures pendant la mesure NAP-XPS.

III. Étude de l'effet sur les électrodes Ni/YSZ imprégnées de nanoparticules de céramique dopées au vanadium et au cobalt

Encouragés par les nanoparticules de céramique dopées au nickel, nous avons commencé à explorer l'application d'autres cations dopés dans les nanoparticules de céramique à l'électrode Ni/YSZ pour l'électrolyse de l'eau à haute température. Les éléments vanadium (V) et cobalt (Co) se présentent comme de bons choix. En nous basant sur différentes méthodes de synthèse trouvées dans la littérature, nous avons produit des nanoparticules VO_x, des nanoparticules de V fabriquées avec des schiffs bases (abrégées V-L NPs) et des nanoparticules de V-octa ajoutées avec de l'octadecanol pour ajuster la taille des particules. De plus, nous avons synthétisé des nanoparticules de céramique dopées au V ($VCeO_x$) et des nanoparticules de céramique dopées au Co ($CoCeO_x$). Après caractérisation DRT, nous avons constaté que la taille moyenne des nanoparticules VO_x, V-L et V-octa est d'environ 38 nm, tandis que la taille des nanoparticules $VCeO_x$ est d'environ 12,9 nm et celle des nanoparticules $CoCeO_x$ est d'environ 4,5 nm.

Nous avons ensuite procédé à des tests de performance électrolytique sur les trois types de nanoparticules de V, en utilisant une méthode similaire à celle appliquée pour les $NiCeO_x$ et CeO_y. Les résultats n'ont toutefois pas montré d'effet de promotion des nanoparticules de V sur l'électrolyse de l'eau à haute température.

Nous avons utilisé la technologie NAP-XPS pour caractériser les effets de dopage des nanoparticules $VCeO_x$ et $CoCeO_x$, afin d'explorer l'impact de ces deux éléments sur la réductibilité du Ce. Pendant la caractérisation, 1 mbar de H_2 a été introduit, avec des températures variant de 200 °C à 800 °C avec une montée de 10 °C /min. Les résultats montrent que les nanoparticules VCe se distinguent par leur comportement, car entre 200 °C et 400 °C, le Ce est presque complètement réduit. La courbe de réduction du Ce dans les nanoparticules $CoCeO_x$ est très similaire à celle des $NiCeO_x$.

Les résultats des expériences électrochimiques montrent que les nanoparticules $VCeO_x$ ont presque un effet négatif lors des expériences d'électrolyse de l'eau à haute température ; plus la quantité d'imprégnation est élevée, plus la performance se dégrade, entraînant une augmentation de la résistance à la polarisation. En revanche, les électrodes Ni/YSZ imprégnées de nanoparticules $CoCeO_x$ affichent effectivement de meilleures performances, bien que l'augmentation de la quantité d'imprégnation ne conduise plus à une amélioration des performances (voir Figure 6).

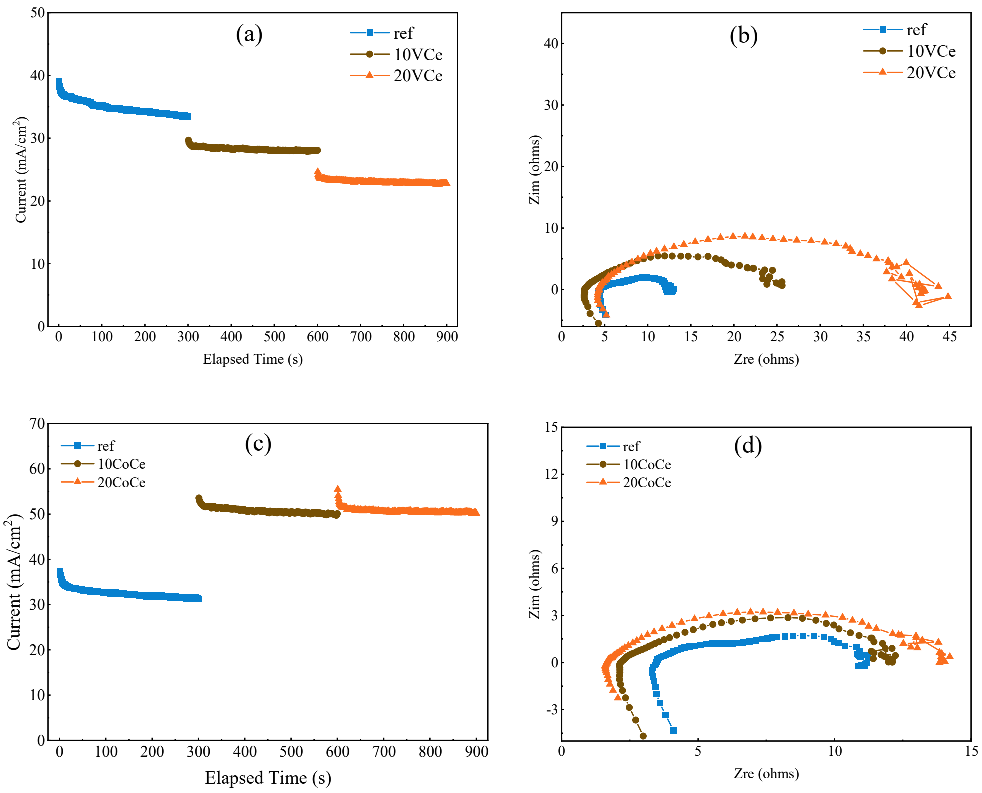

Figure 6. (a) Résultats de l'électrolyse CA de H_2O + H_2 avec différentes charges de nanoparticules VCe. Il est à noter que différentes charges de solution de nanoparticules ont été imprégnées sur la même électrode Ni/YSZ ; **(b)** EIS des résultats de H_2O + H_2 avec différentes charges de nanoparticules VCe ; **(c)** Résultats de l'électrolyse CA de H_2O + H_2 avec différentes charges de nanoparticules CoCe; **(d)** EIS des résultats de H_2O + H_2 avec différentes charges de nanoparticules CoCe.

Nous avons utilisé la spectroscopie XAFS combinée à des mesures de température programmée sous atmosphères contrôlées pour fournir des résultats de caractérisation spectroscopique plus complets. Les mesures de XAFS au seuil K du nickel ont été réalisées en mode transmission. Les nanoparticules de cérium dopées et non dopées au nickel, au cobalt et au vanadium ont ensuite été imprégnées dans des électrodes Ni/YSZ, puis calcinées dans un four à mufle à 600 °C pendant une heure pour assurer une oxydation complète. Par la suite, une caractérisation de réduction programmée en température par XAFS a été effectuée dans une atmosphère d'hydrogène, avec une plage de température allant de 25 °C à 480 °C (avec un taux de chauffage d'environ 8 °C/min). Les résultats XANES et EXAFS obtenus lors de la montée en température ont été analysés (voir Figure 7). Nous avons réalisé un ajustement par combinaison linéaire

(Linear Combination Fitting, LCF) pour chaque échantillon en fonction de la température, afin de montrer l'ampleur de la réduction à différentes températures.

Les données XANES révèlent un bord de montée distinct pour tous les échantillons. Ce bord de montée est plus prononcé dans les échantillons imprégnés de nanoparticules par rapport à l'échantillon de référence non traité, indiquant la présence d'une certaine quantité de nickel réduit dans ces échantillons. Cela suggère que les nanoparticules imprégnées entravent l'oxydation de l'électrode Ni/YSZ pendant le processus de calcination à 600 °C. En revanche, seul l'échantillon de référence non traité présente des pics Ni-O plus prononcés, qui correspondent à l'état oxydé. Un examen plus attentif révèle que, dans les électrodes imprégnées de nanoparticules CeO_2 et VCe, la majeure partie du nickel existe sous forme de liaisons Ni-Ni, tandis que les échantillons CoCe et NiCe montrent une proportion plus élevée de caractéristiques Ni-O.

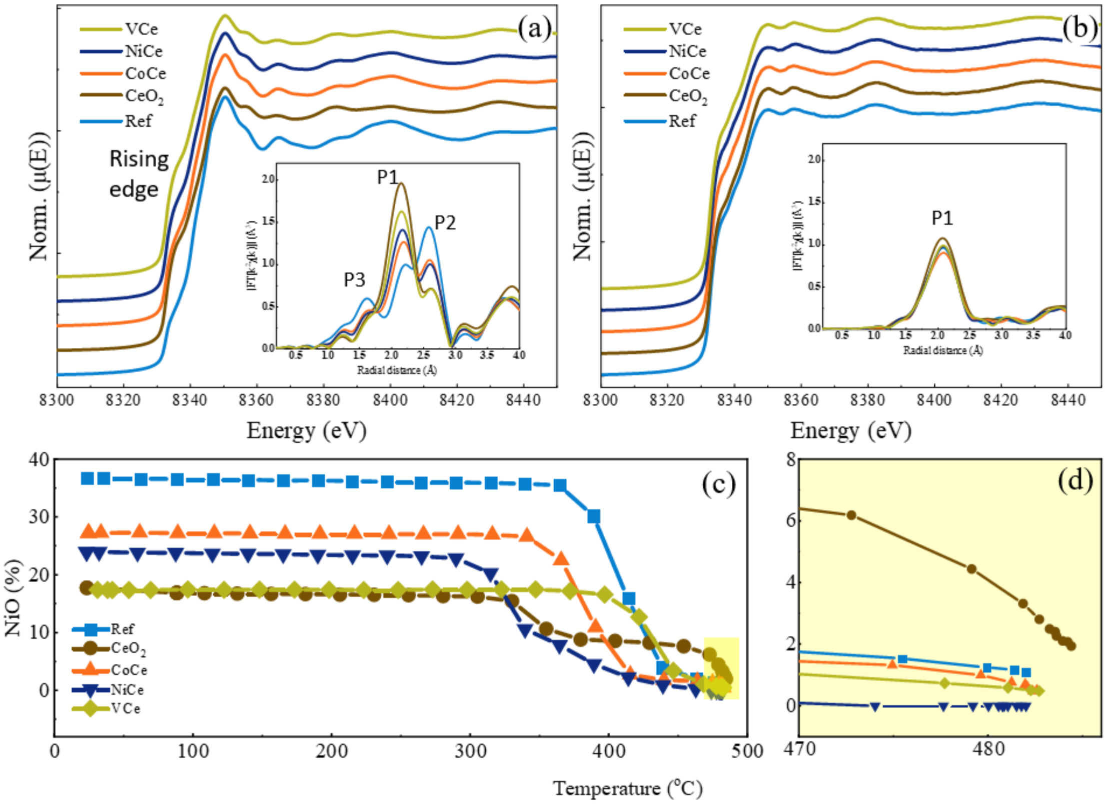

Figure 7. (a) XANES et FT-EXAFS pour cinq échantillons mesurés à température ambiante ; **(b)** XANES et FT-EXAFS pour les mêmes cinq échantillons mesurés à 480 °C; **(c)** Dépendance de la température du LCF pour les cinq échantillons ; **(d)** Zoom sur la région à haute température du graphique (c).

L'ajustement par combinaison linéaire (LCF) de chaque échantillon en fonction de la température révèle que les électrodes Ni/YSZ imprégnées de CeO_2, NiCe et CoCe sont plus facilement réduites. En revanche, les nanoparticules VCe entravent clairement la réduction de l'électrode, ce qui explique pourquoi l'imprégnation de nanoparticules VCe entraîne des résultats électrochimiques moins performants.

IV. Analyse de l'évolution de la surface des électrodes Pr-GDC et LSCF après des tests électrochimiques prolongés.

Un des facteurs critiques limitant le développement des cathodes LSCF est la dégradation des performances causée par la ségrégation de Sr, induite par des facteurs thermiques et électroniques [10,11]. Il est bien connu que la polarisation électrochimique influence de manière significative la ségrégation de Sr à la surface des électrodes poreuses LSCF, le Sr ségrégué ayant tendance à pénétrer à travers la couche de barrière de cérine pour réagir avec l'électrolyte YSZ, formant une phase isolante $SrZrO_3$ [12]. Nous avons discuté des caractéristiques intercalaires de deux électrodes à oxygène et comparé les changements observés avant et après des expériences à long terme. Les électrodes étudiées comprennent $LaNi_{0.6}Fe_{0.4}O_3$ (LNF) / PrO_x-$Ce_{0.9}Gd_{0.1}O_{2-\delta}$ (Pr-GDC) et $La_{0.6}Sr_{0.4}Co_{0.2}Fe_{0.8}O_{3-\delta}$ (LSCF) / $La_{0.6}Sr_{0.4}Co_{0.2}Fe_{0.8}O_{3-\delta}$-$Ce_{0.8}Gd_{0.2}O_{2-\delta}$ (LSCF-GDC, 50:50 %) en tant qu'électrodes à oxygène dans des cellules électrolytiques de type pérovskite. Les cellules analysées ont été fabriquées et ont subi des tests électrochimiques dans notre laboratoire collaboratif.

Nous mettrons l'accent sur les deux couches de l'électrode. Pour faciliter la présentation, nous désignerons la couche supérieure de l'électrode à oxygène architecturée en double couche comme la couche collectrice de courant, abrégée en CCL. La couche située sous la CCL, plus proche de l'électrolyte, a été optimisée pour l'activité électrocatalytique et est désignée comme la couche fonctionnelle, abrégée en FL. Nous avons exposé une partie de la FL par grattage mécanique afin de faciliter les études par photoémission.

Concernant les autres parties de la structure des cellules électrolytiques, à savoir la couche de barrière poreuse GDC (BL) et la couche électrolytique $Y_{0.16}Zr_{0.84}O_{1.92}$ (8YSZ), ainsi que l'électrode H_2 poreuse Ni-YSZ, nous ne nous y attarderons pas ici. Les deux cellules électrolytiques ont subi des expériences d'électrolyse à long terme dans des conditions définies dans le laboratoire collaboratif, accompagnées de leurs échantillons témoins respectifs. Quatre échantillons ont été nommés pour faciliter les références ultérieures: Pr-GDC_{REF} (échantillon témoin) et Pr-$GDC_{3.6k}$ (échantillon ayant subi une électrolyse H_2O+H_2 pendant 3600 heures), ainsi que $LSCF_{REF}$ (échantillon témoin) et $LSCF_{DRY}$ (échantillon ayant subi une électrolyse H_2O+H_2 pendant 5000 heures).

Nous avons d'abord utilisé la technique NAP-XPS pour quantifier la composition de surface des échantillons Pr-GDC_{REF} et Pr-$GDC_{3.6k}$. Les spectres de balayage caractéristiques enregistrés avec une énergie de photon de 1300 eV ont confirmé la présence d'impuretés de silicium sur ces deux échantillons. Par la suite, nous avons effectué une caractérisation par spectroscopie à rayons X à dispersion d'énergie (EDS ou EDX). Les deux caractérisations ont été réalisées sur les mêmes échantillons et aux mêmes emplacements. La quantification basée sur EDS fournit la composition en vrac de l'échantillon, tandis que l'AP-XPS reflète la composition de surface. Les concentrations atomiques (%) des électrodes Pr-GDC_{REF} et Pr-$GDC_{3.6k}$ dans les régions CCL et FL ont été calculées et sont résumées dans la Figure 8a. Les concentrations atomiques calculées à partir des spectres EDS pour chaque échantillon dans les zones d'électrode CCL et FL sont présentées dans la Figure 8b.

L'observation la plus frappante est que les éléments LNF et Pr-GDC ne sont pas confinés dans la zone attendue. Pour l'échantillon GDCREF, environ 40 % des éléments détectés correspondent à LNF, une proportion qui augmente à 58 % après les tests d'électrolyse. De plus, la CCL contient des quantités significatives de praséodyme (Pr), atteignant jusqu'à 45 %, alors qu'on s'attendait à ce que le Pr soit limité dans la FL. La concentration de surface de Ce augmente légèrement après l'électrolyse, suggérant une possible reconstruction entraînant une plus grande exposition de GDC à la surface de l'électrode. En comparant la composition de surface des échantillons Pr-GDC_{REF} et Pr-$GDC_{3.6k}$, l'électrode O_2 avant et après l'électrolyse, la composition de la CCL reste pratiquement inchangée. Cependant, dans la FL, la concentration des éléments associés à LNF augmente au détriment de Pr. Les profils de concentration dépendants de la profondeur révèlent que Pr est plus concentré à la surface, tandis que La (représentant les particules LNF) est plus présent à des profondeurs plus importantes. Pendant ce temps, Ce maintient une concentration relativement constante à travers la profondeur analysée.

a) AP-XPS (surface)

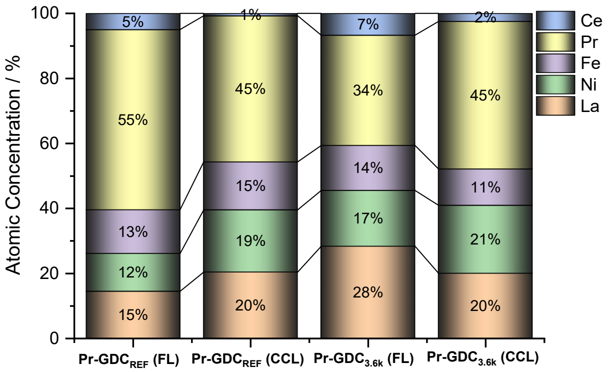

b) EDS (bulk)

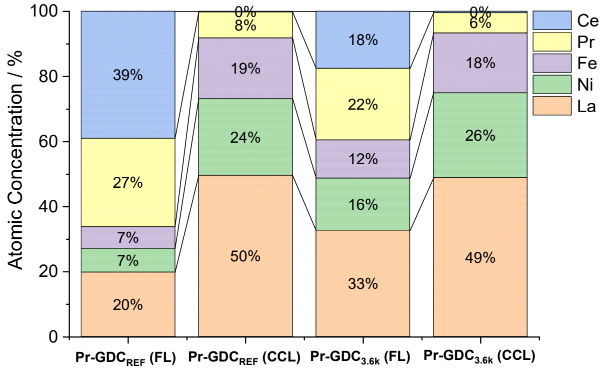

Figure 8. Des graphiques en colonnes empilées illustrant les concentrations atomiques des éléments de surface (en at. %) dans la FL et la CCL des électrodes Pr-GDC$_{REF}$ et Pr-GDC$_{3.6k}$, basés sur **(a)** les spectres NAP-XPS et **(b)** les spectres EDS. Il convient de noter que les profondeurs d'analyse des deux méthodes diffèrent considérablement, l'AP-XPS sondant environ 2 nm (composition de surface) et l'EDS sondant environ 2 µm (composition en vrac), permettant ainsi une corrélation entre les mesures de surface et en vrac des électrodes.

Les résultats de quantification des données EDS montrent à la fois des similarités et des différences par rapport à ceux fournis par les mesures NAP-XPS. Ces résultats confirment la présence de LNF dans la région FL et indiquent une augmentation significative de la concentration de LNF après électrolyse. Cela suggère également que le LNF forme probablement des agrégats distincts au contact du Pr-GDC, plutôt que de se répandre uniformément sur sa surface. En revanche, la quantité relative de Pr est significativement plus élevée dans les mesures NAP-XPS par rapport à l'EDS. Cela peut s'expliquer par la tendance du Pr à migrer vers la surface des particules de GDC et de LNF.

L'analyse de l'état chimique de surface révèle l'absence du satellite à 945,6 eV, et le rapport relativement faible entre la zone des pics principaux et celle des satellites dans l'échantillon Pr-GDC$_{3.6k}$ suggère que presque tout le Pr est sous forme de Pr^{3+} dans cet échantillon, probablement en tant que Pr$_2$O$_3$. En revanche, la présence de la caractéristique 4f^1 dans Pr-GDC$_{\text{REF}}$ indique la présence de Pr^{4+}.

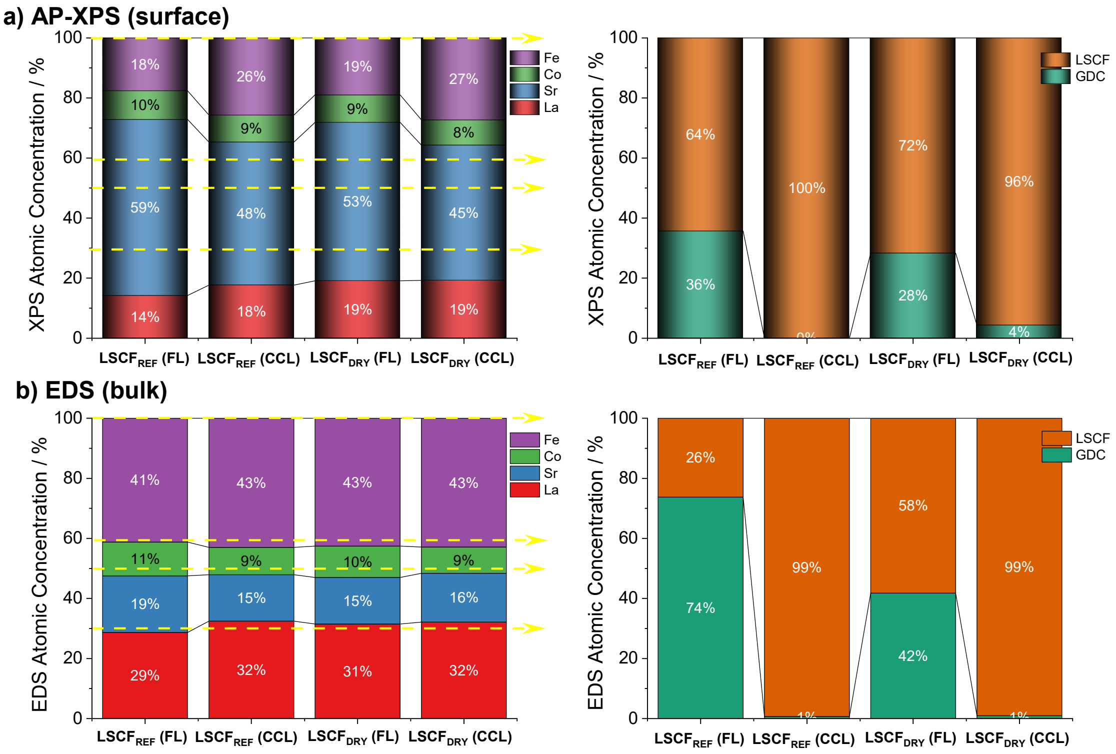

Figure 9. Les graphiques en colonnes empilées des concentrations atomiques dans les zones FL et CCL des électrodes LSCF$_{\text{REF}}$ et LSCF$_{\text{DRY}}$, dérivés des spectres **(a)** NAP-XPS et **(b)** EDS. Les graphiques à gauche montrent la composition de LSCF, tandis que ceux à droite présentent la distribution entre LSCF et GDC. Il est à noter que les profondeurs d'analyse des deux méthodes diffèrent considérablement, l'AP-XPS sondant environ 2 nm (composition de surface) et l'EDS environ 2 µm (composition en vrac), permettant ainsi d'établir une corrélation entre les mesures de surface et de volume des électrodes.

Un deuxième ensemble d'électrodes (LSCF) a été analysé en utilisant la même approche. Aucune impureté de surface commune, telle que le silicium, n'a été détectée non plus. Plusieurs observations intéressantes peuvent être tirées des concentrations atomiques (Figure 9a à gauche). Premièrement, le Sr est détecté à des concentrations significativement plus élevées, variant de 45 % à 59 %, par rapport à la composition en vrac attendue du pérovskite, qui est d'environ 20 %. Cela indique une ségrégation de surface substantielle du Sr, déjà survenant avant l'opération électrochimique lors du prétraitement de réduction de l'électrode H_2. La Figure 9a à droite révèle une concentration de Sr significativement plus élevée dans la zone FL, au détriment du Fe, que l'électrode soit soumise à l'électrolyse ou simplement à une cellule de référence de réduction. Fait intéressant, après 5000 heures d'électrolyse ($LSCF_{DRY}$), il y a une diminution relative de la concentration de Sr dans les zones FL et CCL de l'électrode. Ces résultats suggèrent qu'une réorganisation significative de la surface ne se produit pas pendant l'électrolyse, mais est largement achevée pendant la phase de prétraitement. Un autre résultat intéressant est qu'après l'opération d'électrolyse (c'est-à-dire, $LSCF_{DRY}$), la concentration de GDC diminue dans la FL.

La quantification EDS de la composition en vrac présentée dans la Figure 9b révèle que l'augmentation du signal de Sr observée dans les mesures NAP-XPS n'est pas détectée dans l'analyse EDS, ce qui confirme que la ségrégation de Sr est localisée dans la couche de surface la plus externe. Enfin, l'analyse de la distribution de surface indique que le pourcentage de Sr plus élevé et de La plus faible pourrait résulter de la substitution partielle de La par des cations Sr aux sites A du réseau pérovskite.

c) Conclusion générale

Cette thèse examine les performances électrochimiques ainsi que la chimie de surface des cellules d'électrolyse à oxyde solide avancées (SOEC), en mettant un accent particulier sur le comportement des électrodes Ni/YSZ durant l'électrolyse de l'eau. Les SOEC présentent un potentiel considérable pour produire de l'hydrogène via l'électrolyse de l'eau et pour le stockage d'énergie, tandis que les piles à combustible à oxyde solide (SOFC) utilisent l'hydrogène pour générer de l'électricité. Étant donné la rentabilité, la compatibilité thermique et la haute conductivité des composites à base de nickel, qui sont largement employés dans les applications industrielles, cette recherche se concentre sur l'amélioration de ces matériaux par le biais de modifications de surface.

L'interaction entre les électrodes Ni/YSZ et la vapeur d'eau a été analysée à l'aide de la spectroscopie de photoélectrons par rayons X à pression quasi ambiante (NAP-XPS), dans des conditions de circuit ouvert et de polarisation. Des adaptations ont été effectuées sur les cathodes poreuses traditionnelles en Ni/YSZ pour permettre l'observation directe des zones fonctionnelles situées à proximité de l'électrolyte YSZ. Les résultats ont mis en évidence des variations dynamiques des états d'oxydation et de la composition de Ni/YSZ dans des atmosphères de H_2 et de H_2O. De plus, cette étude met en avant l'effet de l'oxydation des électrodes sur la dégradation au cours de l'électrolyse, tout en soulignant le lien entre l'état d'oxydation de la surface du nickel et les performances électrochimiques de la cellule.

Des nanoparticules de cérium (NP) ont été intégrées pour modifier la surface des électrodes Ni/YSZ. Deux types de nanoparticules — cérium dopé au nickel ($NiCeO_x$) et cérium non dopé (CeO_y) — ont été synthétisés et utilisés pour imprégner des électrodes métalliques Ni/YSZ préfabriquées. L'analyse comparative a révélé que $NiCeO_x$ offrait de meilleures performances en raison d'une dispersion accrue et d'une taille de particules réduite. Les résultats obtenus par synchrotron ont aussi montré que le dopage au nickel modifiait les propriétés rédox du cérium, entraînant une réduction plus marquée de Ni/YSZ par rapport à CeO_y, ce qui augmentait le nombre de sites actifs et améliorait l'efficacité de l'électrolyse.

En outre, des essais expérimentaux ont impliqué des nanoparticules de cérium dopées au vanadium et au cobalt, bien que les améliorations de performances aient été limitées. En conclusion, cette recherche souligne l'influence significative des modifications de surface des nanoparticules sur les performances électrochimiques des électrodes Ni/YSZ dans l'électrolyse de l'eau, mettant en évidence des avancées notables en termes d'efficacité et de stabilité. La combinaison d'une conception novatrice des matériaux avec des techniques de caractérisation avancées offre des perspectives précieuses pour le développement de solutions énergétiques durables.

Enfin, les mécanismes de dégradation des électrodes $La_{0.6}Sr_{0.4}Co_{0.2}Fe_{0.8}O_{3-\delta}$ (LSCF) ont été étudiés, en se concentrant sur la ségrégation du Sr, qui provoque la formation de phases isolantes telles que le $SrZrO_3$, entravant les réactions de réduction de l'oxygène (ORR). L'étude a également exploré l'utilisation du Pr_6O_{11} comme catalyseur électrochimique alternatif pour les applications RSOC, montrant son potentiel à réduire la dégradation associée au Sr.

This page intentionally left blank

Chapter 1. Literature Review

1.1 Background

In the face of the world's rapidly growing population and economy, the challenges of energy scarcity and environmental pollution have become critical issues that threaten the sustainable development of human society. Problems related to greenhouse gas emissions, energy supplies and their costs, health issues and climate change are strong motives to shift towards environmentally friendly and sustainable energy resources. The current major energy suppliers are based mainly on non-renewable fuel sources like coal, petrol and natural gas. The expected time horizon of fossil fuels usage, expressed as the ratio of resources to production (R/P), is currently estimated to be about 50 years for natural gas and crude oil, and about 139 years for coal [13]. A progressive increase is observed in the demand for primary and final energy, e.g. electricity consumption in 1985 – 2023 increased 3 times from the level of 9879.2 TWh to 29924.8 TWh [14]. International Energy Agency (IEA) [15] predicts that the global energy demand will increase by about 50% until 2030.

Unfortunately, consumption of energy is directly related to the depletion of non-renewable resources (NRR) and rejection of harmful substances and greenhouse gases (GHG) into the environment. The high consumption rate threatens the availability of NRR for future generations as mentioned on the 2023 BP Energy Outlook [16] shown in Figure. 1.1a. Nevertheless, in an optimistic scenario it is predicted that in the coming 25 years the consumption of renewable energy sources will reach about 30% of the global energy consumption as shown in Figure. 1.1b.

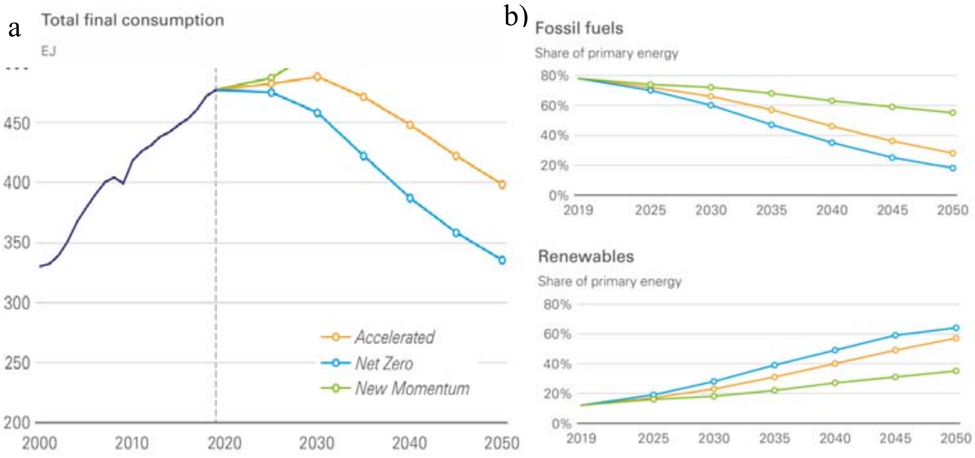

Figure 1.1 a) Primary energy consumption by end use sector expected scenario, **b)** The global energy consumption prediction from 2023 BP Energy Outlook. Reproduced with permission of Ref. [16], Copyright of ©2024 BP p.l.c.

A deep energy transformation is required to slow down the climate change and degradation of the natural environment. One of the ways to reduce these negative effects is increasing the share of renewable energy sources (RES) in the global energy balance, Figure 1.2 presents the projected future energy demand structure as forecasted by the BP Energy Outlook. However, RES, such as wind and solar, are usually intermittent in the sense that they are not continuously available. This fact points to the necessity of efficient technologies to store energy during power peak loads by converting it into another energy form easy to store and transfer [17]. IEA predicts that grid-scale battery storage in particular needs to grow significantly. In the Net Zero Scenario, installed grid-scale battery storage capacity expands 35-fold between 2022 and 2030 to nearly 970 GW [18].

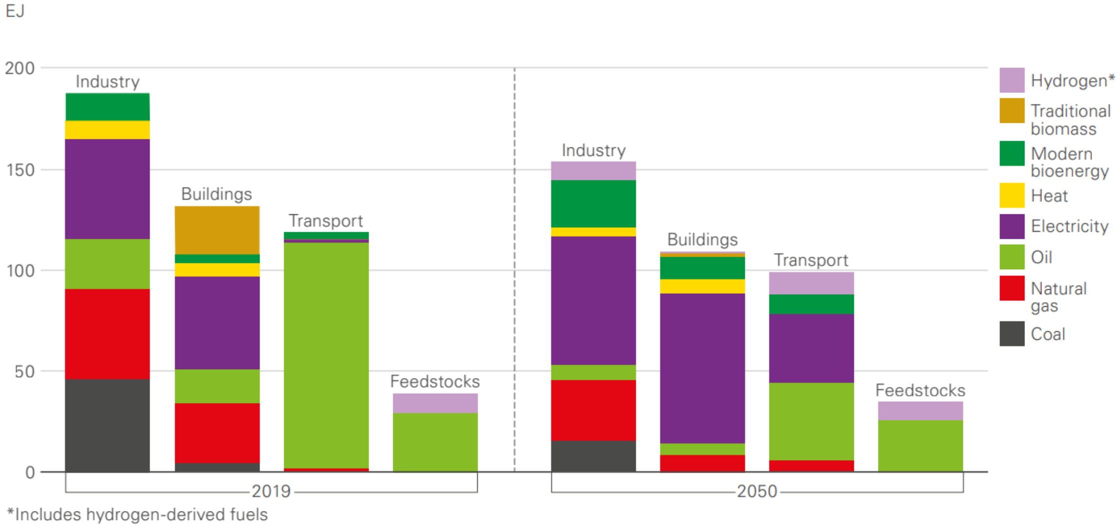

Figure 1.2. Final energy demand by sector and fuel in Accelerated. Energy gradually electrifies, together with an increasing role for hydrogen and bioenergy in hard-to-abate sectors. Reproduced with permission of Ref. [16], Copyright of ©2024 BP p.l.c.

Hydrogen is considered as an attractive energy carrier and storage medium for intermitted energy sources. Additionally, as compared to other fuels, hydrogen has the highest calorific value, which is the amount of heat released during the combustion of a specified amount of it [1,2,19]. Hydrogen is barely found as pure element in nature but it is a main component of other compounds. The global production of hydrogen is mainly based on fossil fuels (i.e. by using steam reforming and coal gasification processes). Synthesis gas (syngas, i.e. a mixture primarily of CO and H_2) is the result of steam reforming and coal gasification reactions, which is usually followed by the water gas shift (WGS) reaction to produce more hydrogen [8,9,20,21].

Application and the increase of share of hydrogen is a key factor for future sustainable development of global energy systems [22–28]. As shown in Figure 1.3, many countries have announced low-emission hydrogen production projects. As a consequence of development of RES, hydrogen will become more and more important as a component of energy storage systems.

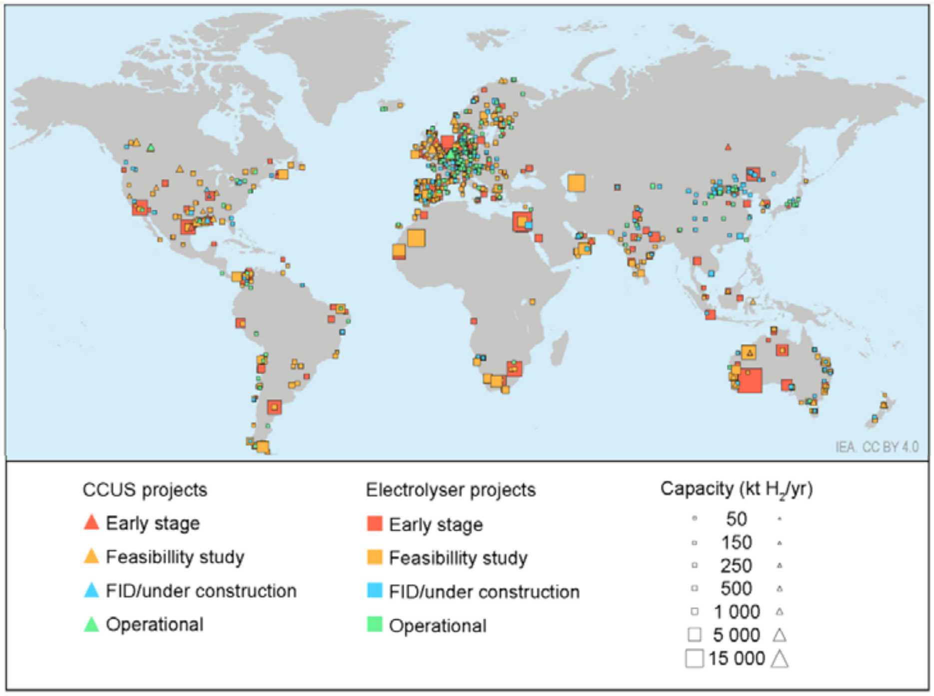

Figure 1.3. Map of announced low-emission hydrogen production projects Reproduced with permission of Ref. [15], Copyright of ©2023 IEA.

Note: CCUS = carbon capture, utilization and storage

1.2. Current Methods of Hydrogen Production

1.2.1 Non-catalytic processes

Biomass is considered as a renewable resource and can serve as a viable source for hydrogen fuel production. A variety of biomass feedstocks, such as agricultural residues, animal waste, and municipal solid waste, have been extensively studied in this context [29–40]. The primary technologies employed for hydrogen production from biomass are categorized into gasification and pyrolysis, which are typically followed by reforming processes [41]. The fundamental reactions involved in the biomass gasification process are outlined in Table 1.1. The hydrogen yield in these processes is significantly influenced by the intrinsic characteristics and composition of the biomass, which are further affected by various process parameters, including temperature, heating rate, moisture content, particle size, and reactor configuration [42,43].

Table 1.1. Basic reactions biomass gasification processes [42] .

Reaction mode	Reaction equation
Pyrolysis	$C_6H_{10}O_5 \rightarrow 5CO+5H_2+C$
	$C_6H_{10}O_5 \rightarrow 5CO+3H_2+CH_4$
Partial oxidation	$C_6H_{10}O_5+12O_2 \rightarrow 6CO+5H_2$
	$C_6H_{10}O_5+O_2 \rightarrow 5CO+5H_2+CO_2$
	$C_6H_{10}O_5+2O_2 \rightarrow 3CO+5H_2+3CO_2$
Steam reforming	$C_6H_{10}O_5+H_2O \rightarrow 6CO+6H_2$
	$C_6H_{10}O_5+3H_2O \rightarrow 4CO+2CO_2+8H_2$
	$C_6H_{10}O_5+7H_2O \rightarrow 6CO_2+12H_2$

1.2.1.1 Biomass Gasification Process

The gasification process, commonly applied to both biomass and coal, is extensively used for commercial hydrogen production. This process is predicated on the partial oxidation of feedstock materials, resulting in a mixture of gases, including hydrogen, carbon monoxide, and methane. However, the gasification process is often characterized by low thermal efficiency due to the substantial energy required for moisture vaporization within the biomass [44]. Numerous studies have investigated gasification processes, both with and without catalysts, utilizing fixed-bed and fluidized-bed reactors [35,45–47]. Notably, fluidized-bed reactors have demonstrated superior performance compared to fixed-bed systems. The efficiency of these reactors, based on their lower heating values, ranges between 35% and 50% [48,49].

1.2.1.2 Biological Hydrogen Production Process

In recent years, there has been a marked increase in research on bio-hydrogen production, driven by the growing emphasis on sustainable development and waste reduction [48,50,51]. This approach utilizes biological processes, involving either anaerobic bacteria in dark fermentation bioreactors or algae in photo-fermentative processes [52]. The principal biological methods include photolysis for hydrogen production from water using green algae, dark fermentation via anaerobic digestion, two-stage dark/photo-fermentative processes, and the water gas shift reaction (WGS) method [53–55]. Biological methods are particularly valued for their low environmental impact [56]. In dark fermentation, anaerobic microorganisms metabolize carbohydrates, converting them into hydrogen and other byproducts [57]. The chemical reaction for this process is represented as follows:

$$C_6H_{12}O_6 + 2H_2O \rightarrow 2CH_3COOH + 2CO_2 + 4H_2 \qquad (Eq. 1)$$

Despite the promise of dark fermentation, one of its major challenges is the relatively low hydrogen production yield compared to the capital investment required [58]. Consequently, extensive research has focused on enhancing energy output by developing and optimizing new two-stage systems [59].

1.2.2 Heterogenous Catalytic methods

The main catalytic technologies currently used in the production of hydrogen include Steam Methane Reforming (SMR), Partial Oxidation (POX) and Electrolysis. SMR and POX processes utilize as feedstock fossil fuels such as natural gas, but it is also possible to use biomass or biomass-derived fuels [60]. Other commercially available technologies for producing hydrogen from natural gas are Autothermal Reforming (ATR) and Catalytic Dehydrogenation. Alternatively, photocatalytic processes, plasma reforming, membrane reactors, and biological processes can be used, though they are still in the development stage [61–65]. Table 1.2 presents the ranges of energy efficiency of hydrogen production technologies in terms of higher heating value (HHV).

Table 1.2. Range of energy efficiency and technological maturity of hydrogen production technologies (based on [61–65]).

Technology	Input	Energy efficiency	Technological maturity
Steam reforming	Hydrocarbons	70–85%	Commercial
Partial oxidation	Hydrocarbons	60–75%	Commercial
Autothermal reforming	Hydrocarbons	60–75%	Near term
Plasma reforming	Hydrocarbons	9–85%	Long term
Biomass gasification	Biomass	35–50%	Commercial
Aqueous phase reforming	Carbohydrates	35–55%	Medium term
Electrolysis	H_2O + electricity	50–90%	Commercial
Photolysis	H_2O + sunlight	0.5%	Long term
Thermochemical water splitting	H_2O + heat	N/A	Long term

In the following section, the most advanced technologies for hydrogen production from both renewable and non-renewable sources will be presented. Each production technology will then be evaluated based on its state of the art, commercial applicability, environmental impact, and energy efficiency.

1.2.2.1 Steam reforming

Steam reforming is an industrial process used to produce hydrogen, syngas (a mixture of hydrogen and carbon monoxide), or other useful chemicals from hydrocarbons, typically methane. Various types of steam reforming reactors have been applied in specific scenarios [66]. Methane Steam Reforming (SMR) is widely regarded as the preferred hydrogen production technology due to its endothermic reaction nature, typically operating at lower temperatures than the POX and ATR methods, while achieving a higher H_2/CO ratio [28]-[32]. Equation 2, 3 outlines the reactions occurring during the steam reforming process.

$$CH_4 + H_2O \leftrightarrow CO + 3H_2 \qquad \Delta H°_{298°C} = +206\,kJ \cdot mol^{-1} \qquad \text{(Eq. 2)}$$

$$CO + H_2O \leftrightarrow CO_2 + H_2 \qquad \Delta H°_{298°C} = -41\,kJ \cdot mol^{-1} \qquad \text{(Eq. 3)}$$

Studies indicate that temperatures exceeding 180°C are required during fuel processing [28]-[35]. To enhance the kinetics of steam reforming in microchannel reactors, research has been conducted on the limitations of mass and heat transfer [70,75–77]. These systems have explored alternatives to Group VIII noble metal catalysts, such as Rh and Co-based catalysts [78–80]. Compared to nickel catalysts, these alternatives generate less coke and exhibit higher catalytic activity [77,81–83]. The use of the SMR process to produce hydrogen from methane is considered a common industrial method, with thermal efficiency reaching up to 85% based on higher heating values[84]. However, the storage and transportation of hydrogen present challenges, leading to intensive research in the field [46]-[52].

1.2.2.2 Partial oxidation

Hydrogen production from natural gas and heavier hydrocarbons is achieved by partial oxidation (POX) represented in Equation 4. In the POX process, the hydrogen produced is sent to a water-gas shift (WGS) reactor and subsequently treated using appropriate purification techniques. Compared to the steam reforming process, studies have shown that the efficiency of the POX process is lower. Moreover, the requirement for a substantial amount of pure oxygen leads to higher operational costs [92]. Table 1.3 lists the reaction enthalpies of methane and isooctane as examples of POX reactions.

$$C_nH_m + \frac{n}{2}O_2 \rightarrow nCO + \frac{m}{2}H_2 \qquad \text{(Eq. 4)}$$

Example of the (POX) reaction:

$$CH_3OH + \frac{1}{2}O_2 \rightarrow CO_2 + 2H_2 \qquad \Delta H = -193.2[kJ \cdot mol^{-1}] \qquad \text{(Eq. 4a)}$$

Table 1.3 Standard enthalpies at (298 K, 1 atm), ΔH in [kJ/mol] [93].

	Methane	**Isooctane**
Partial oxidation	−36.1	−675.8
Steam reforming	205.7	1258.8
Dry CO_2 reforming	246.9	1596.3

The POX has been applied in commercial uses and automotive fuel cells [93–97]. Research has also explored the effect of adding ruthenium to molybdenum catalysts in the partial oxidation of methane to produce syngas [98].

Alternatively, the catalytic partial oxidation (CPO) reaction illustrated in Figure 1.4. can be performed under various conditions of space velocity (low or medium) and residence time (1s or more) [99–104]. Another aspect of the CPO process involves investigating the importance of operational and design parameters to prevent explosion risks [105]. Temperature control proves to be challenging due to the formation of hotspots since the reaction is inherently exothermic [94–97]. The efficiency of POX reactors is typically between 60% and 75% based on the higher heating value of methane fuel [84].

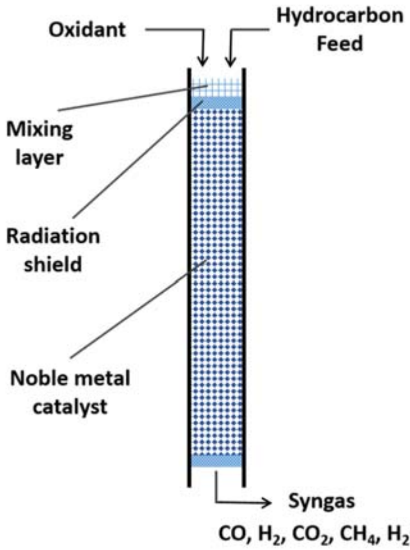

Figure 1.4. Catalytic partial oxidation principle. Reproduced with permission of Ref. [77]. Copyright © 2011 Elsevier B.V.

1.2.3 Electrochemical methods

Water electrolysis plays a vital role in generating hydrogen from renewable electricity. In a simple definition, water electrolysis is a process that uses electrical energy to split water into hydrogen and oxygen gases. There are three main types of electrolysis commonly used:

- Alkaline Electrolysis (AEL): Uses an alkaline electrolyte, typically potassium hydroxide (KOH) or sodium hydroxide (NaOH), and operates at low temperature.
- Proton Exchange Membrane Electrolysis (PEM): Utilizes a solid polymer electrolyte (a proton exchange membrane) that conducts protons, and it operates at low temperature.
- Solid Oxide Electrolysis (SOE): Operates at very high temperatures and uses a solid oxide (ceramic) electrolyte.

Each type has distinct characteristics and is suited for different applications [106]. Among the different water electrolysis methods, the AEL is the most common, primarily due to its lower capital costs (Figure 1.5). However, it also has the lowest efficiency, leading to higher electricity costs. In contrast, PEM (Figure 1.5) exhibits higher efficiency than AEL, typically ranges between 60% to 80%**,** depending on the specific system and operational conditions [106]. The main drawback of PEM technology lies in its high cost, attributed to the use of rare and expensive materials as electrocatalysts (e.g., Pt and IrO_2). Additionally, other challenges are associated with the corrosive acidic environment created by the proton exchange membranes, necessitating the use of costly materials.

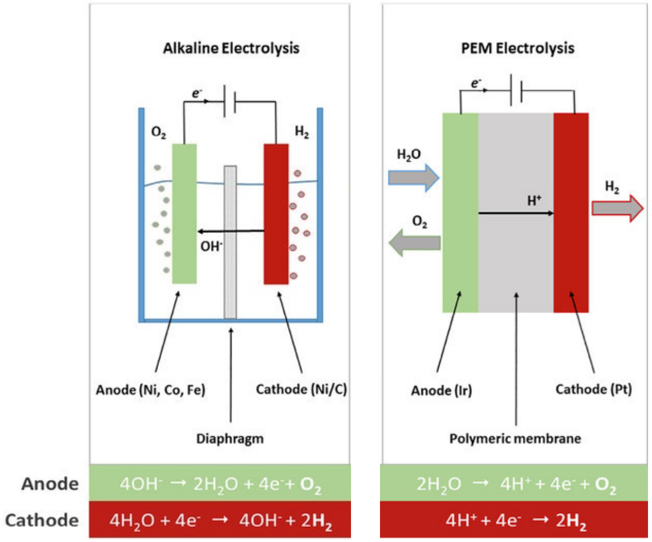

Figure 1.5. Schematic of the operating principle of the low temperature electrolysis technology (alkaline and PEM water electrolysis cell), Reproduced with permission of Ref. [107]. Copyright of ©2017 Elsevier Ltd.

Though still a relatively new technology, SOE offers substantially higher electrical efficiency than other electrolysis methods, positioning it as a promising option for large-scale hydrogen production from renewable energy sources. Table 1.4 provides an overview of the typical specifications of the above water electrolysis technologies.

Table 1.4. The typical specifications of alkaline, PEM and SOE [108].

Specification	AEL	PEM	SOE
Technology maturity	State of the art	Demonstration	R & D
Cell temperature, ℃	60 - 80	50 - 80	900 - 1000
Cell pressure, bar	<30	<30	<30
Current density, A/cm^2	0.2 - 0.4	0.6 - 2.0	0.3 - 1.0
Cell voltage, V	1.8 - 2.4	1.8 - 2.2	0.95 - 1.3
Power density, W/cm^2	Up to 1.0	Up to 4.4	-
Voltage efficiency, %	62 - 82	67 - 82	81 - 86
Specific system energy consumption, kWh/Nm^2	4.5 - 7.0	4.5 - 7.5	2.5 - 3.5
Partial load range,%	20 - 40	0 - 10	-
Cell area, m^2	<4	<300	-
Hydrogen production, Nm^2/hr	<760	<30	-
Stack lifetime, hr	<90,000	<20,000	<40,000
System lifetime, yr	20 - 30	10 - 20	-
Hydrogen purity, %	>99.8	99.999	-
Cold start-up time, min	15	<15	>60

A more detailed description of the electrolysis technologies is provided below, with a special focus on Solid Oxide Electrolysis (SOE), which is the central topic of this thesis.

1.2.3.1 Alkaline Electrolysis

Alkaline electrolyzers are commonly employed in large-scale electrolysis applications. AEL systems use alkali solutions, which are divided into two main electrolyte types. The first type involves potassium hydroxide (KOH) with a concentration ranging from 20% to 40% by weight [109]. In the second type, sodium hydroxide (NaOH) and sodium chloride (NaCl) are used as alternative alkaline electrolytes [57]. The separator between the two electrodes is an asbestos diaphragm with a typical thickness of 3 mm, which limits the operating temperature of the electrolyzer to 80 °C due to the inherent properties of asbestos [108]. In the electrolysis process, hydrogen and hydroxide ions are generated at the cathode, and the hydroxide ions then migrate to the anode where oxygen is produced. The reactions at the anode and cathode are as follows:

Anode reaction:

$$4OH^{-} \rightarrow O_2 + 4e^{-} + 2H_2O$$

Cathode reaction:

$$4H_2O + 4e^{-} \rightarrow 2H_2 + 4OH^{-}$$

Overall reaction:

$$H_2O \rightarrow H_2 + \frac{1}{2}O_2 \qquad \Delta H = -288\ [\mathrm{kJ \cdot mol^{-1}}]$$

A gas-liquid separation unit is used to extract the hydrogen gas generated in the electrolyzer [109]. The efficiency of alkaline electrolyzers has been reported to range between 50% and 60% at current densities of 100 - 300 $\mathrm{mA \cdot cm^{-2}}$, based on the lower heating value of hydrogen gas [57]. The primary challenge with this method is corrosion due to the use of alkali solutions. Therefore, new materials are being developed as alternatives for the diaphragm.

1.2.3.2 Proton Exchange Membrane Electrolysis

To address the corrosion issues associated with alkaline electrolyzers, solid polymer membranes have been explored for use in Proton Exchange Membrane (PEM) technology [110]. In the PEM electrolyzer, high-purity deionized water [109] undergoes oxidation at the anode, producing oxygen, electrons, and protons. Protons then move to the cathode side through the proton conducting membrane, where are reduced to generate hydrogen gas. The reactions in the PEM electrolyzer are as follows:

Anode reaction:

$$2H_2O \rightarrow O_2 + 4H^{+} + 4e^{-}$$

Cathode reaction:

$$4H^{+} + 4e^{-} \rightarrow 2H_2$$

The overall reaction is identical to that of the alkaline electrolyzer. PEM electrolyzers have been shown to function effectively with fluctuating power supply sources, due to the rapid proton transport through the PEM membrane [108]. However, the high manufacturing cost remains a significant challenge for PEM systems.

1.3. Solid Oxide Electrolysis

1.3.1. Introduction to Solid Oxide Cells

Solid Oxide Cells (SOCs) consist of an oxygen-ion conducting electrolyte positioned between two electrodes (cathode and anode), operating at high temperatures (750–1000 °C) to facilitate the effective transport of oxygen ions, as schematically shown in Figure 1.6. SOECs are electrochemical devices that convert electrical and thermal energy into chemical energy stored in a fuel. The operational principle of SOECs is the reverse of that of Solid Oxide Fuel Cells (SOFCs). So SOC can work in reversible (dual) mode, both as fuel cells and electrolysers, fulfilling both requirements in a single device [111]. High-temperature SOECs are considered an efficient method for water electrolysis due to favorable kinetics and thermodynamics at elevated temperatures [3,4,112–114]. Besides their high efficiency, SOECs also produce pure oxygen, significantly improving the economic viability of the process [115]. This technology not only boasts the highest Faraday efficiency among electrolysis methods, but has a high fuel flexibility. For example, it enables the direct electrolysis of CO_2, as well as the co-electrolysis of H_2O and CO_2, generating syngas that can be further refined into synthetic fuels [116,117]. Consequently, SOECs provide a means of chemical energy storage or as a carrier by converting renewable energy, or excess energy from fossil power plants, into hydrogen or syngas. Despite few large installations, SOECs are not yet commercially viable, primarily due to challenges in developing materials that can meet the performance and durability demands at high operating temperatures. The elevated temperatures required for the process necessitate the use of specialized materials capable of withstanding these extreme conditions.

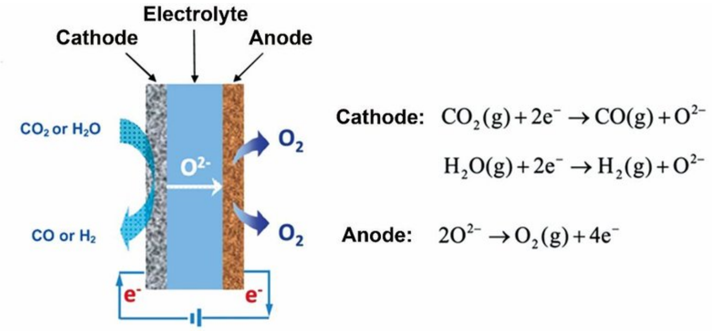

Figure 1.6. Schematic of the operating principle of the high temperature electrolysis technology (SOECs), Reproduced with permission of Ref. [118]. Copyright of ©2020 Elsevier

The development of SOCs began in the early 1900s when Walther Nernst, a German physical chemist, created a high-temperature electrolyte material, zirconium oxide (ZrO_2) doped with 15% yttrium oxide (Y_2O_3), commonly known today as Yttria-Stabilized Zirconia or YSZ. YSZ became the cornerstone of SOFC and later of SOEC technologies, and it remains the only commercially utilized electrolyte to date. In the late 1960s, NASA first demonstrated the electrolysis of H_2O, CO_2, and H_2O/CO_2 mixtures in SOECs for oxygen production in submarines and spacecraft [5,6,119]. Significant research attention emerged in the early 1980s, with Dönitz and Erdle (1985) reporting the first SOEC results under the HOT Elly project using electrolyte-supported tubular SOECs, achieving 100% Faraday efficiency at 1.07 V with a current density of -0.3 A/cm^2.

Research on SOCs has predominantly focused on water electrolysis for hydrogen production, with recent advancements demonstrating the effectiveness of SOECs in reducing simultaneously CO_2 and H_2O [120–123] to produce syngas. The electrochemical reduction of CO_2 in SOECs has also been extensively studied [124–126].

1.3.2 Theoretical aspects

1.3.2.1 Thermodynamic Analysis

Thermodynamic analysis of the process entails applying the First and Second Laws of Thermodynamics as outlined below: [127]:

The First Law is expressed as:

$$Q_H - Q_L = \Delta H_R \qquad (Eq.5)$$

The Second Law is expressed as:

$$\Delta S_R \geq \frac{Q_H}{T_H} - \frac{Q_L}{T_L} \qquad (Eq.6)$$

Here, ΔH_R represents the enthalpy change during the electrolysis process, while ΔS_R denotes the entropy change. The overall thermal-hydrogen conversion efficiency of the process can be defined as the ratio of the net increase in enthalpy from reactants to products to the high-temperature heat supplied to the system. This efficiency is given by:

$$\eta H = \frac{\Delta H_R}{Q_H} = \frac{Q_H - Q_L}{Q_H} = \frac{T_H \cdot \Delta S_H - T_L \cdot \Delta S_L}{T_H \cdot \Delta S_H} \qquad (Eq.7)$$

For reversible reactions, applying both the First and Second Laws to calculate efficiency yields:

$$\Delta S_R = \frac{Q_H}{T_H} - \frac{Q_L}{T_L} = \frac{Q_H}{T_H} - \frac{Q_H - \Delta H_R}{T_L} \qquad (Eq.8)$$

This can be further expanded to:

$$\varDelta S_R T_H \cdot T_L = Q_H T_L - Q_H \cdot T_H + T_H \varDelta H_R \qquad (Eq.9)$$

Thus, we have:

$$\frac{\varDelta S_R (T_H \cdot T_L) - T_H \varDelta H_R}{T_L - T_H} = Q_H \qquad (Eq.10)$$

The maximum efficiency can be expressed as:

$$\eta H = \frac{\varDelta H_R}{\frac{\varDelta S_R (T_H \cdot T_L) - T_H \varDelta H_R}{T_L - T_H}}$$

$$= \frac{T_L - T_H}{\frac{\varDelta S_R}{\varDelta H_R}(T_H \cdot T_L) - H_R}$$

$$= \frac{1 - \frac{T_L}{T_H}}{1 - \frac{\varDelta S_R \cdot T_L}{\varDelta H_R}} = \eta_{Hmax} \qquad (Eq.11)$$

In the water electrolysis process, which is the reverse of hydrogen and oxygen combustion, the enthalpy change ΔH_R is the negative of the combustion heat enthalpy, also defined as the higher heating value (HHV) of hydrogen. Assuming the water entering the reaction unit is in liquid form, we have:

$$\varDelta H_R = HHV \qquad (Eq.12)$$

If further assuming standard state conditions for temperature (T) and pressure (P), and $T_L = T_0$, then:

$$\varDelta H_R - T_L \cdot \varDelta S_R = -\varDelta G^0_{f \cdot \mathrm{H_2O}} \qquad (Eq.13)$$

Thus, the maximum efficiency can be derived as:

$$\eta_{Hmax} = (1 - \frac{T_L}{T_H}) \cdot \frac{HHV}{\Delta \mathrm{H} - \mathrm{T}_L \cdot \Delta \mathrm{S}_R} = \left(1 - \frac{T_L}{T_H}\right) \cdot \frac{1}{0.83} \qquad (Eq.14)$$

Since the higher heating value of hydrogen and the standard Gibbs free energy are fixed, the second term on the right side of the equation is a constant. From a thermodynamic perspective, the energy required for water electrolysis decreases as temperature increases. The electrolysis process is generally isothermal. According to the First Law of Thermodynamics:

$$Q - W = \varDelta H_R \qquad (Eq.15)$$

For a reversible process:

$$Q_R = T \cdot \varDelta S_R \qquad (Eq.16)$$

$$W_R = \varDelta H_R - T \cdot \varDelta S_R = \varDelta G_R \qquad (Eq.17)$$

From the Nernst equation, we have:

$$V = \frac{\varDelta G_R}{\mathrm{nF}} \qquad (Eq.18)$$

Thermodynamic analysis shows that the Gibbs free energy change of the electrolysis reaction decreases with increasing system temperature, lowering the theoretical decomposition voltage of water and increasing the product of temperature and entropy change. Consequently, the electrical work required in a reversible reaction decreases with rising temperature. As shown in Figure 1.7, at 100 °C, ΔG_R accounts for approximately 93% of the total energy ΔH_R required, which drops to around 72% at 1000 °C [128]. At high temperatures, a significant portion of the enthalpy change during electrolysis is supplied as thermal energy, i.e., $T\cdot\Delta S_R$. The total energy requirement ΔH_R increases slightly with temperature, with its value being very close to the higher heating value of hydrogen. Pressurizing the SOEC can also reduce its resistance, and waste heat from nuclear power plants can be utilized to heat the inlet steam, achieving pressurization. The CEA (French Alternative Energies and Atomic Energy Commission) conducted pressurized operation tests to study the impact of pressure on energy consumption, testing current-voltage curves at pressures ranging from 1 to 30 bar [129]. At pressures between 1 and 10 bar, the energy consumption only increases by a few percent at a current density of -1 A/cm^2, with no significant impact observed above 10 bar. However, pressurizing the electrolysis system reduces the compression work required in subsequent steps, potentially improving overall system efficiency.

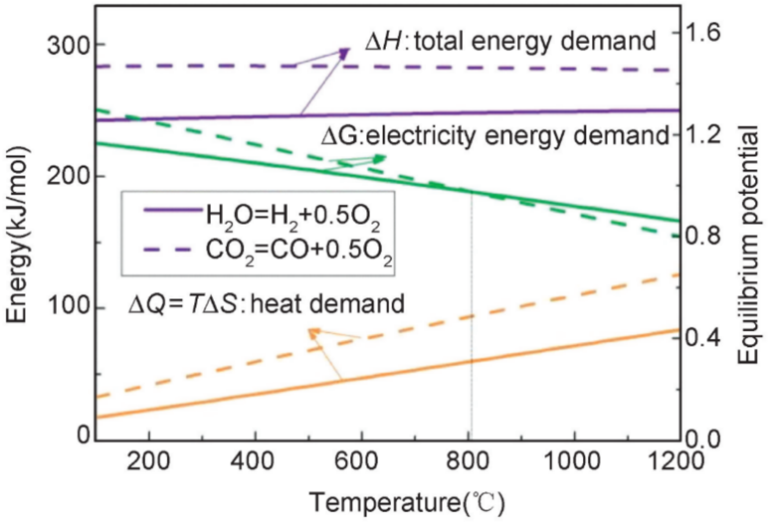

Figure 1.7. Thermodynamic analysis of H_2O electrolysis and CO_2 electrolysis. Reproduced with permission of Ref. [128], Copyright of ©2015 THU.

1.3.2.2 Kinetic Analysis

Computational fluid dynamics (CFD) analysis of H_2 production using high-temperature solid oxide electrolysis cells (SOECs) [130], revealed significant differences in gas flow distribution between the cathode and anode. When the operating potential is below the thermal neutral voltage (TNV), the SOEC temperature decreases along the main flow channel, whereas it increases when the potential exceeds the TNV. The study also found that increasing the inlet gas flow rate reduces the H_2/H_2O ratio downstream of the cathode, resulting in a lower Nernst potential and higher local current density. However, the inlet gas flow rate has a minimal impact on SOEC temperature, as the cooling effect of downstream gases through convective heat transfer helps maintain system temperature stability. The porous structure of the electrodes also influences cell performance, as gases can more easily diffuse in porous electrodes, reducing the Nernst potential and increasing local current density. However, the increase in local current density is limited by the higher mole fractions of H_2 and H_2O, which restrict further increases in current density. Consequently, the impact of electrode porosity on local current density is relatively limited.

Ni et al. modeled high-temperature CO_2 electrolysis, finding that ohmic overpotential loss is the primary component of total overpotential loss, with activation polarization overpotential also being significant due to the slow CO_2 electrolysis rate [131]. In the cathode, the formation of CO_2 and CO mixture, with a less effective diffusion system, results in a larger concentration overpotential compared to the anode. This can be mitigated by increasing the operating pressure or electrode porosity. This study also showed that when the voltage is below the TNV, the average electrolyte temperature initially decreases before increasing with further voltage increases. When the operating voltage reaches the TNV, the average electrolyte temperature aligns closely with the input gas temperature, with the heat required for CO_2 electrolysis balanced by ohmic heat. Increasing the operating voltage leads to higher local current density, resulting in a lower CO_2 mole fraction and a higher Nernst potential.

Building on previous research, further studies have analyzed the mass and heat transfer and electrochemical reactions during the co-electrolysis of H_2O and CO_2 mixtures in reversible electrolysis cells using a 2D model [132]. This model integrates CFD, electrochemical, and chemical reaction models. The study demonstrated the significant impact of different operating conditions on the reversible water-gas shift reaction, WGSR. With a cathode gas molar composition of 50% H_2O and 50% CO_2, the WGSR reaction rate increases with rising temperature, with the reverse WGSR reaction being more likely at high temperatures. When the inlet temperature reaches 1073 K, the CO_2 mole fraction decreases while the H_2O mole fraction increases at the inlet, leading to an increase in co-electrolysis current density.

1.3.3 State of the art SOECs materials for H_2O electrolysis

1.3.3.1 Requirements of Electrode Materials

As mentioned above a SOEC device consists of a ceramic electrolyte sandwiched between two porous electrodes. These components enable ion conduction and the electrochemical reactions needed for energy conversion. The device also includes interconnects for electrical conduction between cells, seals to prevent gas leakage, and current collectors to manage power flow. The SOC can be configured as a single cell or a stack, housed in a structure that handles fuel, air flow, and thermal management. The efficiency of SOECs largely depends on the electrochemical reaction rates at the cathode and anode, as well as the oxygen transport rate within the electrolyte. Although some research seeks to reduce operating temperatures to medium or low levels to lower costs and enhance durability [133], optimal conductivity and reaction efficiency are achieved at higher temperatures. Consequently, the development of SOECs will likely remain focused on medium to high-temperature operation for the foreseeable future. While research into key materials and system design for SOECs is still in its early stages, the materials used in SOFCs are relatively well-developed and can provide valuable insights for advancing SOEC applications.

The key requirements of the *electrode materials* and their effect on SOC operation are:

- Sufficient porosity to facilitate the inlet and outward flows of gasses,
- Good chemical stability and thermal compatibility with the other materials in contact (electrolyte and interconnect),
- Inert to the reacting gas species,
- Matching thermal expansion coefficient to other contacting materials,
- Chemical stability of fuel and oxygen side electrodes in reducing and oxidizing atmospheres respectively,
- Long lifespan, ease of processing and low cost.

1.3.3.2 Materials for the SOEC Cathode (Fuel or Hydrogen Electrode)

In SOECs the cathode, also referred as the fuel or hydrogen electrode, facilitates the reduction of water vapor molecules, resulting in the production of H_2 and O^{2-}. The H_2 is released from the hydrogen electrode, while the O^{2-} ions, driven by the applied potential, migrate into the electrolyte. The materials used for the hydrogen electrode must exhibit excellent ionic and electronic conductivity, high stability at elevated temperatures, good catalytic activity for the dedicated reactions, appropriate porosity, and compatibility with the electrolyte and other stack components. Unlike SOFCs, SOECs operate in high humidity conditions, which accelerates degradation processes.

The most widely used material for the cathode electrode is currently Ni-YSZ cermets. Ni is considered a superior electrode material even compared to Pt, as Pt exhibits a lower exchange current density in H_2/H_2O mixtures [134]. However, due to nickel's susceptibility to oxidation, alternative cathode materials have been developed. These include Ni nanoparticle-dispersed Sm-doped ceria (SDC) [135], and titanate/CeO_2 composites [136], which have emerged as promising new hydrogen electrode materials.

The electrochemical charge transfer reaction occurs near the active three-phase boundary (TPB). For Ni/YSZ electrodes, the TPB is defined as the interface where the Ni network, YSZ network, and open porosity intersect, forming permeation paths for electrons, ions, and gases [137]. In order to increase the reactive area of the fuel electrode, a common method is to mix nickel particles with ion-conductive particles of solid electrolyte material, forming a ceramic and metal composite, known as cermet electrode. At 950 °C, when electrolyzing a 50% H_2O-50% H_2 gas mixture, the area-specific resistance (ASR) of a Ni-YSZ-based cell (Ni-YSZ | YSZ | LSM-YSZ) is as low as 0.15 $\Omega\cdot cm^{-2}$ [138]. When the operating temperature decreases to 850 °C and 750 °C, the ASR increases to 0.27 $\Omega\cdot cm^{-2}$ and 0.60 $\Omega\cdot cm^{-2}$, respectively. Besides temperature, the cell structure also significantly influences the ASR.

Oxide electrodes. Several types of oxides have been applied as cathode materials for H_2O and CO_2 electrolysis under appropriate reaction conditions, including samarium-doped ceria (SDC), strontium ferrite manganite (SFM), lanthanum-doped strontium vanadate (LSV), and partially Cr-substituted strontium-doped lanthanum manganite (LSCM). Certain materials, such as Nb-doped strontium titanate (STN) [139], lanthanum-doped strontium titanate mixed with cerium oxide (LST-CeO_2) [140], and various molybdate-based cells, have shown better performance in electrolysis mode compared to fuel cell mode. The LST-CeO_2 electrode performs better in electrolysis mode than the Ni-YSZ electrode. This material reportedly exhibits electronic conductivity in a reducing atmosphere that surpasses that of traditional ceramic materials, and the electrolysis process does not require the addition of H_2 in the feed gas to maintain the reduced state of $La_{0.2}Sr_{0.8}TiO_{3+\delta}$, allowing for the direct electrolysis of steam to produce hydrogen [140].

Several studies suggest that LSCM $(La_{0.75}Sr_{0.25})_{1-x}Cr_{0.5}Mn_{0.5}O_{3-\delta}$ $(0\leqslant x\leqslant 0.1)$ holds significant promise as an alternative to cermet electrodes for both H_2O and CO_2 electrolysis [142,143]. LSCM's advantages include remarkable stability in both oxidizing and reducing atmospheres, with a volume change of only 1% when transitioning from an oxidizing to a reducing atmosphere. Research indicates that SOECs with LSCM, LSCM/YSZ, and LSCM/SDC electrodes can be used for direct CO_2 electrolysis, with the LSCM/SDC electrode demonstrating the best electrolysis performance, followed by LSCM/YSZ. Under the same conditions, SOECs with LSCM/SDC composite electrode performs 5 to 10 times better than those with LSCM electrode.

LSCM electrodes has been directly used for steam electrolysis, but the low electrocatalytic efficiency limits the electrode's performance and Faraday efficiency. It is possible though to enhance LSCM electrode's performance and Faraday efficiency by loading Fe catalysts [143]. At 800 ℃, in a working gas mixture of 3% H_2O/5% H_2/Ar and 3% H_2O/Ar, the current efficiency of the Fe-loaded LSCM cathode increased by 30% and 40%, respectively, compared to the pure LSCM cathode. $La_{0.7}Sr_{0.3}VO_3$ (LSV) has shown good performance and potential as cathode electrode for steam electrolysis [144]. However, a key drawback of this material is its low electrocatalytic activity. To address this, catalytic metal nanoparticles, such as Ni or Fe were introduced using infiltration techniques to enhance the performance of LSV composites.

Compared to Ni/YSZ cermet composites, single-phase oxide ceramics usually maintain stable properties during redox cycling, allowing the cathode to operate without hydrogen gas in the inlet. Irvine et al. reported that high-stoichiometry oxides like $La_{0.3}Sr_{0.7}TiO_{3+a}$ and site-deficient compounds like $La_{0.2}Sr_{0.7}TiO_3$ perovskite are highly reactive and stable hydrogen electrodes for SOEC systems, exhibiting superior chemical, mechanical, thermal, and redox stability [145]. These materials perform well in electrolysis systems, regardless of whether H_2 is present in the cathode feed gas, while also exhibits excellent conductivity due to the presence of Ti^{3+}/Ti^{4+} ion pairs within the cathode, contributing to high ion mobility. Doping the B site of A-site-deficient LST materials with Ni and Ru, in particular, results in even higher conductivity. LST materials also show much higher stability than Ni/YSZ during redox cycling, avoiding the formation of NiO due to oxidation. Consequently, LST cathodes, with their high stability and efficient conductivity, have become a key research area.

1.3.3.3 Materials for the SOEC Anode *(Oxygen Electrode)*

The anode (or oxygen electrode), where O_2 is generated, can be made of electronic conductors, ion-electronic conductors, or mixed ionic-electronic conductors (MIEC). For electronic conductors, oxygen release is restricted to the active TPB with the electrolyte, similar to Ni-YSZ fuel electrodes (Figure 1.8a). For MIEC oxygen electrodes, oxygen release extends across the electrochemically active area in contact with gas phase, as illustrated in Figure 1.8b [146,147]. Current applications focus predominantly on MIEC anode materials [148], that can be broadly categorized into three types based on their crystal structures: perovskite-type oxides, double perovskite-type oxides, and Ruddlesden-Popper (RP) type oxides.

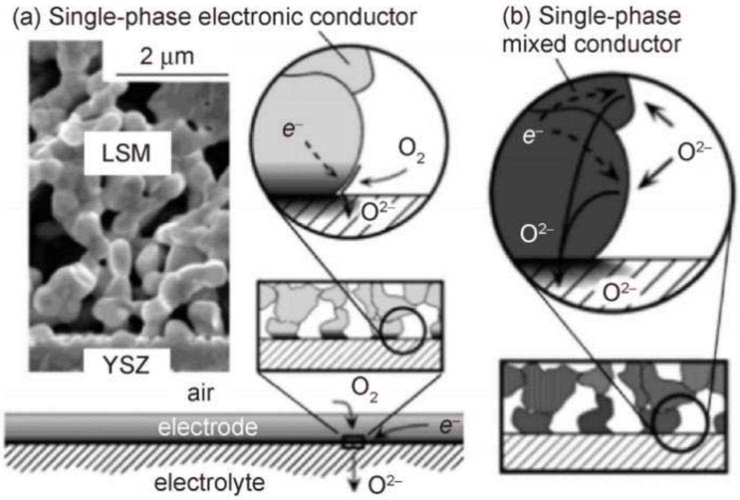

Figure. 1.8. a) Porous single phase electronically conductive oxygen; **b)** porous single-phase mixed conductor. Reproduced with permission of Ref. [147] Copyright of ©2004 ACS

Typically, anode materials are mixed oxides with a perovskite structure, such as LSM. LSM was widely used as an oxygen electrode material early on, demonstrating good performance. The conduction mechanism of LSM is vacancy-driven, where the substitution of lower-valence B-site cations creates oxygen vacancies in the perovskite crystal, facilitating oxygen ion migration [149]. As an ion-electron mixed conductor, LSM (formed by doping Sr^{2+} into $LaMnO_3$) exhibits relatively low ionic conductivity, in the order of 10^{-7} S·cm^{-1} in the temperature range of 800–1000 °C. To enhance ionic conductivity, yttria-stabilized zirconia (YSZ) can be added, forming a composite anode that effectively improved performance. LSM shows good chemical compatibility and thermodynamic matching with YSZ with no significant interface reactivity at high temperatures. However, in SOEC mode, LSM or LSM-YSZ experiences noticeable polarization, leading to performance degradation. Additionally, LSM anodes tend to delaminate in SOEC mode, a phenomenon not observed in SOFC mode. To address this, Li et al. loaded varying amounts of catalytically active Fe_2O_3 nanoparticles onto LSM materials and tested the resulting electrodes [150]. They found that with a 4 wt% Fe_2O_3 loading, the electrochemical performance was optimal, with current efficiency increasing by 15%, compared to unloaded LSM.

Several alternative materials have been explored to replace LSM, including lanthanum cobalt oxide (LC) [151], strontium-doped lanthanum cobalt oxide (LSC), lanthanum ferrite (LSF), strontium-doped and cobalt-substituted lanthanum ferrite (LSCF), strontium-doped and copper-substituted lanthanum ferrite (LSCuF), and strontium-doped and cobalt-substituted barium ferrite (BSCF) [152]. Other promising materials include neodymium nickelate (NNO) [153], lanthanum nickelate (LNO) [154], praseodymium nickelate (PNO), and strontium-doped and cobalt-substituted lanthanum nickelate (LSCN). Additionally, LSM-YSZ oxygen electrodes have demonstrated better operational performance after infiltration with gadolinium-doped ceria (CGO or GDC) [155]. However, high strontium content reduces chemical stability, and at temperatures above 750°C, electrodes require a barrier layer (usually doped ceria) to prevent the formation of insulating secondary phases at the electrode-electrolyte interface [156].

In recent years, a variety of anode materials based on the lanthanum-strontium-cobalt-iron system, including LSC, LSF, and LSCF, have been developed. LSCF is particularly advantageous because it can operate at relatively high current densities. Tietz et al. used LSCF as an anode material, achieving stable SOEC operation at 780 ℃ for 9000 hours without significant degradation [157]. However, other studies found that $SrCrO_4$, $CrO_{2.5}$, and Cr_2O_3 are formed on LSCF electrodes surface during operation, leading to poisoning, a phenomenon closely related to Sr segregation under polarized conditions. Sr segregation causes A-site defects in the lattice, reducing the redox activity of the oxygen electrode [158]. Typically, a barrier layer is needed on the surface to maintain long-term stability, with materials like LDC/SDC/GDC being commonly used as barrier layers.

$Ba_xSr_{1-x}Co_{0.8}Fe_{0.2}O_{3-\alpha}$ (BSCF) materials have garnered significant attention after Shao et al. discovered that BSCF has high oxygen permeability, facilitating oxygen reduction reactions and lowering the operating temperature of SOFC systems [159]. Compared to SCO and LSCF, BSCF ($Ba_{0.5}Sr_{0.5}Co_{0.8}Fe_{0.2}O_{3-\delta}$) demonstrates superior catalytic performance [160]. To enhance its compatibility with YSZ electrolytes, an intermediate layer of $Sm_{0.8}Ce_{0.2}O_{1.9}$ (SDC) can be added. Theoretical studies proposed that BSCF has an inherent catalytic activity for OER that is an order of magnitude higher than iridium oxide materials [161]. Based on molecular orbital theory, a volcano-shaped distribution between the OER specific activity and the e_g orbital filling of B-site anions in perovskite oxides was proposed, as shown in Figure 1.9

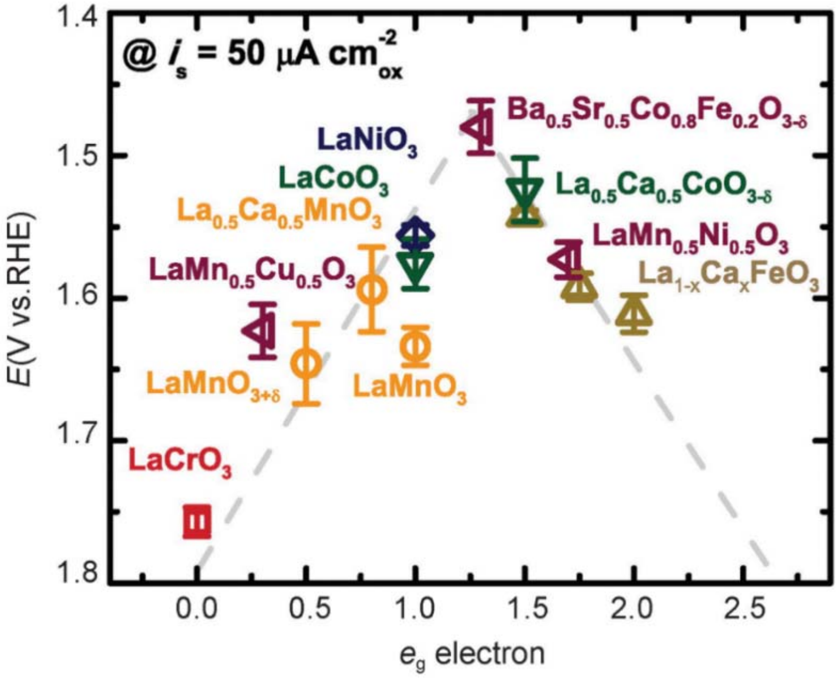

Figure 1.9. Relationship between transition metal (B in ABO_3) e-symmetric electron occupancy and OER catalytic activity. Reproduced with permission of Ref. [161], Copyright of ©2011 Science.

$La_{2-x}Sr_xCo_{0.5}Ni_{0.5}O_{4\pm\delta}$ (LSCN), a novel layered perovskite structure with a K_2NiO_4- type structure, is another promising candidate that performs well in both electrolysis and fuel cell mode [162]. The material remains stable under both oxygen-rich ($Ln_2NiO_{4+\delta}$) and oxygen-deficient ($Ln_2NiO_{4-\delta}$) conditions, thus enabling stable operation in both SOEC and SOFC modes [163]. The interlayer gaps can accommodate excess stoichiometric oxygen, preventing the electrode-electrolyte interface from fracturing. Theoretical and experimental studies on $(La,Sr)_2CoO_4$, highlighted an improve in the number of oxygen reaction sites and oxygen diffusion pathways [164,165]. Unlike the oxygen vacancy transmission mechanism of LSM and LSCF materials, LSCN transmit ions through an interstitial mechanism under oxygen-rich conditions in electrolysis mode. As shown in Figure 1.10, cations can occupy A and B sites, enhancing the oxygen surface exchange kinetics improving oxygen electrode performance and reactivity.

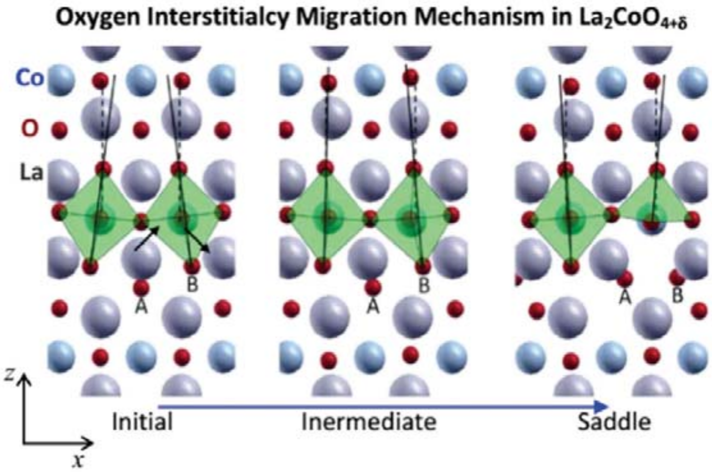

Figure 1.10. Atomic structure along the interstitial migration path in $LA_2CoO_{4+\delta}$ with K_2NIF_4 Ruddlesden-Popper structure. A: Migrating interstitial oxygen atoms; B: Oxygen atoms on the LaO plane Reproduced with permission of Ref. [166], Copyright of ©2010 RSC.

The performance of oxygen electrodes can also be significantly enhanced by selecting appropriate materials to create composites, providing new avenues for oxygen electrode material research. Chen et al. prepared $Nd_2NiO_{4+\delta}$ impregnated with scandia stabilized zirconia (NNO-SSZ) composites using an infiltration method and tested their performance in electrolysis mode [167]. In the Ni-YSZ/SSZ/NNO-SSZ solid oxide electrolysis cell, the NNO-SSZ oxygen electrode exhibited high redox catalytic activity, achieving a hydrogen production rate of 306.6 $mL\cdot cm^{-2}\cdot h$ at 750 °C under 80% H_2O-20% H_2. No degradation was detected during short-term operation. Li et al. investigated a new $Sr_2Fe_{1.5}Mo_{0.5}O_{6-\delta}$-$Zr_{0.84}Y_{0.16}O_{2-\delta}$ (YSZ-SFM) composite oxygen electrode, prepared by impregnating SFM into the YSZ matrix [168]. At 750 °C and an electrolysis voltage of 1.2 V, the electrolysis current reach up to -327 $mA\cdot cm^{-2}$, achieving a hydrogen production rate of 11.46 $NL\cdot h^{-1}$.

Yashiro et al. fabricated LSC composite electrodes using screen printing which showed reduced electrode resistance, improved interfacial conductivity and good oxygen transfer rate [169]. Sase et al. used secondary ion mass spectrometry (SIMS) to study the $La_{0.6}Sr_{0.4}CoO_3$ /$(La_{0.5}Sr_{0.5})_2CoO_4$ thin film composite material [170], while Jeong et al. performed simulation calculations, revealing that in perovskite materials, oxygen conduction occurs only through a vacancy mechanism [171].

Recently, $PrCoO_3$ has also attracted attention as an oxygen electrode material [172], but its thermal expansion coefficient mismatch with YSZ electrolytes leads to degradation during thermal cycling. These oxygen electrode materials generally exhibit superior initial performance compared to LSM electrodes.

1.3.4 SOE Electrolyte

The primary function of the electrolyte in a solid oxide electrolysis cell (SOEC) is to transport oxygen ions between the cathode and anode, while also serving to separate the oxidative and reductive gases at the two electrode sides. Therefore, in addition to high-temperature stability, electrolyte materials are required to possess high ionic conductivity, sufficiently low electronic conductivity, a dense structure, and good redox stability. The resistivity of the YSZ electrolyte, considerably higher than that of the electrode materials, making the electrolyte the main source of ohmic impedance in the electrolysis cell. To reduce these losses, it is necessary to develop new materials or fabricate the electrolyte in thin-film form.

At high-temperature SOECs, 8 mol% Y_2O_3-stabilized ZrO_2 is commonly used as the electrolyte due to its relatively high ionic conductivity and good mechanical stability. Using only 3 mol% Y_2O_3 for stabilization can improve the brittleness of the electrolyte, but results in lower ionic conductivity [173]. Certain electrolyte materials used in medium- to low-temperature SOFCs can also be employed in SOECs, such as samarium-doped ceria (SDC) and strontium-doped lanthanum gallate (SLG). When SDC replaces YSZ as the electrolyte, it positively impacts electrode overpotential in electrolysis mode. However, due to the high electronic conductivity of ceria under strongly reducing conditions, it is unsuitable as an SOEC electrolyte, as it may cause internal short-circuiting of the cell [174]. Another electrolyte Sc-doped ZrO_2 (ScSZ) exhibits higher oxygen ion conductivity compared to YSZ, and its mechanical properties at high temperatures are comparable to those of YSZ, making it a promising electrolyte material.

Lower operating temperatures are advantageous for SOECs in the production of synthetic fuels, such as methane synthesis, particularly when operating below 700 ℃ [175]. In such cases, YSZ may not be the best electrolyte material, and doped lanthanum gallate (with strontium doping and partial substitution by manganese: LSGM) could be used instead. However, this necessitates improvements in the nickel-based fuel electrode to prevent the formation of $LaNiO_3$ [176] and to avoid fractures caused by the mismatch in thermal expansion coefficients between the electrolyte and the electrode.

1.3.5 Other Materials used in SOC

To increase hydrogen production, it is necessary to combine individual cells into a stack using interconnect materials. These interconnect materials link adjacent cells and facilitate the transport of gases (anode and cathode) and electrons. The materials used for interconnects must maintain good electrical and thermal conductivity, chemical stability, and have an appropriate coefficient of thermal expansion at high temperatures that fits with the rest of the cell components. Traditionally, $LaCrO_3$ has been used as the interconnect material due to its excellent electronic conductivity under operating conditions. However, it has drawbacks in terms of mechanical processing strength, thermal conductivity, and high cost. To address the issue of chromium volatilization from interconnect materials, conductive protective layers can be prepared on the surface of metal interconnects. Current research on SOEC mode focuses on coatings such as perovskite, spinel, and nitride coatings [177].

In SOEC stacks, sealing materials play a crucial role in isolating the air and fuel gas compartments. Glass and glass-ceramic sealants are the most studied materials and are considered rigid sealants. However, rigid sealants are prone to stress accumulation and cracking when subjected to multiple thermodynamic cycles. Copper alloys can also serve as rigid sealants, though they offer lower strength compared to ceramic materials and can undergo plastic deformation. Compressible sealants deform under external pressure, allowing for better conformity with other components, which gives them a broader coefficient of thermal expansion (CTE) range. Metals, due to their ductility, can be used as metallic compressible sealants. To maintain stability, metals that are resistant to oxidation, such as gold and silver, should be selected.

1.4. Performance and Degradation of SOECs

1.4.1 Long and medium term performance

In the late 1960s, Spacil began researching the use of doped ZrO_2 as an electrolyte for hydrogen production via water electrolysis [178]. Their preliminary studies investigated the thermodynamics, kinetics, and material composition of SOECs. By the early 1980s, many researchers had joined the field. For example, Donitz and colleagues developed a tubular SOEC using Ni-YSZ | YSZ | LSM configuration, constructing a stack containing 1000 individual cells, which achieved a hydrogen production rate of 0.6 Nm^3/h [179]. Concurrently, Westinghouse Electric Corporation reported a tubular electrolysis cell stack operating at 1000 °C with an area-specific resistance (ASR) of 0.6 $\Omega\cdot cm^{-2}$, capable of producing hydrogen at a rate of 17.6 Nm^3/h. By the late 1990s, Japan’s Atomic Energy Research Institute had developed both tubular and planar solid oxide cells, with the planar cell achieving a maximum hydrogen production rate of 38 Nm^3/·h at 850 °C.

In the 21st century, the development of second-generation SOECs began. In 2004, the Idaho National Laboratory (INL) and Ceramatec reported preliminary results from single-cell [180] with Ni-YSZ as the hydrogen electrode, ScSZ as the electrolyte, and LSM as the oxygen electrode, with an efficiency of hydrogen production ranged from 45% to 52%. Subsequently, INL developed a 25-cell stack operated for over 1000 hours, reaching a hydrogen production rate of 0.16 Nm^3/h. In 2009, INL completed a 15 kW high-temperature electrolysis experiment, integrating three electrolysis modules comprising 720 electrolyte-supported cells, achieving a peak hydrogen production rate of 5.7 Nm^3/h [181].

In 2010, INL simulated the operation of a 600 MW high-temperature gas-cooled nuclear reactor-driven syngas production plant [182], with a syngas generation rate of 10 kg/s and an efficiency of 48.3%. They conducted various scale experiments, including an electrolysis module consisting of two 60-cell stacks. As part of a demonstration project, the syngas produced was used as feedstock for a Fischer-Tropsch reactor to produce liquid hydrocarbon fuels. In 2012, a 1000-hour operational test on two 40-cell stacks [183] was reported. The hydrogen electrode was supplied with a mixture of 10% H_2 and 90% N_2, while air was fed to the oxygen electrode, with flow rates of 50 slpm and 100 slpm, respectively, at a current density of 0.42 A/cm^2. The DC voltage scan showed that at the experimental flow rate of 71.7 slpm and a maximum current of 60 A, the actual current was 50 A, with an average ASR of 0.74Ω·cm^{-2}. The voltage increased almost linearly with current density, reaching a maximum of 53.3 V at a current density of 0.42 A/cm^2 (total current of 84 A) with an ASR of 1.04 Ω·cm^{-2}, and a total power of 4.52 kW. The long-term operation at 750 °C and 4 kW for 920 hours showed no significant performance degradation. In 2012, Zhang et al. also conducted stable operation tests on several hundred-watt SOEC stacks for up to 1000 hours, achieving a minimum performance degradation rate of 3.2% per 1000 hours [184].

The same year (2012) the Jülich Research Center achieved a 9000-hour long-term operation test in SOEC mode [185], with the stack operating stably at 780 °C under a current density of -1 A/cm^2, showing an overall degradation rate of only 3.8% per 1000 hours. The same year, researchers from the same institute conducted an 8100-hour long-term operation experiment on a planar reversible stack [186], exploring fuel cell, steam electrolysis and co-electrolysis of steam and CO_2 modes. In SOEC mode, after 2000 hours of operation at 800 °C, -0.3 A/cm^2, and a fuel utilization rate (FU) of 15%, no voltage degradation was observed. Upon increasing the electrolysis current, the stack was operated at 800 °C, J = -0.875 A/cm^2, FU = 44% for 1000 hours, resulting in a voltage degradation rate of 15% per 1000 hours. In subsequent co-electrolysis experiments, the voltage degradation was higher than in steam electrolysis mode, with more CO produced by reverse reactions than by electrochemical conversion under low fuel utilization and low current density.

Petipas et al. optimized parameters such as temperature and efficiency in high-temperature electrolysis [187]. They used the Simlink grey-box model, coupling the electrolyzer and balance-of-plant (BoP) models, and employed pinch analysis to calculate the thermodynamically feasible minimum energy consumption method. The thermoneutral voltage at -0.662 A/cm^2 was 1.287 V, slightly higher than the thermoneutral voltage calculated theoretically from Gibbs free energy changes. As the electrolyzer load increased, the efficiency of the electrolyzer unit gradually decreased. They also calculated the proportion of energy consumption in the electrolyzer, finding that electrolysis power accounted for approximately 78% to 81% of the system power, BoP heating accounted for about 13% to 16%, and compression power accounted for about 5%. The use of external heat sources can significantly improve system efficiency.

Risø National Laboratory in Denmark conducted research on the co-electrolysis of H_2O/CO_2 [121]. They proposed a process for coupling high-temperature co-electrolysis of H_2O/CO_2 for CO_2 recycling to produce clean synthetic hydrocarbon fuels, and found it economically feasible through simulation. Initial performance analysis through polarization curves and electrochemical impedance spectroscopy showed that the co-electrolysis performed well, surpassing CO_2 electrolysis and slightly below H_2O electrolysis. They also discovered that under low current density (-0.25 A·cm^{-2}), the performance degradation of co-electrolysis was mainly due to the degradation of the Ni-YSZ electrode. At higher current densities (-0.5 and -1 A·cm^{-2}), performance degradation was primarily due to the ohmic resistance of the electrolyte and the degradation of the LSM electrode. Economic analysis calculations indicated that under low current density, co-electrolysis coupled with nuclear energy for the production of synthetic hydrocarbon fuels was economically viable; for intermittent renewable energy sources, operating at higher current densities was economically more interesting.

In 2011, Risø conducted a long-term co-electrolysis experiment with a stack [121]. The stack, composed of ten 12 cm × 12 cm planar cells made of Ni-YSZ/YSZ/LSM-YSZ, was operated at 850 °C in a gas mixture of 45% H_2O, 45% CO_2, and 10% H_2 at -0.50 A/cm^2 for 800 hours, with no observed performance degradation, validating the feasibility of long-term stable CO_2-H_2O co-electrolysis in SOEC stacks.

Shao et al. studied steam electrolysis using tubular solid oxide cells [188]. They found that the porosity of the Ni-YSZ hydrogen electrode significantly impacts the performance of tubular stacks, and this porosity can be adjusted by varying the amount of pore-forming agent in the support slurry. The mechanism behind this is that in electrolysis mode, increasing the pore-forming agent content reduces the ratio of electronic to ionic conductivity in the NiO-YSZ electrode, which significantly affects the charge transfer process of the electrode.

1.4.2 Degradation and proposed mechanisms

The major obstacle to the economic viability and large-scale adoption of SOECs is the degradation of the stack over prolonged operation. Enhancing the lifespan and stability of the electrolysis cells necessitates a deeper understanding of the material changes occurring during system operation. Due to the typical input of mixed H_2 and H_2O gases in SOEC systems, the high-temperature, high-humidity environment results in more severe degradation in SOECs compared to SOFCs. Experimental results indicate that polarization resistance in electrolysis mode significantly increases, often being 2 to 3 times that of the fuel cell mode [189]. Furthermore, the degradation of the oxygen electrode is more pronounced than that of the fuel electrode.

Figure 1.11 illustrates the degradation rate observed during a 1,000-hour electrolysis test conducted by INL on a 25-cell stack, which resulted in an 18% decrease in hydrogen production [187]. The degradation mechanisms of SOFC materials can offer insights also into the degradation of SOECs. However, the specific degradation mechanisms may differ in the two operation modes due to differences in their electrochemical and thermodynamic environments, as well as the opposite directions of ion and electron transport [190,191]. Therefore, further understanding of SOEC degradation mechanisms is essential for the advancement of electrolysis technology. Several primary causes of SOEC degradation reported in the literature, including Cr poisoning of the oxygen electrode [192], cation segregation on catalyst surfaces [193,194], interfacial cation diffusion between the electrolyte and electrode, and the redox stability of the hydrogen electrode. The primary degradation mechanisms proposed in the literature are discussed separately below for the two electrodes and the electrolyte.

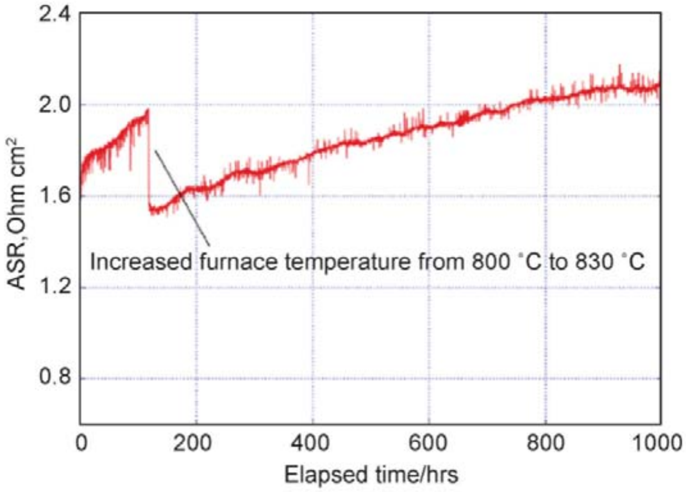

Figure 1.11. ASR variation of 25-cell stack after 1000 h of operation. Reproduced with permission of Ref. [187], Copyright of ©2005 NURETH-11 Conference.

1.4.2.1 Fuel Electrode: SOEC Cathode

At high temperatures, elements such as Cr, Ni, and Si from the interconnect and seal materials may volatilize and deposit on the electrode surface, potentially blocking active sites or forming secondary phases that impede electrode reactions [145]. The kinetics of SOFC degradation are well-studied, allowing effective control of the degradation rate to within 2% per 1000 hours [195]. However, research into SOEC electrode material poisoning is still in its early stages. Understanding the sources of contaminants and their transport mechanisms, along with the passivation of reaction sites, can aid in better controlling electrode poisoning. Lay-Grindle et al. used 3D reconstruction methods to investigate the degradation of Ni-YSZ cathodes after high-temperature electrolysis [196]. They developed a 3D reconstruction model based on data from two long-term stack tests and X-ray observations of the experimental materials. Their method revealed changes in the microstructure of the SOEC cathode, such as tortuosity factor and triple-phase boundary (TPB) length density, both of which showed significant changes during long-term testing. Evolutionary morphological parameters were introduced in both micro and macro models to represent their effects on electrode and stack performance degradation. The results indicated that the TPB length density degraded at a rate of approximately 22% per 1,000 hours of operation at 800 ℃, -0.8 A/cm^2, 10% H_2 - 90% H_2O. This loss of TPB length density contributed to an increase in electrolysis voltage at a rate of 1.3% per 1000 hours, partially explaining the stack's degradation rate.

Researchers at Risø National Laboratory discovered that, unlike the SOFC process, Si poisoning is the primary mechanism leading to hydrogen electrode degradation during SOEC operation [197]. This was attributed to the volatilization of glass from the sealing materials as gaseous $Si(OH)_4$, which subsequently decomposed on the electrode surface, forming SiO_2 deposits that blocked hydrogen generation sites and suppressed the reaction. The deposition of SiO_2 was driven by the higher vapor pressure within the SOEC system, a phenomenon not observed in the same electrode under SOFC mode. It was found that SiO_2 primarily accumulated within a few microns of the hydrogen electrode, near the electrode-electrolyte interface. Redox cycling process in SOECs has been also identified as a significant issue affecting the stability of the Ni/YSZ electrode. In the Ni/YSZ electrode, the consecutive reduction and oxidation of Ni particles can lead to microstructural changes.

The high-temperature steam environment at the hydrogen electrode during electrolysis is a key factor to understand cell degradation, with NiO formation of NiO decreasing the performance. Risø National Laboratory conducted stability tests on SOECs, revealing significant degradation of the Ni/YSZ electrode under high steam pressure and high current density conditions. At 950 °C, -2 A/cm^2 current density, and 0.9 atm pressure, the SOEC operated for only 68 hours before the polarization resistance increased by 200% [197]. Post-experiment microchemical analysis showed significant microstructural changes at the hydrogen electrode/electrolyte interface, attributed to NiO oxidation. Due to the migration of Ni particles, a 2-4 μm thick Ni layer formed at the YSZ interface, severely impeding the transfer of oxygen ions from the cathode to the electrolyte. The authors proposed the development of new hydrogen electrode entirely based on ceramic materials, to deal with this problem.

Nickel migration is primarily attributed to reactions between water and Ni particles, which produce volatile substances like $Ni(OH)_2$. These substances then volatilize and deposit on the YSZ surface, as illustrated in Figure 1.12 [197]. Below 1000 °C, $Ni(OH)_2$ can coexist with NiO and Ni in 20%H_2O/H_2 mixtures. According to Osinkin et al., if the water content during operation exceeds 45 vol%, the degradation process accelerates [198]. Hauch et al. reported that after testing at 850 °C, 50 vol% water content, and -1 A/cm^2 for 700 hours, Ni particles became coarser and increased in volume [197]. When a 98%H_2O/H_2 mixture was introduced into the system, the polarization loss of the Ni/YSZ electrode nearly doubled. At higher current densities and/or with higher humidity inlet gases, Ni migration due to volatile $Ni(OH)_2$ could cause the Ni-YSZ layer at the hydrogen electrode/electrolyte interface to become denser. After 1,300 hours of operation at 850 °C, -0.5 A/cm^2, and 50% steam concentration, the voltage degraded by 2%, and the ohmic resistance increased by 10%. However, when the operating temperature, current density, and absolute humidity were increased to 950 ℃, -2.0 A/cm^2, and 90%, respectively, the ohmic resistance doubled after 68 hours. This phenomenon was attributed to the increased partial pressure of $Ni(OH)_2$ (~10^{-8} atm).

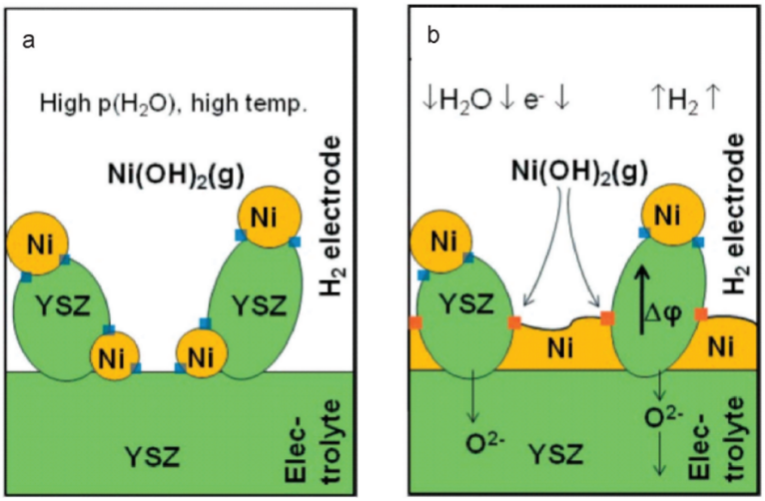

Figure 1.12. Illustration of the possible mechanism for microstructural changes observed at the YSZ-Ni/YSZ interface in a high current density SOEC test. Reproduced with permission of Ref. [197], Copyright of © 2008 ECS.

The hydrogen electrode is also highly sensitive to impurities typically found within the YSZ, such as Si, Na, and Al. Hauch et al. [121], conducted multiple 1000-hour experiments under electrolysis mode to study this effect. After a period of passivation, they observed reactivation and long-term degradation processes in the cells. The passivation and reactivation were attributed to the segregation of impurities, such as Si from the glass sealing materials (albite, $NaAlSi_3O_8$) and electrolyte powders. The corrosion effect of SiO_2 is primarily due to its volatile hydrated form, $Si(OH)_4$ as already mentioned above. High steam pressure, high-temperature and high-current density environments within the operating system increase the partial pressure of $Si(OH)_4$. The formation of impurities at the TPB sites hinders their hydrophilicity; however, as the impurities further crystallize, partial activation can be observed. This activation phenomenon is mainly controlled by changes in the water vapor pressure gradient in the Ni/YSZ electrode. Additionally, the reversal of O^{2-} migration direction when the stack transitions from SOEC mode to SOFC mode can lead to the movement of impurities from the TPB into the interior of the Ni/YSZ composite electrode leading to reactivation. According to Hauch's research [121], Si poisoning can be avoided by using seal materials with lower Si content. The

Si contamination in the hydrogen electrode was significantly controlled when using mica gaskets or ceramic sealing paste as sealing materials for a stack composed of 720 cells.

1.4.2.2 Oxygen Electrode: SOE Anode

Research indicates that the degradation of oxygen electrode performance is the primary factor contributing to SOEC degradation, as illustrated in Figure 1.13 Current literature on the accelerated degradation of SOECs consistently indicates that the cause is the delamination or structural decay at the oxygen electrode-electrolyte interface. The studies in question utilize LSM oxygen electrodes, with the cells being either electrode-supported or electrolyte-supported, using YSZ (8 mol% Y) and ScSZ (6 mol% Sc) electrolytes. The reports identify the formation of secondary oxide phases as the main cause of oxygen electrode decay, leading to increases in both non-ohmic and ohmic impedance.

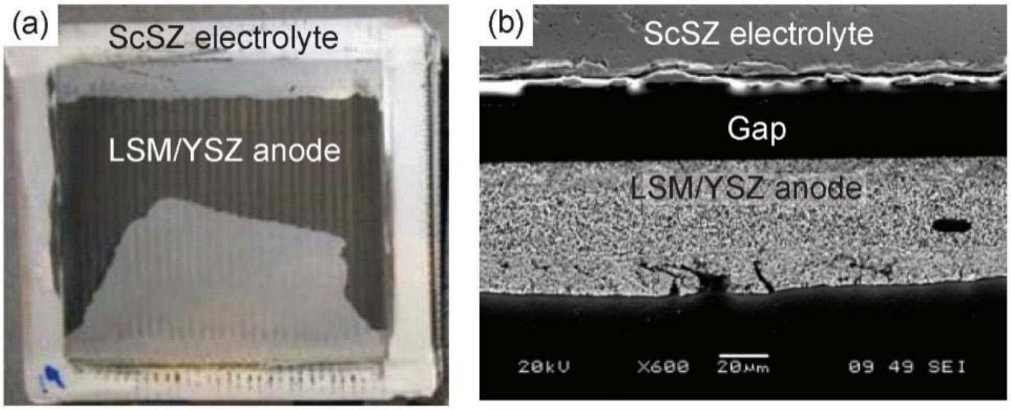

Figure 1.13. a) A 10 cm × 10 cm solid oxide electrolysis cell surface shown from the anode side after operation; **b)** A cross-section SEM image demonstrating the detachment. Reproduced with permission of Ref. [199], Copyright of ©2009 OSTI.GOV.

Poisoning of the oxygen electrode in SOFCs has been extensively documented in literature, with two primary hypotheses proposed for the degradation. The first hypothesis suggests that at high temperatures, volatile chromium-containing compounds from the stainless-steel interconnect materials, such as CrO_3 or $CrO_2(OH)_2$ [200], deposit on the electrode and electrolyte surfaces, and decompose into chromium oxides, leading to polarization losses [201]. The second hypothesis posits that, alongside gas-phase transport, solid-state diffusion and decomposition of chromium-containing elements are potential mechanisms for chromium deposition [202]. Recently, it has been proposed that the chromium deposition process is a nucleation reaction occurring between chromium-containing compounds and condensation nuclei on the electrode, driven by thermodynamics and controlled by kinetics.

The formation of chromium-containing secondary phases hinders the active sites at the TPB interface, rendering them insulating. To mitigate the issue of chromium diffusion, a common method is to fabricate a conductive protective layer on the surface of the interconnect material. Spinel and perovskite materials are the most widely used coating materials and have begun to be applied to the coating preparation of commercialized cell stacks, but their oxidation resistance and long-term stability need further verification.

Since oxygen enters the electrode from the electrolyzer, it can form excessive local pressure at the electrode/electrolyte interface, causing the oxygen electrode to delaminate [203]. Currently, several theoretical models are used to explain the causes of delamination at the oxygen electrode/electrolyte interface. According to Virkar's model [204], a higher chemical potential and ultra-high pressure of neutral substances will form near the electrode/electrolyte surface. Current research in this area is primarily limited to non-in situ observations, focusing on material decay and the assessment of critical damage after operation [205].

Jacobsen and Mogensen's model points out [206] that a harmful internal "oxygen partial pressure" may form inside the SOEC, leading to delamination of the oxygen electrode or the electrolyte near the SOEC anode. When operating in SOEC mode, the positive potential of the anode increases while the negative potential decreases, leading to an increased electrochemical potential gradient in the electrode. Since the anode has a higher chemical potential during operation, more and more oxygen accumulates at defects around the solid-solid interface of the electrolyte and oxygen electrode.

Rashkeev et al. proposed that the interdiffusion of different metal ions at the oxygen electrode-electrolyte interface at high temperatures can significantly accelerate the delamination process [207]. They specifically analyzed the diffusion of La/Sr/Mn elements from the LSM electrode to the YSZ electrolyte, and Zr from the YSZ electrolyte to the LSM electrode. The active mechanisms under SOEC mode are as follows: first surface migration of SrO forming oxygen vacancies on the LSM electrode [208] and then enrichment of Mn^{2+} on the YSZ surface. Backhaus-Ricoult et al. detected this phenomenon, which led to an increase in the electronic conductivity of the YSZ area [209]. In addition, the diffusion of La^{3+} and Sr^{4+} towards the triple phase boundary may form lanthanum zirconate on the YSZ surface [210], which is also contributes to delamination.

Zheng et al. tested and compared the degradation performance of three types of oxygen electrode materials, LSM-YSZ, LSC-GDC, and LSCF-GDC, in large solid oxide electrolyzer stacks [211]. High-temperature electrolysis experiments were conducted at a current density of -0.50 A/cm^2, 750 °C, with a H_2O/H_2 ratio of 90/10, lasting for 640 hours. Post-test analysis was performed by dividing a 10 cm × 10 cm cell into four areas: air inlet area, water vapor inlet area, water vapor outlet area, and air outlet area. The results showed that the phenomenon of oxygen electrode delamination mainly occurred in the vapor and air inlet areas of LSM and LSC, with delamination in the vapor inlet area being much more severe.

he activity and stability of LSM-based SOEC oxygen electrodes can be enhanced by expanding the reaction area beyond the electrode/electrolyte interface to include the surfaces of the microparticles within the LSM electrode. Hauch et al. noted that optimizing the contact between the electrode and electrolyte surfaces is crucial for achieving and maintaining this enhancement [197]. Alternative strategies include developing YSZ-LSM composite electrodes, utilizing mixed ionic-electronic conductors like LSCF, and incorporating superoxide ion conductors such as GDC nanoparticles. Additionally, adding Pd nanoparticles and other oxygen diffusion aids to the LSM electrode can help reduce the oxygen partial pressure at the TPB interface [185,212].

1.4.2.3 Electrolyte

To prevent chemical reactions between the oxygen electrode and the YSZ electrolyte, a CGO protective layer is usually applied on YSZ. Tietz et al. conducted post-analysis on the SOEC system with a LSCF electrode on a CGO film coated on YSZ, which operated at -1.0 A/cm^2 [157]. After testing the LSCF oxygen electrode-supported cell, the characterization reflected that the main reason for the cell voltage decay was related to the increase in series voltage. The series voltage is related to the electrolyte and the electrolyte/CGO-LSCF oxygen electrode interface. After 9000 hours of testing at -1.0 A/cm^2, several changes occurred in the cell materials: (1) The fine structure of the crystal boundaries of the electrolyte changes; (2) Capillary pores appeared parallel to the horizontal at the 8YSZ/CGO interface; (3) Material transfer and the formation of a dense layer at the 8YSZ/CGO interface; (4) Fluctuations in the composition of the LSCF electrode (affecting ohmic impedance); (5) Recrystallization of LSCF in the electrochemically active area (affecting the catalytic behavior of the electrode); (6) Instability at the 8YSZ/Ni-YSZ interface (affecting mechanical properties); (7) Changes in the surface roughness of Ni particles.

Knibbe et al.[213] reported that solid oxide cells operating in electrolysis mode exhibit degradation when the current density exceeds -1 A/cm^2. Analysis of the SOEC system using electron scanning microscopy after testing, revealed the composition of capillary pores at the crystal boundaries near the LSM/YSZ interface of the YSZ electrolyte. They attributed the formation of capillary pores at the YSZ crystal boundaries near the oxygen electrode. Moreover, the higher the current density and operating temperature, the more severe this phenomenon. They found that in electrolysis mode, the oxygen formation sites may be at the grain boundaries of the electrolyte. The rate of oxygen formation depends on the nucleation rate and the growth mechanism of YSZ crystals. The aggregation of oxygen molecules at the grain boundaries blocked the transport of ions, increasing the resistance of the electrolyte. In some observations, voids grew along the grain boundaries, creating cracks inside the electrolyte, which also weakened the connection between the oxygen electrode and the electrolyte, increasing the ohmic resistance.

Tietz et al. observed changes in the electrolyte material after operating at -1 A/cm^2 for 9000 hours: longitudinal pores and voids grew along the grain boundaries [157]. They believed that the void layer was caused by the cation diffusion of the electrolyte. The driving force for this diffusion is the oxygen partial pressure. The difference in transfer coefficients during the mass transfer process led to the production of voids, known as Kirkendall voids. The observed structural changes may affect the specific ionic conductivity of the electrolyte. They suggested that at high current densities, the formation of vacancies leads to the production of voids, causing damage to the electrolyte structure. The production of voids can be explained by the aggregation of $(V_{Zr} \cdot 2V_O)_x$ according to the reaction:

$$4O_O + Zr_{Zr} \rightarrow 4O_i' + 2V_O + (V_{Zr} \cdot 2V_O)_x \downarrow + Zr \downarrow \qquad (Eq. 19)$$

O_O: represents a normal lattice oxygen ion.

Zr_{Zr}: represents a normal lattice zirconium ion.

O_i': represents an interstitial oxygen ion.

V_O: represents an oxygen vacancy.

V_{Zr}: represents a zirconium vacancy.

$(V_{Zr} \cdot 2V_O)x \downarrow$: represents the precipitation of the complex defect consisting of a zirconium vacancy and two oxygen vacancies.

Zr ↓ : represents the precipitation of zirconium ions.

At low current densities, oxygen interstitial vacancies hardly move and have no significant impact on the electrolyte.

1.5. Modification of SOEC electrodes

1.5.1. Element Doping

Perovskite oxides known for their mixed ionic and electronic conductivity, anti-coking properties, impurity tolerance, redox stability and durability, present a promising option for SOEC fuel electrodes. However, they face challenges such as lower electron conductivity and catalytic activity compared to nickel-based cermet materials. To overcome these limitations, strategies like element doping, in situ precipitation, and infiltration have been explored. The physical and chemical properties of perovskite oxides can be effectively tailored by doping with various elements to meet specific application needs [214,215]. Doping enhances mixed conductivity, allowing single-phase perovskite oxides to function as fuel electrodes by expanding active sites across the surface exposed to reaction gases.

For A-site doping of perovskite oxides, the main dopants are alkaline earth metals and rare earth elements from the lanthanide series. For example, doping La into the A-site of SFM increases the unit cell volume, slightly reduces conductivity but significantly improves the oxygen surface exchange rate and bulk diffusion coefficient [216]. B-site doping typically involves transition metals from groups IB-VIIIB. High-valence dopants such as Ti^{4+}, Nb^{5+}, and Mo^{6+} in the B-site of LSF effectively inhibit Sr segregation and $SrCO_3$ formation [217].

Furthermore, $La_{0.9}Sr_{0.8}Co_{0.4}Mn_{0.6}O_{3.9-\delta}$ doped with F exhibits excellent stability, even in reaction gases containing 100 ppm H_2S [218]. This suggests that suitable F doping at the O-site in perovskite-related oxides could provide novel SOEC fuel electrodes with enhanced performance and stability for H_2O electrolysis.

1.5.2 In Situ Exsolution

In situ exsolution, also known as redox exsolution, involves doping metal elements into the oxide matrix in an oxidizing atmosphere, followed by precipitation at the surface of the electrode in a reducing atmosphere. This process forms metal nanoparticles on the electrode surface, which exhibit strong interfacial interactions with the substrate, enhancing electron and atomic oxygen transfer during electrolysis. These nanoparticles may act as active catalytic phases for H_2O electroreduction [219] and can re-integrate into the lattice upon re-oxidation [220,221]. The matrix oxide used can be a simple perovskite, double perovskite, or RP oxide. During in situ treatment, A-site deficient simple perovskites are more likely to produce numerous metal nanoparticles on the substrate. The substrate's crystal structure may either match or differ from the matrix oxide. Stoichiometric simple perovskites exsolves many metal nanoparticles and often decompose, resulting in a mixture of the A-site element's oxide and metal particles [222–225]. Besides A-site deficiency, factors such as oxygen vacancy concentration, the type of doping metal element, and reduction conditions significantly influence nanoparticle exsolution. Transition metals are typically used as doping elements, with Fe, Co, Ni, and Ru being the most suitable due to their higher reducibility. The exsolved nanoparticles may be pure metals or alloys, depending on the dopants [226].

After the reduction of $La_{0.6}Sr_{0.4}Co_{0.7}Mn_{0.3}O_3$, Co nanoparticles exsolved and the substrate transformed into $La_{1.2}Sr_{0.8}Co_{0.4}Mn_{0.6}O_4$ with an RP structure, as illustrated in Figures 1.14a and 1.14b [227]. These Co nanoparticles are uniformly distributed, and the high oxygen vacancy concentration in the RP substrate contributes to exsolution. Furthermore, calculations of reaction energy and activation energy suggest that Fe, Ru, Co, and Ni-Fe are promising candidate materials, as shown in Figure 1.14c [228].

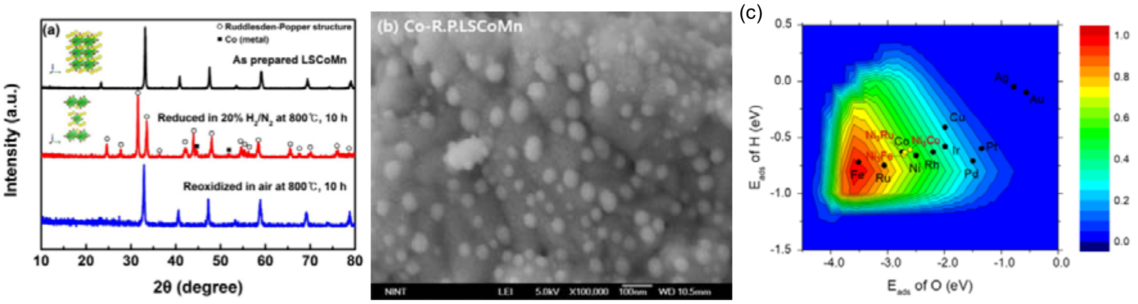

Figure 1.14 a) XRD patterns of $La_{0.6}Sr_{0.4}Co_{0.7}Mn_{0.3}O_3$ in reduced and oxidized states, showing reversible phase change between single perovskite $La_{0.6}Sr_{0.4}Co_{0.7}Mn_{0.3}O_3$ and RP $La_{1.2}Sr_{0.8}Co_{0.4}Mn_{0.6}O_4$; **b)** exsolved Co nanoparticles on $La_{1.2}Sr_{0.8}Co_{0.4}Mn_{0.6}O_4$ substrate in Co–$La_{1.2}Sr_{0.8}Co_{0.4}Mn_{0.6}O_4$ fuel electrode reduced from $La_{0.6}Sr_{0.4}Co_{0.7}Mn_{0.3}O_3$; **c)** Normalized activity for H_2O-CO_2 co-electrolysis on substrate of pure transition metals at 800 and 1.3 V, confirming that Fe, Ru, Co, Ni-Fe, etc., are promising fuel electrode candidates for H_2O-CO_2 co-electrolysis. Reproduced with permission of Ref. [227] [228], Copyright of ©2019 Elsevier and 2018 ACS

1.5.3 Infiltration

Infiltration of catalytic nanoparticles in a scaffold forming an electrode plays a crucial role in developing high-performance SOEC electrodes. This approach enables the creation of unique microstructures with optimized particle size and dispersion. Solution infiltration is a traditional method used to introduce a second phase into solid oxide electrodes, enhancing their conductivity and catalytic activity for electrolysis. By ensuring a well-dispersed distribution of nanoparticles, this method boosts both ionic and electronic conductivity through the formation of an extensive, interconnected nanoparticle network. This network increases the TPB length and lowers overall cell resistance. Furthermore, infiltration prevents adverse phase interactions with the electrolyte and avoids the formation of insulating phases due to the reduced thermal requirements for phase formation. These improvements in electrochemical properties enable infiltrated cells to operate at lower temperatures enhancing their long-term stability. [229–231]. Several papers have shown improvement of cell performance after infiltration. For instance, Hanifi et al. demonstrated that infiltrating SDC into a Ni–YSZ anode creates a nano-SDC particle network (as illustrated in Figure 1.15a), leading to the improvement of electrochemical reactions. Similarly, the infiltration of LSM into a YSZ scaffold (Figure 1.15b) enhances SOEC performance compared to conventional LSM–YSZ composites [229]. The morphology of the YSZ scaffold has a significant impact on the surface area, TPB length, and consequently, the cell's electrochemical performance. Ni–YSZ supports prepared from calcined/milled YSZ and infiltrated with LSM nanoparticles exhibit a uniform microstructure and more homogeneous infiltrate distribution, resulting in superior performance compared to conventional LSM–YSZ cathodes [229,232].

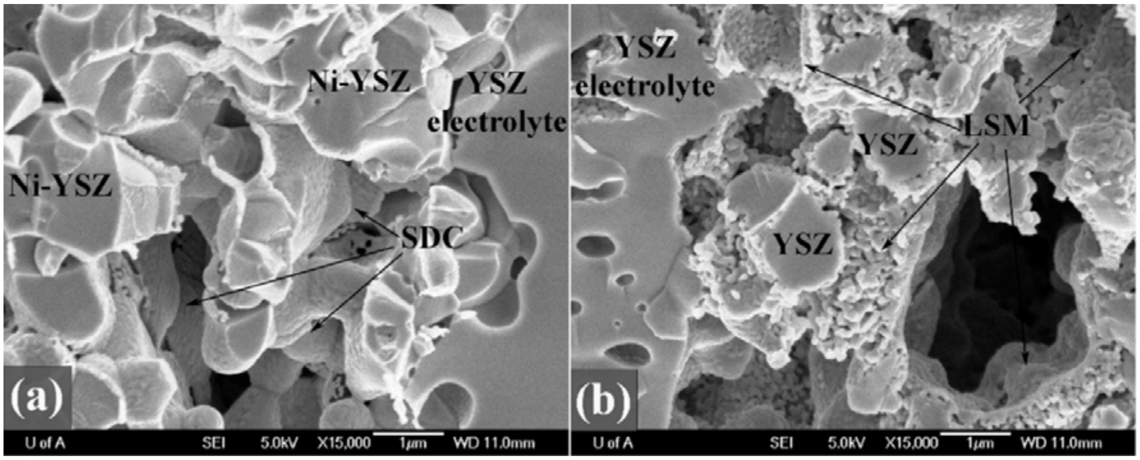

Figure 1.15 a) Ni–YSZ coverage by SDC near the interface of the fuel electrode and electrolyte, **b)** YSZ coverage by LSM near the interface of the cathode and electrolyte. Reproduced with permission of Ref. [229], Copyright of ©2014 Elsevier

Infiltration of various types of materials, including both metals and oxides, have been reported so far. The infiltration of ceria significantly increases the catalytic surface area for fuel oxidation [233,234]. Cu infiltration is preferred for CO_2 electrolysis applications due to the enchantment of the carbon tolerance and electrical conductivity [235,236]. Infiltrating porous YSZ scaffolds with Ni presents a promising alternative to conventional Ni-YSZ cermets, as it mitigates thermal stresses and improves the mechanical strength of the electrode through the increased YSZ content [237]. In addition, Ni infiltration notably improves a cell's resilience to redox cycling [238]. The nano-sized Ni particles achieved electrical percolation at a lower volume fraction (approximately 9 vol%) than bulk nickel [239,240]. Unlike traditional Ni-YSZ cermets, electrodes prepared by Ni infiltration into YSZ, does not cause significant structural stress preventing electrode and/or electrolyte cracking [233,238,241].

In addition to metal infiltration into a YSZ scaffold, direct particles infiltration into Ni-YSZ cermets has been shown to significantly improve both cell performance and redox stability. Howe et al. showed that infiltrating SDC into the Ni-YSZ electrode improved conductivity and extended the TPB length, resulting in reduced cell degradation after 56 thermal cycles [242]. SEM images (Figure 1.16) show that co-infiltrating Ni and SDC effectively controlled particle growth, maintaining electronic interconnectivity, while SDC-free samples displayed isolated, larger Ni particles connected to a lower conductivity.

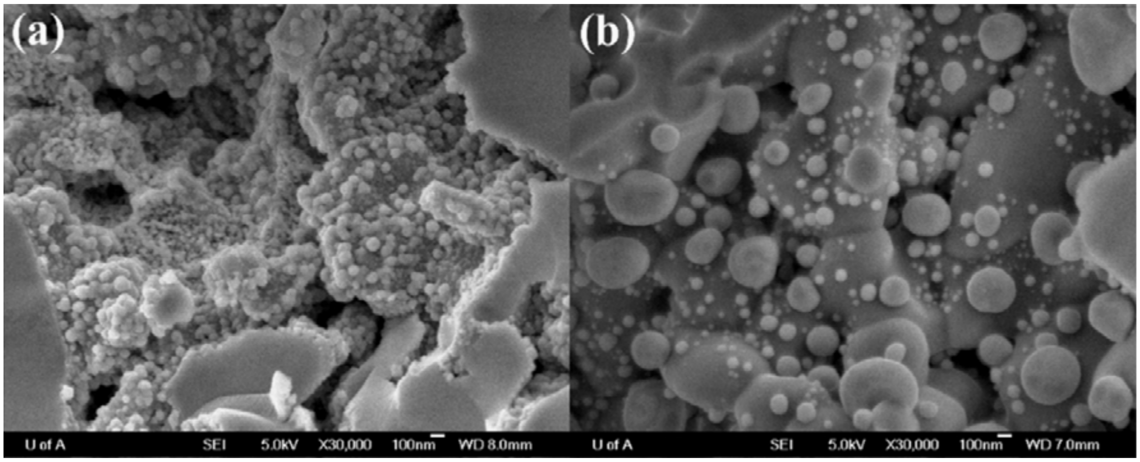

Figure 1.16 SEM images showing the microstructure of infiltrated porous YSZ support structures **(a)** within the Ni–SDC infiltrated porous YSZ anode and **(b)** within the middle of a typical Ni infiltrated porous YSZ support. Reproduced with permission of Ref. [242], Copyright of ©2013 Elsevier.

Buyukaksoy et al. observed that the stability of Ni-YSZ cermets formed by Ni infiltration is highly dependent on the pore size of the YSZ substrate. Uniform Ni particle distribution and high stability were achieved with a fine-grained YSZ scaffold (~200 nm pores), whereas larger pores led to lower stability and performance due to Ni agglomeration [243]. Despite attempts to mitigate Ni coarsening through co-infiltration or reducing pore size, complete control of electrode morphology remains extremely difficult. The infiltration process is also labor-intensive, requiring 25-30 applications for a 500 μm support to achieve percolation of nickel particles [241,244,245], making it unsuitable for commercial use despite improved cell stability.

In conclusion, infiltrated electrodes demonstrate greater long-term durability under high-temperature steam electrolysis compared to conventional electrodes. However, the infiltration methods developed so far are quite labor-intensive and challenging to implement on a large industrial scale.

1.6. In situ and *Operando* spectroscopic studies of SOECs

The advancement in understanding the complex electrochemical processes within SOCs is increasingly dependent on in situ and operando characterization techniques [246–248]. These methods have not only accelerated the understanding of degradation mechanisms and the identification of active sites but have also driven the development and synthesis of advanced, nano-engineered materials. In situ measurements generally focus on a single cell component, such as the cathode electrode, within a controlled environment. In contrast, operando techniques—derived from the Latin word for "working"—provide real-time monitoring of a device during operation. However, applying operando methods to SOCs presents a considerable challenge due to the need for a complex cell design. This design must incorporate heating systems, gas connections, fuel supply, and secure isolation of the electrode atmosphere, in addition to the necessary experimental probes and instrumentation.

This section provides an overview of state-of-the-art in situ and operando characterization techniques, including transmission and scanning electron microscopy, surface-enhanced Raman spectroscopy, electrochemical impedance spectroscopy, X-ray diffraction, and synchrotron-based methods such as X-ray photoelectron spectroscopy and X-ray absorption spectroscopy.

1.6.1 Laboratory-based techniques

1.6.1.1 Transmission and scanning electron microscopies

In situ transmission electron microscopy (TEM) is a potent, albeit intricate and costly, characterization method that may provide real-time atomic-scale visualization of electrochemical processes. It has been extensively applied to a variety of energy materials and devices, including batteries, catalysts, fuel cells, and solar cells, with recent advancements and specific setups detailed in notable review articles [249,250]. Despite in situ TEM's ability to perform analyses under various atmospheres, the operating pressures are typically limited to few mbar, which do not accurately represent the actual operating conditions of electrochemical systems.

A remarkable application of in situ TEM, in conjunction with scanning TEM (STEM) and electron energy loss spectroscopy (EELS), was documented in the study of $Pr_xCe_{1-x}O_{2-\delta}$ (PCO) thin films on YSZ [251]. Through consecutive experiments at different temperatures—room temperature, 300 °C, and 650 °C—in both oxidizing and reducing conditions, the authors characterized chemical strains and oxidation state changes within PCO cross sections. Notably, structural defects exhibited variations; periodic strain fields, indicative of misfit dislocations, altered in size during thermochemical expansion (Figure 1.17), while threading dislocations, capable of trapping reduced cations, emerged upon sample reoxidation. Additionally, the sample demonstrated anisotropic chemical expansion, releasing oxygen from the lattice, with the extent varying across the interface.

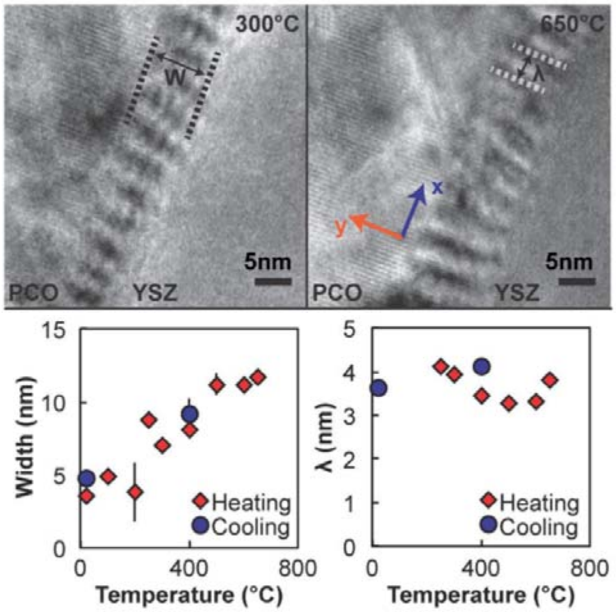

Figure 1.17 In situ phase contrast TEM images of $Pr_xCe_{1-x}O_2$-YSZ interface at 300 °C and 650 °C (upper panels) and temperature evolution of interfacial fringe width, W and periodicity, λ (lower panel). Reproduced with permission of Ref. [251], Copyright of ©2018 ACS.

Niania et al. [252] presented an in situ high-temperature environmental scanning electron microscopy (HT-ESEM) investigation of Sr segregation in LSCF under three distinct atmospheres: O_2, pure H_2O, and ambient lab air. They discovered that water accelerates and amplifies Sr particle formation. Furthermore, common atmospheric constituents, such as CO_2,

SO_x, or NO_x, may lead to surface passivation. The authors, based on their observations, proposed a stepwise mechanism for Sr precipitate formation: strontium segregation to the surface, monolayer development, nucleation at grain boundaries or defects, Sr-based particle formation, and ultimately, particle agglomeration.

1.6.1.2 Fourier-transform infrared spectroscopy (FTIR)

Infrared (IR) absorption spectroscopy is widely recognized as a powerful analytical tool for characterizing heterogeneous catalytic systems. Various modifications can be applied to adapt the technique to specific system requirements, as shown in Figure 1.18 [253]. Among these, in-situ Fourier Transform Infrared (FTIR) spectroscopy is particularly useful for providing real-time insights into the chemical properties of adsorbates during electrochemical reactions, thus aiding in the understanding of complex electrocatalytic mechanisms [249,251–253].

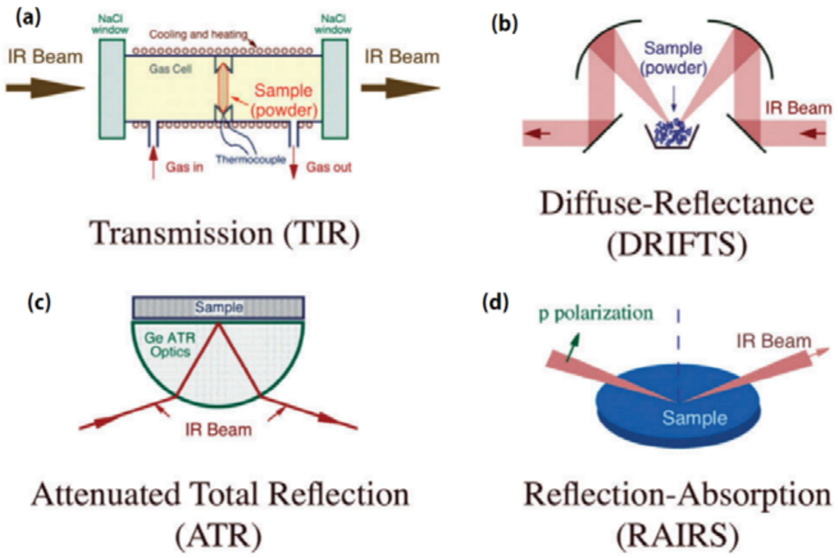

Figure 1.18 Common setups used for the characterization of catalytic samples using infrared absorption spectroscopy. **a)** transmission (TIR) mode, where the IR beam is directed through a self-sustained sample placed inside the catalytic reactor and collected after exiting for analysis. **b)** diffuse reflectance (DRIFTS) mode, where powder samples are radiated by a focused IR beam and the scattered light collected using a high-area parabolic mirror. **c)** attenuated total reflection (ATR) mode, where the sample is placed on the outside of the flat surface of the prism used to direct the beam. **d)** reflection–absorption (RAIRS) mode, where the beam is bounced from a flat reflective surface before collection. Reproduced with permission of Ref. [253], Copyright of ©2014 RSC.

In the context of CO_2 and H_2O co-electrolysis in SOECs, a detailed understanding of the involved reactions, transport phenomena, and degradation processes is essential. In-situ monitoring of reactants, products, and adsorbents is crucial for thorough characterization [254]. Since most molecular vibrational modes fall within the energy range of mid-infrared light (2.5–50 µm, 4000-200 cm^{-1}), IR spectroscopy is particularly well-suited for this purpose.

Conducting operando FTIR studies in transmission mode poses challenges, as it requires samples transparent to IR radiation. A more practical alternative is diffuse reflectance infrared Fourier transform spectroscopy (DRIFTS), depicted in Figure 1.19 [254], a technique well-established in catalysis research. DRIFTS allow for the experimental setup to be adapted by replacing the traditional powder-basket configuration with a compact solid oxide cell, closely resembling typical lab-scale electrochemical testing conditions. This method is particularly suitable for in-situ monitoring of co-electrolysis, as it can detect both gaseous and adsorbed species of CO and CO_2.

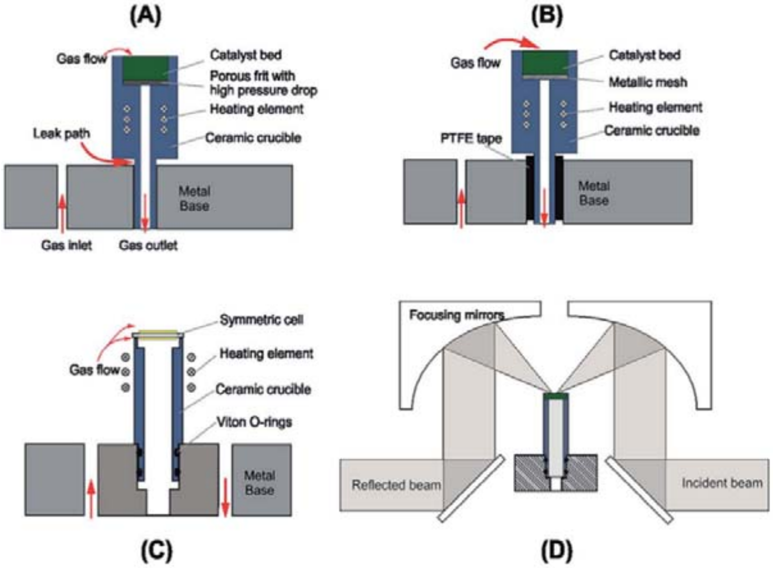

Figure 1.19 Schematic drawing the evolution of the base unit design and the optical path through the DRIFTS apparatus. **A)** As purchased Spectra-Tech configuration. **B)** Modification to reduce gas leak in chamber. **C)** SOC operation configuration. **D)** Full schematic view of DRIFTS rig showing mirror assembly and beam path. Reproduced with permission of Ref. [254], Copyright of ©2015 RSC.

The use of FTIR in solid oxide cell studies is relatively limited, with most research focusing primarily on SOFCs. FTIR was utilized in a simplified the experimental setup by using symmetric Pt/YSZ/Pt cells to study the oxygen reduction reaction [255]. The results highlighted that both the electrode microstructure and silica contamination have a significant impact on electrochemical performance and spectroscopic responses. Overall, there are very few operando IR studies related to SOC and all of them focus on reaction involving CO_2 and CH_4 [256].

1.6.1.3 Surface-enhanced Raman spectroscopy

Raman spectroscopy is recognized for its simplicity and efficacy, frequently applied both in situ and ex situ to analyze oxygen, sulphur, hydrocarbons, and water [257]. It also monitors structural shifts due to oxidation or reduction, which manifest as alterations in the vibrational modes of electrode materials. Despite Raman's sensitivity limitations, surface-enhanced Raman spectroscopy (SERS) has emerged as an advantageous alternative to provide information about the surface of the materials. SERS leverages metal nanoparticles, such as gold (Au) or silver (Ag), to significantly enhance the signal emitted by nearby molecules. The implementation of isolated $Ag@SiO_2$ core-shell nanoparticles has extended the utility of SERS to higher temperatures (around 400 °C), thereby enhancing its sensitivity over traditional Raman methods.

Pioneering the application of this technique to SOFC materials, Liu's team [258] demonstrated its effectiveness in examining coking (as depicted in Figures 1.20(a)–(c)) and the removal of carbon from the Ni-based SOFC anode, as well as the dynamics of adsorbed oxygen in ceria, under both oxidizing and reducing conditions. This marks the first instance of SERS being employed for such a purpose, showcasing its potential in advancing the study of SOFC materials.

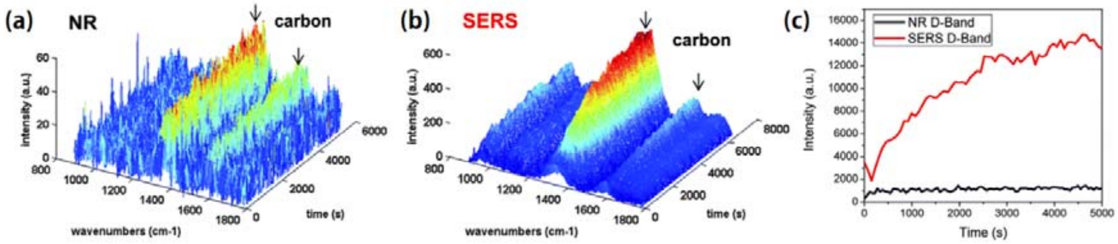

Figures 1.20 In situ analysis of carbon coking on Ni via **a)** normal Raman spectroscopy and **b)** SERS with isolated $Ag@SiO_2$ core-shell nanoparticles. The integrated intensities of carbon D-band mode at 1350 cm^{-1} from **a)** and **b)** are shown in **c)**. Reproduced with permission of Ref.[258], Copyright of ©2013 RSC.

1.6.2 Synchrotron-based X-ray techniques

1.6.2.1 Near ambient pressure X-ray Photoelectron Spectroscopies (NAP-XPS)

Several synchrotron-based characterization techniques are available, with X-ray absorption spectroscopy (XAS), X-ray diffraction (XRD), near ambient pressure XPS (NAP-XPS), and X-ray Raman spectroscopy (XRS) being particularly significant for characterizing electrochemical oxide materials. These techniques benefit from the high brilliance and tunability of synchrotron radiation, enabling faster data acquisition and significantly enhanced data quality. Current research in solid oxide cells predominantly focuses on Ni-cermet-based electrodes and perovskite-type electrode materials [259–262].

The application of in situ XPS studies is particularly valuable, as it offers real-time chemical information about the surface of the material under investigation. This insight is crucial for understanding surface chemistry and developing effective strategies for electrode optimization. Additionally, these studies are essential for establishing a solid foundation for comprehending electrode reactions in solid-state electrochemistry. Today some synchrotron beamlines allow the simultaneous combination of several complementary measurement techniques within a single experiment. When used with dedicated electrochemical cells, these techniques can provide time-resolved structural, chemical, and electrochemical information as materials evolve or as devices operate.

Klötzer et al. [263] studied the surface chemistry and water splitting kinetics of the perovskite-type mixed conductor $La_{0.6}Sr_{0.4}FeO_{3-\delta}$ (LSF) under electrochemical polarization in humid H_2 atmospheres using NAP-XPS. Figure 1.21 presents the I-V curves for the LSF working electrode, along with the in situ Fe 2p spectra corresponding to various polarization states. The formation of metallic iron species (Fe^0) was observed at relatively low cathodic overpotentials. This Fe^0 species significantly enhanced the electrochemical water splitting activity on the LSF surface, resulting in a highly asymmetric current-voltage curve that deviated from typical exponential behavior, such as that predicted by the Butler–Volmer equation, indicating a change in the reaction mechanism at the LSF surface. Upon removal of polarization, the cathodically formed Fe^0 was rapidly re-oxidized to a mixed Fe^{2+}/Fe^{3+} state within approximately 400 sec, as observed during simultaneous XPS and impedance measurements.

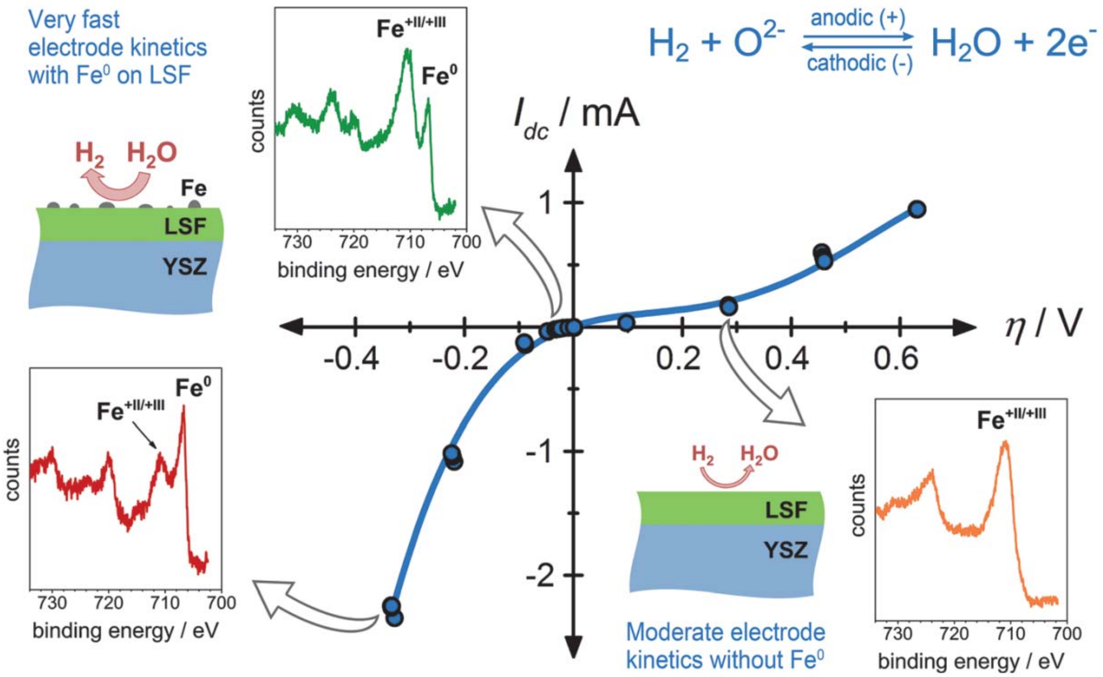

Figure 1.21 Current–overpotential curve (Idc vs. h) of LSF in a humid reducing atmosphere (0.25 mbar H_2 + 0.25 mbar H_2O). The symbols represent measured values; the line is not a fit but a guide for the eye. The reaction proceeding on the surface of the LSF working electrode is given top right. For selected points of the curve (indicated by arrows), Fe 2p XPS spectra are shown as insets. The sketches indicate the situation for the LSF surface and the resulting reactivity, respectively. Reproduced with permission of Ref. [263], Copyright of ©2014 Wiley-VCH.

Wen et al. [264] conducted in situ NAP-XPS on epitaxial LSC thin films, both with and without a ZrO_2 thin layer deposited by atomic layer deposition (ALD). The ZrO_2 coating was found to stabilize the surface by reducing the concentration of oxygen vacancies through cation exchange between Co and Zr in the surface region. This stabilization led to a significantly lower polarization resistance and greater stability at 550 °C over more than 330 hours compared to the uncoated LSC. Finally, Opitz et al. [265] combined in situ NAP-XPS and Electrochemical Impedance Spectroscopy (EIS) measurements to investigate Sr segregation in LSC thin films. Their study revealed the formation of a La-containing Sr phase that initially appeared on the surface. This phase, even before covering the entire surface, was responsible for blocking active Co sites, which contributed to the degradation of electrode activity. Interestingly, further increases in temperature also led to Sr segregation, but this had a minimal impact on electrode activity.

1.6.2.2 Combination of NAP-XPS and Near-edge X-ray Absorption Fine Structure Spectroscopies (NEXAFS)

Near edge X-ray absorption fine structure (NEXAFS) is a technique that provides insights into the valence state and local symmetry of an element. It is not only element-specific but also highly sensitive to the local coordination environment [266]. Zafeiratos et al. [260] conducted a comparative study on the surface reactivity of Ni/YSZ cermet and $La_{0.75}Sr_{0.25}Cr_{0.9}Fe_{0.1}O_3$ perovskite electrodes. These experiments, carried out at intermediate temperatures and under gas-phase conditions relevant to both SOC modes, utilized in situ synchrotron-based NAP-XPS and NEXAFS, supported by theoretical spectral simulations, microscopy, and electrochemical measurements. The results revealed that both electrode types rapidly adjust their surface composition in response to the reactive gas atmosphere. For Ni/YSZ, these adjustments were marked by significant changes in the oxidation state of nickel. In contrast, $La_{0.75}Sr_{0.25}Cr_{0.9}Fe_{0.1}O_3$ exhibited fine tuning of the Cr valence and pronounced Sr segregation. A key distinction between these electrodes was their ability to retain adsorbed hydroxyl groups on the surface, which is anticipated to be crucial for their electrocatalytic properties.

Chen et al. [267] studied $La_{0.6}Sr_{0.4}Co_{0.2}Fe_{0.8}O_3$ (LSCF) electrodes coated by a $PrNi_{0.5}Mn_{0.5}O_3$ (PNM) thin film with exsoluted PrO_x nanoparticles. Using NAP-XPS and XANES measurements, they discovered that the PrO_x NPs significantly increased the density of states (DOS) in the valence band compared to pristine LSCF. A temperature-dependent decrease in the O K-edge XAS (near edge EXAFS) was attributed to the formation of oxygen vacancies in PrO_x. The study concluded that the improved oxygen kinetics in PrO_x-coated LSCF was due to the higher number of available oxygen vacancies and electronic states, which facilitated charge transfer.

1.7. Structure and objectives of PhD Thesis

As evident by the literature review presented above, SOCs exhibit significant potential for hydrogen production through water electrolysis (SOEC mode) and power generation using hydrogen (SOFC mode). This thesis primarily focuses on investigating the surface chemistry of commonly used hydrogen and oxygen electrodes, with a particular emphasis on water electrolysis conditions. To explore these phenomena, advanced synchrotron-based spectroscopic techniques are employed, applied under in situ or operando conditions.

Furthermore, the thesis explores strategies to enhance the electrochemical performance of the Ni-YSZ hydrogen electrode, particularly through infiltration with various oxide nanoparticles. This thesis is structured into seven chapters, four of which are dedicated to the presentation and discussion of original experimental findings. Chapter 1 provides a comprehensive literature review, establishing the context for the research presented in this thesis. Chapter 2 then offers an in-depth discussion of the methodologies, experimental techniques, and preparation procedures employed throughout the study. This chapter covers issues such as the theoretical background of the techniques, their instrumentation and their applicability to the study the surface chemistry under water electrolysis conditions. Additionally, it describes the sample preparation and handling procedures, ensuring reproducibility and accuracy in subsequent experimental work. This thorough exploration of methodology ensures a solid framework for understanding and interpreting the experimental results presented in the following chapters.

"In Chapter 3, near-ambient pressure soft and hard X-ray photoelectron spectroscopy is employed to investigate the interactions between Ni/YSZ electrodes and steam under both open-circuit and polarization conditions. The cells, consisting of conventional porous Ni/YSZ cermet cathodes, were specifically adapted to allow direct spectroscopic observation of the functional electrode region near the YSZ electrolyte interface. The results reveal dynamic changes in the oxidation state and chemical composition of the Ni/YSZ electrodes in H_2 and H_2O atmospheres. These findings provide essential insights into the surface chemistry of Ni/YSZ electrodes under conditions relevant to H_2O electrolysis, shedding light on their influence on the cell's electrochemical performance.

In Chapter 4, Ce-based nanoparticles were introduced to modify the surface of Ni/YSZ electrodes, building on previously developed methodologies within the group for nanoparticle synthesis and infiltration. Two types of nanoparticles were synthesized, differing in agglomeration tendencies, liquid-phase dispersion, and particle size. These nanoparticles were infiltrated into pre-fabricated porous Ni/YSZ electrodes, resulting in a notable enhancement of H_2O electrolysis performance compared to pristine, non-impregnated samples. By varying the conditions of nanoparticle infiltration, we identified the optimal nanoparticle loading and determined which type of nanoparticle provided the greatest benefit for electrolysis performance. Synchrotron radiation experiments were conducted to characterize the surface state of both pristine and modified Ni/YSZ electrodes, providing a correlation between surface modifications and the observed improvements in electrolysis efficiency.

In Chapter 5, we explore the potential of using oxide nanoparticles with compositions distinct from those discussed in Chapter 4. Specifically, cobalt-based and vanadium-based nanoparticles were synthesized and tested. Various synthesis methods were employed to fabricate vanadium oxide nanoparticles, V-doped Ce nanoparticles, and Co-doped Ce nanoparticles. However, electrochemical testing following their infiltration into Ni/YSZ electrodes did not yield promising results for water electrolysis. In the case of Co-doped Ce nanoparticles, only a slight improvement in electrolysis performance was observed. Potential reasons for these limited outcomes are thoroughly examined and discussed in detail in this chapter.

In Chapter 6, we examined the surface states of two types of oxygen electrodes, LSCF and Pr-GDC, which had been previously tested for electrolysis in a conventional test rig. These electrodes were analyzed both before and after long-term electrochemical testing, extending up to 5000 hours. Through meticulous preparation of the electrodes prior to photoemission measurements, we were able to study both the current-conducting and functional layers of the electrodes. A key focus of this investigation was the segregation of Sr and Pr, and how these phenomena are influenced by prolonged electrolysis. The findings offer valuable insights into the stability and surface chemistry of these oxygen electrodes during extended operation.

Chapter 7 presents the conclusions and perspectives of this thesis, aiming to elucidate the influence of surface state and the impact of nanoparticle modifications on the performance of Ni/YSZ electrodes during water electrolysis. The findings highlight significant improvements in both efficiency and stability following infiltration with Ni-Ce nanoparticles. By integrating innovative materials design with advanced characterization techniques, this research provides insights that we expect to be highly relevant for future developments.

This page intentionally left blank

Chapter 2. Materials and Experimental Techniques

2.1. Cell fabrication

The electrolyte-supported electrochemical Ni/YSZ half-cells (comprising only the cathode and electrolyte) used in this study were purchased from Kerafol GmbH. The Ni/YSZ electrode (cathode) consists of three layers screen printed on a 150 µm thick 8 mol-% Y_2O_3 stabilized ZrO_2 (8YSZ) electrolyte. The first layer, directly in contact with the electrolyte, has a thickness of about 5 µm and consists only of 8YSZ. On top of this layer is applied the Ni/YSZ catalytic active layer (functional layer) with a thickness of about 25 µm. The NiO-to-8YSZ ratio of this layer is about 60 wt-%/40 wt-%. A final NiO/8YSZ (90/40 wt-%) top layer of about 10 µm was added to improve the electrical contact between the cell and the current collector. The half cells were sintered at 1300 ℃, producing a residual porosity of the active layer of about 30 %, as measured via Hg porosimetry [260]. A Pt electrode (anode) was brushed symmetrically opposite the Ni/YSZ cathode electrode using platinum paste (Pt ink 5542-DG, ESL). Following the application of the Pt electrode, the cells were allowed to dry for approximately 30 minutes at 100 ℃ and subsequently fired in air at 980 ℃ for 10 minutes which produces a dense Pt electrode with thickness of about 3 µm, estimated by cross section SEM imaging, as illustrated in Figure 2.1. [268].

Chapter 4 provides a detailed description of the synthesis of nanoparticles used in the infiltration process, as well as the infiltration procedure itself.

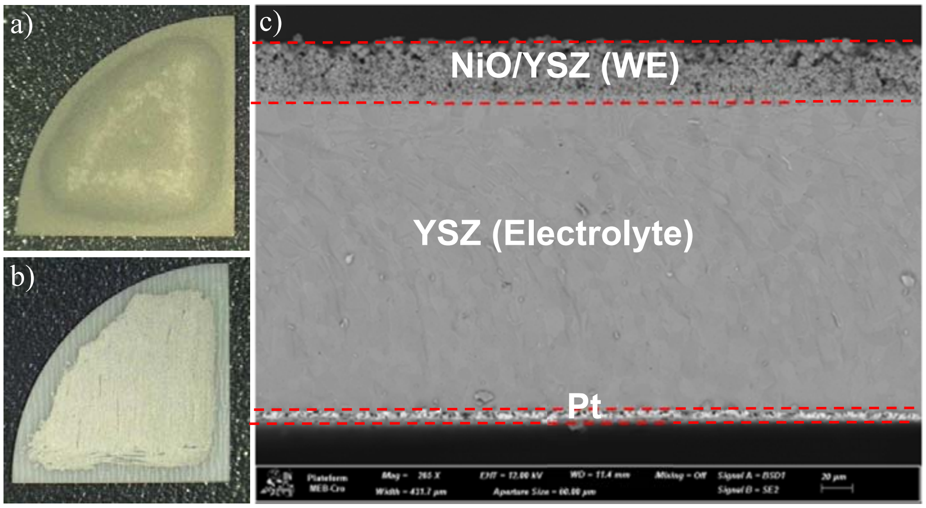

Figure 2.1 Photographs of **a)** NiO/YSZ cathode (WE) infiltrated with 40 µL NiCeOx NPs; and **b)** Pt anode (CE) for the NiO/YSZ//YSZ//Pt cell, **c)** cross-sectional SEM image of NiO/YSZ//YSZ//Pt.

The oxygen electrodes examined in this thesis were part of electrochemical cells provided by Dr. Jérôme Laurencin's research group at Université Grenoble Alpes (CEA, Liten, DTCH, 38000, Grenoble, France) and fabricated at CEA Le Ripault. The cells were hydrogen electrode-supported, featuring a Ni-YSZ composite porous H_2 electrode composed of two layers, with a total thickness of approximately 300 µm (as illustrated in Figure 2.2). The electrolyte is $Y_{0.16}Zr_{0.84}O_{1.92}$ (8YSZ), with a thickness of about 8 µm. The O_2 electrode consists of two layers: the top layer serves as the current collecting layer (CCL), while the layer beneath it, closer to the electrolyte, is designated as the functional layer (FL). Additionally, a 3 µm thick porous GDC barrier layer (BL) was deposited between the O_2 electrode and the YSZ electrolyte, as shown in the cross-sectional SEM image of the cell in Figure 2.2.

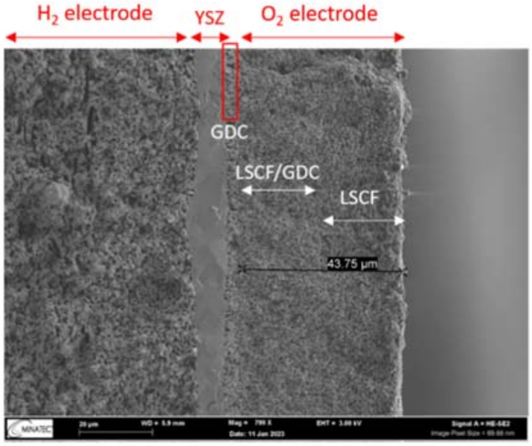

Figure 2.2 A cross-sectional SEM image of the perovskite LSCF cell was analyzed. Image provided by CEA, Liten.

2.2. ICPEES laboratory-based setups used for electrochemistry studies

The electrochemical performance of the cells with Ni/YSZ electrodes was examined using two custom-made laboratory setup, acting as electrochemical test rigs. All electrochemical measurements refereeing to the lab tests were conducted with a computer-controlled VersaSTAT3 potentiostat/galvanostat (AMETEK Scientific Instruments).

2.2.1. Flow through variable pressure reactor for *quasi in situ* XPS measurements and H_2O electrochemical experiments

Part of the electrochemical experiments were conducted in a laboratory flow reactor integrated into an in-house ultra-high vacuum (UHV) system. Samples were processed within the reactor and then transferred under vacuum to the analysis chamber of the spectrometer, where surface characterization was primarily performed using XPS. This type of experiment is referred to as '*quasi in situ XPS experiments*' in the following sections.

As shown in Figure 2.3, the aforementioned UHV system consists of four chambers: i) the main chamber, which is the UHV analysis chamber (base pressure 1×10^{-9} mbar), equipped with a VSW Class WA hemispherical electron analyzer (150 mm radius), a monochromatic Al Kα X-ray source (hv = 1486.6 eV), and a dual anode X-ray source; ii) a preparation chamber with a base pressure of 10^{-8} mbar; iii) a load-and-lock chamber for quick sample introduction; and iv) the variable pressure reaction chamber for electrochemical and gas treatment experiments operating over a pressure range of five orders of magnitude, from 0.01 mbar to 1.0 bar.

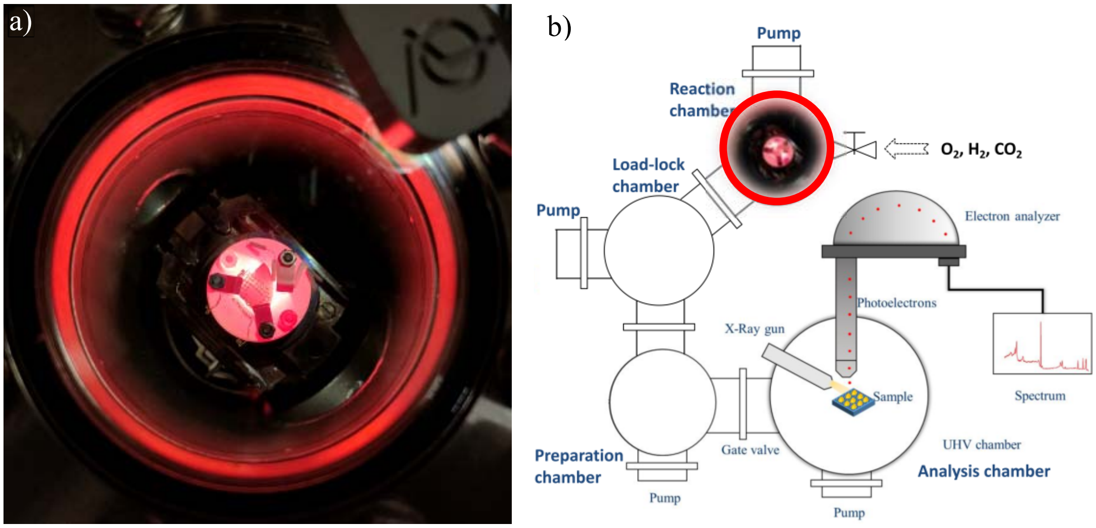

Figure 2.3 a) Flow through reactor and a heated cell on holder; **b)** Quasi in situ XPS laboratory setup [269] schematic drawing for the operation process at ICPEES, France.

The electrochemical cell was mounted directly onto a BN heater (Omnivac) using two stainless steel clamps. Gold mesh grids were employed as contact points for the current collectors on both the cathode and anode sides. The temperature was controlled by a K-type thermocouple, which was positioned on the side of the heater, as shown in Figure 2.3a. The gas flow into the reaction chamber was regulated by calibrated mass flow controllers, and the products were monitored using an online quadrupole mass spectrometer (Pfeiffer PRISMA, QMS). The electrochemical tests were carried out in the reaction chamber of the quasi in situ X-ray photoelectron spectroscopy (XPS) system (Figure 2.3b).

2.2.2. Second Flow-Through Reactor Designed for Fast Sample Introduction

The second flow-through reactor, self-assembled in our laboratory (Figure 2.4), was utilized for some of the electrochemical experiments. This system is designed for conducting H_2O electrolysis tests under low-pressure conditions in flow mode, similar to the first reactor, but it lacks the capability for quasi in situ XPS measurements. However, it features a more robust and efficient heating system using infrared lamp, along with superior control over cell mounting and testing conditions compared to the reactor connected to the UHV system. It consists of a cylindrical stainless-steel chamber, with a gas inlet connected to a mass flow controller, gauge CMR 362, and control unit TPG 362 (Pfeiffer Vacuum) for pressure measurements. The outlet is linked to an online quadrupole mass spectrometer (Pfeiffer PRISMA, QMS), followed by a vacuum pipeline equipped with a valve and a dry scroll vacuum pump IDP-15 (Agilent).

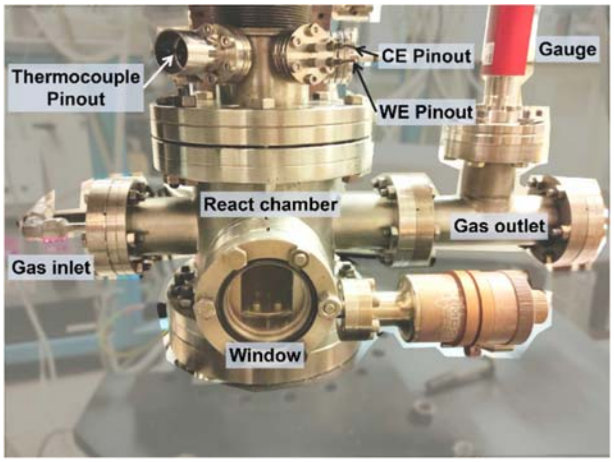

Figure 2.4 The second flow-through reactor along with the descriptions of its components.

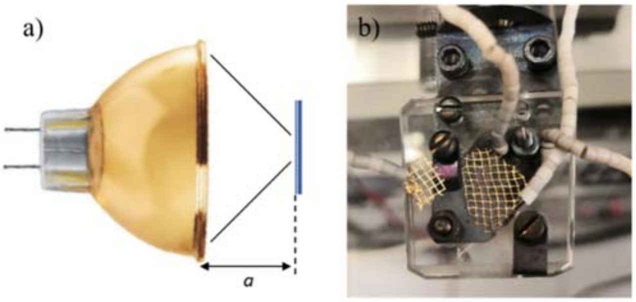

Figure 2.5 a) Infra-red lamp 64635 HLX, Halogen lamps with reflector MR16; temperature at the focal point, approximately 1300 °C; **b)** The two-electrode configuration connection sample holder containing Au grid current collectors and a thermocouple in the setup.

The electrochemical cell is secured to a quartz sample holder using two stainless steel clips, and an infrared lamp (Ostram 64635 HLX, 150W, 15V, temperature at the focal point approximately 1300 °C) positioned behind the sample for heating (Figure 2.5a and b). The sample holder is mounted on a manipulator that allows multi-directional and multi-angle movement, ensuring precise positioning of the sample in the focal point of the infrared lamp, which is critical for efficient heating.

Two gold grids serve as the current collectors on both the cathode and anode sides. These collectors are connected to an electrochemical workstation through gold wires, which are insulated by ceramic rings and linked to a 6-way UHV connector. Temperature regulation is handled by a PID controller, and the temperature readings are obtained from a thermocouple installed on the ceramic sample holder near the sample. Unless otherwise specified, this reactor is also used for the gas treatment experiments discussed in the study.

2.3. In-situ Near-Ambient Pressure spectroscopy (NAP-XPS)

While XPS is one of the most powerful spectroscopic techniques for obtaining chemical information from solid surfaces, conventional XPS instruments require ultra-high vacuum (UHV) conditions (below 10^{-8} mbar). This is essential to prevent both degradation of the instrument due to air oxidation and photoelectron scattering by gas molecules above the sample. However, UHV environments differ significantly from the conditions in which materials typically operate in real-world applications. To overcome this limitation, a new type of XPS systems has been developed over the past two decades, enabling **in situ** and **operando** measurements of catalysts and electrocatalysts in gaseous environments at pressures in the mbar range. Known as environmental XPS or near-ambient pressure XPS (NAP-XPS), these systems have expanded the possibilities for studying dynamic surface processes and correlating them with catalytic and electrocatalytic performance.

In NAP-XPS, electron attenuation caused by scattering with gas molecules is minimized by shortening the distance photoelectrons travel through the gas phase above the sample, i.e., the distance between the sample surface and the entrance to the analyzer lens. This is achieved by positioning the sample in close proximity to a differentially-pumped aperture, which serves as the entrance to the electrostatic lenses of the analyzer, as shown in Figure 2.6. This configuration allows operation at pressures up to 130 mbar, or even higher [270]. As shown in Panel A, the simplest setup includes two or more pumping stages located between the sample and the electron analyzer lens. This straightforward design requires no modification of the lens system, and the differential pumping stages can be easily added. However, this configuration results in significant electron defocusing within the lenses, limiting detection efficiency.

To address this issue, an improved design integrates differential pumping directly into the electrostatic lens system [271], as shown in Panel B, which is used at the ISISS and HIPPIE beamlines of the BESSY II and MAX IV synchrotrons, respectively. This design achieves a pressure differential of 8 orders of magnitude between the analysis chamber and the hemispherical analyzer, significantly enhancing the detection efficiency of photoelectrons by several orders of magnitude. Modern NAP-XPS instruments exclusively utilize the principles depicted in Panel B.

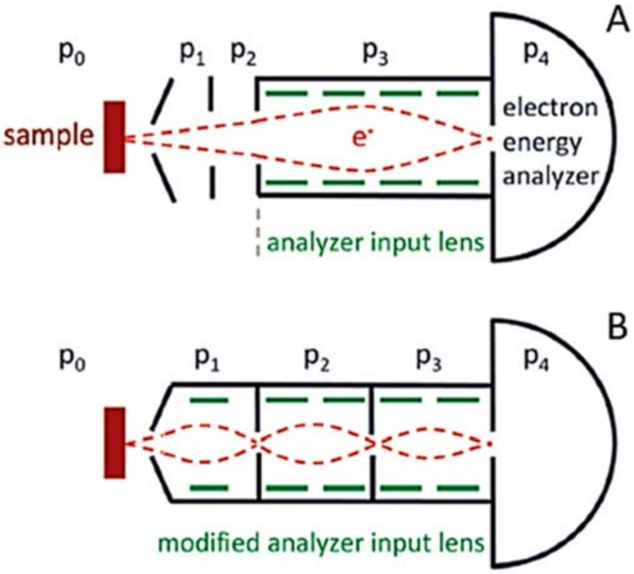

Figure 2.6. Schemes of differential pumping systems used in NAP-XPS. **Panel A** represents a standard analyzer lens with a set of pumping apertures in front of it, while **Panel B** shows the principle used at ISISS beamline of BESSY II synchrotron with a differentially-pumped lens system. Reproduced with permission [272]. Copyright 2013, the RSC.

In this thesis, the NAP-XPS technique plays a crucial role in in elucidating the relationship between the oxidation state of nickel-based electrode surfaces and their electrocatalytic performance in H_2O electrolysis. NAP-XPS measurements presented in the thesis were conducted at the HZB/BESSY II (Berlin, Germany) and MAX IV (Lund, Sweden) third-generation synchrotron facilities. The unique properties of synchrotron radiation— including its broad tunable energy range, high brightness, and high photon flux —were essential for these experiments [273,274]. Details on the beamline configurations, instrumentation, and measurement conditions are provided in the following sections.

2.3.1. NAP-XPS facilities at ISSIS and CAT@EMIL beamlines at HZB/BESSY II

This thesis presents NAP-XPS experiments conducted at the ISISS and CAT@EMIL beamlines at the BESSY II synchrotron radiation facility of the Helmholtz Zentrum, Berlin (HZB/BESSY II), schematically shown in Figure 2.7a. The ISISS (In Situ Spectroscopy Innovation Station) beamline, constructed and operated by the Inorganic Chemistry Department at the Fritz Haber Institute in Berlin is a bending magnet beamline, optimized to provide high photon fluxes in the energy range between 400 and 1600 eV. The CAT branch of the dual-colour Energy Materials In-Situ Laboratory (EMIL) beamline (CAT@EMIL) provides access to both soft and hard (in the case of this thesis 4.9 keV, which is in the border between hard and tender X-ray regime) X-ray radiation (Figure 2.7b). The CAT@EMIL beamline (Figure 2.7b) is a unique synchrotron source, offering an exceptionally wide and continuous photon energy range that spans from the soft X-ray region to the tender X-ray region, all combined into a single focal point. Both the ISIS and CAT@EMIL beamlines utilize the same type of NAP-XPS end station, equipped with on-site infrastructure designed to support experiments with a chemical orientation.

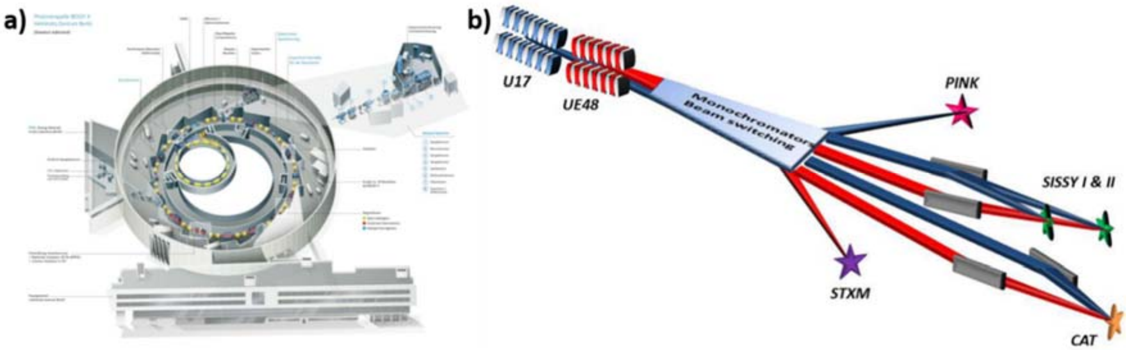

Figure 2.7. a) A three-dimensional schematic of the HZB/BESSY synchrotron facility and the ISISS Beamline, Image from HZB / Ela Strickert, licensed under CC BY 4.0; **b)** A schematic representation of the EMIL beamline, Image from HZB Energy Materials In-Situ Laboratory Berlin (EMIL), licensed under CC BY 4.0.

Both end stations are equipped with a Phoibos 150 electron analyzer (SPECS), with a 2D-CMOS detector from Surface Concept. A nano-thick silicon nitride window separates the beam from the analysis chamber. The mechanical stability of the window is adequate to withstand the high-pressure difference between the chamber and the beamline. The electrochemical cell is mounted on a stainless-steel plate using stainless steel clamps, with gold wires functioning as current collectors, as shown in Figure 2.8b. Infrared laser heating is applied from the rear, while the temperature at the center of the working electrode is monitored by a calibrated pyrometer. The sample holder manipulator allows for manual movement and can be precisely positioned with high accuracy (within a few microns) at the nozzle of the analyzer lenses (see Figure 2.8c).

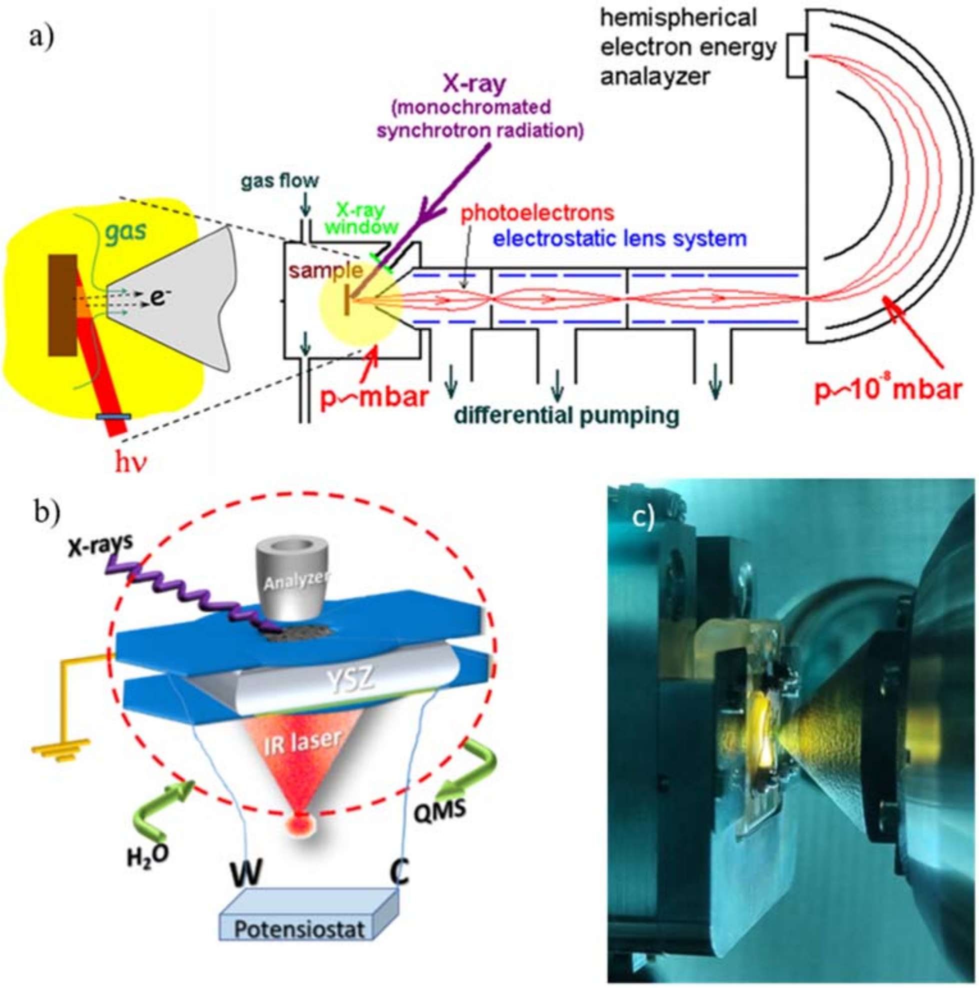

Figure 2.8. a) A schematic diagram illustrating the in-situ NAP-XPS setup under electrochemical gas-phase conditions. Reproduced with permission [275]. Copyright 2019, the RSC. **b)** A schematic representation of the experimental setup. Reproduced with permission [276].Copyright 2018, Springer; **c)** The photograph shows the sample holder mounted on the manipulator, positioned near the nozzle of the analyzer lenses. The light-yellow color observed is caused by laser heating from behind the sample. However, the colors are not accurate, as they are altered by the laser protection window filter.

Calibrated mass flow controllers are used for the introduction of the gasses into the NAP-XPS chamber. The gas phase composition in the analysis chamber is continuously monitored using an online quadrupole mass spectrometer (QMS, Prisma, Pfeiffer Vacuum, Inc., Germany). The working electrode is grounded to prevent the sample from becoming charged, while a bias voltage is applied to the counter electrode. For the XPS measurements conducted at the ISISS beamline, both survey and core-level spectra are collected with a pass energy of 50 eV. Depth-resolved measurements of the Ce 3d and Ni 2p spectra are performed using photon energies of 1065 eV and 4900 eV, corresponding to analysis depths of approximately 1.6 nm and 12.1 nm, respectively.

2.3.2. MAX IV-HIPPIE Beamline

HIPPIE is a soft X-ray beamline on the 3 GeV electron storage ring at the MAX IV synchrotron. It operates within a photon energy range of 250 to 2200 eV, offering one of the highest photon fluxes in this range along with exceptional resolving power. It is an elliptically polarizing undulator beamline and its endstation is equipped with a NAP-XPS setup (Figure 2.9), enabling measurements of solid samples in the presence of a gaseous atmosphere. The gas inlet system allows the introduction of up to eight gases and vaporized liquids, with real-time analysis of the inlet and outlet gas composition via online mass spectrometry [277]. This analysis chamber features a cell-in-cell configuration that allows for precise control of pressure and gas flow conditions during measurements. This is also the main difference with the BESSYII systems which were using a backfilling cell configuration [278]. The cell, referring to the chamber where the sample is placed, is retractable. The surrounding analysis chamber can maintain a pressure below 10^{-7} mbar, even when the cell itself contains up to approximately 5 mbar of gas. The X-ray beam from the undulator source enters the cell through an X-ray window composed of 200 nm silicon nitride on a silicon frame. Additionally, the cell is equipped with viewports for a camera and a visible light source, allowing for direct observation during experiments.

The electron energy analyser was a ScientaOmicron HiPP-3, equipped with a differentially pumped electrostatic lens system, enabling ambient pressure operation at up to 30 mbar with a 0.3 mm nozzle diameter. A special property of the HiPP-3 electron analyser is that spatially resolved experiments which allows spatial resolution of the analyser up to 8 μm. Gas pumped thourgh the electron analyzer nozzle was sampled and analyzed using a quadrupole mass spectrometer (QMS). Samples are mounted on a flag-style sample holder with an on-board thermocouple connection. Samples are heated using an infrared laser, and their temperature is monitored with a K-type thermocouple welded to the sample plate. The analysis area in the photoemission measurements is determined by the beam size of the synchrotron accelerator, creating a parallelogram with dimensions of 60 μm × 25 μm.

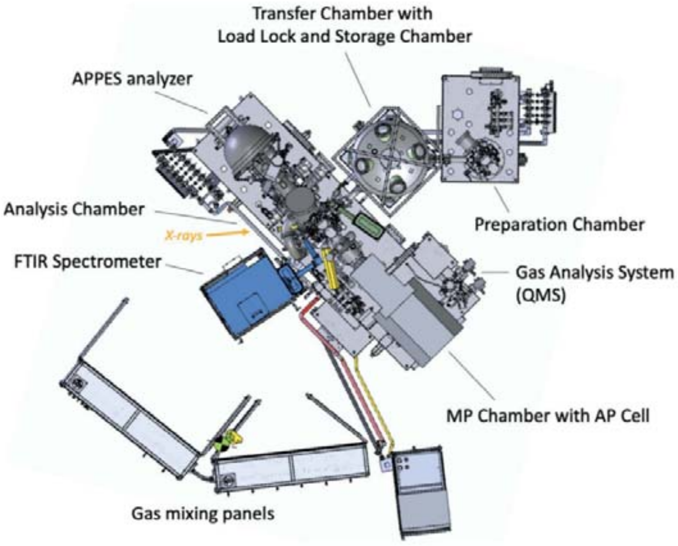

Figure 2.9. Schematic of the **NAP-XPS** endstation at HIPPIE beamline in MaxIV synnchnotron. Reproduced with permission [278], Copyright 2021, Journal of synchrotron radiation.

2.3.3. XPS data Processing

This section outlines the methods used for fitting the Ni 2p and Ce 3d spectra, along with the quantitative analysis of the XPS results. The peak fitting of the XPS spectra was performed using CasaXPS software (CasaXPS vs 2.3.25 PR1.0). The relative amounts of NiO, Ni, CeO_2, and Ce_2O_3 were estimated by fitting the overall Ni 2p and Ce 3d spectra into individual components, utilizing reference peaks corresponding to the pure phases.

2.3.3.1 Ni 2p and Ce 3d peak fitting method

Complex photoemission spectra, such as Ni 2p and Ce 3d, can be fitted using two primary approaches. The first method involves employing a synthetic line shape formed by a combination of individual Voigt-type peaks, each corresponding to a photoemission or satellite peaks [279–282]. To prevent over-interpretation, various constraints should be applied regarding the intensity ratios and relative positions of each component. For instance, ten individual peaks are typically necessary for the Ce 3d spectra, which reflect the Ce^{3+} and Ce^{4+} oxidation states [281]. In contrast, 20 components are needed for the Ni^0 and Ni^{2+} states [283], leading to a total of up to 30 individual peaks required for fitting both the Ni 2p and Ce 3d spectra. Establishing universal constraints for fitting is challenging, which raises questions about the reproducibility of the fitting results [284].

Alternatively, when reference material spectra are available, the overall spectrum can be fitted more easily by employing a linear combination of predefined peak line shapes (obtained under identical recording conditions) from the reference components [285]. This latter approach simplifies the fitting procedure, as it requires a significantly reduced number of peaks. For instance, only a maximum of four peaks are needed for the Ni 2p and Ce 3d spectra [286], in contrast to the 30 peaks required by the earlier method.

In the current study, the Ni 2p and Ce 3d spectra were fitted using line shapes recorded in situ from reference materials subjected to oxidative or reductive treatments. The reference Ni 2p peak for metallic Ni (Ni^0) was measured from a Ni/YSZ sample fully reduced in H_2, while the NiO peak was obtained under O_2 at 400 ℃. For the Ce 3d peak, ceria powder samples were utilized. During the fitting procedure, the full width at half maximum and the energy differences between various reference peaks were fixed. The absolute binding energy and intensity (area) of each peak were allowed to vary until the difference between their sum and the experimental spectrum (residual standard deviation, STD) was minimized, with typical STD values ranging from 0.8 to 1.6. Background subtraction was carried out using a flexible background shape based on Cubic Spline Polynomials (spline linear profile), allowing for adaptation to potential differences in the background profiles between the reference peaks and the spectra of interest. For example, Figure 2.10 illustrates the fitting results for Ni/YSZ electrodes in a $H_2O + H_2$ atmosphere. The Ni 2p peak can be deconvoluted into two components: a sharp Ni $2p_{3/2}$ peak around 853 eV, corresponding to Ni metal, and a broader Ni $2p_{3/2}$ feature at 856 eV, associated with Ni oxide [287–289].

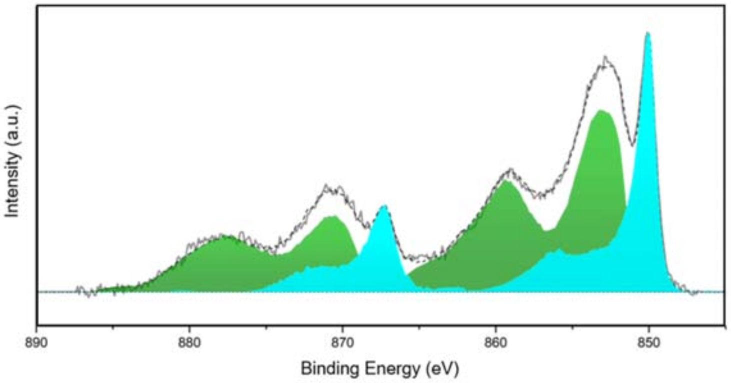

Figure 2.10 A peak fitting example for the estimation of nickel stoichiometry of Ni/YSZ cathodes via NAP-XPS measurements at 700 ℃ under 1mbar H_2O+H_2 atmosphere during electrolysis

2.3.3.2 Calculation of Ni and Ce oxidation states using XPS spectra

The relative amounts of NiO, Ni, CeO_2, and Ce_2O_3 were estimated by deconvoluting the overall Ni 2p and Ce 3d spectra into individual components, utilizing reference spectra from pure phases, as mentioned above. The mean valences x and y for cerium and nickel, respectively, were calculated using the following formulas:

$$x = \frac{NiO}{NiO + Ni} \qquad Eq. 1$$

$$y = 2 \times \left(\frac{CeO_2}{CeO_2 + Ce_2O_3}\right) + 1.5 \times \left(\frac{Ce_2O_3}{CeO_2 + Ce_2O_3}\right) \qquad Eq. 2$$

Where: CeO_2, Ce_2O_3, NiO and Ni are the areas of each component in the photoelectron spectrum calculated after the deconvolution procedure.

2.3.3.3 Estimation of the error in the oxidation state

The error associated with the calculation of oxidation states for Ni and Ce comprises both systematic and random (statistical) errors. The systematic error is mainly linked to the reference peak profiles, whereas the random error arises from variations in the signal-to-noise ratio across the spectra and the selection of the background. In this study, systematic errors are effectively canceled out, as the fitting results are assessed on a comparative basis. The signal-to-noise ratio for the various Ni 2p and Ce 3d spectra, typically around 40, remains relatively stable. Consequently, the fitting results' error primarily stems from the selection of the background's starting and ending points, as well as its shape.

The standard deviation was calculated based on the variation in the areas of NiO, Ni, CeO_2, and Ce_2O_3 resulting from four different fitting attempts of the same Ni2p and Ce3d spectrum. In each attempt, the background was chosen slightly differently (while always adhering to rational criteria), and the four reference spectra were allowed to vary to minimize the standard deviation (STD) value. Utilizing this method, the STD for the area of each spectral component was approximately 0.5% across the four fitting attempts. From this figure, an error of about 0.01 was estimated for the calculations of the x and y valences.

2.3.3.4 Quantitative calculations

The surface atomic ratios for nickel based electrodes were calculated based on the intensities of the XPS spectra using the following equation [274]:

$$\frac{A.r(a)}{A.r\,(b)} = \frac{\frac{I(a)}{Cs(a).f(a)}}{\frac{I(b)}{Cs(b).f(b)}} \qquad Eq.3$$

Where $\frac{A.r(a)}{A.r\,(b)}$ is the atomic ratio of elements (a) and (b),

I– the intensities obtained from the XPS spectra for the corresponding element,

f– the energy dependent incident photon flux,

Cs– the photoelectric cross-section for the interested atomic orbital,

Figure 2.11 shows indicative incident photon flux curves as a function of photon energy for the CAT@EMIL beamline at BESSY II.

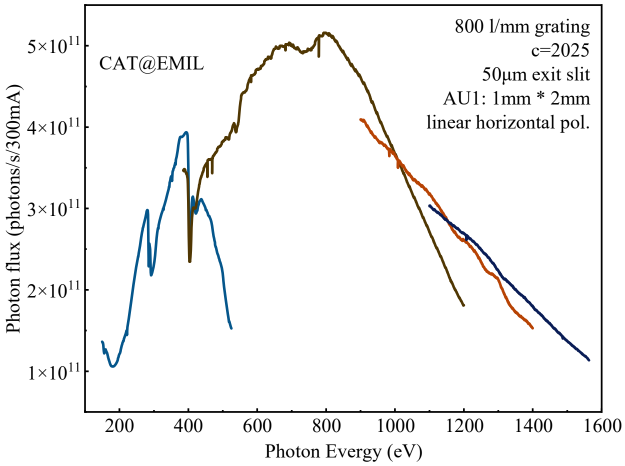

Figure 2.11. Incident photon flux vs photon energy recorded at ISISS beamlines of BESSY II synchrotron correspondingly. Please note that this graph is given as an indication of the flux in each energy but the absolute flux between the two beamlines cannot be compared by this graph.

2.4. ESRF-BM23 Beamline for EXAFS and XANES measurements

The X-ray absorption near edge structure (XANES) experiments were conducted at the BM23 beamline of the ESRF synchrotron facility. BM23 is a wiggler beamline optimized for high-quality EXAFS over a wide energy range of 5~75 keV. The high-intensity beamline enables investigations of materials at micron depths. The specific arrangement of the sample and support is illustrated in Figure 2.12.

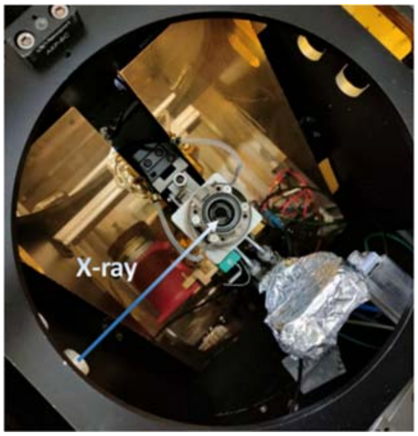

Figure 2.12. Photo of XAFS and FTIR analysis chamber and holder, and schematic of X-ray angle of incidence

2.5. Electrochemical testing techniques (EIS and Chronoamperometry)

2.5.1. Chronoamperometry

Chronoamperometry is an electrochemical technique in which a constant potential (voltage) is applied to an electrochemical cell, and the resulting current is measured over time. The current response provides insights into the evolution of the oxidation state of the electrode materials and clearly indicates degradation phenomena, evidenced by an increasing current. NAP-XPS measurements in synchrotron facilities and most of the performance tests of H_2O electrolysis were conducted under constant applied voltages between the working and counter electrodes. These measurements will be discussed in more detail in Chapters 4 and 5.

2.5.2. Electrochemical Impedance Spectroscopy (EIS)

Electrochemical impedance spectroscopy (EIS) is a widely used technique for characterizing battery changes and understanding the electrochemical behavior of batteries. This method has previously enhanced our understanding of the state of charge (SOC) during fuel cell operation [290,291]. The resistance of electrochemical cells is influenced by various processes, which may include the gas transport of reactants and products, charge transfer reactions at the three-phase boundary (TPB), gas conversion, and both electronic and ionic conduction within the electrodes and electrolyte. These processes typically exhibit different time constants and occur over distinct timescales, allowing the application of alternating current (AC) impedance to provide detailed information about them and their contributions to the overall resistance. Because AC can be generated at a range of frequencies, it offers a means to probe these processes using various time constants [292].

AC impedance is typically obtained by applying a small AC voltage superimposed on a DC voltage and then measuring the current flowing through the battery. The applied AC voltage is kept sufficiently small (~10 mV) to avoid affecting the steady-state conditions, ensuring a near-linear AC current response to the sinusoidal potential. The resulting impedance spectra are often fitted to an equivalent electrical model, serving as an electrical fingerprint of the sample and providing insights into its properties and behavior. EIS is fundamentally conducted as follows: in one of its two configurations, known as "potentiostat EIS," a sine-wave voltage (as represented in Eq. 4) is applied to the sample under investigation, and the induced current is measured (as shown in Eq. 5). The complex impedance is then calculated according to Eq. 6 [293].

$$V(t) = \bar{V} + \hat{V} \cdot \sin(\omega t) \qquad Eq.4$$

$$I(t) = \bar{I} + \hat{I} \cdot \sin(\omega t + \varphi) \qquad Eq.5$$

$$Z(j\omega) = \frac{V(j\omega)}{I(j\omega)} = \frac{\hat{V}}{\hat{I}} \cdot e^{-j\theta} = |Z| \cdot e^{j.Arg(z)} \qquad Eq.6$$

$$= Re(z) + j \cdot Im(Z)$$

In this context, $\hat{V}$ and $\hat{I}$ denote the amplitudes of voltage and current, respectively; $\bar{V}$ and $\bar{I}$ represent the voltage and direct current (DC) values; f is the signal frequency; $\omega = 2\pi f$ indicates the angular frequency; φ is the phase difference between $V(t)$ and $I(t)$; and $V(j\omega)$ and $I(j\omega)$ are the Steinmetz transforms of $V(t)$ and $I(t)$, respectively. In the alternate version of EIS, termed "galvanostat EIS," the sample is excited with a sine-wave current while the resulting voltage drop is measured, with the impedance still expressed by (Eq. 6). Generally, the investigations using either potentiostat EIS or galvanostat EIS yield equivalent results, with the optimal choice depending on application-specific conditions.

The impedance $Z(j\omega)$ is defined for linear time-invariant systems, which exhibit three key conditions: (a) linearity, (b) stability, and (c) causality. However, electrochemical systems often demonstrate nonlinear behavior; thus, to minimize excessive perturbations to the sample under test (SUT), small values of $\hat{V}$ (typically ranging from 10 to 100 mV) are utilized to operate within a pseudo-linear region where $Z(j\omega)$ is independent of $\hat{V}$.

Nyquist and Bode plots are commonly employed to illustrate impedance spectra. The Nyquist plot (complex plane plot) displays experimental data points *Zre* and *Zim* measured at various frequencies, with each point representing the real and imaginary components of impedance at a specific frequency. On the complex plane, the real part of the impedance *Zre* is plotted on the x-axis, while the imaginary part *Zim* is represented on the y-axis; an example of this plot can be seen in Figure 2.13.

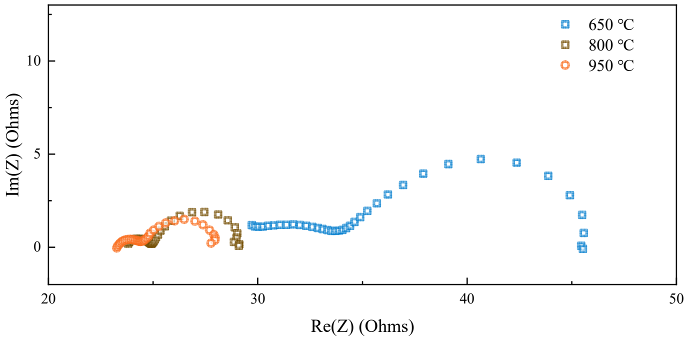

Figure 2.13. Examples of impedance graphs of Ni/YSZ measured at different temperatures, gas condition: 1mbar H_2O+H_2, applied voltage: 2.5V

2.5.3. Chronoamperometry and EIS normalization

This section outlines the normalization procedure applied to the electrochemical measurements, specifically Chronoamperometry and EIS, utilized throughout this thesis. The same procedure was implemented for both Ni/YSZ//YSZ//Pt and modified Ni/YSZ//YSZ//Pt electrochemical cells. In the normalization process for the Nyquist plot obtained from Potentiostatic EIS measurements and chronoamperometry, the surface area of the working electrodes (WE) was taken into account. Simple formulas Eq.7, Eq.8, and Eq.9 were employed to normalize the plots and current density *I* (mA/cm^2). A representative example can be seen in Figure 2.14.

$$Zre\ (Ohm.cm^2) = Zre * WE\ surface\ area \qquad Eq.7$$

$$Zim\ (Ohm.cm^2) = |Zim| * WE\ surface\ area \qquad Eq.8$$

$$I = \frac{\text{Current}}{\text{WE surface area}} \qquad Eq.9$$

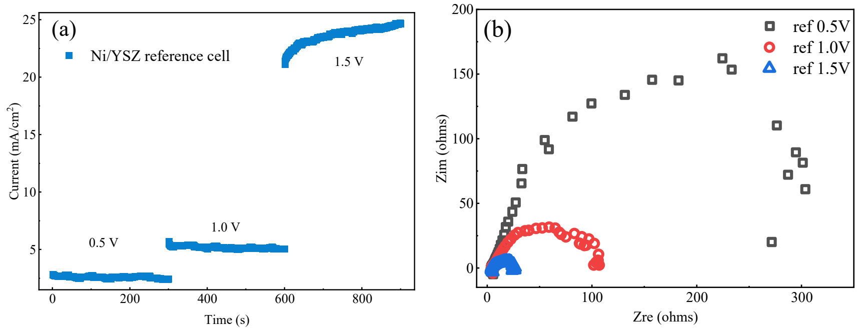

Figure 2.14. a) Current density and **b)** Nyquist plot after normalization over Ni/YSZ//YSZ//Pt cell under 1mbar H_2O electrolysis at 700 °C at the second flow through laboratory setup (ICPEES, France).

2.6. Estimation of potential curves between NiCeO$_x$ NPs and CeO$_y$ NPs in hexane

According to the DLVO theory [294–296], the total interaction force V_{Total} between two particles that are coated with an organic protective layer is the sum of the van der Waals attraction V_{vdW} and the total steric repulsive forces, which include osmotic V_{osm} and elastic V_{elas} components.

$$V_{Total} = V_{vdW} + V_{osm} + V_{elas} \qquad Eq. 10$$

Osmotic repulsion arises from the energetic balance between solvent-ligand tail interactions and tail-tail interactions, while elastic repulsion is a result of the entropy loss associated with the compression of stabilizing ligands. Dispersion stability is primarily governed by the osmotic term, which becomes effective once the ligands begin to overlap. In contrast, the elastic term has little impact on V_{Total} until the ligands are subjected to compression. The van der Waals attraction V_{vdW} can be calculated using Equation 11:

$$V_{vdW} = -\frac{A}{6}\left[\frac{2r^2}{d^2-4r^2} + \frac{2r^2}{d^2} + ln\left(\frac{d^2-4r^2}{d^2}\right)\right] \qquad Eq. 11$$

A is Hamaker constant of cerium nanoparticle in the hexane (3.5×10^{-20}J)[297], r is nanoparticles radius, d is center-to-center separation distance between two nanoparticle cores. According to Vincent et al., [294,295,298], V_{osm} results from the energetic balance between solvent-ligand tail and tail-tail interactions, which was estimated as following:

$$V_{osm} = \frac{4\pi r k_B T}{v_{hexane}} \emptyset^2 \left(\frac{1}{2} - \chi\right)\left(l - \frac{d-2r}{2}\right)^2 \quad (l < d - 2r < 2l) \qquad Eq. 12$$

$$V_{osm} = \frac{4\pi r k_B T}{v_{hexane}} \emptyset^2 \left(\frac{1}{2} - \chi\right)\left[l^2\left(\frac{d-2r}{2l} - \frac{1}{4} - ln\left(\frac{d-2r}{2}\right)\right)\right] \quad (d - 2r < l) \qquad Eq. 13$$

k_B is Boltzmann's constant, v_{hexane} is the molecular volume of the solvent hexane, $\emptyset$ is the volume fraction profile of the organic species surrounded nanoparticle (oleylamine) ($\emptyset = 1 - \frac{r^3}{(r+l)^3}$), l is oleylamine length ~2 nm, and χ is the Flory-Huggins interaction parameter, which is written as the follows [298]:

$$\chi = \frac{v_{hexane}}{RT}\left(\delta_{hexane} - \delta_{oleylamine}\right)^2 + 0.34 \qquad Eq. 14$$

Here, R is gas constant, T is the temperature (298 K), δ_{hexane} (14.9MPa$^{1/2}$) and $\delta_{oleylamine}$ (16.6MPa$^{1/2}$) are the solubility parameters of hexane and oleylamine, respectively. v_{hexane} is calculated to be 2.17x10^{-28} m^3. By using eq.14 χ parameter is calculated to be 0.49.

The elastic repulsionV_{elas} originates from the entropy loss that occurs upon compression of the organic species oleylamine, namely, in the range of $d - 2r < l$.

$$V_{elas} = \frac{2\pi r k_B T l^2 \emptyset \rho_{oleylamine}}{M_{oleylamine}} \left\{ x ln \left[x \left(\frac{3-x}{2} \right)^2 \right] - 6 ln \left(\frac{3-x}{2} \right) + 3(1-x) \right\} \quad (d - 2r < l) \; Eq. 15$$

$$x = \frac{d - 2r}{l} \qquad Eq. 16$$

where, $\rho_{oleylamine}$ and $M_{oleylamine}$ represent the oleylamine density and molecular weight, respectively.

In this study, the basic parameters of the nanoparticles we used are shown in Table 2.1.

Table 2.1. The parameters for the calculation of the potential curves of NiCeO$_x$ and CeO$_y$ NPs in organic solution.

	NiCeO$_x$ NPs	**CeO$_y$ NPs**
$\boldsymbol{r}$ (nm)[a]	3.8	4.8
$\boldsymbol{l}$ (nm)	2	2
$\emptyset$	0.72	0.65

[a]Nanoparticle radius values r are taken from XRD results of pristine cerium-based nanoparticles in Chapter 4.

2.7. Ex-situ Material Characterization

Pristine and post-mortem electrochemical cells have been characterized ex-situ using methods described in the following subsections.

2.7.1. X-ray Diffraction

The phase composition of the catalyst powders and electrodes was analyzed using X-ray powder diffraction (XRD) on a Bruker D8 Advance diffractometer equipped with a Cu source. For the pristine ceria NPs analysis, the hexane solution was drop-cast onto an amorphous glass substrate and allowed to air-dry. Reference data were obtained from the International Centre for Diffraction Data (ICDD) database. The XRD patterns were recorded over the 20–80° (2θ) range, with a scan step of 0.02°.

2.7.2. Scanning Electron Microscopy and Energy-Dispersive X-ray Spectroscopy

The SEM instrument used in chapter 3 is Zeiss Gemini SEM 500 with a lattice resolution of 1 nm. The measurements were done by Dr T. Dintzer (ICPEES, France). Energy dispersive X-ray spectroscopy (EDXS) was combined with the SEM images to resolve the different elements at the surface of the electrodes.

2.7.3. FTIR spectroscopy

FTIR spectra of nanoparticle organic solution were obtained by using a PerkinElmer infrared spectrometer model Spectrum 1000. Spectra were taken using 0.5 cm^{-1} resolution and 30 scans for statistical averaging.

2.7.4. Thermogravimetric analysis (TGA)

The TGA tests of nanoparticle organic solutions were conducted on a thermal analyzer at 10 ℃/min with the flow rate of air (99.99%) at 20 ml/min via using Q 5000IR from TA Instruments.

2.7.5. Dynamic Light Scattering (DLS)

The hydrodynamic particle size analysis was performed using Litesizer^{TM} 500 Particle Analyzer (Anton Paar) by DLS (Dynamic Light Scattering) method (ECPM, France). Nanoparticle solution was diluted and then sonicated in a bath sonicator for 10min. Particle size measurement was carried out at room temperature (25 ℃) and laser wavelength of 660 nm.

Chapter 3. Unveiling Key Interface Characteristics of Ni/YSZ Solid Oxide Cell Electrodes in H_2O Electroreduction using Operando X-ray Photoelectron Spectroscopy

3.1. Introduction

The substantial increase in the utilization of renewable energy as a substitute of fossil fuels represents a key pathway toward global carbon neutrality. This emphasizes the necessity of advancing energy storage technologies to address the intermittent nature of renewable energy sources [299]. Hydrogen emerges as an alternative energy vector to fossil fuels and seems capable of mitigating the environmental concerns associated with traditional energy sources, offering a cleaner and more sustainable solution for the future when compared to fossil fuels. One of the most promising approaches for hydrogen production is water electrolysis by the utilization of surplus electricity from renewable sources and industrial waste heat, offering dual benefits of energy storage and low carbon emissions. Solid Oxide Electrolysis Cells (SOECs) have several advantages over other more-established electrolysis technologies such as alkaline or Proton Exchange Membrane (PEM) cells, including higher Faradaic efficiency, faster reaction kinetics and lower electrical power consumption [300,301]. On the downside, one of the main challenges impeding the widespread adoption of SOEC technology, is the relatively rapid degradation rate associated with the poor long-term durability of the SOEC components at elevated temperatures. Therefore, efforts are ongoing to develop advanced materials and designs for SOECs with improved efficiency and durability [302,303]. SOECs are composed of a dense electrolyte sandwiched between two porous electrodes. Electroreduction of H_2O take place in the fuel electrode (cathode), while oxygen is produced at the air electrode (anode).

While progress has been made in synthesis of novel electrode materials [300,304,305], Ni composites with yttria-stabilized zirconia (YSZ) remain the dominant choice for the cathode electrode (or fuel electrode) in industrial applications [301]. This is because of the low cost, high electronic conductivity, and thermal compatibility of Ni/YSZ with the other cell components [302]. Typically, cells with Ni/YSZ cathode electrodes exhibit good initial performance, but they are prone to progressive deactivation during long-term electrolysis operation [306]. This behavior has been associated to three main degradation mechanisms [301]. The first is related to microstructural changes, including the restructuring of the cathode/electrolyte interface [307] and the coarsening and migration of nickel particles away from the interface with YSZ [308]. The second involves impurities, such as silicon or chromium, which are deposited on the electrode and block the electrochemical active sites. Common sources of impurities are interconnects and glass sealant, while they might also derive from the raw materials via surface segregation. Finally, degradation of Ni/YSZ electrodes may involve nickel oxidation, particularly when operating under high steam content in the cathode compartment or in the event of seal leakage [309,310].

The two first factors leading to degradation are irreversible and can be readily identified through post-mortem characterization of the cells using microscopy techniques combined with elemental analysis such as Energy Dispersive X-ray Spectroscopy [311,312]. On the contrary, detecting nickel oxidation or hydroxylation with post-mortem analysis proves to be considerably more challenging, particularly when seeking detailed information about the initial stages of surface oxidation. This is because nickel is susceptible to oxidation when transferring the sample from the reactor to the spectrometer or microscope. Moreover, post-mortem analysis cannot establish a direct correlation between the electrode's morphological characteristics and the electrochemical performance of the cell. Hence, there is a growing effort to characterize Ni/YSZ electrodes under in situ or operando conditions. In situ analysis typically involves characterizing samples under gas and temperature conditions relevant to electrolysis, whereas under operando measurements the cathode is polarized and the electrical and gas phase responses are monitored as well [313].

As recently summarized by Jeangros et al., various techniques have been employed under in situ or operando conditions to provide insights into the crystallographic properties, microstructural characteristics and chemical state of Ni/YSZ electrodes [314]. Among them, microscopy and surface sensitive spectroscopy are particularly insightful, as they have the capability to reveal fine details of the electrodes at the nanometer scale. Environmental transmission electron and scanning probe microscopies (TEM and SPM respectively) have enabled in situ detailed investigations of the reduction and reoxidation of Ni/YSZ electrodes under few mbar of reactive gas atmospheres [315–321]. However, with only few exceptions [314,315], it turns out to be very challenging to perform microscopy experiments with samples under electrical polarization [322]. On the contrary, several studies exist examining the surface state of solid oxide cell electrodes under operational electrochemical conditions using Near Ambient Pressure Photoelectron Spectroscopy (NAP-XPS) [313,323]. Among them, the number of operando NAP-XPS studies focusing on Ni/YSZ electrodes show an inverse relationship with the widespread utilization of this electrode in practical applications [324–326]. Furthermore, conducting NAP-XPS experiments using higher energy photons (ranging between 2 and 10 keV), known as Hard X-ray Photoemission Spectroscopy (HAXPES), presents the opportunity to significantly enhance the analysis depth of the technique [327–330].

This enables investigations of samples under considerably higher gas pressure or exploration of buried liquid/solid interfaces.

In the present study, we employ synchrotron-based NAP-XPS and NAP- HAXPES techniques to investigate the surface and subsurface characteristics of Ni/YSZ electrodes during both open circuit and polarization conditions. The spectroscopic results are combined with the online gas phase analysis and electrochemical characterization of the cell, allowing the correlation of surface chemical states with electrocatalytic performance.

This chapter is based on the article: J. Zhang, M. Barreau, T. Dintzer, M. Haevecker, D. Teschner, A. Efimenko, W. Luo, S. Zafeiratos, Unveiling Key Interface Characteristics of Ni/Yttria-Stabilized Zirconia Solid Oxide Cell Electrodes in H_2O Electroreduction Using Operando X-ray Photoelectron Spectroscopy, *ACS Appl. Mater. Interfaces*, 2024, 16, 29, 37915–37926.

3.2. Experiments and methods

3.2.1. Cell fabrication

Commercially available electrolyte-supported Ni/YSZ half-cells obtained from Kerafol GmbH were employed in this study as depicted in section 2.1. A Pt electrode (anode) was brushed symmetrically opposite the Ni/YSZ cathode electrode using platinum paste to produces a Pt anode.

3.2.2. Ex-situ characterization

Scanning electron microscopy (SEM) measurements were conducted utilizing a Zeiss GeminiSEM 500 microscope. The samples were attached to the sample holder by using a double-sided carbon tape. The X-ray diffraction (XRD) patterns were recorded with a Bruker D8 advance diffractometer operating at 40 kV and 40 mA using Cu Kα X-ray source.

3.2.3. Synchrotron-based operando photoemission and absorption experiments

Photoemission experiments were performed at ISISS and CAT@EMIL beamlines at the synchrotron radiation facility BESSY II of the Helmholtz Zentrum, Berlin [331–333] as introduced in section 2.3.1.

Spectroscopic experiments were conducted on miniature Ni/YSZ//YSZ//Pt cells (geometric area around 25 mm^2) which were fragmented from an initial button cell with a diameter of 2 cm. A photograph and a schematic representation of the cell mounted on the holder are shown in Figure 3.1a and 3.1b respectively. The cell was mounted on a sapphire holder with a whole at its center allowing direct heating by illuminating the stainless-steel back plate with an IR laser. The temperature was measured at the center of the working electrode with a calibrated pyrometer. For the photoemission measurements the working electrode was connected to the ground, and the voltage was applied to the counter electrode so as the O^{2-} ions are moving towards the Pt counter electrode as shown in Figure 3.1b. This configuration corresponds to a single chamber electrochemical experiment meaning that both, cathode and anode sides of the cell are exposed to the H_2O/H_2 mixture.

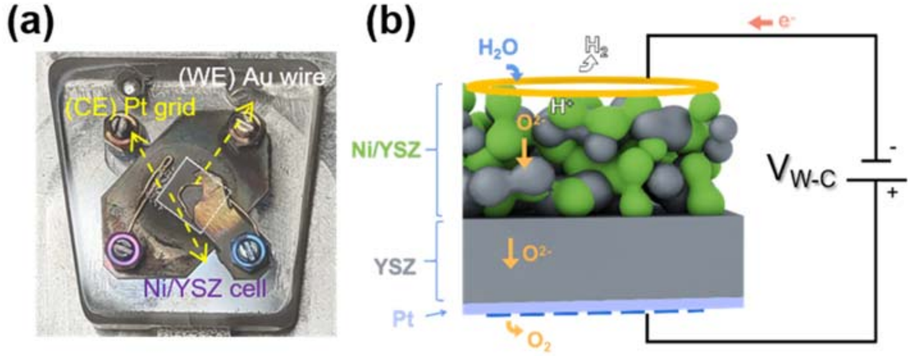

Figure 3.1. (a) Photograph of the NiYSZ//YSZ//Pt cell mounted on the NAP-XPS sample holder. **(b)** cross-section schematic of the cell mounted for spectroscopy

Following the introduction to the spectrometer, each sample underwent calcination at 400 °C in 1 mbar O_2 for a duration of 30 minutes, aimed at removing any adventitious carbon species present on the Ni/YSZ electrode. Electrolysis experiments were performed at constant potential mode at 750 °C in H_2O:H_2 (9:1) flow and 1 mbar total pressure. The electrochemical performance was evaluated through chronoamperometry and electrochemical impedance spectra (EIS) using a computer-controlled potentiostat (SP-300 Potentiostat, BioLogic Scientific Instruments). The electrical values presented in this article have been normalized to the geometric area of the cell. The open-source software EISART was used to interpret the EIS outcomes into DRT (Distribution of Relaxation Times) results [334]. Detailed procedures for calculating the analytical DRT of common equivalent circuit elements have been documented by Dierickx et al. in reference [335]. This analysis showed that the peak with the highest frequency (denoted as P1 below) represents ionic transport in the Ni-YSZ fuel electrode (cathode) structure; P2 corresponds to the charge transfer reaction in the fuel electrode (cathode); P3 corresponds to the O_2 surface exchange kinetics (occurring on the Pt side); and the peak with the lowest frequency (P4) corresponds to gas-phase diffusion in the fuel electrode (cathode). Thus, the relative contribution of the Pt side to DRT plots is minimal compared to that of Ni/YSZ.

The XPS spectra were subjected to spline Shirley background subtraction and fitted using peak shapes previously recorded on reference Ni and NiO samples [336], while symmetrical Gaussian–Lorentzian line shapes were used to fit the Zr 3d and O 1s spectra. In all cases constrains on the width and the relative binding energy position of the fitting components were imposed. The binding energies (BE) of the core-level spectra are referred to the Fermi edge cut-off position, measured using the same photon energy. The accuracy of BE calibration was estimated to be ±0.1 eV.

The presented Ni $L_{3,2}$-edge soft X-ray absorption (sXAS) spectra were measured in the total electron yield (TEY) mode at the same instrument, using a Faraday cup installed in the first aperture of the analyzer electrostatic lenses.

3.3. Result and discussion

3.3.1. Temperature-dependent H_2-reduction and H_2O-oxidation of Ni/YSZ electrodes

3.3.1.1 Evolution of surface oxidation state and composition

Calcined Ni/YSZ electrodes were exposed to 0.5 mbar H_2 at 250 °C and the temperature subsequently increased in a stepwise manner. Ni 2p and Zr 3d NAP-XPS spectra were acquired after 15 minutes at each specific temperature. The Ni 2p spectrum was occasionally measured twice: once at the beginning and again at the end of each temperature step to confirm stability over time. The evolution of the Ni $2p_{3/2}$ spectra in H_2 and subsequently in H_2O vapor atmospheres as a function of temperature is shown in Figure 3.2a. The Ni $2p_{3/2}$ peak of oxidized Ni/YSZ exhibits a broad feature around 856 eV, accompanied by a higher binding energy satellite both indicative of Ni^{2+} nickel species [337,338]. Upon annealing in H_2, a new feature appears at 852.7 eV indicating the reduction of Ni^{2+} species into metallic Ni (Ni^0) [337,338].

To quantify the progress of the reduction with temperature, Ni $2p_{3/2}$ peaks are fitted by linear combination of Ni^0 and Ni^{2+} reference spectra (Figure 3.3). Figure 3.2b (bottom panel) illustrates that approximately 90% of Ni^{2+} undergoes reduction within a narrow temperature range of 325 to 375 °C, leaving 10% of oxidized nickel, which apparently resists to reduction even at 400 °C. This pattern aligns with the anticipated behavior of NiO reduction by H_2, characterized by a preceding incubation period that diminishes with increasing temperature. Subsequent to the initial formation of metallic Ni, the reduction process accelerates due to the catalytic influence of Ni on H_2 reactivity [315]. This can explain the rather rapid NiO reduction above 325 °C. The observation of 10% unreduced NiO is consistent with previous environmental TEM studies performed in 1.3 mbar H_2 [318,339]. This phenomenon was attributed to the presence of H_2O released during the NiO reduction process, which eventually inhibits the reduction of some NiO grains.

The Ni 2p/Zr 3d peak area ratio ($R_{Ni/Zr}$) included in the lower panel of Figure 3.2b, decreases with temperature, reflecting the reduction of surface-exposed nickel. This can be attributed to volumetric changes and/or possible mass transfer of nickel particles upon reduction. Specifically, volume shrinkage is expected upon reduction of NiO to Ni, while volume expansion is anticipated upon re-oxidation [316]. These changes affect the surface area of the nickel particles and consequently the $R_{Ni/Zr}$. Another potential factor contributing to $R_{Ni/Zr}$ changes is the migration of nickel, either towards or away from the YSZ particles, a process known as wetting [340,341]. This phenomenon is anticipated to impact the photoemission signal due to the high surface sensitivity of NAP-XPS technique. The decrease of $R_{Ni/Zr}$ in H_2 aligns with the expected shrinkage of nickel particles upon reduction.

To estimate if the volumetric changes alone can justify the decrease of $R_{Ni/Zr}$ from 0.85 to 0.67 shown in Figure 3.2b, the Ni 2p peak intensity and consequently $R_{Ni/Zr}$ were calculated using the simulation of electron spectra for surface analysis (SESSA) software [342]. In the simulation we use spherical Ni particles and assume that the reduction of NiO to Ni^0 results in a Ni volume shrinkage of 40% [316]. The simulation results indicated a drop in $R_{Ni/Zr}$ from 0.85 to 0.69, independent of the size of the Ni particles, which aligns well with the experimental findings. Thus, the volumetric change of Ni particles during reduction can account for the decreased $R_{Ni/Zr}$. However, in this scenario, the decline in $R_{Ni/Zr}$ and the reduction of NiO should occur simultaneously, which is not observed, as depicted in Figure 3.2b. This can be elucidated by considering the NiO reduction mechanism. As shown before [343]. the transformation of NiO to Ni occurs through the migration of either O ions or Ni cations towards the surface to react with H_2. If O anions are the primary diffusing species, the outermost NiO layer would be reduced, forming a metal-rich shell, and the reduction process would progress inwards. Conversely, if nickel is the main diffusing species, after reduction it will migrate via defects and grain boundaries towards the interior of the NiO particle, exposing fresh metal oxide at the surface. As discussed previously [343]. at temperatures around 500 °C, the diffusion coefficient of Ni in NiO grain boundaries is much greater compared to that of O into nickel metal, thus exposing NiO on the surface and rationalizing the observations of Figure 3.2b. The SEM/EDX mapping micrographs of the electrode surface, measured after reduction (Figure 3.4), reveal nanoporous nickel particles mixed with YSZ grains. Nanopore formation in nickel particles during the reduction of Ni/YSZ cermets has been previously observed and attributed to volume contraction resulting from the reduction of initially present NiO to nickel.

After the reduction process, the Ni/YSZ electrode was cooled to 250 °C and H_2 was replaced by H_2O vapors, subsequently the temperature is raised again for spectra acquisition under H_2O conditions. As shown at the top panel of Figure 3.2a and in Figure 3.5, above 425 °C new features appear in the Ni $2p_{3/2}$ spectra indicating re-oxidation of Ni^0 by H_2O. However, contrary to reduction by H_2, oxidation by H_2O expands in a quite broad temperature range, while at 600 °C (the maximum temperature) around 40 % of nickel remains metallic (Figure 3.2b). The $R_{Ni/Zr}$ ratio in this case is rather stable up to 500 °C and exhibits a sudden increase above this temperature. If one assumes that the changes of $R_{Ni/Zr}$ are exclusively due to the Ni particle volume changes and do not related to diffusion to and from YSZ particles, the sudden $R_{Ni/Zr}$ increase suggests that at 500 °C Ni oxidation proceeds rapidly towards the interior of the particles. However, it is quite unlikely such important volume changes does not affect at all the evolution of nickel oxidation at the surface as this is depicted by NAP-XPS. It is therefore probable that above 500 °C nickel migrates and wets the interface YSZ contributing to $R_{Ni/Zr}$ changes.

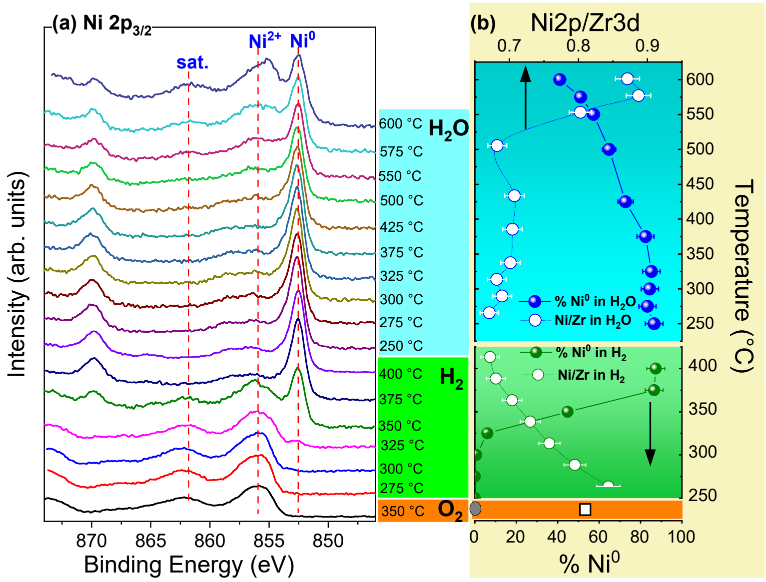

Figure 3.2. (a) The Ni $2p_{3/2}$ NAP-XPS spectra of pre-calcined Ni/YSZ electrodes as a function of the annealing temperature measured by 1065 eV photon energy under 0.5 mbar O_2, H_2 and H_2O. **(b)** The atomic percentage of the metallic Ni component (%Ni^0) to the overall Ni $2p_{3/2}$ spectrum, estimated by peak fitting is shown on the right. The Ni 2p/Zr 3d peak area ratio normalized to the sensitivity factors and the photon flux. The error of $R_{Ni/Zr}$ and $R_{Ni/NiO}$ ratios is estimated to be ±2% and ±5% respectively.

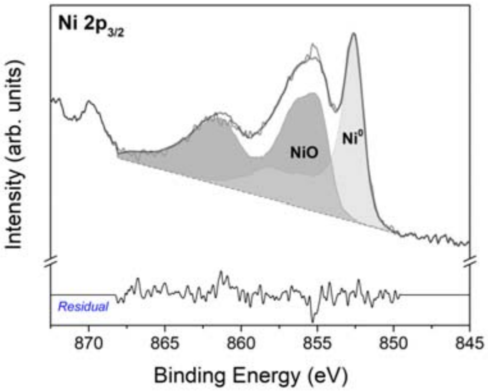

Figure 3.3. Exemplary curve fitting analysis of Ni $2p_{3/2}$ NAP-XPS spectra using peak profiles measured over metallic Ni (Ni^0) and NiO reference samples.

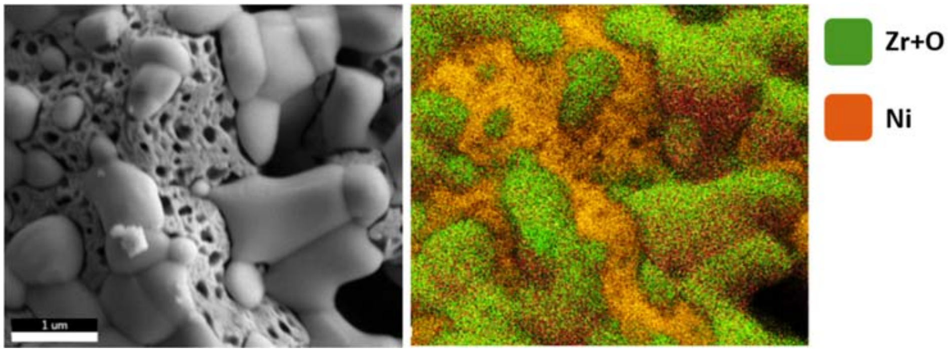

Figure 3.4. Characteristic SEM/EDX mapping micrographs of the Ni/YSZ electrode surface measured after several reduction oxidation cycles.

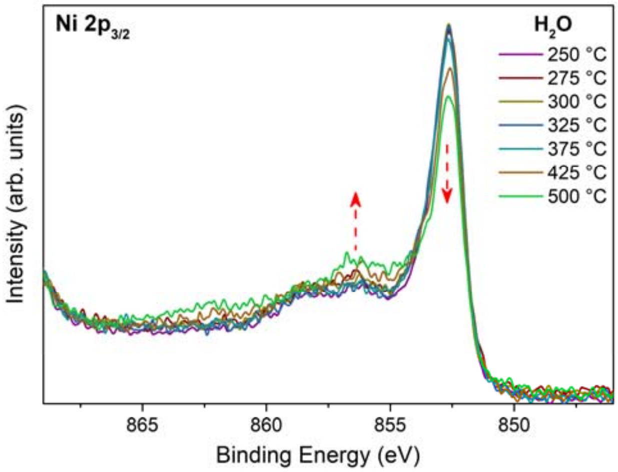

Figure 3.5. The Ni $2p_{3/2}$ NAP-XPS spectra of reduced Ni/YSZ electrode heated in 5 mbar H_2O. Spectra were measured by 1065 eV photon energy. The graph displays a portion of the Ni $2p_{3/2}$ spectra featured in Figure 2 of the main text, aiding in the observation of the initial stages of nickel oxidation above 425 °C.

3.3.1.2 Surface impurities

As highlighted in the introduction, impurities might accumulate at the surface of Ni/YSZ electrode and influence the electrochemical performance of the cell. The surface sensitivity of NAP-XPS allows to identify traces of foreign elements present on the Ni/YSZ electrodes, which holds particular practical interest in this context, as both, the raw materials and the preparation method of the Ni/YSZ electrode follow well established industrial practices. Figure 3.6a shows the survey NAP-XPS spectra of the Ni/YSZ electrode measured in O_2, H_2 and H_2O at the maximum annealing temperature. The measurements were conducted sequentially, with exposure durations of 2.5 hours in O_2, 7.5 hours in H_2, and 12.5 hours in H_2O. As anticipated, photoemission and Auger peaks originating from Ni, Zr, Y, and O are consistently observed.

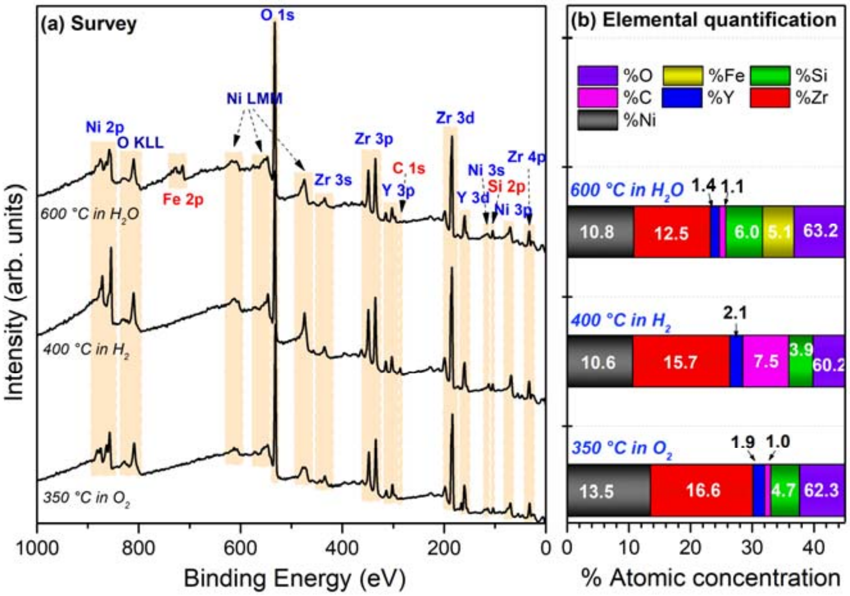

Figure 3.6. (a) Survey spectra of Ni/YSZ electrode measured by 1320 eV photon energy in 0.5 mbar O_2, H_2 and H_2O at the temperatures indicated in the graph. The photoemission and Auger peaks associated to Ni/YSZ and impurities are identified. **(b)** The atomic concentration (at. %) of the surface elements calculated from the photoemission peaks assuming homogenous distribution within NAP-XPS analysis depth. The quantitative calculations rely on photoemission peaks with comparable kinetic energies (approximately 180 eV) to compensate for the attenuation of photoelectrons caused by the gas phase. The error in at.% is estimated around 10% and related to the uncertainties in the flux curves, the atomic sensitivity factors and the photoemission peak areas.

In addition, C, Si and Fe (only for H_2O-treated sample) were also detected. Carbon can originate either from adventitious carbon due to prior exposure to air [344] or be generated in situ from hydrocarbon residues in the NAP-XPS analysis chamber. Silicon impurities has been reported in prior NAP-XPS studies. Their source has been attributed to thermal segregation of bulk impurities to the surface or to gas-mediated transport resulting from the formation of volatile silica species in the NAP-XPS chamber[345,346].

Although the detection of carbon and silicon-based impurities may not come as a surprise, the presence of iron on the H_2O-treated electrode is somewhat unexpected. Chromium evaporation from the stainless-steel interconnects is known as a reason for the long-term degradation of the Ni-YSZ solid oxide cells [347], however in our case iron instead of chromium is detected. Iron is a known impurity in commercial KOH solutions [348], but to the best of our knowledge, it does not exist in Milli-Q water, nor has it been reported in solid oxide cell electrolysis experiments before. The most probable source of iron is the stainless-steel plates used to support and fix the Ni/YSZ sample on the holder (Figure 3.1a), and the deposition of iron may proceed via the formation of volatile iron hydroxide species. Please note that the Ni/YSZ is heated by contact with the laser beam illuminated stainless steel back plate, therefore it is expected that the latter is at temperatures significantly higher than that of the sample (i.e. 600 °C). Although the evolution of iron with time was not studied here, the long-term exposure to H_2O vapours (more than 12 hours) is expected to affect the accumulation of iron on the sample.

The surface atomic concentration is calculated from the photoelectron peak intensities assuming homogenous distribution of all elements within the NAP-XPS analysis depth (about 1.6 nm). As shown in Figure 3.6b, the amount of surface carbon is greatly enhanced in H_2, while silicon and iron impurities reach a maximum in H_2O of 6.0 and 5.1 at.%, respectively. It is also interesting to note that the at.% of Y in respect to Zr remains practically stable (around 11±1%) which excludes yttrium segregation from the YSZ lattice previously observed [349] and confirm the thermal stability of YSZ under the employed conditions.

3.3.2. Operando photoemission measurements of Ni/YSZ electrode during H_2O electrolysis

3.3.2.1 Measurements in the functional and conduction electrode layer regions

As mentioned in the experimental, the top part of the cathode electrode was composed by a Ni/YSZ layer with the high nickel content serving as the electron conduction layer. Aiming to access through photoemission experiments the electrode region proximal to the YSZ electrolyte—commonly regarded as the electrochemically active area [350]—the upper section of the electrode in regions situated at the center of the miniature cell was removed through mechanical scraping. To ensure consistency, a single trained operator conducted the process following a standardized protocol. Figure 3.7 combines SEM micrographs taken from different parts of the cell. Aside from the YSZ electrolyte and the Pt counter electrode areas, Figure 3.7 shows regions where the upper section of the Ni/YSZ electrode is scraped off (referred to as "inner"), along with sections where the electrode remains intact (referred to as "top"). The position of photoemission measurements was aligned to the inner electrode area with the assistance of a laser beam illuminating the measurement spot. Apart from the visual verification, the inner and top electrode areas (functional and conduction layers) can be distinguished by their difference in the electrode composition containing 60 and 90% Ni, respectively.

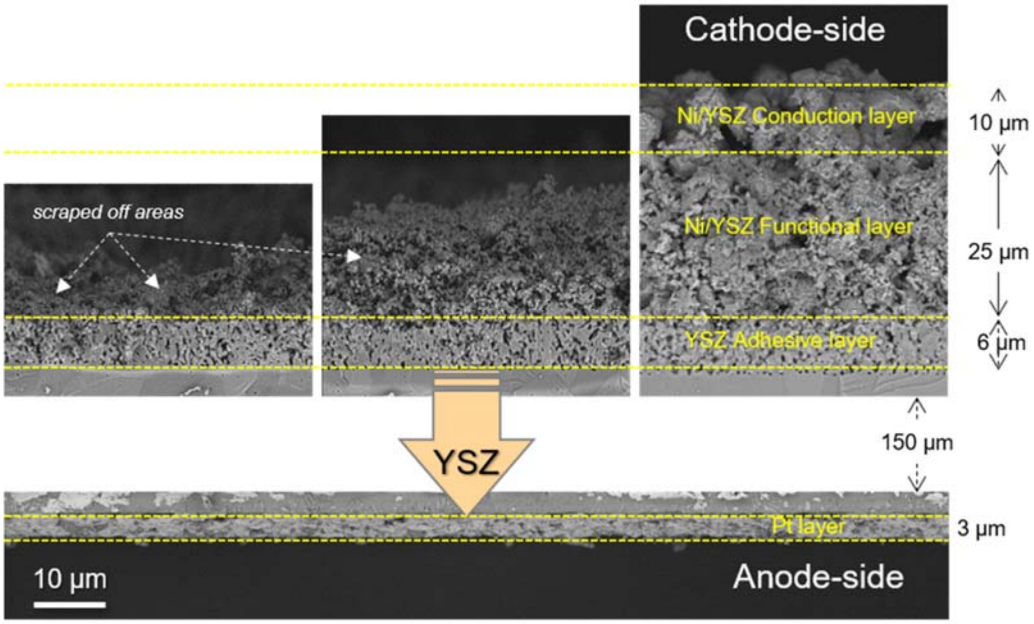

Figure 3.7. SEM micrographs of cross-section views of the Ni/YSZ//YSZ//Pt miniature cells used in the NAP-XPS experiments. The top section depicts the cathode side of the cell (i.e., Ni/YSZ electrode), illustrating areas where the Ni/YSZ functional layer remains intact (on the right side) and where it has been scraped off (on the left and middle sections). The SEM micrograph at the bottom corresponds to the anode electrode side, which comprises a thin Pt layer.

Figure 3.8a and 3.8b shows the Ni 2p and Zr 3d spectra respectively, obtained in inner and top electrode regions with the cell under electrolysis conditions ($V_{W\text{-}C}$ =2.5 V, 1 mbar H_2O at 750 °C). The atomic percentage of Ni at each measurement spot, calculated from the Ni 2p and Zr 3d spectra, reveals a significantly lower Ni concentration in the inner section compared to the top part of the electrode. This finding is consistent with the expected composition of the electrode in the two areas. The Ni 2p spectra measured during H_2O electrolysis for all measured spots are assigned to NiO, owing to their close resemblance with the Ni 2p peaks recorded in O_2 atmosphere (Figure 3.9a). It is important to highlight that the increased nickel oxidation degree observed here, in comparison to that depicted in the oxidation experiment of Figure 3.2, can be attributed to the elevated H_2O pressure and temperature during electrolysis. Nickel oxidation is expected to negatively impact the electrolysis performance of the cell [306]. Indeed, as depicted in the table within Figure 3.8, there is a rapid deactivation of the cell with about 40% reduction in the current density (j) during the NAP-XPS measurement period (15 min). This is followed by an increase in the ohmic resistance (R_{Ω}) for about 1.2 $\Omega \cdot cm^{-2}$ as determined from the Nyquist plots (not shown). The fast degradation of the performance suggests that the cell is in a dynamic mode and not in equilibrium state under these measurement conditions. Hence, co-feed H_2 with H_2O is essential to prevent electrode oxidation and the consequent rapid deactivation.

We now turn our focus to the Zr 3d peak, which as shown in Figure 3.8b displays a significant BE shift between the inner and top measurement sections. Given that the Zr 3d peak shape is identical in all cases, the observed shift should not be misconstrued as a chemical shift, which typically indicates a change in the chemical state of an element. The origin of this shift in Figure 3.8b should be connected to the difference in the electric potential between inner and top areas. Note that the Ni/YSZ electrode is grounded via the Au wire pressed on its top, implying that its Fermi level is aligned to that of the analyser. However, a potential gradient is expected within the cathode electrode, between the top part and the interface with the YSZ electrolyte [341,351]. As shown before, changes in the local electric potential are manifested by equivalent changes in the BE of photoemission peaks [325,352]. Therefore, the shift of Zr 3d peak towards higher BE under polarization, reflects the potential difference between the conduction and functional layer within the Ni/YSZ electrode depth, as shown schematically in the inset of Figure 3.8b.

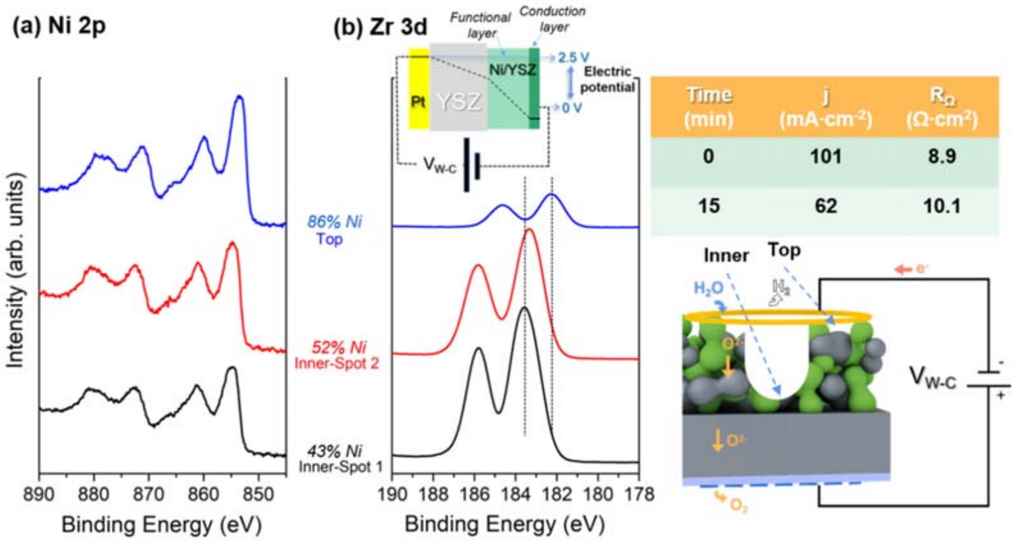

Time (min)	j (mA·cm⁻²)	R_Ω (Ω·cm²)
0	101	8.9
15	62	10.1

Figure 3.8. (a) Ni 2p (hv=1065 eV) and **(b)** Zr 3d (hv=390 eV) NAP-XPS spectra measured at different spots within a Ni/YSZ electrode under electrolysis conditions ($V_{W\text{-}C}$ =2.5 V, 1 mbar H_2O at 750 °C). A simplified representation of the electric potential distribution within the polarized cell is given in the inset. A schematic representation of inner and top parts of the electrode as well as the electrical characteristics of the cell while measuring the NAP-XPS spectra are given at the right panel of the figure.

The extended surface oxidation of Ni mentioned above provides an opportunity to contribute to the discussion regarding the mechanism of Ni coarsening and migration during long term operation. This phenomenon has been recognized as a contributing factor to the degradation of Ni/YSZ electrodes during long-term H_2O electrolysis [353]. In particular, two main mechanisms have been put forward in literature to explain the Ni migration in Ni/YSZ electrodes. The first is related to the formation and diffusion of volatile Ni-hydroxide species (i.e. $Ni(OH)_x$) enhanced by dynamic NiO/Ni redox processes [341,354], while the second does not involve $Ni(OH)_x$ and is based on Ni spreading and covering of YSZ areas following a wetting process [340,355]. Although Ni migration requires longer periods and higher current densities from those used here, our results can relatively safely distinguish the formation or absence of $Ni(OH)_x$. This is crucial for elucidating if the mechanism of Ni coarsening and migration proceeds via volatile $Ni(OH)_x$ or primarily follows the wetting process. As mentioned above, under H_2O electrolysis conditions our Ni 2p NAP-XPS spectra resemble those of NiO (Figure 3.9a), while similar conclusions can be drawn by the absence of the characteristic OH features at about 532 eV in the O 1s peak (Figure 3.9b) [356].

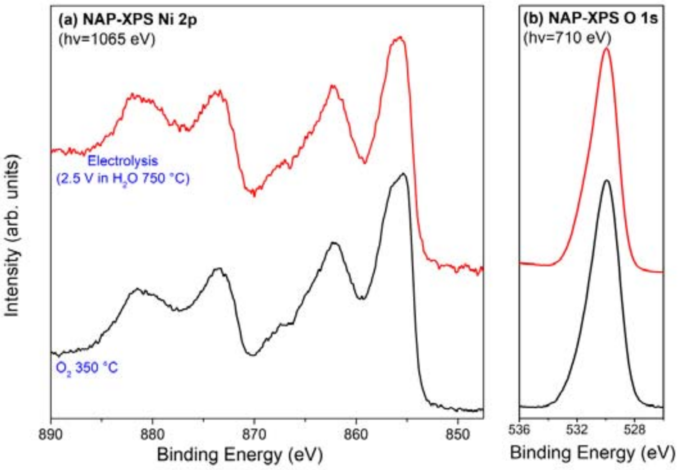

Figure 3.9. (a) Ni 2p and **(b)** O 1s NAP-XPS spectra of the Ni/YSZ electrode under 1 mbar O_2 at 350 °C (bottom) and under H_2O electrolysis conditions (top).

Additional evidences about the nickel oxide phase come from Ni $L_{3,2}$-edge X-ray adsorption spectra shown in Figure 3.10. Previous sXAS studies have shown that the Ni L-edge is particularly sensitive to changes in the Ni coordination environment, therefore not only distinguishes the difference in the nickel oxidation state but also in the eventual formation of different nickel oxide and hydroxide phases [357,358]. As shown previously, notable differences exist in the Ni L-edge absorption spectra when comparing NiO with β-$Ni(OH)_2$, β-NiOOH, and γ-NiOOH compounds [358]. In particular the intensity ratio between the two absorption features at 869.9 and 871.0 eV in the Ni L_2-edge changes dramatically in favour of the 871 eV peak in Ni-(oxy)hydroxides as compared to NiO [358]. Figure 3.10 shows that the Ni L-edge in O_2 and the electrolysis conditions is almost identical and resembles that of NiO samples reported in literature [357,358]. Hence, based on the above discussion, the formation of $Ni(OH)_x$ species should be ruled out, attributing Ni oxidation to $Ni + H_2O_{(g)} \rightarrow NiO + H_{2(g)}$ reaction. This result supports that Ni depletion from the YSZ interface observed during long-term electrolysis operation, most likely follows Ni spreading via the wetting mechanism rather than the formation of volatile Ni-hydroxide species.

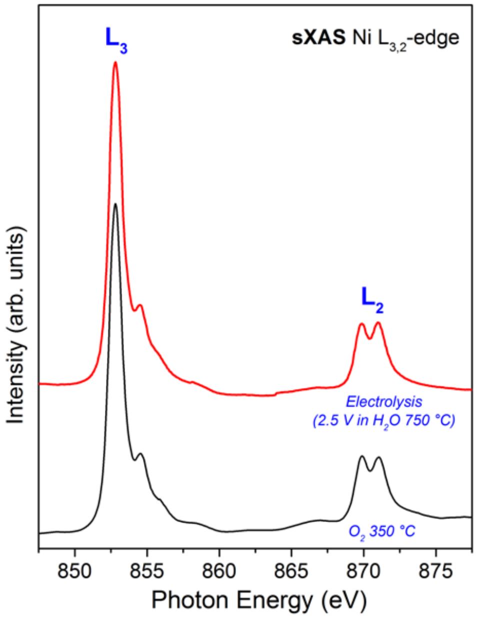

Figure 3.10. Ni $L_{3,2}$-edge soft X-ray adsorption spectra (sXAS) of the Ni/YSZ electrode under 1 mbar O_2 at 350 °C (bottom) and under H_2O electrolysis conditions (top).

3.3.2.2. Effect of the nickel oxidation state in the H_2O/H_2 electrolysis performance

The findings discussed in section 3.3.2.1. suggest that, in direct H_2O electrolysis conditions (i.e., without the presence of a reducing gas), nickel oxidation is followed by a fast degradation of the cell performance. The nickel oxidation state at equilibrium depends on factors such as temperature, pressure, applied potential and gas phase composition. Nevertheless, the kinetic barriers might impede the progression of surface reactions toward equilibrium. Consequently, varying the initial electrode chemical state can result in the preservation of metastable surface compositions under identical electrolysis conditions [359]. In line with this concept, Ni/YSZ electrodes with two distinct Ni oxidation states were prepared following slightly different pretreatments. Subsequently, the electrodes were subjected to H_2O/H_2 electrolysis conditions to examine how the nickel surface oxidation state influences cell performance.

Specifically, the electrode underwent an initial treatment under pH_2O/pO_2 (9/1) at 750 °C for 15 minutes. As evidenced by the Ni 2p NAP-XPS and NAP-HAXPES spectra presented in Figure 3.11, this treatment was adequate for the complete oxidation of nickel. Consequently, O_2 was swapped by H_2 and the cell was tested for H_2O/H_2 electrolysis ($E_{W\text{-}C}$ = 2.5 V, pH_2O/pH_2=9/1 at 750 °C). The Ni 2p spectra measured at the inner section of the electrode during electrolysis (Figure 3.12a) indicate that nickel is in a partially reduced state containing both Ni^0 and NiO species. It is important to note that the operando electrolysis experiments were carried out within a short timeframe (between 15-20 minutes) to prevent substantial alterations in the Ni oxidation state. The Ni 2p spectra acquired at the beginning and at the end of the electrolysis cycle (Figure 3.12a) reveal ongoing reduction of NiO during the experiments. The relative amount of Ni^0 and NiO is estimated by Ni 2p peak fitting evidences a rise in the Ni/NiO ratio ($R_{Ni/NiO}$) from 0.48 initially to 0.66 at the end. For the sake of brevity, we will refer to this electrode as "oxidized".

A second electrode was subjected in a similar H_2O/O_2 pretreatment process however, to further reduce NiO before the onset of electrolysis, the composition of the H_2O/H_2 mixture was momentarily enriched in H_2 (pH_2O/pH_2 was raised to 2/1 for less than 1 minute). As illustrated at the bottom panel of Figure 3.12a, this treatment results in a substantially more reduced and stable electrode surface which is maintained during electrolysis compared to the previous case. Specifically, the $R_{Ni/NiO}$ experiences a slight increment from 1.57 to 1.68 over the course of the experiment. From now on, this electrode will be referred to as "reduced". For both pretreatments, the BE of the Zr 3d peak remains stable at 183.5 eV, suggesting that the electric potential at the NAP-XPS measurement area is very similar in both cases. Overall, photoemission experiments show that by controlling the pretreatment, the Ni/YSZ electrode can be measured at identical electrolysis conditions but with a different degree of nickel surface oxidation.

Having shown this, we now direct our attention to how the oxidation state of nickel affects the electrochemical performance of the cell. The mean current density and O_2 production, illustrated in Figure 3.12b, suggest that the cell with "reduced" Ni/YSZ exhibits higher current densities and O_2 production than the "oxidized". Furthermore, the Nyquist plots in the two cases (Figure 3.12c), show that lower current densities are accompanied by higher R_Ω and R_p values. According to the above-mentioned data the electrochemical performance is degraded on more heavily oxidized Ni/YSZ electrodes. Such behavior might be anticipated though, since nickel oxidation is frequently linked to a decline in the performance of solid oxide cells. This can be explained by the increase in the ohmic resistance of the cathode since NiO has significantly lower electronic conductivity compared to metallic nickel. Nickel oxidation can also impact the charge transfer resistance at the Ni-YSZ interface, as the distinct catalytic properties of NiO and Ni^0 influence the adsorption and dissociation of water molecules at the electrode surface and thus the kinetics of the electrochemical reaction.

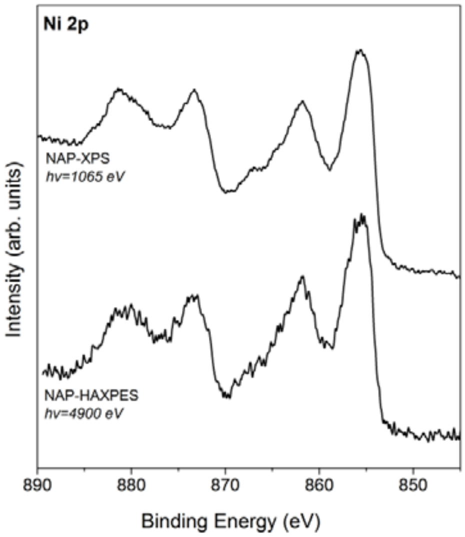

Figure 3.11. Ni 2p NAP-XPS (top) and NAP-HAXPES (bottom) spectra of the Ni/YSZ electrode before the electrochemical testing treated under pH_2O/pO_2 (9/1) at 750 °C.

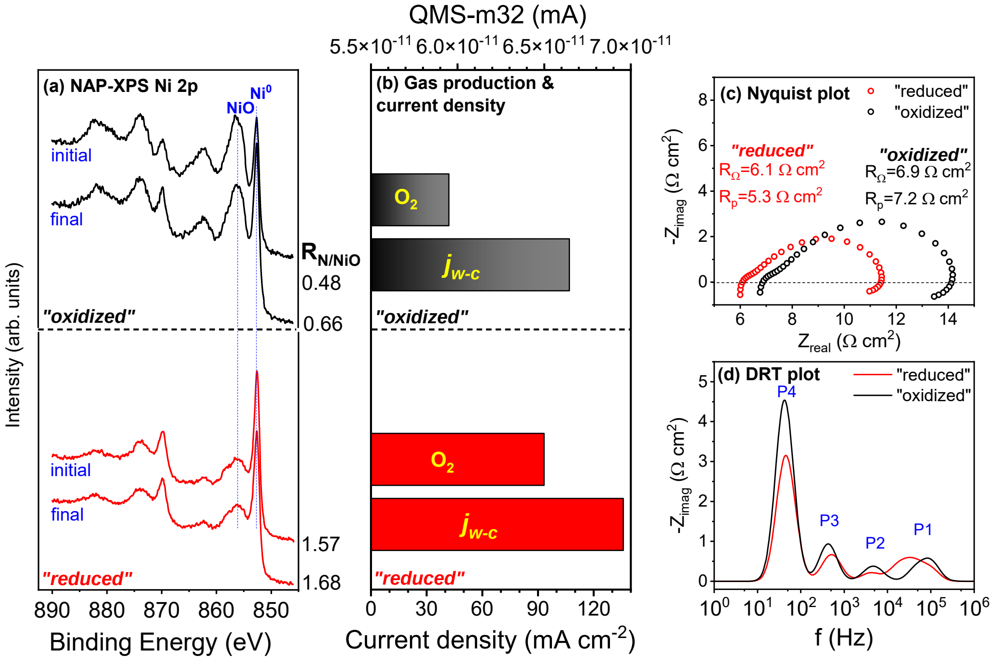

Figure 3.12. (a) Operando Ni 2p (hv=1065 eV) NAP-XPS spectra measured under electrolysis conditions (E_{W-C} = 2.5 V, pH_2O/pH_2=9/1 at 750 °C) at the inner section of Ni/YSZ electrodes underwent different pretreatments, **(b)** The mean current density of the cell and the production of gas phase O_2 measured on line during the photoemission experiments of **(a)**. Impedance spectra presented as **(c)** Nyquist and **(d)** DRT plots for the two cells.

Distribution of Relaxation Times (DRT) analysis is applied to further comprehend the electrode processes involved in H_2O electrolysis. Four main electrode processes are identified in Figure 3.12d labeled P1 to P4 in descending order of relaxation frequency. Each peak area corresponds to the polarization resistance of the associated electrode process, with relaxation frequencies ranging from 10^5 to 10^4 Hz (P1), 10^4 to 10^3 Hz (P2), 10^3 to 10^2 Hz (P3), and 100 to 10 Hz (P4). According to literature, P1 is linked to O^{2-} transport resistance, P2 is associated with charge transfer process-related resistance, P3 is connected to the diffusivity resistance of O^{2-}, and P4 is related to gas phase diffusion process-related resistance[335]. Notably, P2, P3, and P4 exhibit more significant changes as the oxidation state of Ni increases, indicating that the electrode processes they represent are influenced by the oxidation state of surface Ni. As the oxidation state of surface Ni varies, there is almost no observable change in the absolute value of P1, but the characteristic peak of P1 widens and shifts towards lower frequencies. The DRT results further confirm that the charge transfer reaction and ion transport process represented by P4 play a dominant role in H_2O electrolysis performance.

3.3.2.3 Depth-distribution of NiO and Ni phases during H_2O/H_2 electrolysis

The XRD patterns of the Ni/YSZ cells after the operando photoemission experiments (Figure 3.13) are dominated by the diffraction lines of YSZ and metallic Ni phases. The depth distribution of oxide and metallic nickel phases was addressed through the analysis of Ni 2p spectra acquired in the NAP-XPS and NAP-HAXPES measurements. The use of the incident photons with 1065 eV and 4900 eV in the two cases enables non-destructive depth profiling from the outermost surface to the subsurface layers. Estimating the analysis depth as 3 times the inelastic mean free path, the aforementioned measurements correspond to analysis depths of approximately 1.6 and 12.1 nm, respectively [342]. Figures 3.14a and 3.14b display the Ni 2p NAP-XPS and NAP-HAXPES spectra obtained during H_2O/H_2 electrolysis from Ni/YSZ electrodes with varying degrees of oxidation. Spectra recorded on a partially oxidized Ni/YSZ electrode at open circuit (without polarizing the electrode) are included in Figure 3.14c for comparison. As depicted in Figure 3.14 and the $R_{Ni/NiO}$ presented in Table 1, during electrolysis conditions the Ni 2p spectra exhibit significant similarity at both analysis depths, whereas at open circuit, they are notably different.

The surface morphology corresponding to the experimental $R_{Ni/NiO}$ was further elaborated using the SESSA software [342]. To do so, the Ni 2p photoemission spectra of Figure 3.14 where calculated using 2 types of surface morphology; flat planar layered surface (hereafter designated as planar-morphology) and islands on top of a flat layered surface (hereafter designated as island-morphology). In both cases the interface between the various layers is assumed to be ideally flat. In the planar-morphology simulation two configurations were tested. The first is a homogenous mixture of Ni^0 and NiO phases and the second considers two layers, with the upper (overlayer) composed of NiO and the underlying (substrate) of a Ni^0 and NiO mixture. It is important to note that attempts to simulate the Ni 2p spectra with a single nickel phase at the substrate, instead of Ni^0 and NiO mixture, were unsuccessful. The varying parameters of the SESSA simulation was (i) the Ni^0 to NiO composition of the substrate and (ii) the thickness and coverage (in case of island-morphology) of the overlayer. To note that the size and the periodicity of the islands defines their coverage on the support (< 1 monolayer). The $R_{Ni/NiO}$ was calculated by trial and error until a reasonable match between the simulated and experimental $R_{Ni/NiO}$ values found for both analysis depths.

The morphologies that give both the best match between simulated and experimental $R_{Ni/NiO}$ are represented in 2D and 3D at the top and the inset of Figure 3.14 respectively, while the simulated $R_{Ni/NiO}$ values are included in Table 1. As depicted, in all cases, the subsurface consists of a Ni^0 and NiO mixture with varying compositions, whereas the overlayer arrangement is quite different in each sample. In particular, the "oxidized" Ni/YSZ electrode has a slightly increased $R_{Ni/NiO}$ in deeper analysis depth, meaning that part of NiO is preferentially located at the surface. Efforts to reproduce the experimental $R_{Ni/NiO}$ by employing morphologies characterized by a monolayer-thick NiO layer (0.21 nm) atop a Ni/NiO mixture failed to describe the data in both analysis depths. The morphology able to simulate the $R_{Ni/NiO}$ consists of a 45%Ni^0-55%NiO substrate covered by 0.55 nm thick NiO islands at a coverage of 17%. In case of the more reduced electrode (Figure 3.14b), the experimental $R_{Ni/NiO}$ is practically the same in the two analysis depths. This indicates a homogeneous mixture of Ni and NiO, with a composition of 63% Ni and 37% NiO, extending at least within the outer 12.1 nm. In case of Ni 2p spectra measured at open circuit (Figure 3.14c) they were best simulated by a dense 0.37 nm thick NiO layer over a 40%Ni-60%NiO substrate. It is important to note that while these models serve as feasible representations of the studied states, we cannot completely rule out the possibility of other, potentially much more complex models being capable of reproducing the experimental $R_{Ni/NiO}$ as well.

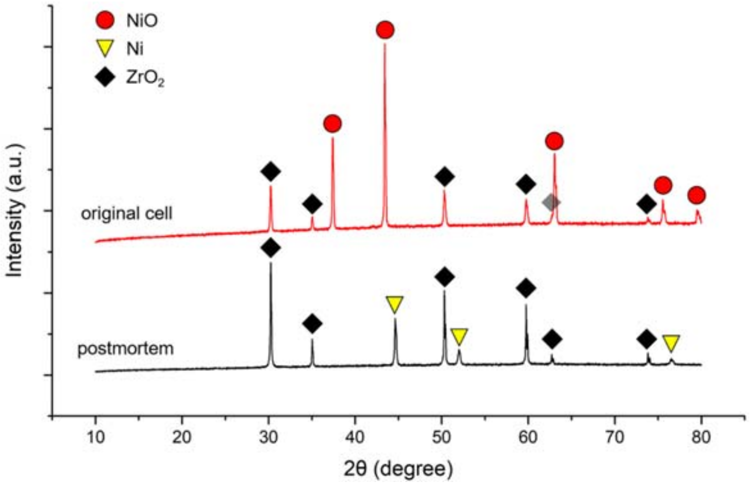

Figure 3.13. X-ray diffraction patterns of Ni/YSZ cell in the calcined (original) state and after the operando NAP-XPS and NAP-HAXPES experiments (post mortem).

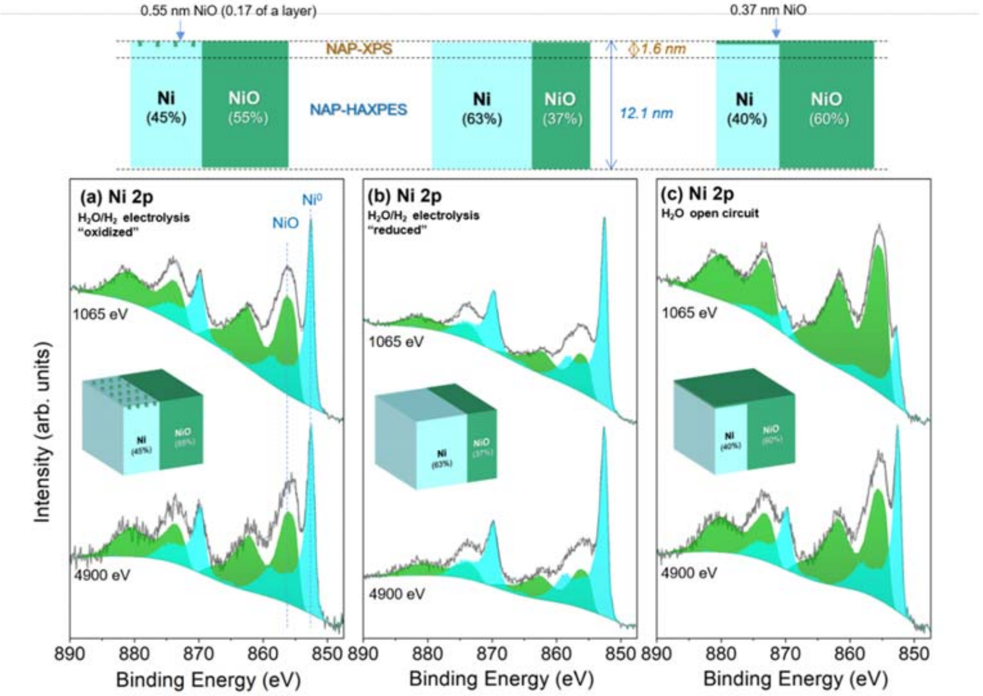

Figure 3.14. Ni 2p core-level spectra measured using 1065 eV (NAP-XPS) and 4900 eV (NAP-HAXPES) photon energies over Ni/YSZ electrode during **a)** E_{W-C} = 2.5 V, 1 mbar H_2O:H_2=9:1 at 750 °C (after mild reduction pre-treatment), **b)** E_{W-C} = 2.5 V, 1 mbar H_2O:H_2=9:1 at 750 °C (after harsh reduction pre-treatment) and **c)** open circuit, 1 mbar H_2O at 750 °C (after reduction in H_2). The time interval between NAP-XPS and NAP-HAXPES measurement was around 3 minutes. The surface morphology that resulted in the optimal fit for the experimental $R_{Ni/NiO}$ in SESSA simulation is depicted at the top of the figure.

Table 3.1. Comparison of experimental and simulated $R_{Ni/NiO}$. The error in the experimental $R_{Ni/NiO}$ ratios is estimated around ±5%.

Conditions	$R_{Ni/NiO}$ (NAP-XPS)		$R_{Ni/NiO}$ (NAP-HAXPES)	
	Experiment	**Simulation**	**Experiment**	**Simulation**
E_{W-C} = 2.5 V, 1 mbar H_2O:H_2=9:1 at 750 ℃ (after **mild** reduction pre-treatment)	0.66±0.03	0.66	0.79±0.04	0.79
E_{W-C} = 2.5 V, 1 mbar H_2O:H_2=9:1 at 750 ℃ (after **harsh** reduction pre-treatment)	1.68±0.08	1.70	1.70±0.09	1.70
open circuit, 1 mbar H_2O at 750 ℃ (after reduction in H_2)	0.20±0.01	0.20	0.56±0.03	0.58

The results presented above suggest a rather unexpected configuration between Ni^0 and NiO in the partially oxidized Ni/YSZ electrode. Typically, the oxidation of transition metals, begins with the formation of a thin oxide layer at the surface, which often acts as a protective barrier for further oxidation. This configuration was partially observed in case of Ni/YSZ at open circuit, however at this point it is not clear if this is due to the higher degree of oxidation of this sample or it is related to the absence of cathodic polarization. Recent work by Cheng et al. [341] has demonstrated that under electrolysis conditions in Ni/YSZ electrodes, the oxygen chemical potential varies significantly within the electrode. Specifically, at the Ni-YSZ interface region, the chemical potential is oxidative, while inside bulk nickel particles, the chemical potential is reductive. This means that metallic and oxidized Ni phases can coexist simultaneously at different locations within the electrode. This observation can explain the findings of depth-dependent measurements, which show a relatively homogeneous distribution of Ni and NiO phases under applied bias. In any case, operando photoemission experiments give solid evidences that during electrolysis NiO is mainly occurring in a horizontal or sideways manner rather than progressing from the surface towards the interior of the nickel particles as for conventional gas phase oxidation. This suggests that metallic nickel remains accessible at the surface even in partially oxidized electrodes, thereby maintaining a certain level of electrocatalytic performance in the cell.

3.4. Conclusions

In this study, operando X-ray photoelectron spectroscopy was combined with electrochemical characterization to investigate the interplay between the surface chemical states and electrocatalytic performance of Ni/YSZ solid oxide cell cathode electrodes during H_2O electroreduction. The use of modified miniature cells enables direct observation of electrode areas near the YSZ interface revealing dynamic changes of Ni/YSZ composition under H_2 and H_2O treatments. By adjusting the cell pre-treatment conditions, a correlation between nickel surface oxidation and the cell H_2O electroreduction performance is established. The study unequivocally shows a preference of NiO as the oxidized Ni phase during H_2O electrolysis, providing critical insights into Ni-phase redistribution during long-term operation. The surface chemical analysis excluded the formation of Ni-hydroxide. Depth-dependent photoemission measurements reveal a uniform mixing of NiO and Ni phases on the surface suggesting that metallic nickel remains accessible at the surface even for partially oxidized electrodes.

Chapter 4. Nickel-doped and undoped ceria NPs to promote the Ni/YSZ cathodes electrochemical performance in H_2O electrolysis

4.1. Introduction

Amidst the growing concerns of climate change and the depletion of fossil fuel reserves, the pursuit of sustainable and clean energy sources has become increasingly urgent [360–364]. Among the various methods for generating clean energy, water electrolysis stands out as a promising approach [360–362,364–366]. This process produces hydrogen by splitting water into hydrogen and oxygen through the application of electricity. The effectiveness and efficiency of electrolysis largely hinge on the materials selected for the electrodes, which are vital components of the electrolysis cell [367–370].

Cerium dioxide (CeO_2), commonly referred to as ceria, is well known for its distinctive catalytic properties, particularly its capacity to enable reversible transitions between Ce^{4+} and Ce^{3+} oxidation states [371,372]. Nickel-doped cerium dioxide further enhances ceria's reducibility, not only increasing catalytic activity but also facilitating the formation of single-atom catalysts by promoting the even distribution of metal ions within the oxide support [373–376].

Modifying the surface of cathode electrodes by depositing metals or oxides has become a widely adopted strategy to enhance the performance and durability of solid oxide cell (SOC) devices [147,377–381]. One effective preparation method involves infiltrating catalytic promoters into the pores of ceramic electrodes, which can increase the triple-phase boundary (TPB) and improve the ionic and electronic conductivity, as well as the catalytic activity of the electrodes [377,382–384].

However, achieving uniform dispersion of these materials is a major challenge, as conventional synthesis techniques often lead to the formation of separate metal/ceria aggregates. The infiltration process is particularly difficult due to nanoparticle agglomeration, which can block pores and restrict gas access [230,385–388]. To address this issue, our research group has developed a novel synthesis approach that uses Schiff base complexes as inorganic precursors. In this method, a hexane-based solution containing ceria nanoparticles is infiltrated into pre-formed Ni/YSZ cermet electrodes [277,386]. This technique avoids the complications associated with aqueous solutions, such as poor wettability and precipitation of precursors, while also simplifying the process by eliminating the need for surfactants. Using organic solutions enables better nanoparticle penetration and dispersion within the electrode structure, significantly enhancing the efficiency of both infiltration and catalyst loading. This method has been shown to facilitate the formation of nickel-doped ceria nanoparticles, improving their reducibility.

Organic solutions containing two types of cerium oxide nanoparticles ($Ni_{0.2}Ce_{0.8}O_{2-x}$ NPs and CeO_y NPs) were subsequently infiltrated into pre-reduced Ni/YSZ cermet electrodes, which served as a porous support. The morphology and microstructure of the modified Ni/YSZ electrodes were investigated through multiple analytical methods. Alongside the synthesis and characterization of these nanoparticles, their influence on the electrochemical performance of NiCe@NiYSZ cathode electrodes was evaluated. The results revealed that $Ni_{0.2}Ce_{0.8}O_{2-x}$ nanoparticles significantly outperformed conventional ceria particles in H_2O electrolysis, as well as the unmodified Ni/YSZ electrode.

This chapter is based on an article in preparation: Jinming Zhang, Mathias Barreau, and Spyridon Zafeiratos et al. Study on mechanism of the nickel-doped and undoped ceria NPs influence the Ni/YSZ cathodes electrochemical performance in H_2O electrolysis.

4.2. Material and Methods

4.2.1. Synthesis of NiCeOx NPs organic solution

Un-doped CeO_2 nanoparticles (CeO_y) and 20% Ni-doped CeO_2 nanoparticles ($Ni_{0.2}Ce_{0.8}O_{2-x}$), referred to as $NiCeO_x$, were synthesized using Schiff base metal complexes, following a previously established protocol [277,386,389]. The synthesis process began with the preparation of two monometallic Schiff base complexes, Ce-L and Ni-L. This involved refluxing a mixture of o-vanillin, 1,3-diaminopropane, and the appropriate metal salts (cerium nitrate hexahydrate for Ce-L or nickel acetate tetrahydrate for Ni-L) in methanol. The nanoparticles were then synthesized by combining the Schiff base complexes and subjecting them to pyrolysis in an oleylamine medium at 180 ℃ under an inert argon (Ar) atmosphere. After synthesis, the nanoparticles were precipitated with methanol and collected via centrifugation (illustrated in Figure 4.1). A portion of the resulting nanoparticles was dispersed in hexane solution, while the remainder underwent calcination in air at 450 ℃ for one hour. This calcination step was necessary for characterization techniques such as XPS and XRD [386,389].

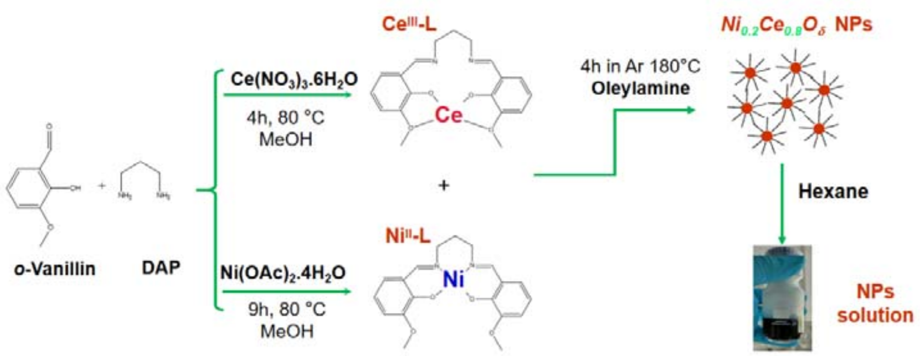

Figure 4.1. Synthesis procedure of Ni-doped CeO_2 nanoparticles. Reproduced with permission of Ref. [389], Copyright of ©2023 Wiley

4.2.2. Description of the prefabricated electrochemical cells with Ni/YSZ cermet cathodes

The $NiCeO_x$ and CeO_y nanoparticles (NPs) were directly infiltrated from a hexane solution onto commercially available electrolyte-supported half-cells produced by Kerafol GmbH as depicted in section 2.1.

Before impregnating the Ni/YSZ cathode, we prepared the anode side (Pt anode). Once the anode electrode is coated, the porous ceramic Ni/YSZ cathode is impregnated with nanoparticles using a micropipette. The nanoparticle solution was infiltrated directly onto the surface of the Ni/YSZ electrode of approximately 0.785 mm^2 area. In this study, various amounts of $Ni_{0.2}Ce_{0.8}O_{2-x}$ or CeO_y NPs in hexane were impregnated onto the electrodes, which were subsequently referred to as, for example, 10 $NiCeO_x$ or 10 CeO_y, depending on the volume of solution used. After each infiltration step, the hexane solvent was allowed to evaporate in air at 80 °C for approximately 90 min. A calcination process was then carried out at 450 °C in air to eliminate any organic residues from the NPs coating (as shown in Figure 4.2). For the electrochemical tests, the calcined cells underwent a second reduction step in H_2.

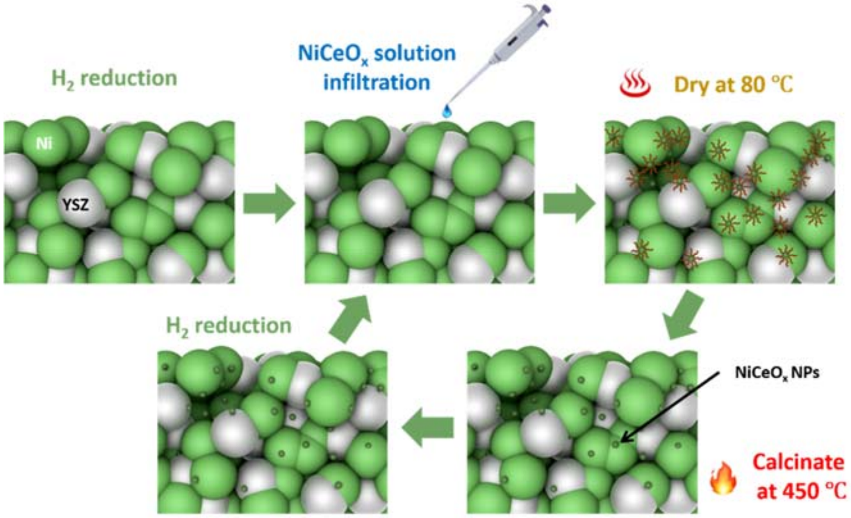

Figure 4.2. Schematic representation of the $NiCeO_x$ and CeO_y NPs infiltration process over pre-fabricated Ni/YSZ electrodes.

4.2.3. Benefits and limitations of electrochemical tests on miniature cells

As previously discussed, for electrochemical testing, a quarter segment of a 2 cm diameter button cell (miniature battery) was employed. The compact size of these cells allows for efficient investigation of the infiltration process and subsequent characterization after infiltration. Preparation of miniature cells facilitates electrochemical tests and limits uncertainties that may arise when scaling up to a full 2 cm diameter button cell. This ensures that the morphology and chemical properties of the cells used in electrochemical measurements align with the detailed characterization findings presented in other chapters of this thesis.

However, due to the small size of these miniature cells, traditional SOC testing equipment could not be utilized. Instead, the tests were carried out in a single-chamber reactor attached to a UHV system, as described in the experimental section. The specific conditions applied during H_2O electrolysis—such as low temperature, low pressure, and reduced fuel flow rates—resulted in current densities that were lower than those typically observed in conventional button cell tests at different applied voltages. Consequently, the results are consistently analyzed on a comparative basis, with primary emphasis on the current-voltage (I-V) curves of cells featuring both pristine and modified Ni/YSZ cathodes under identical reaction conditions.

The use of this specialized setup for electrochemical testing provides several key benefits. It enables surface characterization of the electrodes both prior to and following electrochemical tests, facilitating the detection of surface impurities or carbon deposits that might influence electrochemical performance and potentially obscure the effects of surface modifications. Therefore, it is better suited to the aims of this thesis, which focus on understanding how surface changes impact the overall behavior of the cell.

4.2.4. Electrolytic performance characterization

For the SOEC water electrolysis experiment, the reaction conditions were set at 700 ℃ and a pressure of 2 mbar. According to the literature, water vapor can act as an oxidant for Ni [277,286]. To maintain the Ni/YSZ in a reduced state, a 1:1 H_2O to H_2 ratio was used.

The electrochemical performance was evaluated by chronoamperometry and electrochemical impedance spectroscopy (EIS) measurements, using a VersaSTAT3 potentiostat. In the chronoamperometry experiments, three constant potentials were applied between the working and counter electrodes, and the current response was monitored over time. EIS spectra were recorded at each potential, spanning a frequency range of 100 KHz to 0.01 mHz, with a signal amplitude of 10%. The intersection of the impedance arc with the real axis at high frequencies represents the series or ohmic resistance (R_Ω) of the cell, while the difference between the arc's intercepts with the real axis at high and low frequencies defines the polarization resistance (R_p). This precise configuration enables a thorough analysis of the electrochemical behavior under the specified conditions, offering valuable insights into the reaction dynamics and the resistance properties of the materials involved.

4.2.5. Electrochemical reactor

The electrochemical reactor described in section 2.2.2 was utilized to evaluate the performance of the electrolytic cell. Gas flow into the cell was managed using calibrated mass flow controllers, and the reaction products were analyzed in real time using an online quadrupole mass spectrometer (QMS). The electrochemical cell is fastened to a quartz sample holder using two stainless steel clamps and is heated from the back with the infrared lamp as shown schematically in Figure 4.3a. For the anode and cathode sides, a platinum grid and a gold grid serve as current collectors, respectively. These current collectors are connected to a 6-way UHV connector on the manipulator via gold wires that are shielded by ceramic rings, as illustrated in Figure 4.3b. The temperature is regulated by a PID controller, with measurements taken from a thermocouple placed on the ceramic sample holder adjacent to the sample. The the samples underwent calcination in 1.0 mbar O_2 at 400 ℃ or reduction in 1.0 mbar H_2 at 700 ℃ for 30 minutes prior to electrochemical tests.

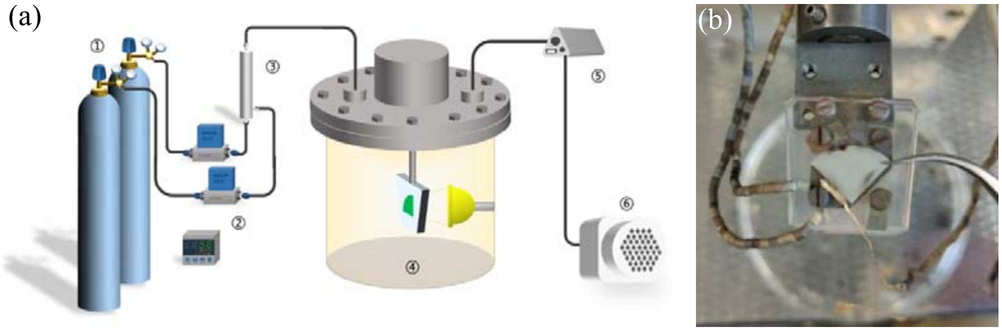

Figure 4.3. a) Schematic of electrochemical experimental chamber self-assembled in the laboratory, ①Gas, ②Mass flow controller, ③Gas mixer, ④Reactor chamber, ⑤Mass Spectroscopy, ⑥Pump; **b)** Holder and infiltrated Ni/YSZ cell.

4.2.6. Material characterization

Ex-situ characterization techniques, including FTIR spectroscopy, TGA, XRD, and DLS are discussed in detail in Chapter 2.

4.3 Result and discussion

4.3.1 Concentration of $NiCeO_x$ and CeO_y nanoparticles

The concentration of $NiCeO_x$ and CeO_y nanoparticles (NPs) in their organic solutions was assessed using Thermogravimetric Analysis (TGA). TGA measurements were conducted in air for three different volumes of $NiCeO_x$ and CeO_y NP solutions: 100 µL, 200 µL, and 300 µL. The characteristic TGA thermograms for the 100 µL solutions of $NiCeO_x$ and CeO_y are shown in Figure 4.4a, while the results for all three volumes are summarized in Table 4.1. For both $NiCeO_x$ and CeO_y solutions, the initial weight loss depicted in Figure 4.4a is attributed to the evaporation of the hexane solvent at approximately 70 ℃. Following this, above 200 ℃, the weight loss is associated with the decomposition of the oleylamine (OLA) coating enveloping the NPs [390]. The weight curve stabilizes at 450 ℃ for both types of NPs, signifying the complete decomposition of the organic coating.

From these findings, the mass concentration of the two NPs in their organic solutions was calculated. The data presented in Table 4.1, along with the graphical representation in Figure 4.4b, illustrates a linear relationship between the weight of NPs and the volume of the solution, resulting in mass concentrations of 4.9 mg/mL for $NiCeO_x$ and 5.4 mg/mL for CeO_y NPs.

The TGA data presented in Table 4.1 indicate that the final percentage weight of $NiCeO_x$ is lower than that of CeO_y NPs, with average values of 23.0±1.0% and 33.2±1.2%, respectively.

Considering that the mass concentrations of both NPs in their organic solutions are comparable, this difference implies that the average weight of the protective OLA layer surrounding $NiCeO_x$ is less than that of the OLA layer encasing CeO_y NPs.

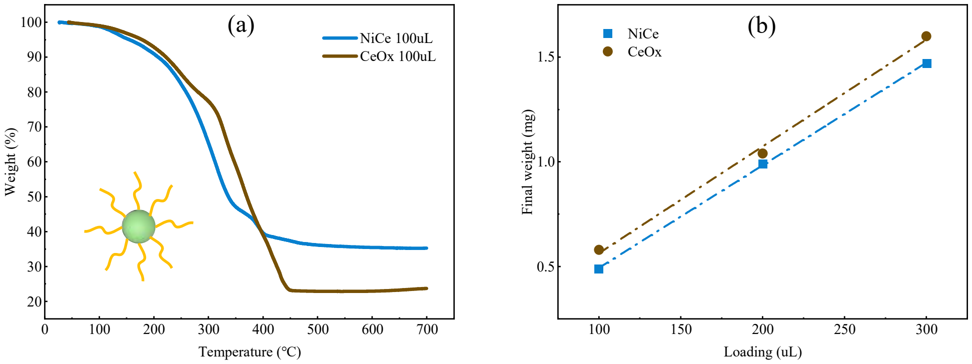

Figure 4.4. a) The TGA thermogram of 100µL $NiCeO_x$ and CeO_y NPs in their organic solutions. **b)** The final weight of $NiCeO_x$ and CeO_y NPs at 600 °C as a function of different quantities of organic solutions in TGA measurement.

Table 4.1. TGA quantitative analysis of $NiCeO_x$ and CeO_y NPs in organic solutions.

Loading (µl)	**Initial weight(mg at 25 °C)**	**Final weight(mg at 600 °C)**	**Calculated final mass concentration (mg/ml)**	**Final weight(% at 600 °C)**
		$NiCeO_x$		
100	1.48	0.49	4.9	33.1
200	2.88	0.99	5.0	34.4
300	4.57	1.47	4.9	32.2
		CeO_y		
100	2.45	0.58	5.8	23.7
200	4.72	1.04	5.2	22.0
300	6.87	1.60	5.3	23.3

4.3.2 Size of the nanoparticles in solution and after calcination

Dynamic light scattering (DLS) was utilized to evaluate the size distribution profile of $NiCeO_x$ and CeO_y particles in their respective solutions [391]. It is crucial to understand that DLS measurements provide the hydrodynamic radius, which accounts for the total size of the particles, including the organic protective layer. As shown in Figure 4.5a and summarized in Table 4.2, a significant proportion (77.9%) of $NiCeO_x$ nanoparticles in hexane solution forms aggregates with an approximate size of 0.75 µm. In contrast, CeO_y nanoparticles exhibit a larger aggregate size of around 1.32 µm, with 79.9% of the particles falling within this size range. The notable difference in size between the two types of nanoparticles in the hexane solution may be attributed to agglomeration effects, as schematically illustrated in Figure 4.5b, which will be discussed in detail later.

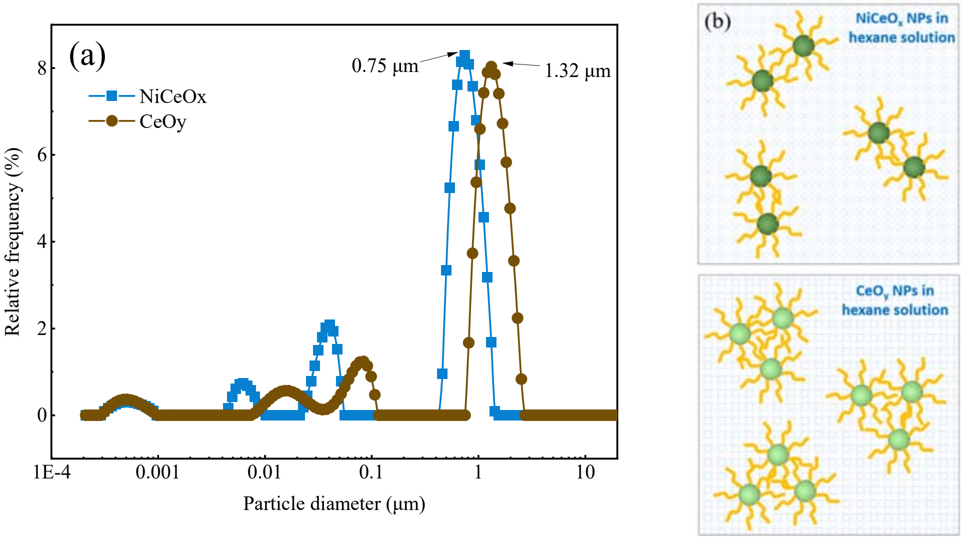

Figure 4.5. a) The particle size distributions of $NiCeO_x$ and CeO_y NPs in their organic solutions in DLS measurement. **b)** Schematic representation of $NiCeO_x$ and CeO_y NPs arrangement in their organic solutions.

Table 4.2. The DLS results of $NiCeO_x$ and CeO_y NPs in their organic solutions.

Sample	**Peak 1**		**Peak 2**		**Peak 3**	
	Particle diameter (µm)	Area (%)	Particle diameter (µm)	Area (%)	Particle diameter (µm)	Area (%)
$NiCeO_x$ NPs	0.75	77.9	0.04	14.2	0.0006	4.7
CeO_y NPs	1.32	79.9	0.084	9.8	0.0015	6.74

The crystallinity of both pristine and calcined $NiCeO_x$ and CeO_y nanoparticles (NPs) was examined using X-ray diffraction (XRD), as illustrated in Figure 4.6. The corresponding crystallite sizes were determined using the Debye-Scherrer equation, applied to the most intense (111) diffraction peak. The diffraction patterns for both types of samples revealed characteristic peaks corresponding to the fluorite structure of CeO_2. Importantly, no additional peaks associated with nickel-containing phases were detected in the $NiCeO_x$ NPs, suggesting that there are no isolated nickel aggregates. This observation confirms the successful incorporation of all Ni ions into the CeO_2 lattice [277]. The estimated crystallite sizes for pristine $NiCeO_x$ and CeO_y NPs, as shown in Table 4.3, were approximately 3.8±0.3 nm and 4.8±0.5 nm, respectively (refer to Figure 4.6a). After calcination, the crystallite sizes were calculated to be 6.5±0.2 nm and 7.4±0.2 nm, respectively (as shown in Figure 4.6b). These findings indicate that both types of cerium-based nanoparticles are well dispersed in hexane solution and exhibit relatively small sizes (3-5 nm), highlighting the succesful production of nanoscale ceria particles [277,392].

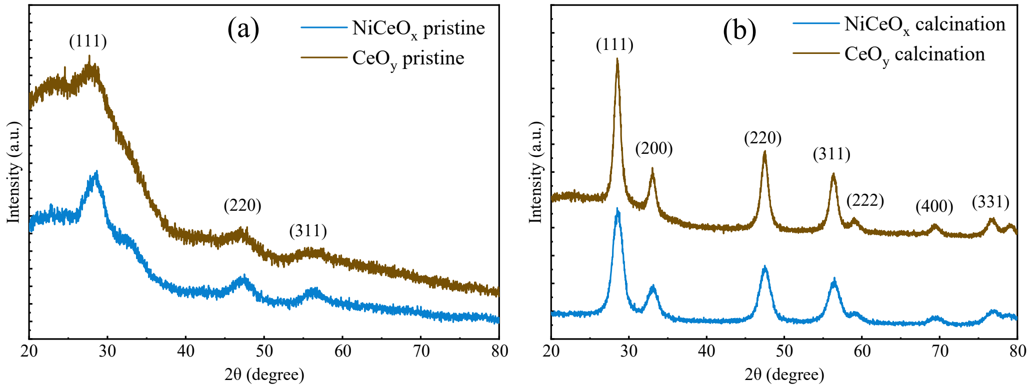

Figure 4.6. a) prisine XRD patterns of $NiCeO_x$ NPs and CeO_y NPs as well as **b)** these two NPs after calcination ($NiCeO_x$ or CeO_y solution was calcinated with a ramp of 5 °C/min for 1h at 450 °C in air).

Table 4.3. Crystallite size results of $NiCeO_x$ and CeO_y NPs measured directly on the $NiCeO_x$ and CeO_y solutions and calcinated samples respectively, after two infiltration/co-firing steps.

Sample	Pristine Crystallite size (nm)	Calcination Crystallite size (nm)
$NiCeO_x$	3.8±0.3	6.5±0.2
CeO_y	4.8±0.5	7.4±0.2

While the XRD results indicated that CeO_y NPs should be larger than $NiCeO_x$ NPs, the sizes measured by DLS revealed both types of nanoparticles to be on the micron scale. This discrepancy cannot be solely attributed to the presence of the surrounding coating, given that oleylamine (OLA) molecules generally have a chain length of approximately 2.0 nm. Consequently, the DLS data suggest that CeO_y nanoparticles tend to form larger aggregates in hexane solution compared to $NiCeO_x$ nanoparticles.

4.3.3 Infiltration of $NiCeO_x$ and CeO_y NPs into the prefabricated Ni/YSZ electrodes

Before infiltration, the cell underwent reduction in H_2, a process that generally leads to a significant reduction in nickel particles volume, resulting in the formation of nanopores. Following reduction, an appropriate quantity of both types of nanoparticles was infiltrated onto the surface of the Ni/YSZ electrode. Post-infiltration images (Table 4.4) indicate that CeO_y NPs were more challenging to infiltrate into the electrode's pores compared to $NiCeO_x$ NPs. After applying only 10 µL of CeO_y, a substantial quantity of nanoparticles remained on the surface, unable to penetrate. In contrast, infiltration of $NiCeO_x$ NPs was smooth until 80 µL of solution are deposited on the support. To ensure effective infiltration, a maximum amount of impregnated solution, i.e. 160 µL of $NiCeO_x$ and 10 µL of CeO_y, was applied in two separate infiltration/co-firing steps. For all the other solutions amounts, the nanoparticle were infiltrated through a single infiltration/co-firing step. For clarity, simple calculations reveal that each 10 µL of $NiCeO_x$ NPs results in a loading of 15.6 mg/cm^3, while for CeO_y, each 10 µL yields a loading of 17.2 mg/cm^3.

Table 4.4. Photos of cells after the $NiCeO_x$ NPs and CeO_y NPs infiltration procedure and after calcination

$NiCeO_x$ NPs	 0 µL	 40 µL	 80 µL	 After calcination
CeO_y NPs	 0 µL	 5 µL	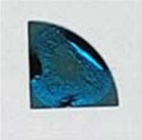 10 µL	 After calcination

The challenges associated with the infiltration of ceria nanoparticles into the electrode pores may stem from agglomeration. The differing dispersion behaviors of the two types of ceria nanoparticles (NPs) in hexane can be elucidated through DLVO (Derjaguin, Landau, Verwey, and Overbeek) theory, which is frequently applied to describe colloidal system behaviors [294–296]. Specifically, the dispersion of ceria NPs that are coated with an organic layer is governed by the interplay between van der Waals attraction forces at the core (ceria NPs) and the steric repulsive forces from the attached ligands, in this case, oleylamine (OLA). The calculated potential curves (Figure 4.7) indicate that the core size of ceria-based NPs significantly affects their dispersion in hexane solution. Larger nanoparticles exert stronger van der Waals forces compared to smaller ones. Given that both types of NPs are covered with the same OLA layer (as shown in Figure 4.1), the larger crystallite size of CeO_y NPs, as determined by XRD, accounts for their reduced dispersibility in the solution, as evidenced in Figure 4.5b.

In conclusion, the analysis confirms that both $NiCeO_x$ and CeO_y NPs are nanoscale particles coated with an OLA layer. While both types tend to aggregate in hexane, CeO_y exhibits a more pronounced tendency to agglomerate, resulting in clusters that are approximately twice the size of those formed by $NiCeO_x$.

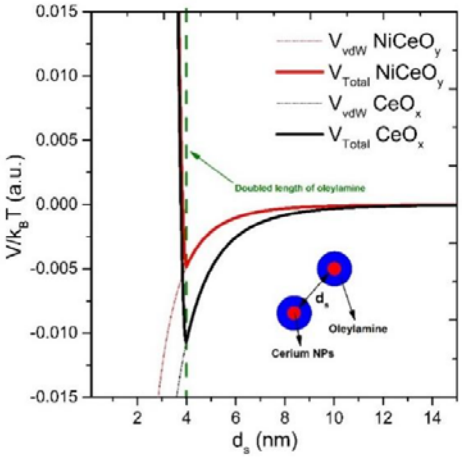

Figure 4.7. The calculated total potential curves between $NiCeO_x$ and CeO_y NPs. The inter-particle distance d_s ($d_s = d - 2r$) was defined as surface-to-surface separation distance between two nanoparticles. As shown in the figure, the repulsive forces arise at the distance, where oleylamine surrounded ceria-based nanoparticles contacts each other [386].

4.3.4 Electrolysis characterization of samples infiltrated with $NiCeO_x$ and CeO_y nanoparticles

We performed multiple sets of electrochemical performance tests to evaluate the performance of cells with Ni/YSZ cathodes, before and after infiltration with $NiCeO_x$ and CeO_y nanoparticles (NPs). In these comparative experiments, we systematically increased the amount of infiltrated solution onto Ni/YSZ in order to determine the optimal nanoparticle loading for electrolysis performance. Initially, the Ni/YSZ cathodes underwent oxidation at 400 °C in O_2 followed by reduction at 700 °C in H_2, with each treatment lasting 30 minutes. The pre-oxidation step was primarily intended to eliminate residual carbon from the surface, while the pre-reduction aimed to reduce nickel and enhance electrode porosity. This modification facilitated deeper penetration of the nanoparticles into the electrode's pores and formation of more triple-phase boundaries (TPBs).

For $NiCeO_x$, we started with an infiltration amount of 10 μL, subsequently doubling it to 20 μL, 40 μL, 80 μL, and finally 160 μL, in order to quickly ascertain the optimal loading amount. For CeO_y, we examined loading amounts of 5 μL and 10 μL. It is important to note that each infiltration was conducted on a fresh Ni/YSZ sample underwent exactly the same pretreatment.

This strategy was implemented to avoid unpredictable effects, related to sample aging, that may occur after multiple cycles of oxidation, reduction, and electrolysis testing.

Following infiltration, each cell underwent chronoamperometry, staircase linear scanning, long-term stability testing, and electrochemical impedance spectroscopy experiments. Theese experiments were performed in 2 mbar of H_2O:H_2 (50% each) atmosphere at 700 ± 5 °C. During the electrolysis experiments, a quadrupole mass spectrometer (QMS) was utilized to analyze the composition of the outlet gases, ensuring that the applied voltage or current generated the anticipated quantities of gas phase products. Due to the presence of a single reaction chamber, the QMS monitored both the inlet and outlet gases simultaneously. Unfortunatelly the signal from the inlet H_2O:H_2 gas mixture completely overshadowed the H_2 signal produced by H_2O electrolysis. However, the evolution of gas phase O_2 signal was quite consistent with the current response of the cell.

4.3.4.1. Chronoamperometry (CA) comparison of pristine and infiltrated cells in H_2O+H_2 electrolysis

The chronoamperometry (CA) experiments were conducted at three voltages—0.5 V, 1.0 V, and 1.5 V—each maintained for 5 minutes. As shown in Figures 4.8a and 4.8b, the current density at all three voltages increased following infiltration with NiCeOx nanoparticles, indicating an improvement in water electrolysis performance. At 80 μL loading, the increase in electrolysis current was approximately fourfold at 0.5 V, sixfold at 1.0 V, and fivefold at 1.5 V, reaching 130 mA/cm^2. The performance declined at a loading of 160 μL, suggesting that 80 μL is the optimal loading for electrolysis. Consequently, it was decided not to conduct any further infiltrations with loadings exceeding 160 μL. Each experimental set was repeated twice, yielding highly reproducible results with variations of approximately 10%, indicating good reproducibility.

In the infiltration experiments with CeO_y NPs, illustrated in Figure 4.8c and 4.8d, the electrolysis current increases up to 2.5 times at 5 μL CeO_y loading, but decreases aging at 10 μL, suggesting that 5 μL is the optimal loading for CeO_y. Moreover, during the infiltration with a pipette, the last few drops of the solution were observed to be less readily absorbed (Table 4.4), indicating that larger agglomerates of CeO_y NPs in hexane contributed to rapid blocking.

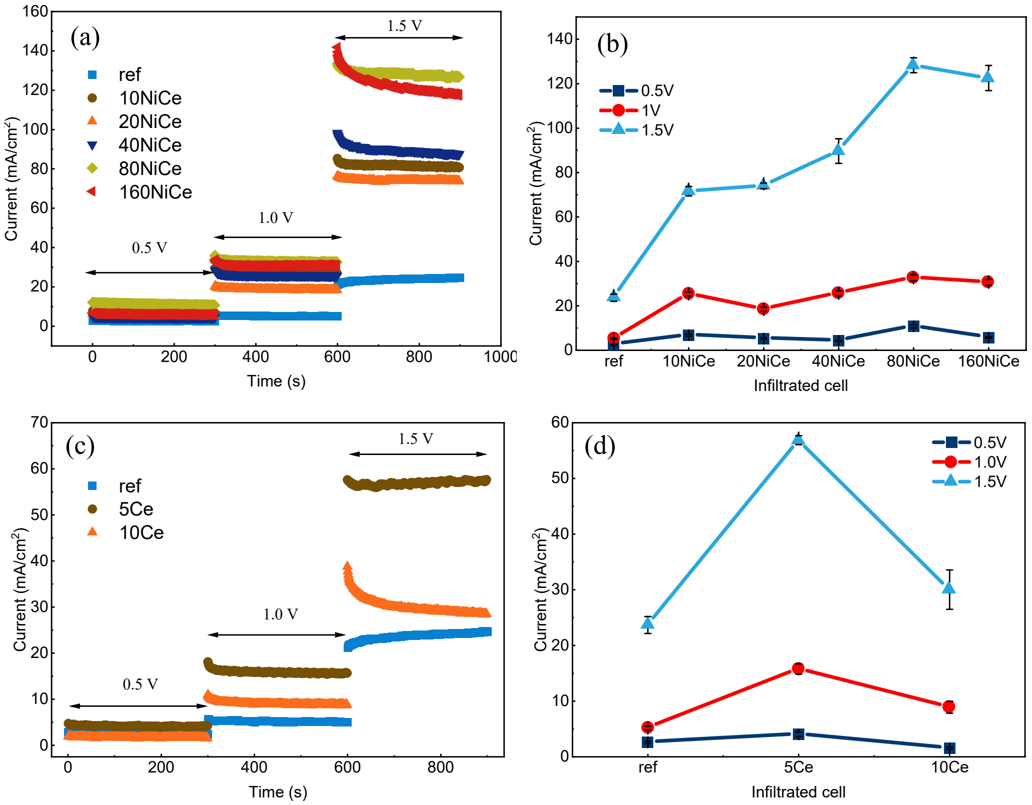

Figure 4.8. a) 6 groups of CA experimental results of NiYSZ impregnated with different amounts of $NiCeO_x$ NPs; **b)** The corresponding current of each potential in $NiCeO_x$ NPs experiments; **c)** 3 groups of CA experimental results of NiYSZ impregnated with different amounts of CeO_y NPs; **d)** The corresponding current of each potential in CeO_y NPs experiments. Each point corresponds to a steady state current attained after 5min at the selected potential

When considering the results from Figures 4.8, it can be concluded that while a 5 µL loading of CeO_y NPs led to a more than twofold increase in electrolysis current, this enhancement remains less significant than the sixfold improvement observed with $NiCeO_x$ NPs.

4.3.4.2. Gas production during the CA experiments

The gas phase analysis results obtained through online QMS, as depicted in Figure 4.9, indicate that the 80 NiCe cell produce significantly more O_2 compared to the 5 Ce and the reference, pristine Ni/YSZ cell. This finding aligns well with the electrical measurements, confirming that the enhanced performance is attributed to the greater electrocatalytic activity of the electrodes post-modification.

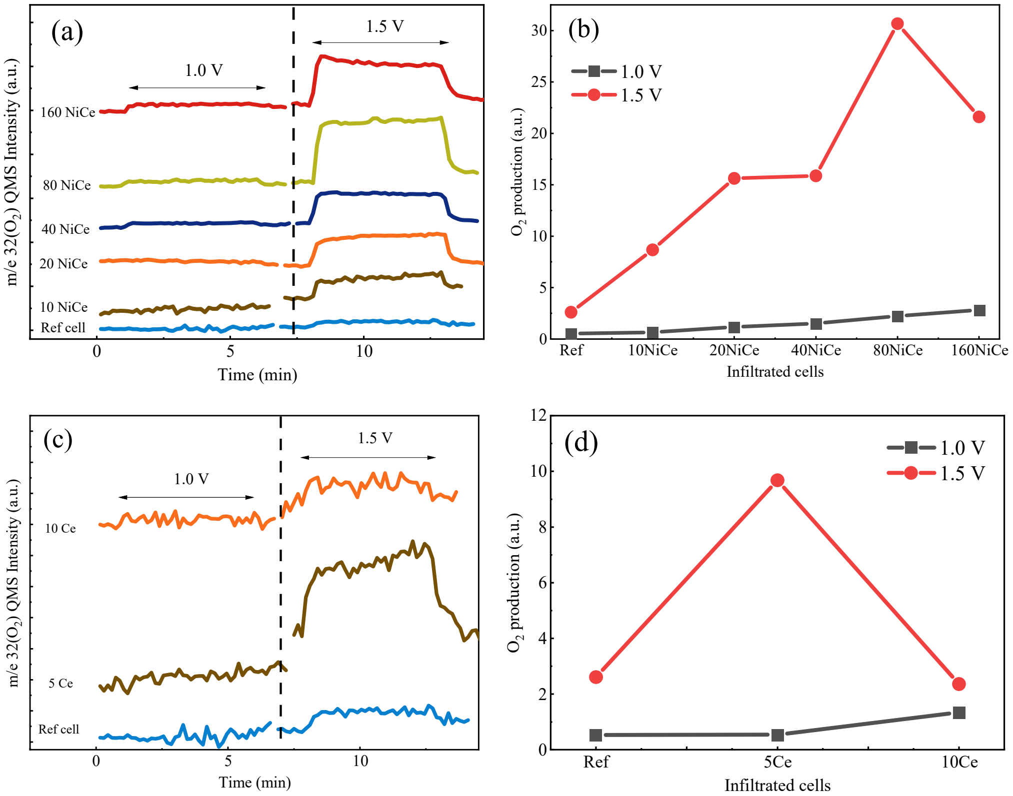

Figure 4.9. a) The evolution of the O_2 (m/e 32) gas phase signals as a function of time during $NiCeO_x$ NPs experiments recorded in the reaction chamber by on line mass spectrometry. Reaction conditions: 2 mbar H_2O+H_2(50%+50%) at 700 °C. **b)** Corresponding integrated O_2 gas QMS signal at each potential during $NiCeO_x$ NPs experiments; **c)** The evolution of the O_2 (m/e 32) gas phase signals during CeO_y NPs experiments; **d)** Corresponding integrated O_2 gas QMS signal at each potential during CeO_y NPs experiments. Results for the voltage applied at 0.5 V are not shown due to the exceedingly low gas production observed during these experiments, which fell below the detection limit and was completely masked by the background noise baseline.

4.3.4.3. EIS of pristine and infiltrated cells in H_2O+H_2 electrolysis

Following CA experiments, a corresponding electrochemical impedance spectroscopy (EIS) test was performed at each applied voltage. The results for $NiCeO_x$ infiltration are illustrated in Figure 4.10. Each EIS result presents an arc shape, from which the ohmic resistance (R_Ω) and the polarization resistance (R_p) of the cell can be calculated as mentioned in paragraph 4.2.4.

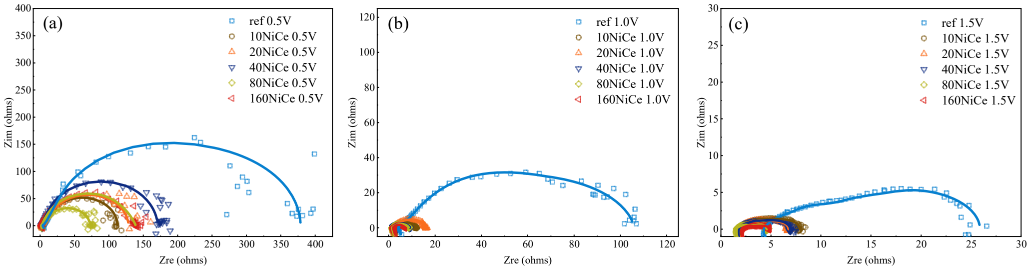

Figure 4.10. Potential static EIS of samples loaded with 6 different amounts of $NiCeO_x$ at three different voltages， **a)** for 0.5V, **b)** for 1.0 V and **c)** for 1.5 V.

Given the difficulty in determining the resistance values from the Nyquist plot, we conducted a fitting analysis and subsequently to present the data more clearly. From Figure 4.11, it is apparent that the R_Ω for the reference cell is approximately 4 Ω/cm^2, whereas the impregnated cell displays an ohmic resistance is slightly decreased ranging between 1.5 and 2 Ω/cm^2. The ohmic resistance for both cells remains stable as the voltage increases, which is consistent with their physical interpretation. The R_p between the pristine and infiltrated cells exhibits significant variation. Specifically, the reference cell shows a polarization resistance of approximately 380 Ω/cm^2, while the lowest polarization resistance for the 80 μL $NiCeO_x$ impregnated cell is around 75 Ω/cm^2.

Another notable observation is that the sample impregnated with 80 μL consistently exhibits the lowest R_p across all applied voltages. R_p effectively reflects the ease of the electrode reactions, and its decrease with increasing applied voltage can be explained by the kinetics of electrochemical reactions. In redox reactions, the activity of surface-active sites on the electrode varies with different potentials. Near the equilibrium potential, the reaction rate is slow, resulting in higher polarization resistance. However, as the applied voltage deviates from the equilibrium potential, the rates of oxidation or reduction reactions increase, leading to a typical decrease in polarization resistance.

The relationship between the current of the electrochemical reaction and the overpotential can be described by the Tafel equation [393]:

$$\eta = a + b\log(i)$$

In this context:

η represents the overpotential,

i denotes the current density,

a and ***b*** are constants.

According to the Tafel equation, the current density of the electrochemical reaction increases exponentially with the rise in electrode potential, leading to an elevated reaction rate. This decrease in the activation energy barrier for the electrode reaction results in a reduction of polarization resistance.

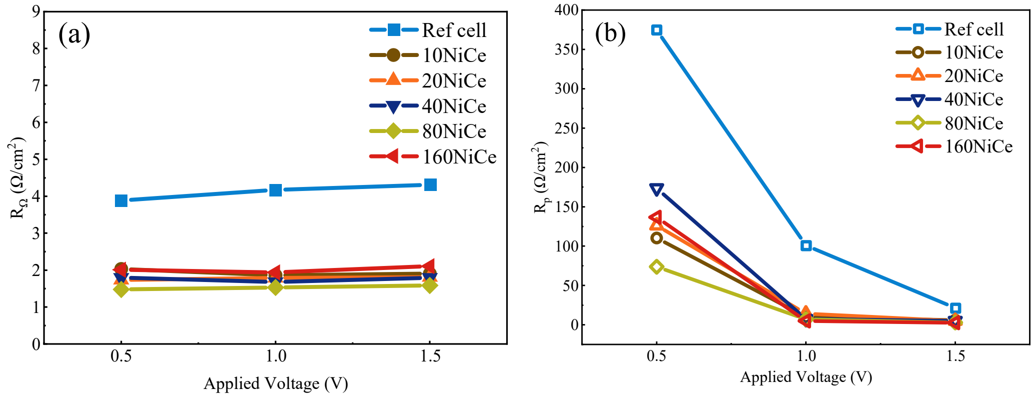

Figure 4.11. a) Ohmic resistance (R_Ω) and **b)** polarization resistance (R_p) were calculated based on the fit result of impedance spectra of Figure 4.10a,b,c.

As the experimental voltage increases, there is a marked decrease in polarization resistance (R_p). At 1.0 V, the Rp of the impregnated cells reduces to a range of 8 to 18 Ω/cm^2, and at 1.5 V, it further declines to between 5 and 8 Ω/cm^2. The Rp for the reference cell at 1.5 V decreases to 25 Ω/cm^2, representing only 6.5% of its initial value.

The results observed after CeO_y infiltration align with the previously described pattern for $NiCeO_x$ (Figure 4.12). The modified electrolysis cells consistently demonstrate lower impedance values. Notably, the cells impregnated with 5 μL of CeO_y exhibit the lowest impedance values for both R_Ω and R_p. More specifically, as presented in Figure 4.13, the fitted results indicate that in Figure 4.13a, the R_Ω of the reference sample and the 5Ce sample remains relatively constant, while the R_Ω of the 10Ce sample increases with rising voltage. In Figure 4.13b, the R_p of the 10Ce sample exhibits the most significant variation, rapidly decreasing from approximately 600 Ω/cm^2 at 0.5V to about 23 Ω/cm^2 at 1.0 V. This behavior clearly illustrates that the agglomeration effect of the 10Ce nanoparticles at the electrode surface adversely affects the conductivity of the Ni/YSZ surface conductive layer and alters the rate of electrochemical reactions during the transition from low to high voltage in the activation-controlled phase [386,394,395].

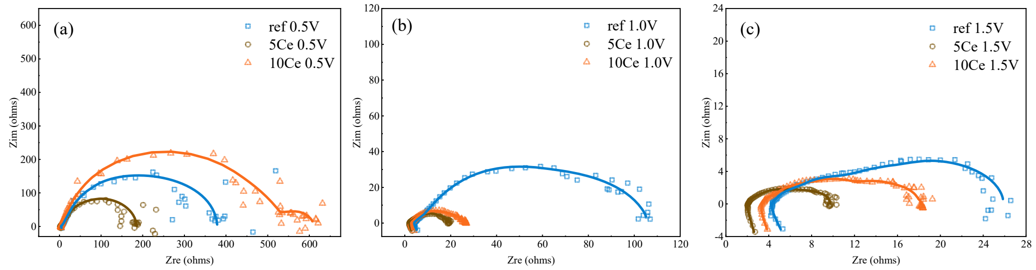

Figure 4.12. Potential static EIS of samples loaded with 3 different amounts of CeO_y at three different voltages, **a)** for 0.5V, **b)** for 1.0 V and **c)** for 1.5 V.

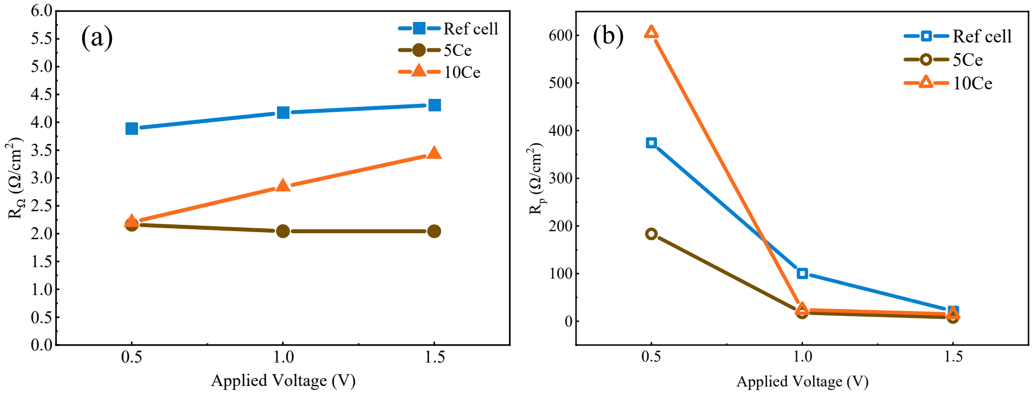

Figure 4.13. a) Ohmic resistance (R_Ω) and **b)** polarization resistance (R_p) were calculated based on the impedance spectra of Figure 4.12a,b,c.

These findings validate that the incorporation of CeO_y NPs effectively lowers the overall resistance of the cells, similar to the enhancements observed with $NiCeO_x$ NPs, albeit with some differences in efficiency. The reduced impedance values signify an improved electrochemical activity and enhanced ion transfer within the cell.

The impedance experimental results correlate well with those obtained from the CA experiments, emphasizing the differences in performance before and after modification, as well as the varying performance between the two types of nanoparticles. The comparative analysis of EIS spectra highlights the distinctly modified performances of Ni/YSZ electrodes when are inflitrated with $NiCeO_x$ and CeO_y NPs.

4.3.4.4. Staircase linear scan comparison of pristine and infiltrated cells in H_2O+H_2 electrolysis

The findings from the Staircase linear scan provide additional valuable insights. Each sample underwent two forward and reverse Staircase linear scans, which can be interpreted as single-cycle Cyclic Voltammetry curves. Notably, there is minimal difference between the two scans for each sample, indicating stability and reversibility. To enhance clarity, the reverse scans are omitted in Figure 4.14.

In Figure 4.14a, which shows the curves for samples with varying $NiCeO_x$ loading amounts, it is evident that the reference cell consistently demonstrates the lowest performance across all voltage levels. Interestingly, the performance of the samples does not follow a simple trend of increasing current with greater loading amounts; for instance, the 20 μL and 40 μL samples display lower currents than the 10 μL sample at voltages below 0.8 V.

We noted that the initially lower-performing 20 μL, 40 μL, and 160 μL samples begin to show improvement after 0.8 V. The Staircase linear scan results clearly illustrate the trend of increasing electrolysis current with higher applied voltage. Throughout the voltage scan experiments, the 80 μL sample generally maintained the highest electrolysis current, only equaled by the 160 μL sample after 1.0 V and eventually being slightly surpassed. These results indicate that $NiCeO_x$ NPs significantly promote the electrochemical activity of the cell, irrespective of the specific loading quantity.

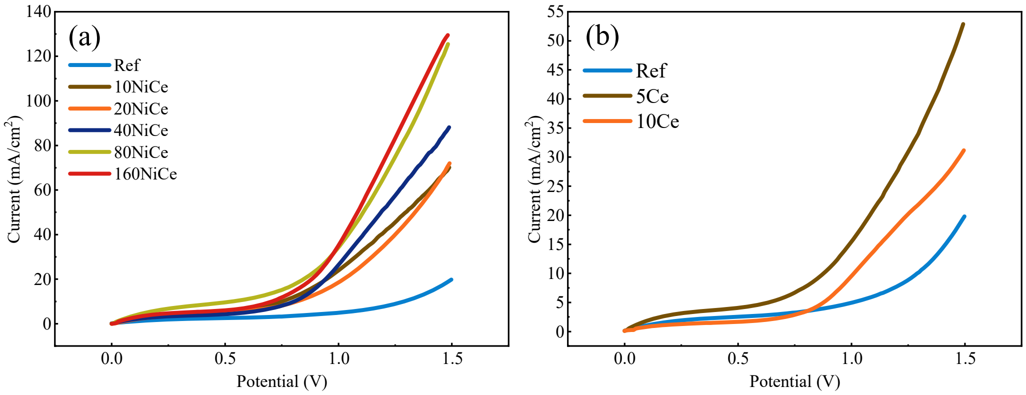

Figure 4.14. a) Staircase linear scan of different $NiCeO_x$ impregnated cell under potential scans between 0~1.5V; **b)** Staircase linear scan of different CeO_y impregnated cell under potential scans between 0~1.5V.

From Figure 4.14b, it is evident that the 5 μL CeO_y impregnated sample achieves the highest electrolysis current across all scanned voltages. Notably, the 10 μL CeO_y modified sample initially exhibits lower performance than the reference cell in the low voltage range; however, this trend reverses after 0.8V, with the 10 μL sample outperforming the reference cell. Based on these experimental results, we draw a conclusion similar to that for $NiCeO_x$: an appropriate loading of CeO_y can enhance both non-Faradaic current (Current at low voltage) and Faradaic current (Current at higher voltage) of the Ni/YSZ electrode. However, exceeding the optimal loading amount can impede the non-Faradaic current. It is only when the electrochemical reactions commence that the presence of CeO_y NPs significantly boosts the Faradaic current. These findings underscore the necessity of optimizing the nanoparticle loading amount to balance enhancement effects and avoid excessive infiltration, which may hinder performance at lower voltages.

4.3.4.5. Medium-term stability comparison of pristine and infiltrated cells in H_2O+H_2

In the final stage of our electrochemical experiments, we evaluate the stability of each sample using medium-term chronopotentiometry tests. During these tests, the cell is maintained at a constant current throughout the electrolysis process, while the cell voltage is continuously recorded as a function of time. We selected a current density of 25 mA/cm^2 for these tests, based on preliminary experiments that ensured it was optimally balanced— neither too low, which could impede the electrochemical reaction, nor too high, which could risk overloading the electrochemical workstation during extended assessments. It is also noteworthy that, considering laboratory safety and equipment limitations, we chose an 18-hour duration for our long-term experiments. This timeframe was adequate for observing performance differences among the various samples, as well as assessing the performance degradation of individual samples. The results of these experiments are presented in Figure 4.15.

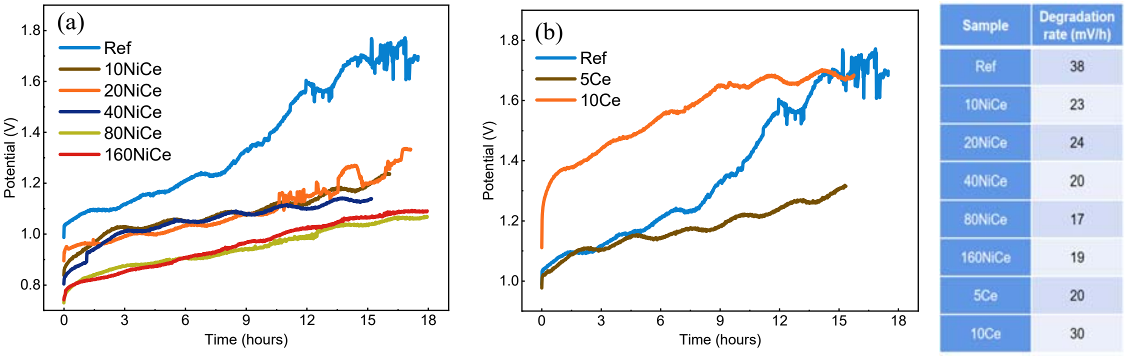

Sample	Degradation rate (mV/h)
Ref	38
10NiCe	23
20NiCe	24
40NiCe	20
80NiCe	17
160NiCe	19
5Ce	20
10Ce	30

Figure 4.15. long-term performance test of **a)** 6 $NiCeO_x$ infiltrated cells and **b)** 3 CeO_y infiltrated cells. Reaction conditions: 6 mbar H_2O+H_2(50%+50%) at 700 °C.

As illustrated in Figure 4.15a, although all cells show a quite important degradation of their performance, manifested by the voltage increase, the 80NiCe sample consistently demonstrates the lowest degradation rate, around 17 mV/h, with the 160NiCe sample showing comparable results. The 10NiCe, 20NiCe, and 40NiCe samples fall into a second tier of performance, while the Ref sample exhibits the poorest stability with degradation rate of 38mV/h, displaying a noticeable decline in performance after 18 hours. As shown in Figure 4.15b, the 10Ce sample undergoes rapid degradation within the first hour. After this initial phase, the degradation stabilizes into a more linear pattern, eventually reaching the voltage level of the Ref sample after approximately 15 hours. In such short term, the degradation of electrolysis cells might be caused by the oxidation of the Ni/YSZ electrode surface [198], or the coarsening of nickel particles [197].

A notable feature observed across all samples is a time-varying oscillatory pattern, with an average cycle of approximately 160 minutes. Similar experiments conducted with Ni/GDC samples under the same electrolysis conditions (not included in this thesis) also exhibited a comparable periodic wave phenomenon, though with smaller and more organized amplitudes compared to Ni/YSZ. The changes in oxidation and reduction states on the surface are expected to occur over a short duration and remain stable, making periodic reversals unlikely. We hypothesize that this phenomenon is likely linked to a passivation process that can be reactivated, which is influenced by the oxidation of the electrode surface by the produced oxygen. Since our system operates with both the cathode and anode in a single reaction chamber, the supply and product gases both interact with the electrode surface, affecting the oxidation state of the Ni. The oxygen produced at the platinum electrode can oxidize nickel at the cathode, which not only reduces the electronic conductivity but also results in the gradual disappearance of TPBs and 2PBs. This diminishes contact with the gas, reducing the amount of product oxygen until it can no longer compete with the supply hydrogen and product hydrogen. At this stage, the hydrogen in the gas supply primarily acts to reduce the electrode surface, gradually restoring the electrochemical reaction, leading to the observed electrochemical oscillation. In the pure steam electrolysis experiments, without supplied hydrogen, only the competing product gases (H_2 and O_2) interact, making the voltage oscillations even more pronounced.

4.3.5 XRD Analysis of Post-Electrolysis Cells

After the electrolysis experiments, the samples were analyzed using XRD. It is important to note that the samples were exposed to air during both the transfer to the XRD instrument and the XRD measurements. This exposure likely affected the oxidation state of nickel in an uncontrolled manner, preventing reliable conclusions about the nickel oxidation state during the electrolysis reaction. The diffractograms in Figures 4.16a and 4.16c reveal peaks corresponding to both metallic Ni and NiO, indicating that nickel remains in a partially oxidized state in both electrodes. Additionally, no shift in the diffraction peaks is observed between the reference Ni/YSZ and the modified samples, suggesting that the incorporation of ceria-based nanoparticles does not alter the bulk structure of the Ni/YSZ electrode. A closer examination of the region where ceria diffraction peaks are expected, shown in Figures 4.16b, reveals that the CeO_2 signal is only clearly detectable at the highest nanoparticle loading (160 NiCe). This finding suggests that, at this concentration, NiCe nanoparticles begin to agglomerate into larger particles, resulting in a detectable XRD signal. The formation of larger particles may eventually block the pores of the electrode, potentially explaining the decline in cell performance mentioned earlier.

In the case of the electrodes infiltrated with CeO_2 nanoparticles, the diffractograms in Figure 4.16d do not show any detectable ceria-related peaks. This absence of signal is likely due to the small volume of infiltrated solution in these samples. It also serves as evidence that the decline in the H_2O electrolysis performance of 10Ce sample, evidenced in Figure 4.8d, cannot be due to significant pore blocking, as larger particles would have been detectable in the diffractograms if pore obstruction had occurred. Additionally, considering that the cell's Ohmic resistance remains largely unaffected after CeO_2 nanoparticle infiltration, as demonstrated by the EIS data in Figure 4.13a, it can be inferred that the deactivation effect of CeO_2 nanoparticles may be linked to their poor electrocatalytic properties for H_2O electrolysis compared to doped NiCe particles. This hypothesis underscores the need for a more detailed analysis of the surface chemistry of the CeO_2 and $NiCeO_x$ nanoparticles.

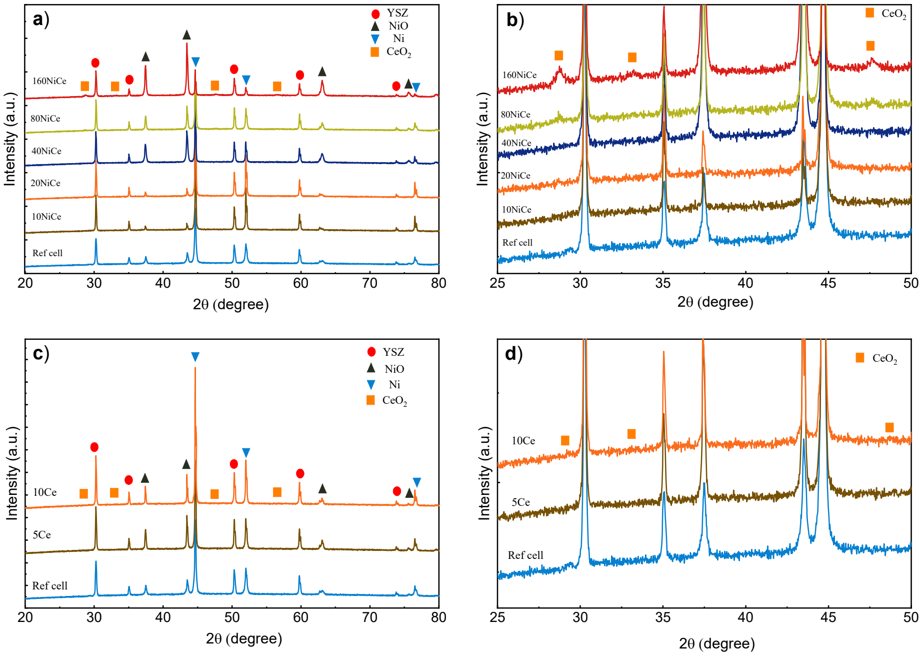

Figure 4.16. Postmortem XRD characterization of the Ni/YSZ cells infiltrated with **a),b)** $NiCeO_x$ NPs and **c),d)** CeO_y NPs

4.3.6 NAP-XPS Analysis of Ni-Doped and undoped CeO_x Nanoparticles

NAP-XPS experiments were conducted at the HIPPIE beamline of the MAX IV synchrotron facility in Sweden. For the sample preparation, nanoparticles from a suspension were deposited onto a thin gold foil. A fine layer of carbon adhesive tape was used to divide the central area of the foil into separate sections, preventing cross-contamination of nanoparticles due to the surface tension of the hexane solvent. Before conducting the photoemission measurements, the adhesive tape was removed since it could not withstand high temperatures. For each type of nanoparticle, we deposited 10 μL (approximately 0.05 mg) evenly onto the designated areas. The samples were then subjected to a drying and a calcination process at 450 ℃ in air to remove the oleylamine coating, leaving only the nanoparticles on the gold foil for subsequent analysis (see Figure 4.17 e).

The sample was exposed to 1 mbar of H_2 and heated from the backside using an IR laser, with the temperature monitored by a K-type thermocouple attached beneath the gold foil. The temperature was stepwise increased to 400 °C, 450 °C, 500 °C, and 550 °C at a rate of 10 °C/min. Each target temperature was maintained for 10 minutes before cooling to 250 °C for NAP-XPS characterization. Uniform heating ensured consistent reduction times across all nanoparticles on the gold foil. Cooling to 250 °C before photoemission measurements is crucial for maintaining the stability of the samples' oxidation states during NAP-XPS analysis. Two different photon energies (1065 eV and 1800 eV) were used to analyze each sample, with the goal of comparing the chemical states of the surface and subsurface layers and identifying any potential layered structures in the nanoparticles.

The Ce 3d region of both samples and in the two analysis depths is presented together in Figures 4.17a, b, c, and d. After fitting the Ce 3d spectra using Ce^{3+} and Ce^{4+} reference curves, the average Ce valence for both analysis depths is plotted in Figure 4.17f. Reduction is evident for both nanoparticle types at 400 °C in the surface-sensitive mode (hv = 1065 eV), with surface layers showing a greater degree of reduction than deeper layers, indicating that Ce^{3+} is preferentially located at the surface. However, notable differences exist between the two nanoparticle types: CeO_y shows a gradual reduction with increasing temperature, while $NiCeO_x$ undergoes rapid reduction at 450 ℃, followed by a slowdown from 450 ℃ to 550 ℃. Additionally, the mean valence state of $NiCeO_x$ is consistently lower than that of CeO_y by approximately 0.32 (shallow layer) and 0.2 (deep layer). This finding highlights a clear difference in the reducibility between the two types of ceria particles, which may explain their differences in their promotion efficiencies of the electrolysis reaction. In particular, higher reducibility is related with higher electronic conductivity and the ability of reduced ceria to accommodate oxygen ions, while might also provide additional sites for H_2O adsorption. These factors are expected to be beneficial for enhancing electrolysis performance.

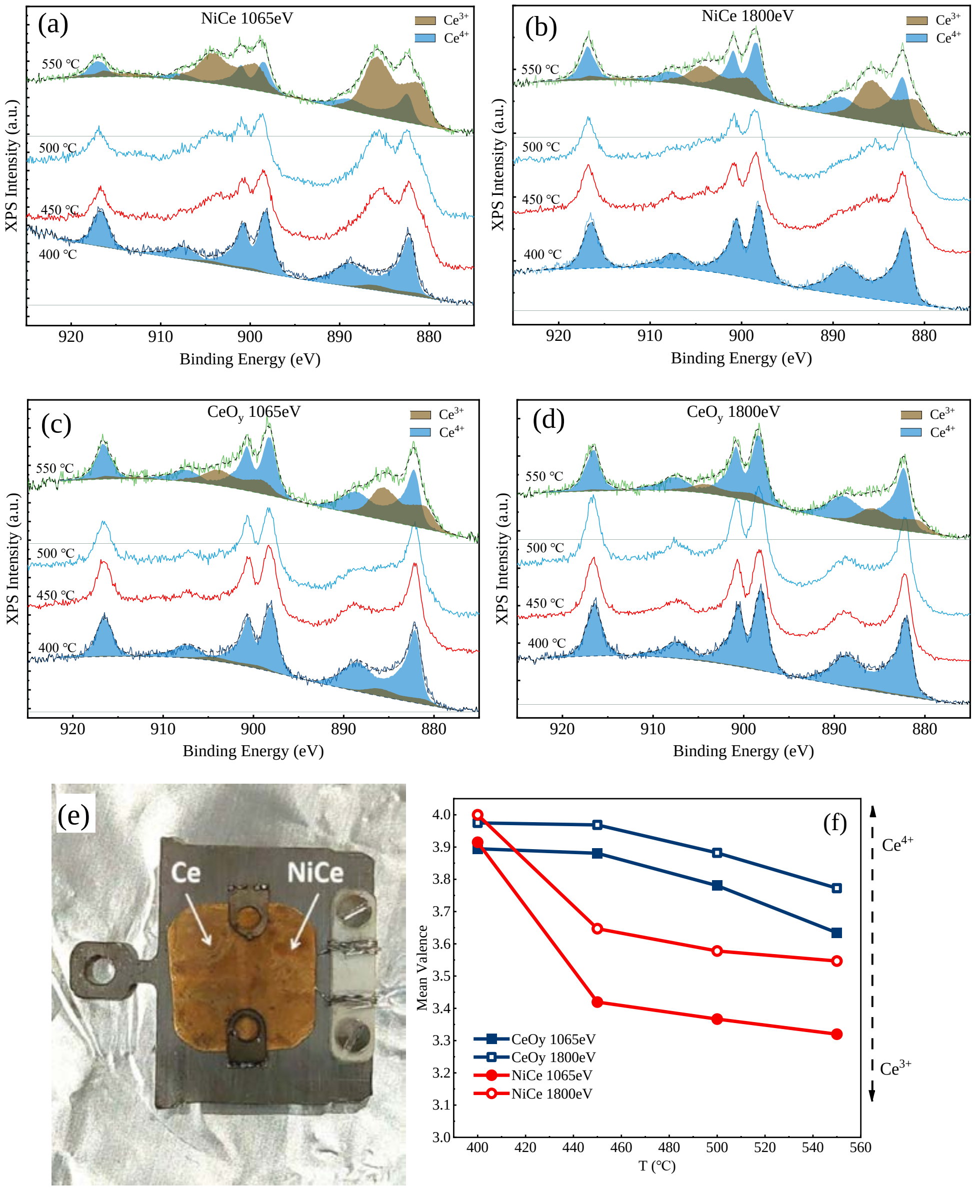

Figure 4.17. a) Spectra of Ce in NiCe NPs via photon energy 1065 eV at 400 °C, 450 °C, 500 °C and 550 °C during NAP-XPS measurement under 1 mbar H_2 atomsphere; **b)** Spectra of Ce in NiCe NPs via photon energy 1800 eV at 4 temperatures during NAP-XPS measurement; **c)** Spectra of Ce in CeO_y NPs via photon energy 1065 eV at 4 temperatures during NAP-XPS measurement; **d)** Spectra of Ce in CeO_y NPs via photon energy 1800 eV at 4 temperatures during NAP-XPS measurement; **e)** Photograph of gold foil with different nanoparticles deposited in different areas mounted on the holder; **f)** Evolution of mean valence of Ce of 2 different NPs corresponding to NAP-XPS results.

4.4 Origin of the Promotion Mechanism of Ceria-Based NPs on Ni/YSZ electrodes

The presented results demonstrate that infiltrating Ni/YSZ electrodes with Ni-doped CeO_x nanoparticles significantly improves water electrolysis performance, a benefit less pronounced with the use of CeO_y nanoparticles alone. This enhanced activity likely arises from several factors, including the good oxygen ion conductivity and oxygen storage capacity of ceria, which are known to be beneficial for the performance and stability of both SOEC and SOFC operations [396–398]. NAP-XPS measurements reveal that Ni enhances the reducibility of CeO_2, which in turn reinforces oxygen ion conductivity and oxygen storage capacity. Additionally, optimizing the size and morphology of CeO_2-based nanoparticles further enhances their effectiveness [396,399,400], while their compatibility with Ni and YSZ contributes to the long-term cell stability [396,401,402]. Ceria NPs have also been shown to improve the electrochemical reduction of CO_2 in SOECs [397,399,403].

Our findings reveal that doping ceria NPs with Ni further boosts the electrochemical performance of Ni/YSZ cells after infiltration. Several mechanisms may contribute to this improvement. First, Ni-doped ceria nanoparticles in solution are smaller than undoped ceria particles, which facilitates better penetration into the electrode's porous structure, minimizing the risk of pore clogging.

Although our experimental results show a significant reduction in polarization resistance and enhanced charge transfer in Ni/YSZ cells following infiltration with $NiCeO_x$ nanoparticles, it remains challenging to determine whether these nanoparticles directly participate in the electrochemical reaction by providing additional reaction sites on the electrode surface. Nonetheless, theoretical studies of CeO_2-Ni systems suggest that Ni-ceria sites are more favorable than pure Ni for H_2O dissociation during steam reduction reactions (see Figure 4.18a) [287,404–406]. Thus, introducing $NiCeO_x$ nanoparticles likely creates additional reaction sites beyond the well-known Ni-YSZ triple-phase boundary (TPB). These extra reaction sites may consist of three types:

1. TPB points formed at the interface between Ni grains in Ni/YSZ and ceria nanoparticles,
2. TPB points formed at the interface between Ni dopants and Ce atoms within Ni-doped ceria nanoparticles (Figure 4.18b), and
3. TPB points at the interface between YSZ and surface-bound ceria particles.

Higher nanoparticle loading could significantly increase the number of reaction sites and may also create an extensive network of nanoparticles, establishing multiple ion conduction pathways. Finally, the incorporation of Ni-doped ceria may improve the electrode's microstructural stability. Ni/YSZ electrodes are susceptible to degradation over long-term operation due to Ni coarsening and migration. The addition of Ni-doped ceria nanoparticles could mitigate this degradation by impeding Ni migration and providing a stabilizing effect.

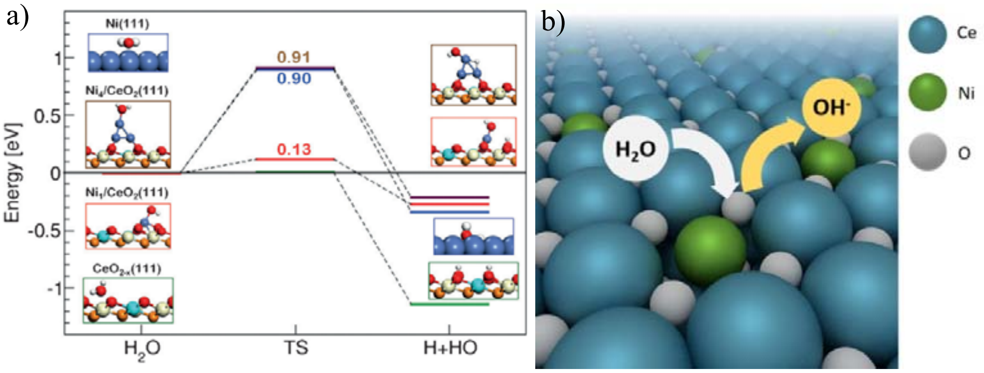

Figure 4.18. a) Reaction energy profile for H_2O dissociation on the CeO_{2-x} (111), Ni_1/CeO_2(111), Ni_4/CeO_2(111), and Ni(111) surfaces. Reproduced with permission of Ref. [404]; **b)** Schematic of H_2O atoms undergo redox reactions on the active sites of doped Ni and Ce.

4.5 Conclusions

This chapter examined the performance enhancement of both Ni-doped and undoped ceria NPs on the Ni/YSZ cathode for water electrolysis. In summary, ceria NP infiltration effectively enhances the electrochemical performance and stability of the Ni/YSZ cathode, offering a promising strategy for advancing hydrogen production technologies. Notably, Ni-doped ceria NPs significantly reduce polarization resistance and improve charge transfer in the Ni/YSZ cell, leading to superior electrochemical activity and increased H_2 production compared to undoped CeO_y NPs. This improvement is likely due to differences in the NPs sizes and the formation of additional electrocatalytic active sites on the Ni/YSZ surface.

Chapter 5. Ni/YSZ electrodes impregnated with Vanadium doped and Co doped Ceria Nanoparticles

5.1 Introduction

In the previous chapter, it was demonstrated that doping ceria nanoparticles with Ni enhances their capacity to improve the electrocatalytic performance of Ni/YSZ electrodes. This prompted us to explore whether elements other than Ni can be doped into CeO_x nanoparticles to improve the performance of Ni/YSZ SOEC. Thus, we aim to determine if there are other dopant elements, besides Ni, that can enhance the electrocatalytic performance of Ni/YSZ electrodes in water electrolysis.

In solid oxide electrodes, numerous perovskite-based SOFC or SOEC electrodes incorporate vanadium [407–412]. Vanadium (V), as a transition metal, exhibits multiple oxidation states (e.g., V^{2+}, V^{3+}, V^{4+}, V^{5+}). It enhances electronic and oxygen ion conductivities, promotes redox reactions, improves electrochemical and chemical stability, adjusts the thermal expansion coefficient, and boosts electrocatalytic performance [413–421]. Consequently, vanadium plays a crucial role in electrochemical applications and is a good potential candidate for the puropose of this thesis.

According to Zhou et al. [422], who studied LSCF type perovskite electrodes, the introduction of vanadium into $La_{0.5}Sr_{0.5}Fe_{1-x}V_xO_{3-\delta}$ (LSFC) SOEC cathodes promotes the formation of oxygen vacancies in $LSFV_x$/GDC. Vanadium doping can introduce additional O^-/O^{2-} and Fe^{3+}/Fe^{4+} as well as V^{5+}/V^{4+} electron pairs, which enhance charge transfer and oxygen ion transport in $LSFV_x$/GDC. When compared to LSF/GDC, the $LSFV_{0.05}$/GDC cathode demonstrated 51.2% increase in current density at 1.6 V and 800 °C. Kisa et al. [423] conducted a study on the impact of vanadium doping on the crystal structure and electrical properties of LaVSrCo perovskite oxide used as SOFC cathode material. Their findings indicated that substituting La^{3+} cations with V^{4+}/V^{5+} cations within the perovskite structure enhances ionic conductivity and the catalytic activity for the oxygen reduction reaction. Additionally, Vo at al. [424] discussed the effects of vanadium deficiency on the catalyst stability in La-Sr-Vanadate (LSV) SOFC anodes. The researchers examined LSV anodes with varying degrees of vanadium deficiency and found that the electronic conductivity of LSV decreased as the level of vanadium deficiency increased. They also observed that the addition of CeO_2 further stabilized the anode performance. These studies collectively underscore the significant role of vanadium in applications related to solid oxide cell electrodes. However, research on the infiltration modification of Ni/YSZ SOEC electrodes with V and Ce co-doped nanoparticles remains relatively unexplored.

Cobalt is another widely used transition metal due to its excellent electrocatalytic and catalytic properties in oxygen reduction and evolution reactions. Positioned adjacent to Ni in the periodic table, cobalt can integrate into the Ni lattice similarly to Fe. The easy transition between Co(III), Co(II), and Co^0 oxidation states can lead to modifications in the electronic properties of Ni-based catalysts [425,426]. Research by Alrafei et al. [427] demonstrated that Co enhances both the reducibility and dispersion of the Ni phase. However, as the operating temperature decreases, one significant drawback of cobalt-containing perovskite materials is their high coefficient of thermal expansion (CTE) [428,429]. This limitation might be circumvented through surface infiltration techniques. Błaszczak and colleagues modified SOEC with a small amount of cobalt, discovering that the addition of Co significantly improved the electrochemical efficiency of co-electrolysis of water and CO_2 [430]. Other researchers have experimented with modifying solid oxide electrodes by adding elements like Fe and Cu, achieving promising results [431–438].

In this chapter, we primarily focus on studying the elements vanadium (V) and cobalt (Co) as dopants of ceria nanoparticles. We replicated the nanoparticle synthesis methods described in the preceding chapters, substituting the doped Ni with V and Co. This led to the synthesis of CeO_y doped with V and Co. Subsequently, we tested the performance of CeO_y doped with these two catalytic elements, and conducted synchrotron-based characterizations to better understand the physicochemical caracteristics of these particles.

5.2 Materials and methods

5.2.1 Synthesis of VO_x nanoparticles

In this part, we will introduce various synthesis methods for vanadium nanoparticles. Bergerud et al. [439] developed a colloidal route to synthesize vanadium sesquioxide (V_2O_3) nanocrystals with a metastable bixbyite crystal structure. They synthesized V_2O_3 with a nanoflower morphology directly by vacuum heating and stirring vanadyl acetylacetonate with oleylamine and oleic acid in squalane. This oxidation of the bixbyite phase is also observed in the cerium oxide system with bixbyite Ce_2O_3 readily transforming to fluorite CeO_2 under oxidizing conditions, made possible by the facile conversion between cerium oxidation states [440] and allows for size control through adjustments in synthesis temperature and duration. Dewangan et al. [441] used a two-stage synthesis process to produce vanadium nitride (VN) nanocrystals for superconducting applications. Similarly, they used oleylamine as a surfactant and thermally decomposed vanadium (III) acetylacetonate [$V(acac)_3$] precursor in diphenyl ether, obtaining monodisperse amorphous VO_x nanoparticles with an average size of about 4.64 nm. Based on the synthesis techniques reported in the literature and our prior work, we selected three synthesis pathways to prepare VO_x nanoparticles. After synthesis all nanoparticles, were characterized by DLS, dried and calcined part of the solution to performed XRD characterization tests.

5.2.1.1 1st Synthesis method of VO_x

In the first synthesis (schematically shown in Figure 5.1), we weighed 1.913 g (0.005 mol) of $V(acac)_3$ and placed it into a round-bottom flask. An appropriate amount of oleylamine was added, and the flask was connected to a vacuum apparatus. After evacuating the air, nitrogen gas was introduced. The flask was then heated to 250 °C and maintained at this temperature for 1 hour. After heating, the mixture was cooled at room temperature. The reaction mixture was transferred to a centrifuge tube for centrifugation, and the supernatant was collected. The supernatant was then divided into four centrifuge tubes, each containing 5 mL of methanol. The mixture was shaken well for extraction. After centrifugation, the supernatant was discarded, and the solid precipitate was collected. Hexane was added to the precipitate to disperse and dissolve the separated nanoparticles, forming the desired nanoparticles for subsequent infiltration. Due to the unique chelating structure of $V(acac)_3$, where V ions are encapsulated within the coordination structure, it readily forms dispersed nanoparticles and gets encapsulated by oleylamine. During the subsequent methanol extraction process, the nanoparticles are effectively separated. We refer to these nanoparticles as VO_x nanoparticles.

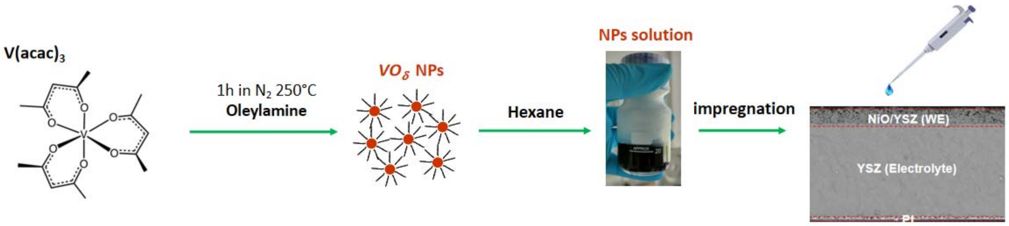

Figure 5.1. The first synthetic route for VO_x nanoparticles

5.2.1.2 2nd Synthesis method of VO_x

In the second synthesis pathway, $V(acac)_3$ was used as a substitute for $Ce(NO_3)_3$ in the production of CeO_x nanoparticles. Specifically, 3.255 g (0.01 mol) of $V(acac)_3$ were measured. The following synthesis steps mirrored those outlined in Chapter 4. Initially, Schiff base complexes (V-L) were synthesized by mixing o-vanillin, 1,3-diaminopropane, and $V(acac)_3$ in methanol, under reflux at 80 °C for 2 hours. Subsequently, nanoparticles were formed by mixing the Schiff base V and subjecting it to pyrolysis in an oleylamine medium at 180 °C under an inert N_2 atmosphere. After the synthesis, methanol was used to precipitate the nanoparticles, which were then collected by centrifugation and dispersed in a hexane solution (as shown in Figure 5.2). Despite the similarities with the main synthesis steps described above, there were some notable differences during the synthesis process.

Upon completion of the synthesis of the vanadium-containing Schiff base (referred to as V-L in Figure 5.2), the reaction mixture was filtered using a vacuum apparatus. The collected solid product was distinctly different from the Ce-L product. During the crystallization of the Schiff base V, very noticeable needle-like crystals were observed. The filtered product was a fine, wet, orange clay-like material that could not be fully dried to a powder, unlike Ce-L, which, after drying, resulted in a loose, fine, bright yellow powder.

After obtaining Schiff base V, it was then dissolved in 40 mL of oleylamine. The mixture was stirred and heated under a pure nitrogen atmosphere. The temperature was raised to 200 ℃ until all solids were dissolved, then cooled to 180 ℃ for one hour of synthesis. This detailed approach ensures the accurate synthesis of V-L nanoparticles(V-L NPs, different from the intermediate product V-L mentioned above), crucial for their application in enhancing the performance of Ni/YSZ electrodes.

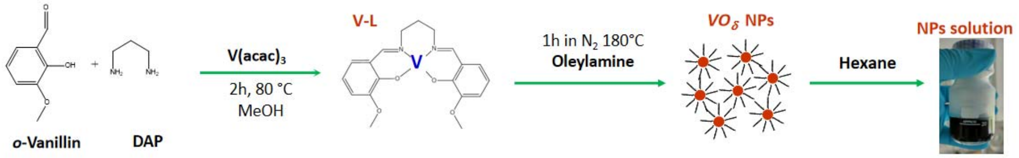

Figure 5.2. Synthesis route of V-L nanoparticles

5.2.1.3 3rd Synthesis method of VO_x

The third synthesis pathway is largely similar to the second one, with a few modifications aimed at achieving smaller nanoparticle sizes. In this method, we added 7.92 g (0.03 mol) of 1-octadecanol to the oleylamine and increased the synthesis temperature to 250 ℃, while reducing the duration to 20 minutes. This adjustment was prompted by the results from the second synthesis pathway, where the V-L nanoparticles, after calcination and characterization via XRD, were found to have an average particle size of approximately 40 nm, which was larger than desired. Based on insights from literature [442,443], we incorporated 1-octadecanol in the synthesis process to produce smaller vanadium nanoparticles. Smaller particle sizes are generally advantageous as they can penetrate easily into the porous structure of the electrode, creating more interfaces and potentially enhancing the performance of the electrochemical cell. We refer to these synthesized nanoparticles as V-octa nanoparticles.

5.2.2 Synthesis method of $VCeO_x$ and $CoCeO_x$

We adapted the synthesis method for $NiCeO_x$ nanoparticles described in Chapter 4 to synthesize $VCeO_x$ and $CoCeO_x$ nanoparticles. First, we synthesized the Schiff base complexes of the different elements: Ce-L, V-L, and Co-Ce-L. For the synthesis of V-doped Ce nanoparticles, we took 3.19 g of the cerium-containing Schiff base complex Ce-L and 2.66 g of the vanadium-containing Schiff base complex V-L (1:1 molar ratio). These compounds were thoroughly ground and mixed before being added to 40 mL of oleylamine. The mixture was stirred and heated to 200 °C until all solids were dissolved, then cooled to 180 °C for 1 hour to complete the synthesis. Subsequent steps included filtering, drying, extraction, and dispersion.

For the synthesis of Co-doped Ce nanoparticles, we directly measured 2.8 g each of Co-Ce-L and Ce-L, also in a 1:1 molar ratio. The two complexes were thoroughly ground and mixed, then added to 40 mL of oleylamine. The mixture was stirred and heated to 200 °C until all solids were dissolved, then cooled to 180 °C for 1 hour. Subsequent steps of filtering, drying, extraction, and dispersion were carried out as previously described.

5.2.3 NAP-XPS experiment of V and Co doped CeO_y nanoparticles

NAP-XPS experiments were conducted at the MAX IV HIPPIE facility in Lund, Sweden. The samples were prepared by depositing nanoparticle suspensions onto a thin gold foil, as described in detail in paragraph 4.3.6. For each type of nanoparticle, 10 µL (approximately 0.05 mg NPs) of the suspension was uniformly deposited on a designated area. The specific arrangement of the samples on the gold foil and their placement in the holder are illustrated in Figure 5.3.

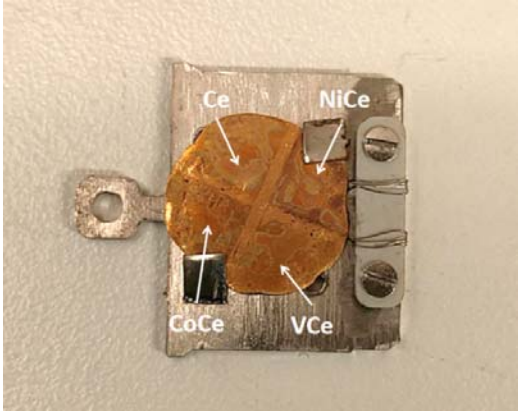

Figure 5.3. Position distribution of four different nanoparticles loaded on the gold foil on the holder

5.2.4 XAFS experiments at BM23 XAS beam line, ESRF

X-ray Absorption Fine Structure (XAFS) experiments were conducted at the BM23 beamline of the European synchrotron radiation facility (ESRF) [444], described in paragraph 2.4. During the XANES measurements, the temperature was gradually increased while the sample was exposed to a 1 bar hydrogen flow.

5.2.5 Electrochemical reactor and electrolysis methods

The electrolysis experiments were conducted in two separate reactors described in paragraphs 2.2.1 and 2.2.2. The first set of tests focused on evaluating the electrochemical performance of VO_x nanoparticle-modified electrodes in H_2O electrolysis. These tests were conducted using the flow-through reaction chamber of the in-house device described in Section 2.2.1 of Chapter 2. Complete cells, with an area of approximately 78.5 mm^2, were directly mounted onto a ceramic heater using stainless steel clamps. Gold mesh was employed as the current collector for both the cathode and anode sides, as depicted in Figure 2.5 of Chapter 2. The temperature was controlled by a K-type thermocouple installed on the side of the heater. The electrolysis testing conditions were as follows, 100% H_2O atmosphere (without dilution or reducing gas) at 1 mbar and a medium-high temperature of 700 ± 5 ℃ (limited by the test apparatus). Before each electrochemical test, the electrodes were calcined at 400 ℃ in 1.0 mbar O_2 for 30 minutes to remove residual carbon and organic residues. Following this, they were reduced at 550 ℃ in 1.0 mbar H_2 for 30 minutes.

The second set of electrolysis experiments focused on evaluating the electrochemical performance of $VCeO_x$ and $CoCeO_x$ nanoparticle-modified electrodes. The reaction setup used was the flow-through reaction chamber described in Section 2.2.2 of Chapter 2, and the samples were evaluated at 1 mbar under H_2O/H_2 atmosphere (50% H_2O/50% H_2) at 700 ± 10 ℃. Electrochemical cells with an area of approximately 78.5 mm^2 were secured on a quartz sample holder, similar to the one shown in Figure 4.3b, using two stainless steel clamps and heated by infrared lamps. Platinum mesh and gold mesh were used as current collectors on the anode and cathode sides, respectively. These were connected to a potentiostat using corresponding gold wires. The temperature was monitored by a thermocouple installed on the quartz sample holder. Before conducting the electrochemical tests, the electrodes were oxidized at 600 ℃ in 1 mbar O_2 for 30 minutes and then reduced at 700 ℃ in 1.0 mbar H_2 for 30 minutes. Following these pretreatments, the H_2O and CO_2 electrolysis experiments were performed under the specified conditions.

Electrochemical experiments were conducted on the same button cell before and after modification with different nanoparticles (NPs). This approach allowed us to focus on the effects of surface modification and eliminate uncertainties that could arise from differences in the bulk properties of the cells. By following this methodology, we ensured that any observed changes in electrochemical performance were attributed to the surface modifications of the electrodes with VO_x, $VCeO_x$, and $CoCeO_x$ nanoparticles.

5.3 Results

5.3.1 Characterization of vanadium oxide-based nanoparticles

After synthesizing the Schiff base complex intermediate V-L, we confirmed its structure to ensure the formation of the desired Schiff base complex before proceeding to further synthesis steps. The infrared absorption spectrum of the powder sample was measured in air at room temperature using a FTIR spectrometer as mentioned in Chapter 2. Background subtraction was performed prior to collecting the sample spectra. The infrared wavelength range was 4000-400 cm^{-1}, with 30 scans at a resolution of 0.5 cm^{-1}.

The infrared absorption spectrum is displayed in Figure 5.4. From this spectrum, it can be observed that the Schiff base complex intermediate, V-L, exhibits characteristic peaks that differ significantly from those of the starting materials, $V(acac)_3$ and o-vanillin. In the low-energy band region of the V-L complex (1200-1700 cm^{-1}), a series of absorption peaks are observed, which are attributed to the characteristic peaks of Ce-L [386,445–448]. Specifically, the absorption band at 1626 cm^{-1} is assigned to the stretching frequency of the azomethine group ν(C=N), indicating the presence of an imine group and confirming the formation of the Schiff base. Additionally, bands corresponding to ν(C=C) and ν(C-O) appear at 1445 cm^{-1} and 1241 cm^{-1}, respectively. The complex bands that seen at 2750-2950 cm^{-1} are represent the $-CH_3$ group. This characterization verifies the successful synthesis of the nanoparticle intermediate complex.

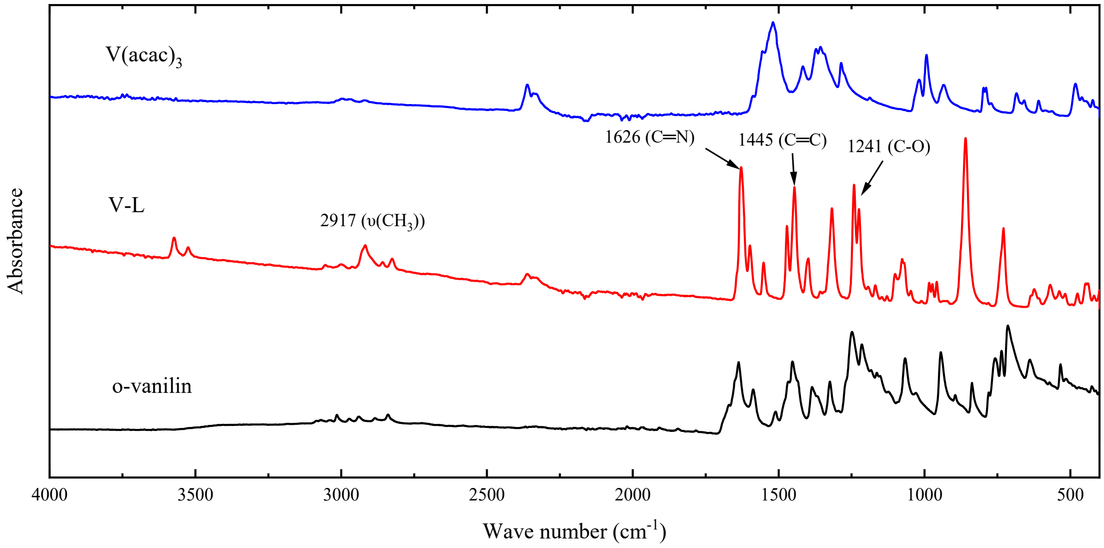

Figure 5.3. Comparison of FTIR results of Schiff base complex intermediate of V-L with $V(acac)_3$ and o-vanilin

The nanoparticle concentrations in the solutions were estimated using TGA, which revealed significant variations among the synthesized nanoparticles. The VO_x nanoparticles had the lowest concentration at 0.4 mg/mL, while the Schiff base complex nanoparticles reached the highest concentration at 8.2 mg/mL. Despite these concentration differences, all nanoparticles displayed similar agglomeration sizes in solution, ranging from 40 to 50 nm, as determined by DLS.

For XRD characterization, the three types of vanadium nanoparticles were calcined at 450 °C with a heating rate of 10 °C/min in an air atmosphere. The XRD patterns (Figure 5.8) showed vanadium pentoxide (V_2O_5) for all samples, with no other phases detected. Particle size estimation using the Scherrer formula (Table 5.1) indicated an average particle size of approximately 37 nm, which is relatively large compared to the cerium-based nanoparticles discussed in Chapter 3. Reducing the particle size of vanadium-based nanoparticles through these three synthesis methods remains a significant challenge.

Table 5.1. Concentration and size characterization of three different V-based nanoparticles

	Concentration (TGA)（mg/ml）	**DLS average Size（μm）**	**NPs size (XRD)（nm）**
VO_x	0.4	0.04	37
V-L	8.2	0.044	37
V-octa	4.3	0.048	39

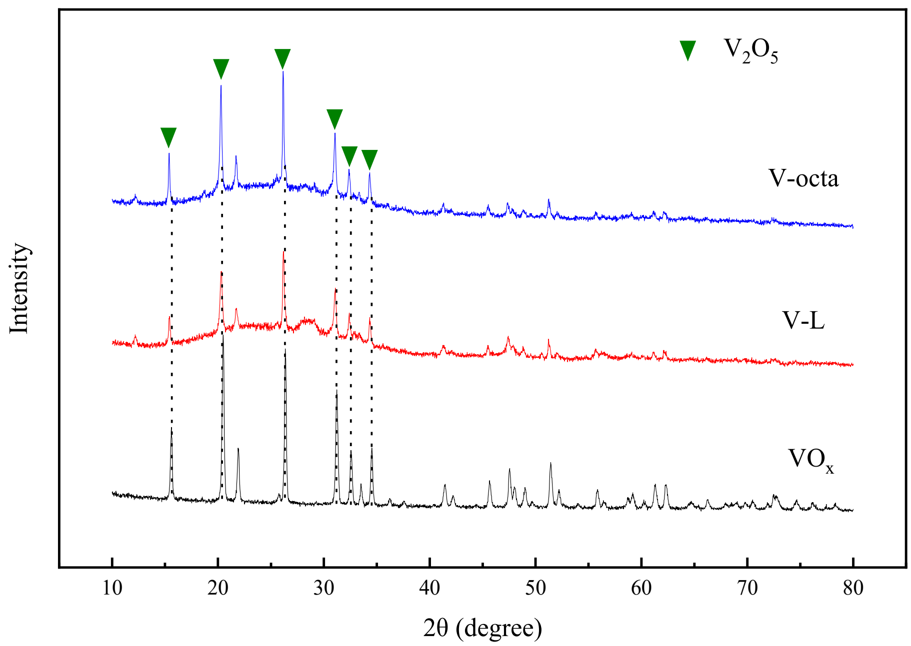

Figure 5.4. Powder XRD characterization of three V-based nanoparticles after calcination.

5.3.2 Electrolysis performance of Ni/YSZ cells modified by V oxide-based nanoparticles

Following the initial characterization of the three vanadium-based nanoparticle solutions, the solutions were infiltrated into Ni/YSZ electrodes to assess their electrolytic performance. The primary focus was on pure water electrolysis experiments. By varying the amounts of nanoparticles impregnated into the Ni/YSZ electrodes, the potential to enhance electrolytic performance was evaluated, and the optimal loading amount was determined.

Similar to the study of NiCe nanoparticles described in Chapter 4, the cells were characterized electrochemically using staircase linear scans, chronopotentiometry (CP), and galvanostatic electrochemical impedance spectroscopy (EIS). The staircase linear scan was performed over a voltage range of 0 to 2.5 V with a scanning rate of 5 mV/s. For CP, we applied a constant current of 25 mA for a duration of 300 seconds, ensuring sufficient time for the electrode to stabilize. Galvanostatic EIS was conducted immediately after the CP experiment, also at a current of 25 mA. The amplitude was set to 1/10 of the current, and the frequency range spanned from 1000 kHz to 0.05 mHz. During EIS, the scanning frequency was manually stopped upon observing any abnormal spectra.

The experimental results for Ni/YSZ cells infiltrated with the 3-type of vanadium oxide particles are summarized in Figure 5.5. From Figure 5.5a, b, and c, it is evident by all three measurement techniques that the addition of 50 μL and 100 μL of VO_x NPs do not improve, but rather deteriorate the performance of Ni/YSZ. Specifically, during the 2.5 V linear sweep, the performance decreases as the loading of VO_x nanoparticles increased, a trend also observed in the CP experiments. Similarly, in Figure 5.5c, the EIS data indicate an increase in polarization resistance (R_p), particularly for the sample loaded with 50 μL. Although there was a minor decrease in the ohmic resistances of the cells after infiltration, this reduction does not appear to be sufficient to positively impact the electrolysis performance.

In case of V-L NPs the electrolysis performance slightly deteriorates after infiltration remains almost unchanged as shown in Figure 5.5d, e, and f. Considering minor variations in cell loading and potential experimental system errors, it can be concluded that the infiltration of V-L nanoparticles had no significant impact on electrolysis performance.

Finally, for V-octa nanoparticles, as shown in Figures 5.5g, h, and i, performance appears to slightly deteriorate after infiltration. While there were no significant differences among the three samples during the linear sweep, the reference cell exhibited better performance in the chronopotentiometry (CP) tests. The impedance results in Figure 5.5i indicate a significant increase in total impedance for the 25 μL sample, and the 50 μL sample failed to complete the test.

Overall, these results do not demonstrate any promising effects on the performance of the Ni/YSZ electrode after infiltration with vanadium-based nanoparticles. It is important to note that these preliminary test experiments have certain limitations. For example, the actual concentrations of the three nanoparticle solutions differed, as determined by the synthesis yield, although the differences were not significant. Another unreported factor is viscosity, which varied among the solutions. This could be attributed to differences in synthesis temperature, duration, and the chemicals used. The variation in nanoparticle viscosity affected the consistency of the infiltration steps. Lastly, the long-term stability of the nanoparticle suspensions should be addressed. Despite being sealed and refrigerated, the VO_x sample became unusable after approximately 20 days, changing from a fully black solution to a white precipitate. The other two samples also showed very small amount precipitation over time. This phenomenon did not occur with the CeO_y and $NiCeO_x$ nanoparticles.

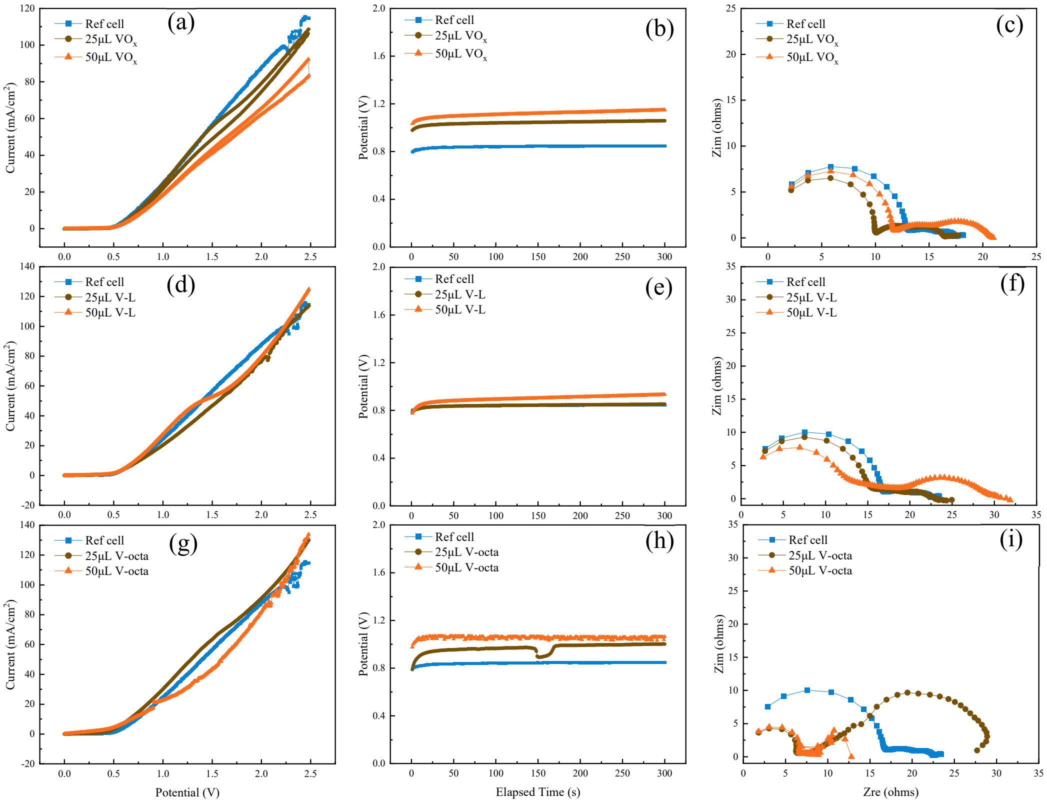

Figure 5.5. Characterization results of the electrochemical performance of three vanadium-based nanoparticles in the electrolysis of pure water, **a), b), c)** are the results of VO_x; **d), e), f)** represent the characterization results of V-L; Figures **g), h), i)** are the performance of V-L with the addition of octadecanol.

5.3.3 Characterization results of $VCeO_x$ and $CoCeO_x$ nanoparticles

After synthesizing and testing the electrochemical performance of vanadium-based nanoparticles, which did not yield promising results in terms of enhancing electrolysis performance, we shifted our focus to cerium-based nanoparticles, doped with vanadium and cobalt. $CeVO_4$ nanoparticles find application in catalysts, electrodes, sensors, lubricants, solar cells, hydrogen storage devices, and supercapacitors [449–455]. Using the previously described fabrication methods, we successfully synthesized vanadium-doped cerium nanoparticles and cobalt-doped cerium nanoparticles. After synthesis, the nanoparticles were calcined and characterized using X-ray diffraction (XRD). As shown in Figure 5.6, the XRD patterns of the vanadium-doped cerium nanoparticles revealed not only the characteristic peaks of cerium dioxide but also peaks corresponding to other components, primarily the complex crystal structure of $CeVO_4$ [455]. The average nanoparticle size as calculated by the XRD patterns is approximately 12.9 nm.

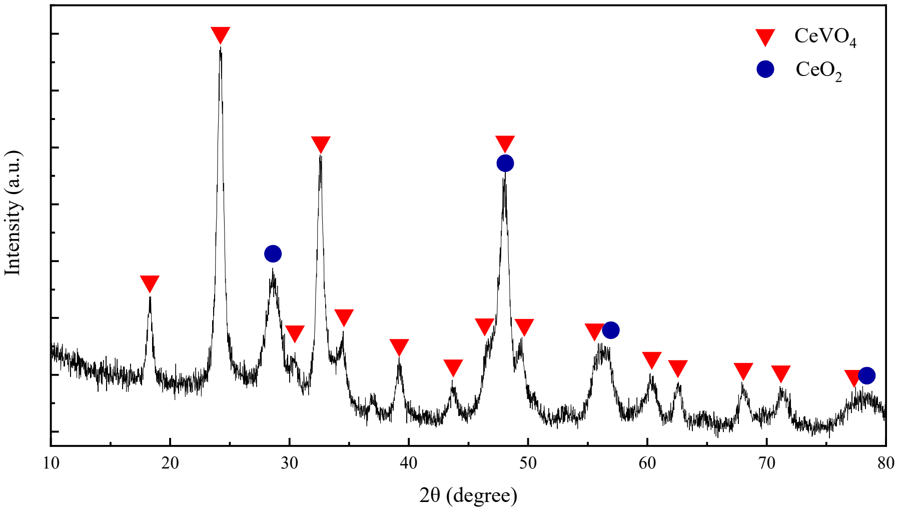

Figure 5.6. XRD data of VCe NPs after calcination

The XRD patterns of the cobalt-doped ceria NPs in Figure 5.7 no distinct cobalt-related peaks are observed. The average nanoparticle size is about 4.5nm. This suggests that cobalt was well-incorporated into the cerium oxide lattice. According to the literature, the characteristic peaks of cobalt-doped nanoparticles diminish in intensity as the cobalt doping level increases, compared to undoped CeO_2. This reduction in peak intensity indicates successful doping of Co ions into the CeO_2 lattice. The ionic radius difference between CeO_2 and Co-doped CeO_2 is likely responsible for the observed decrease in peak intensity. Thus, the XRD results confirm that cobalt is effectively doped into the cerium nanoparticles, potentially enhancing their properties without forming separate cobalt oxide phases.

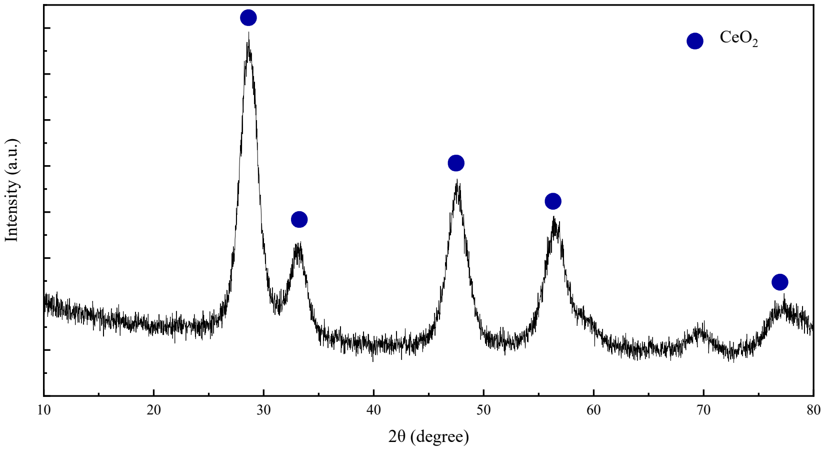

Figure 5.7. XRD data of CoCe NPs after calcination

5.3.4 Effect of V and Co doping on the redox properties of CeO_y nanoparticles

The surface state of doped CeO_y nanoparticles, was studied by NAP-XPS experiments under 1 mbar of H_2 at the HIPPIE beamline of the MAX IV synchrotron in Sweden. We selected temperatures from 200 °C to 800 °C and a heating rate of 10 °C/min. After reaching the set temperature, the samples were measure by XPS immediately. Stability tests showed that the spectra remained almost identical at a certain temperature for at least hour. To compare with previous studies, we also introduced $NiCeO_x$ NPs and CeO_y NPs alongside VCe and CoCe NPs for testing. The oxidation state of ceria, was estimated from the Ce 3d peak fitting and expressed as the mean ceria valence. According to the results shown in Figure 5.8, the four types of nanoparticles exhibit different surface reducibility. Notably, VCe nanoparticles show the most distinctive behavior. They undergo rapid reduction between 200 ℃ and 400 ℃, and by 400 ℃ to 600 ℃, they are almost completely reduced to trivalent Ce.

In contrast, CeO_y nanoparticles display the most gradual and consistent reduction curve, with a nearly uniform slope throughout the entire temperature range. Interestingly, if we focus on the NiCe and CoCe nanoparticles, their reduction curves closely resemble that of Ce up until about 500 ℃. The sharp change occurs between 500 ℃ and 550 ℃, where the presence of Ni and Co elements causes a rapid reduction of Ce. From 550 ℃ to 800 ℃, the reduction trends of both NiCe and CoCe nanoparticles become much more gradual. The reduction curves of these nanoparticles remain largely consistent with the overall trend up to 700 ℃ to 800 ℃.

From these observations, we can conclude that both Ni and Co dopings enhance the reduction ceria NPs. Notably, VCe NPs nanoparticles exhibit superior reducibility, achieving nearly complete reduction to Ce^{3+} at temperatures as low as 400 °C.

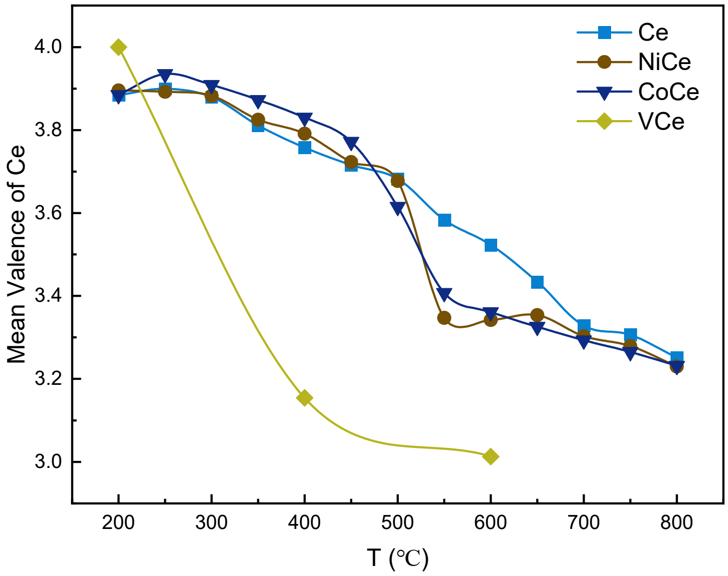

Figure 5.8. Fitting result of NiCe, CoCe and VCe nanoparticles' effect on redox property of Ceria

5.3.5 Electrolytic performance of Ni/YSZ modificatied by $VCeO_x$ and $CoCeO_x$ NPs

The influence of V and Co-doped ceria NPs on the water electrolysis performance of Ni/YSZ electrodes was investigated next. The NPs were prepared using a similar infiltration method as described for NiCe NPs. The performance of electrodes with two different NP loadings was evaluated using staircase linear sweep voltammetry, CA, and electrochemical impedance spectroscopy. For the CoCe-modified cells the staircase linear scan experiments (Figure 5.9a) demonstrated an increase of current density up to 50% at 1V compared to the unmodified Ni/YSZ reference cell. Doubling the loading of CoCe nanoparticles did not lead to any significant improvement in electrolysis performance. Following this, we carried out CA (chronoamperometry) experiments by applying a constant voltage of 1 V for 300 seconds. The results aligned with those from the Staircase linear scan, showing that while the performance improved after the infiltration of CoCe nanoparticles relative to the reference sample, further increasing the infiltration amount did not lead to significant current enhancement.

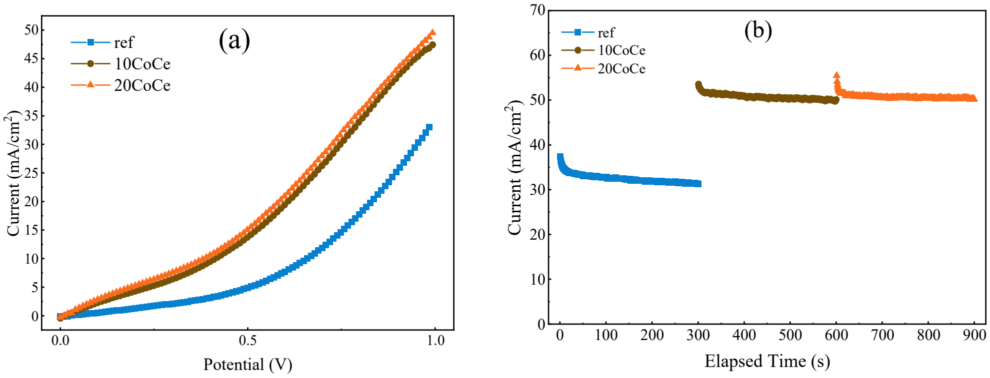

Figure 5.9. a) H_2O + H_2 Staircase linear scan electrolysis experimental results of CoCe NPs with different loading amounts; **b)** CA electrolysis results of H_2O + H_2 with different loadings of CoCe NPs. Please note that different loadings of NPs solution were impregnated on the same Ni/YSZ electrode.

The impedance spectroscopy results in Figure 5.10 show that the reference sample has the highest ohmic (R_{ohmic}) and the lowest polarization resistance (R_p) among the three. As the infiltration amount of CoCe nanoparticles increases, the R_{ohmic} decreases while the R_p increases. This trend contrasts with the results observed for NiCe NPs infiltration, suggesting that the mechanism enhancing electrochemical performance is closely related to the specific dopant ion in ceria.

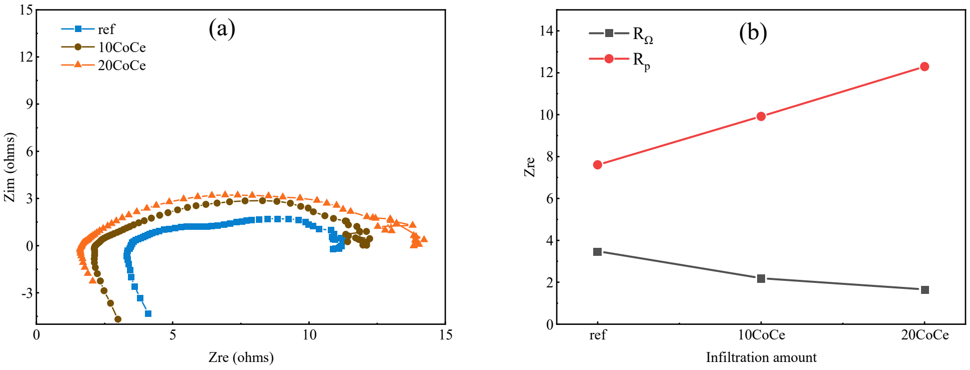

Figure 5.10. a) EIS of H_2O + H_2 results with different CoCe NPs loadings; **b)** R_{ohmic} and R_p calculated based on the EIS. Please note that different loadings of NPs solution were impregnated on the same Ni/YSZ electrode.

In the VCe-modified Ni/YSZ cells, the staircase linear scan and CA tests shown in Figure 5.11 indicate a decline in electrolysis performance following infiltration. As the VCe loading amount increases, the performance further deteriorates.

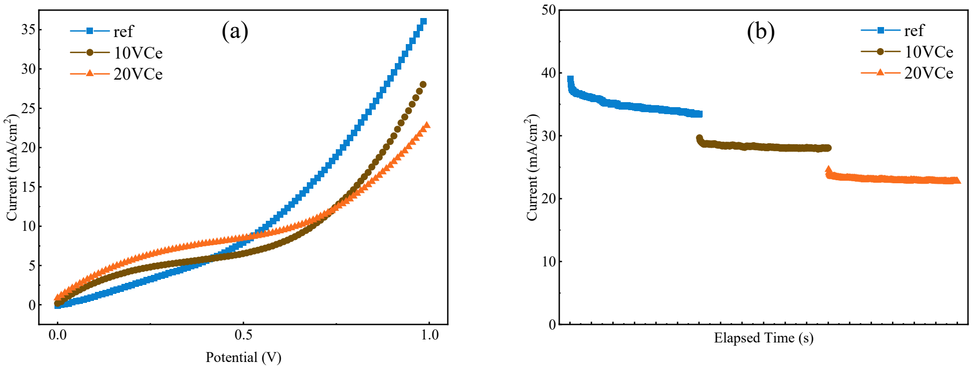

Figure 5.11. a) $H_2O + H_2$ Staircase linear scan experimental results of different loading amounts of VCe NPs; **b)** CA electrolysis results of $H_2O + H_2$ with different loadings of VCe NPs Please note that different loadings of NPs solution were impregnated on the same Ni/YSZ electrode.

This trend became more pronounced in the impedance spectroscopy results (Figure 5.12). As the loading of VCe nanoparticles increases, the ohmic resistance remained relatively unchanged, while the polarization resistance increased sharply with the infiltration amount, reaching 38Ω.

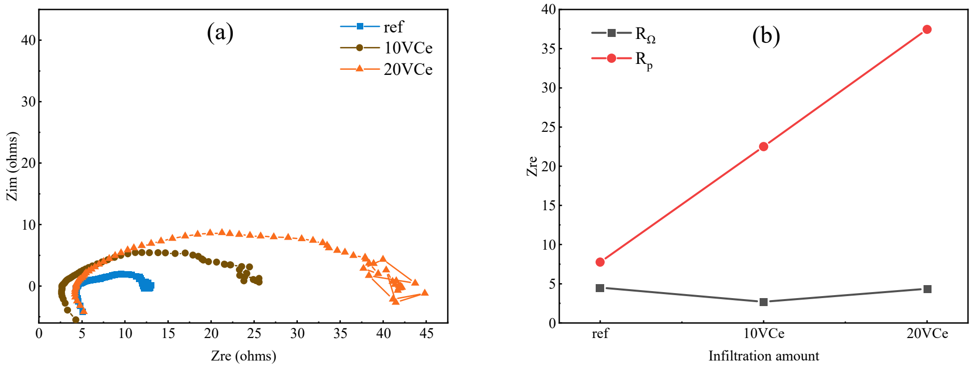

Figure 5.12. a) EIS of $H_2O + H_2$ results with different VCe NPs loadings; **b)** R_{ohmic} and R_p calculated based on the EIS. Please note that different loadings of NPs solution were impregnated on the same Ni/YSZ electrode.

5.3.6 In situ XAFS Investigation of NPs effect on the Ni/YSZ Reducibility

In this section, Ni/YSZ electrodes, both with and without NPs modification, are investigated using in situ X-ray Absorption Fine Structure (XAFS) to assess the impact of these NPs on the reducibility of Ni within the Ni/YSZ cermet electrode. The samples examined included unmodified Ni/YSZ, as well as Ni/YSZ modified with 5Ce, 40CoCe, 80NiCe, and 40VCe (sample codes follow the abbreviations used throughout this manuscript). Prior to XAFS measurements, each sample underwent electrolysis in the setup described in Section 5.2.5, and was calcined in a muffle furnace at 600°C (heating rate of 10°C/min) for one hour before being introduced into the XAFS cell. After recording XAFS spectra at room temperature, the temperature raised to 480 ℃ with a rate of 8 ℃/m in 1 bar H_2 while the Ni K-edge was recorded continusly during heating. Three consequitive scans were taken at 480 ℃ to confirm that the sample attained the equilibrium state. Data analysis was carried out by the "Analysis Toolkit for XAS data" using normalization parameters such as energy shift (ΔE_0), pre-edge range, and norm range corresponding to those used in the Athena and Larch software packages.

Figures 5.13a and 5.13b display characteristic Ni K-edge XANES and FT-EXAFS spectra, respectively, for a Ni/YSZ electrode infiltrated with CeO_2 nanoparticles (5Ce), recorded across a temperature range from 25°C to 480°C. A qualitative comparison in the XANES region (Figure 5.13a) between the Ni/YSZ sample and the reference spectra for NiO (black) and Ni^0 (gray) reveals that, at room temperature, the sample spectra closely resemble to those of Ni^0 phase. However, the prominent white line, particularly visible at room temperature, suggests the coexisting of NiO phase. It should be noted that the rising edge of the Ni K-edge spectra for the 5Ce Ni/YSZ electrode appears more intense than that of the metallic reference. This increased intensity is attributed to the high Ni concentration within the Ni/YSZ electrode (approximately 60%), which is known to cause distortions in fluorescence spectra [456].

In the FT-EXAFS magnitude plot (Figure 5.13b), peaks corresponding to scattering from metallic Ni^0 (Ni-Ni_{Ni}) are clearly observed. Additionally, smaller yet distinct peaks associated with Ni-O scattering from oxidized NiO (Ni-O_{NiO}) and Ni-Ni from NiO (Ni-Ni_{NiO}) interactions are present [457,458], confirming that nickel exists in a mixed oxidation state of metallic Ni and NiO. As the temperature increases, the intensity of these spectral bands decreases, which is consistent with expectations, as higher temperatures increase the Debye-Waller factor, thereby reducing the intensity of these coordination shells [459,460].

Figure 5.13c illustrates the relative abundance of Ni^0 and NiO, estimated by linear combination fitting (LCF) of Ni K-edge XANES spectra, using reference peaks for Ni^0 and NiO. As evident, the reduction of NiO procceds in two distinct steps, beginning at approximately 300°C and 450°C, respectively. It should be noted that while LCF analysis qualitatively captures the evolution in the NiO reduction in H_2, it lacks precision in determining the absolute Ni oxidation state due to uncertainties in the utilized reference spectra.

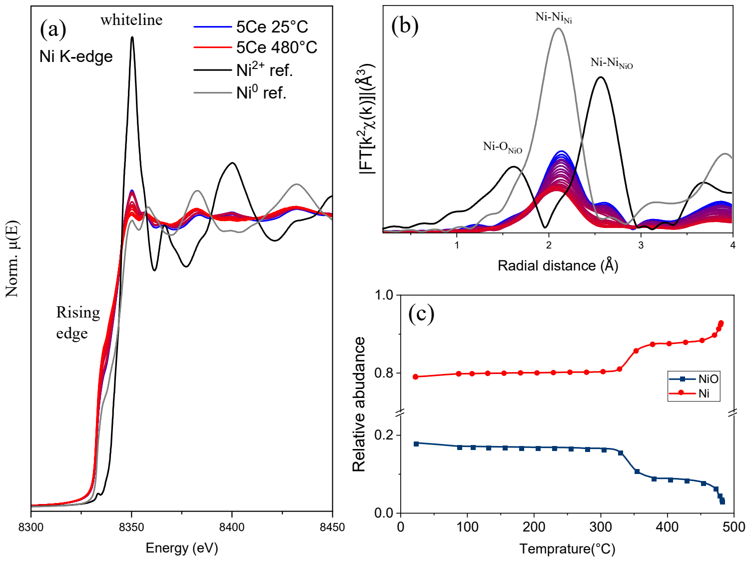

Figure 5.13. a) Ni references and the Ni/YSZ electrode infiltrated with CeO_2 nanoparticles, showing Ni K-edge XANES from room temperature (RT) to 480 °C; **b)** Modulus of the Fourier transform of the k3-weighted Ni K-edge EXAFS for the Ni reference (black and gray) and the temperature-programmed reduced Ni/YSZ electrode infiltrated with CeO_2 (colored); **c)** Relative abundance of Ni^0 and NiO in the sample calculated via Linear Combination Fitting (LCF) using reference spectra.

To compare the effect of various infiltrated NPs on nickel reducibility, the XANES and FT-EXAFS spectra of all samples measured at 25°C and 480°C are plotted in Figure 5.14a and 5.14b, respectivelly. In the FT-EXAFS plots, the Ni-Ni path of Ni^0 are labeled as P1 ($Ni\text{-}Ni_{Ni}$) and the Ni-Ni paths of NiO as P2 and P3. The XANES specrta in Figure 5.14a show a prominent rising edge, which is more pronounced in the infiltrated electrodes compared to the reference Ni/YSZ sample. This is followed by an equal decrease of the white line intensity after infiltration, suggesting a higher concentration of Ni^0 in the infiltrated electrodes after calcination at 600 °C. The EXAFS graphs in the inset of Figure 5.14a further confirmed this, with the P1 peak, being most prominent in the impregnated samples. These finding indirectly indicate that NPs infiltration enhances the resistance of Ni/YSZ to oxidation in oxidative conditions, which is a highly desired propertly for Ni/YSZ electrodes in electrolysis applications.

At 480 °C in H_2 (Figure 5.14b), both the XANES and FT-EXAFS spectra are characteristic of Ni^0, showing that all samples are almost fully reduced under the employed conditions.

However, closer inspection of the FT-EXAFS peaks in the inset suggests that a small portion of nickel remains unreduced in some samples, as will be discussed in more detail below.

Figure 5.14c shows the evolution of NiO fraction with temperature for all five samples, as determined by LCF analysis of the Ni K-edge. As noted earlier, determining the absolute Ni oxidation state using LCF analysis is challenging. Therefore, the focus is on comparing reduction profiles of different cells to show the impact of infiltrated NPs on the Ni/YSZ electrode's reducibility. Figure 5.14c clearly shows that at 25°C, the NiO content across the various electrodes ranges from 20% to 40% (see also Table 5.2). Although all samples were subjected to the same calcination conditions prior to the absorption experiments, differences in prior electrolysis tests, NP loading, and the duration of air exposure prior to XAFS measurements make it difficult to draw precise conclusions about the influence of each NPs type, from this observation. However, it is evident that NP infiltration consistently enhances the oxidation resistance of Ni/YSZ.

Examining the evolution of NiO reduction with temperature more closely reveals that it occurs in at least two distinct stages for each sample. The first stage is marked by a rapid decrease in NiO content over a narrow temperature range, indicating a kinetically fast reduction process. In contrast, as the temperature continues to rise, the reduction rate slows down and extends over a broader temperature window. Notably, the reduction profile of the CeO_2-modified electrode deviates from the typical two-stage pattern observed in the other samples, exhibiting a third slope after 475 °C. When comparing the onset temperarture of NiO reduction—an indicator of the reducibility of the five samples—the order is as follows: NiCe > CeO_2 ~ CoCe > Ref > VCe (see also Table 5.2). This comparison illustrates that, with the exception of the VCe-modified electrode, nanoparticle modification shifts the onset of NiO reduction in Ni/YSZ to lower temperatures, thereby facilitating the reduction process.

Finally, at around 480 °C, the highest reduction temperature employed in this study, slight differences in the remaining NiO amounts across the electrodes are observed (see Figure 5.14d). Specifically, as shown in Table 5.2, while the NiCe sample is fully reduced, approximately 4% of NiO remains in the CeO_2-modified Ni/YSZ electrode.

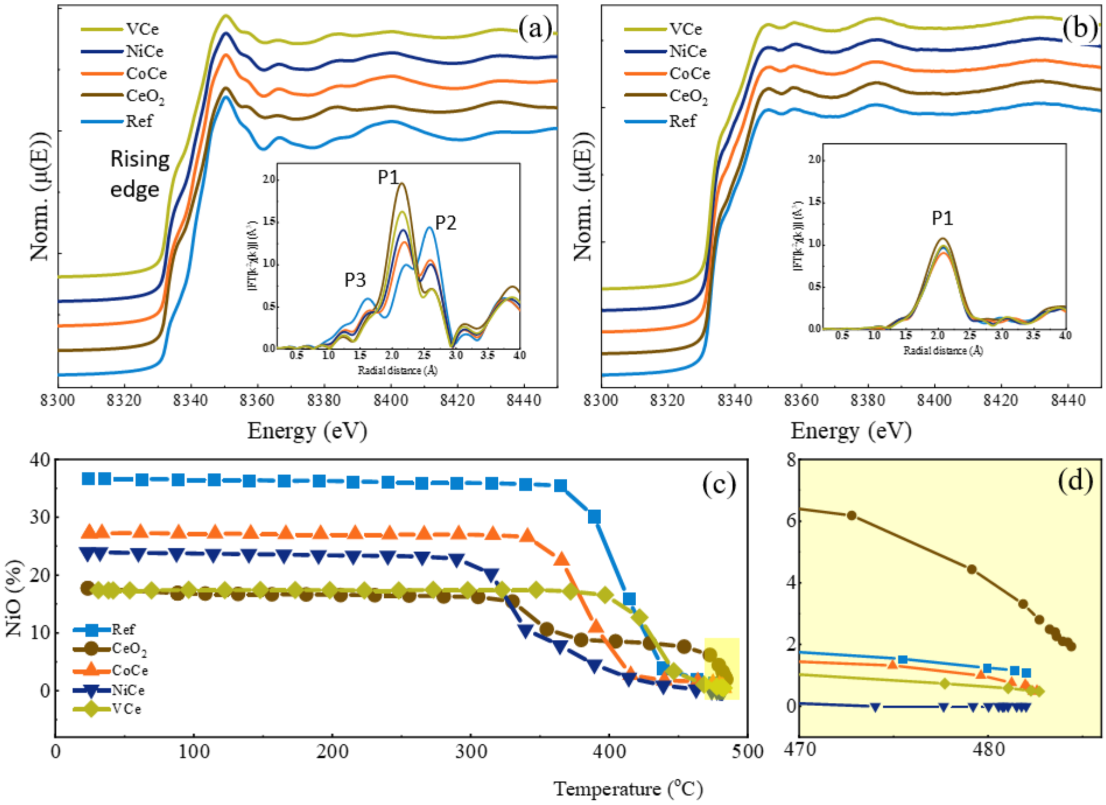

Figure 5.14. (a) XANES and FT-EXAFS for five samples measured at room temperature; **(b)** XANES and FT-EXAFS for the same five samples measured at 480 °C; **(c)** Temperature dependence of the NiO obtained by the LCF analysis of XANES spectr. **(d)** Zoom at the high temperature region of graph (c).

Table 5.2. Critical parameters obtained by the XAFS spectra analysis

Electrode	%NiO (@25 °C)	%NiO (@480 °C)	Onset temperature of NiO reduction (°C)
VCe-Ni/YSZ	18	1	400
NiCe-Ni/YSZ	24	0	290
CoCe-Ni/YSZ	27	1	340
CeO_2-Ni/YSZ	18	4	330
Ni/YSZ	37	1	360

5.3.7 NPs Characteristics and their influence on Ni/YSZ Reducibility

As mentioned earlier, the oxidation of nickel in Ni/YSZ electrodes is a major contributor to cell degradation in SOEC applications. The reducibilities of ceria-based NPs and NiO in the Ni/YSZ, are determined from the NAP-XPS and XAFS experiments respectively. Figure 5.15 correlates the NiO fraction at 480 °C and the NiO reduction onset temperature shown in Table 5.2, with the oxidation state of cerium in the NPs taken from Figure 5.8. It is important to note that although the conditions under which the samples were treated in the two sets of measurements are fundamentally different, the obtained results presented reflect the trends in the reducibility of both ceria-based NPs and NiO, and thus can be utilized for a phenomenological analysis of the reduction process. The graph in Figure 5.15 resembles an inverse volcano plot, with the NiCe-modified electrode situated at the minimum. This indicates that highly reducible NPs, such as VCe, and very stable NPs, such as CeO_2, do not facilitate the reduction of NiO in Ni/YSZ. It appears that there is an optimal level of ceria reducibility, which in our case is achieved by the NiCe NPs, optimizing conditions for NiO reduction.

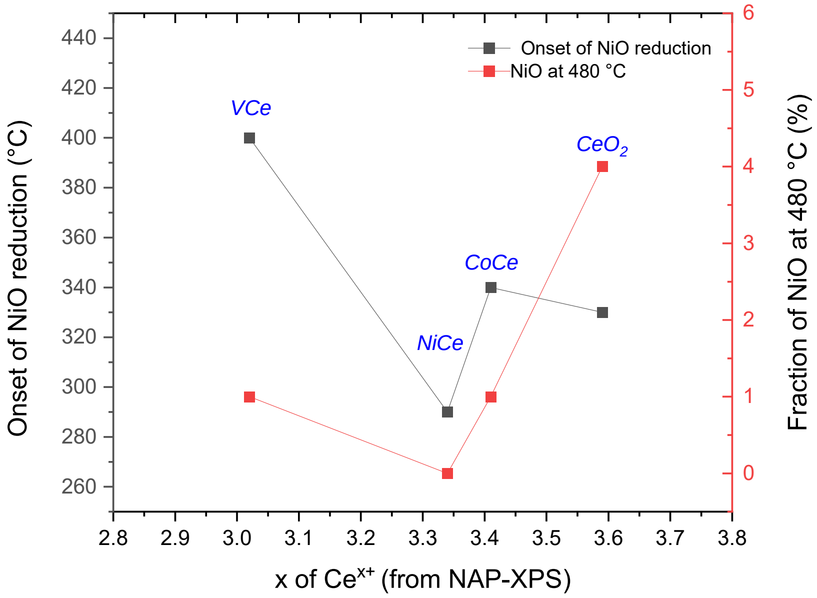

Figure 5.15. Correlation of the cerium oxidation state (x of Ce^{+}) in the Ce-based nanoparticles (x-axis), obtained from NAP-XPS measurements at the characteristic temperature of 550 °C (Figure 5.8), with the onset temperature of NiO reduction (left y-axis) and the fraction of NiO remaining at 480 °C (right y-axis), as retrieved from XANES spectra and detailed in Table 5.2.

The presence of NPs at the surface of Ni/YSZ may influence the reducibility of NiO particles through two primary mechanisms. The first mechanism involves the facilitation of H_2 adsorption and activation, while the second is a solid-state interaction where NiO is reduced by the migration of oxygen ions towards the NPs. Such interface interactions between oxides are rather common and are driven by differences in oxygen affinity between the two phases. Considering that the amount of infiltrated NPs is relatively minor compared to the NiO mass in the electrode, if solid state interactions contributes to the reduction mechanism, it is likely to initiate reduction by removing oxygen from NiO surface, creating Ni^0, which is known to be much more efficient for H_2 activation, thus accelerating the reduction process.

Those mechanism can rationalize the lower NiO reducibility of CeO_2-infiltrated electrodes, since CeO_2 is mostly hard to reduce as compared to other NPs types. However, a question arises as to why VCe NPs, which is the easiest to reduce among the NPs, shifts the NiO reduction onset at higher temperatures. Several factors could explain this behavior. First, VCe nanoparticles may be highly dispersed over the nickel particles, creating a sort of "protective" surface layer that restricts access of H_2 to NiO. Another possible explanation is that, at lower temperatures, the adsorbed surface H_2 is primarily consumed to reduce VCe, and only at higher temperatures, when VCe is nearly fully reduced, does it react with NiO to form Ni^0.

Regardless of the mechanism by which infiltrated NPs influence the reduction of NiO, experimental results show that the NPs that optimally enhance NiO reducibility—namely NiCe and CoCe—also promote the electrolysis reaction, indicating a correlation between these two phenomena.

5.4 Conclusion

Overall, this chapter investigates the effect of infiltrating various NPs on the water electrolysis performance of Ni/YSZ electrodes. The results show that the performance of Ni/YSZ either deteriorates or improves only slightly after infiltration with VO_x, V-doped, and undoped CeO_2 NPs. In contrast, $CoCeO_x$ NPs seem to enhance performance, although to a lesser extent than $NiCeO_x$ NPs. In situ characterization techniques were employed to correlate the reducibility of NiO and the infiltrated NPs with this behavior. Future work should focus on refining infiltration procedure and possibly using ceria NPs with different metal dopants, to maximize the electrolysis performance of Ni/YSZ electrodes.

This page intentionally left blank

Chapter 6. The surface state of Pr-GDC and LSCF type O_2-electrodes after long-term electrochemical testing

6.1 Introduction

The mixed ionic-electronic conductor (MIEC) $La_{0.6}Sr_{0.4}Co_{0.2}Fe_{0.8}O_{3-\delta}$ (LSCF), which has a perovskite structure as shown in Figure 6.1, is widely used as an oxygen electrode in solid oxide cells (SOCs) [461]. LSCF is favored due to its excellent electrical conductivity (~250 S cm^{-1} at 800 °C) [462], oxygen ion conductivity (~0.2 S cm^{-1} at 900 °C), and high electrocatalytic activity for the oxygen reduction reaction (ORR) [463]. Like in SOFC applications, LSCF is also one of the most commonly used materials in SOECs.

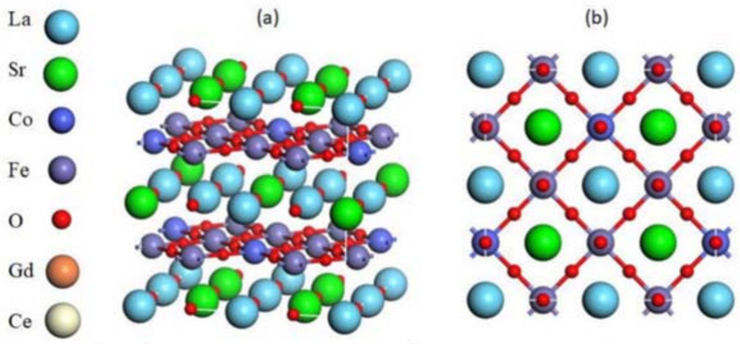

Figure 6.1. a) Side and **b)** top view of the LSCF bulk structure. Reproduced with permission of Ref. [464], Copyright of ©2018 IOP

However, LSCF's coefficient of thermal expansion (CTE) reaches up to 27.4×10^{-6} K^{-1} between 650 and 900 °C [465], which is incompatible with conventional electrolytes such as $Gd_{0.1}Ce_{0.9}O_{1.95}$ (GDC, 12.5×10^{-6} K^{-1}) and $Zr_{0.85}Y_{0.15}O_{1.93}$ (YSZ, 10.5×10^{-6} K^{-1}) [466], leading to significant thermal stresses. To mitigate these thermal stresses and improve compatibility at the electrode-electrolyte interface, ceria-based materials are often combined with LSCF to form composite electrodes, which reduce the overall CTE in most studies. Additionally, since ceria-based materials exhibit fast bulk oxygen ion conductivity, the incorporation of an ion-conducting phase further enhances the reaction kinetics of the composite electrode [467].

Single cells with LSCF electrodes can achieve significant output in the intermediate temperature range, but their long-term stability remains a challenge [468–470]. One of the critical factors limiting the development of LSCF cathodes is performance degradation caused by Sr segregation induced by thermal and electronic factors [10,11,471]. The detrimental effects of Sr segregation on LSCF-based electrodes have been extensively studied and well-documented [472,473]. Simner et al. reported significant performance degradation in an anode-supported YSZ thin-film/GDC barrier layer LSCF cell after 500 hours of operation at 750 °C, and observed Sr segregation on both the inner and outer surfaces of the LSCF electrode [474]. During operation, Sr-rich phases, which exhibit high resistance to the oxygen reduction reaction

(ORR), tend to form on the cathode surface. As a result, the active sites on the surface of the LSCF cathode are gradually occupied by SrO or $Sr(OH)_2$ islands, slowing down the ORR process [475]. Wang et al. investigated the effect of polarization on Sr segregation and diffusion in LSCF electrodes, and observed the formation of $SrZrO_3$ at the GDC/YSZ interface after 400 hours of polarization at 1000 °C, even with the use of a GDC barrier layer [476]. SrO surface segregation can occur under both open-circuit and polarized conditions [12,159,477]. It is well-known that electrochemical polarization significantly influences Sr segregation on the surface of porous LSCF electrodes, with segregated Sr tending to penetrate through the ceria barrier layer to react with the YSZ electrolyte, forming an insulating $SrZrO_3$ phase [12]. However, despite the importance of Sr segregation and interface formation in SOFCs, a systematic study on the mechanisms of polarization-induced interface formation and Sr segregation/diffusion in LSCF has yet to be conducted.

Reversible solid oxide fuel cells (RSOFCs) function as solid oxide fuel cells (SOFCs) to generate electricity from hydrogen, and as solid oxide electrolysis cells (SOECs) to store excess electrical energy as chemical energy (e.g., hydrogen) [478–480]. In the development of novel electrode materials for such applications, those containing Pr cations have demonstrated excellent electrocatalytic performance. Praseodymium oxide (Pr_6O_{11}) has been explored as a potential electrocatalyst for the oxygen reduction reaction (ORR) in fuel cell applications [481]. For example, LSM-YSZ electrodes coated with PrO_x showed an 89% reduction in polarization resistance at 650 °C (compared to untreated electrodes), maintaining a tenfold decrease even after approximately 400 hours of operation [482]. Additionally, the use of Pr_6O_{11} nanocatalysts to enhance and optimize the performance of $La_{0.5}Sr_{0.5}Fe_{0.9}Mo_{0.1}O_{3-\delta}$ (LSFM) oxygen electrodes for RSOC significantly improved the catalytic activity for oxygen reactions [483,484], indicating that LSFM containing Pr_6O_{11} nanocatalysts is a promising RSOC oxygen electrode material.

In this chapter, we will discuss the interlayer characteristics of these two types of oxygen electrodes and compare the changes observed before and after long-term experiments. The goal is to gain more valuable insights into the surface characteristics these electrode materials.

6.2 Experimental

6.2.1 Cell and O_2-electrode description

The cells analysed in this chapter were provided by Dr. Jérôme Laurencin's group at Univ. Grenoble Alpes, CEA, Liten, DTCH, 38000, Grenoble, France. The hydrogen electrode-supported cells were fabricated at CEA Le Ripault and have a typical configuration comprising a dense ceramic electrolyte sandwiched between two porous electrodes. All cells underwent electrochemical testing at CEA Liten, before being transferred to our group for detailed surface spectroscopy analysis. Further information regarding the experimental setup and testing protocols can be found in ref [484]. This chapter describes the analysis of two types of electrolyte-supported cells, both with similar geometry, as schematically illustrated in Figure 6.2 However, the cells differ in the composition of the O_2-electrode. The composition and fabrication process of the cells have been previously detailed in references [484–486], while the specific composition of the O_2-electrode and the treatment it underwent prior to the photoemission measurements are provided in Table 6.1.

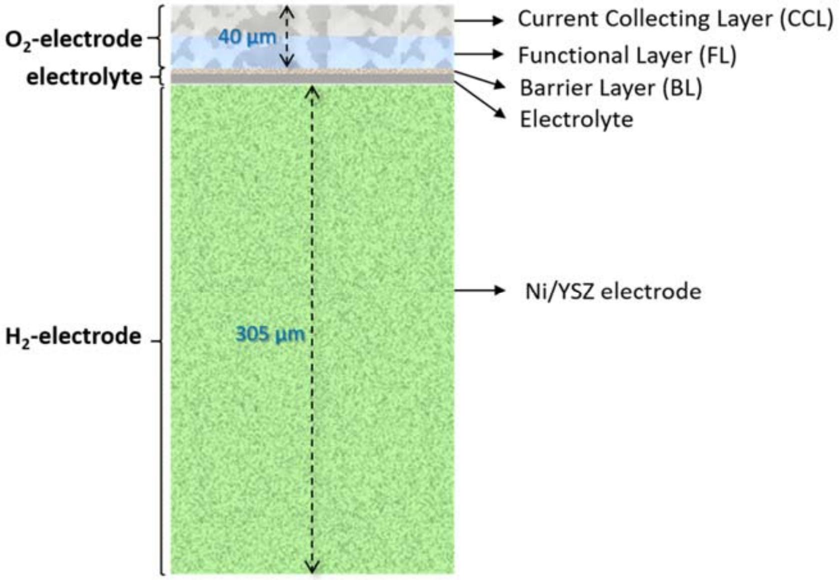

Figure 6.2. Schematic representation of the cell configuration analyzed using surface-sensitive methods in this chapter. The cells are H_2-electrode supported, with the O_2-electrode featuring a double-layer architecture.

As shown in Figure 6.2 the porous O_2-electrode of all studied cells was fabricated using a double-layer architecture, with each of the two layers optimized for a specific function. The top layer, known as the current collecting layer (CCL), was designed to enhance electron conductivity with the current collector plates. The layer beneath the CCL, located closer to the electrolyte, was optimized for electrocatalytic activity and is referred to as the functional layer (FL). Two different O_2-electrode compositions were investigated, as detailed in Table 6.1. The total thickness of O_2-electrode was approximately 40 µm, with a 3 µm thick porous GDC barrier layer (BL) deposited between the O_2-electrode and the electrolyte. The electrolyte was

$Y_{0.16}Zr_{0.84}O_{1.92}$ (8YSZ) with a thickness about 8 µm. The porous H_2-electrode was a Ni-YSZ composite, consisted of two layers with a total thickness of around 300 µm. For each electrode type, one set of photoemission experiments was conducted on a cell immediately after the reduction pretreatment, i.e., before electrochemical testing, and a second set was performed on a cell after long-term electrochemical testing. It is important to note that the two initial cells in both cases were identical.

Table 6.1. Description of the samples measured by surface techniques

	O_2-electrode Composition	Treatment	Notation
Cell 1	**CCL:** $LaNi_{0.6}Fe_{0.4}O_3$ (LNF) **FL:** PrO_x-$Ce_{0.9}Gd_{0.1}O_{2-\delta}$ (Pr-GDC)	**H_2-electrode** gas: H_2/H_2O 10/90 %vol. (12 $NL\cdot h^{-1}$) **O_2-electrode** gas: dry air (36 $NL\cdot h^{-1}$) **Temperature**: 750 °C **Current Density:** −1 Acm^{-2} (SOEC)	Pr-GDC_{REF}
Cell 2		**H_2-electrode** gas: H_2/H_2O 10/90 %vol. (12 $NL\cdot h^{-1}$) **O_2-electrode** gas: dry air (36 $NL\cdot h^{-1}$) **Temperature**: 750 °C **Current Density:** −1 Acm^{-2} (SOEC) **Duration**: 3600 hours.	Pr-$GDC_{3.6k}$
Cell 3	**CCL:** $La_{0.6}Sr_{0.4}Co_{0.2}Fe_{0.8}O_{3-\delta}$ (LSCF) **FL:** $La_{0.6}Sr_{0.4}Co_{0.2}Fe_{0.8}O_{3-\delta}$- $Ce_{0.8}Gd_{0.2}O_{2-\delta}$ (LSCF-GDC, 50:50%)	**H_2-electrode** gas: H_2 (4 $NL\cdot h^{-1}$) **O_2-electrode** gas: dry air (4 $NL\cdot h^{-1}$) **Current Density:** 0 Acm^{-2} **Temperature**: 800 °C **Duration**: 16 hours.	$LSCF_{REF}$
Cell 4		**H_2-electrode** gas: H_2/H_2O 10/90 %vol. (12 $NL\cdot h^{-1}$) **O_2-electrode** gas: dry air (36 $NL\cdot h^{-1}$) **Temperature**: 750 °C **Current Density:** −1 Acm^{-2} (SOEC) **Duration**: 5000 hours.	$LSCF_{DRY}$

6.2.2 Overview of MAX IV Synchrotron-Based Apparatus and measurement conditions

NAP-XPS measurements were performed at the HIPPIE beamline endstation of the MAX IV synchrotron facility [278], as detailed in Section 2.3.2 of this thesis. To access both the CCL and FL regions of the electrode for photoemission measurements, the upper section of the electrode was removed by mechanical scraping. During the measurements, the analyzer's nozzle was positioned approximately 300 µm above the sample, enabling precise visual identification of the measurement spot with the help of a high-resolution optical camera installed in the analysis chamber. The analysis area in the photoemission measurements is determined by the synchrotron beam spot size, which forms a parallelogram measuring 60 μm × 25 μm. All measurements were conducted with the sample at 350 °C in 1 mbar O_2, conditions sufficient to prevent electrostatic charging of the sample and to maintain an oxidizing environment during the measurements. Unless otherwise specified 10 °C/min, linear temperature ramps were applied during heating to 350 °C.

XPS peak fitting was performed using CasaXPS software (version 2.3.25). Shirley backgrounds were predominantly used for background subtraction; however, for spectra where gas-phase interference caused an increasing background, linear backgrounds were employed. Due to the presence of overlapping spectral components, peak positions and profiles were first determined using selected measurements where these components were dominant. Subsequently, data sets were fitted, with these parameters either fixed or allowed to vary within narrow limits. The surface analysis of the samples was conducted using both survey and high-resolution spectra. Depending on the photoelectron peak intensity, the signal-to-noise ratio of the survey spectra ranged from 2 to 60, while the high-resolution spectra ranged from 8 to 90. The survey spectra were used for quantifying surface composition, while the high-resolution scans were employed to determine the chemical state of the sample. Survey scans offer a shorter measurement time (approximately 4 minutes per spectrum) and help avoiding uncertainties related to photon flux, or possible signal instability, common drawbacks when using high-resolution spectra for quantification. However, survey spectra generally have a lower signal-to-noise ratio and are subject to uncertainties due to variations in the scattering of photoelectrons from different peaks in the gas phase, which can affect the accuracy of quantification. We assume any errors due to this fall within the provided error margins for quantitative calculations (±10%). Moreover, since the quantification error is systematic, the comparisons between samples in this study remain reliable.

6.3 Results and discussion

6.3.1 Analysis of praseodymium oxide (PrO_x) based electrodes

6.3.1.1 Sample preparation and mounting

In the cross-sectional SEM/EDS elemental maps of the LNF/Pr-GDC cell shown in Figure 6.3a, the distinct layers of the O_2-electrode are clearly visible, along with the sharp interfaces between them. The Pr-GDC_{REF} and Pr-$GDC_{3.6k}$ electrodes were mounted together on a stainless-steel flag style sample plate (Figure 6.3b), and secured using a top lead with two holes at its center to allow access to the area of interest for photoemission measurements. Prior to the mounting on the sample plate, part of the top CCL layer of the electrode was mechanically scrubbed off to expose the FL layer underneath. The scrubbed areas appear darker in the optical images shown in Figure 6.3b. To ensure the reproducibility of the analysis, several spots in both the CCL and FL electrode areas of each electrode were measured, indicated by small round markers in Figure 6.3b.

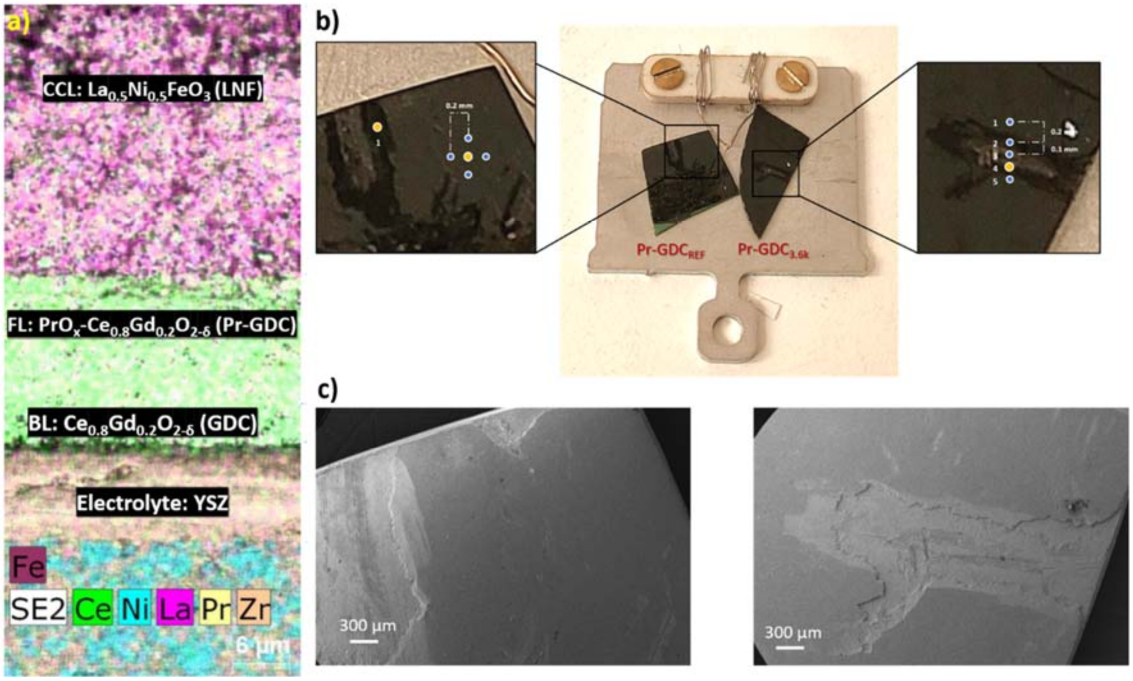

Figure 6.3. (a) Cross-sectional SEM/EDS micrographs with elemental mapping, illustrating the different layers of the LNF/Pr-GDC-based cell. The micrograph was provided by CEA, Liten **(b)** An optical camera photograph of the sample holder showing the two samples positioned on it, with visible the thermocouple wires, while the top lead has been removed to provide a clearer view of the samples. At the left and right part of the image magnified optical images where the NAP-XPS measurements spots for each sample are indicated by cycles can be seen **(c)** SEM micrographs taken from the same areas of the samples as the optical photographs.

6.3.1.2 Quantification of the surface composition by NAP-XPS

Characteristic survey spectra of Pr-GDC$_{REF}$ and Pr-GDC$_{3.6k}$ electrodes, recorded with a photon energy of 1300 eV, are shown in Figure 6.4. All the elements anticipated by the electrode composition are detected and no peaks indicating contamination were observed. The Ni 2p signal overlaps with the Ce 3d and La 3d peaks, therefore the Ni 3p peak was used in the quantification. It is worth noting that the Si 2p peak around 103 eV overlaps with the La 4d peak; however, the absence of the Si 2s peak around 150 eV rules out the presence of silicon impurities. In contrast, a stronger carbon signal is observed in the Pr-GDC$_{REF}$ sample, as highlighted in the inset of Figure 6.4. This carbon signal is likely due to residual carbon tape previously attached to the sample (also visible as the darker areas in Figure 6.3b) and is not an intrinsic characteristic of the sample.

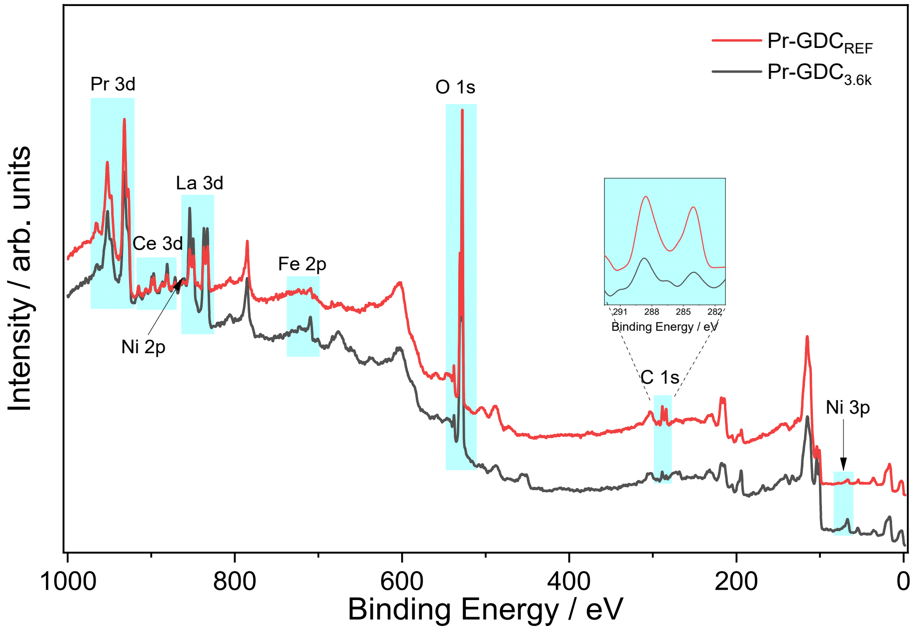

Figure 6.4. Characteristic survey NAP-XPS spectra of the Pr-GDC$_{REF}$ and Pr-GDC$_{3.6k}$ electrodes measured by 1300 eV photon energy in 2 mbar O_2 at 350 °C. The photoemission peaks associated with the main elements of the electrodes are identified in cyan background. A zoom in the C 1s region is shown in the inset.

Based on the peak areas of the primary photoemission peaks for each element, as those highlighted in Figure 6.4 the atomic concentrations (%) of the Pr-GDC$_{REF}$ and Pr-GDC$_{3.6k}$ electrodes in both the CCL and FL regions were calculated and are summarized in Figure 6.5a. It is important to note that the values in Figure 6.5a represent the averages from several measurement spots within each region. Several intriguing observations emerge regarding the surface composition, which appears to deviate from the expected nominal composition of the electrodes based on their fabrication process. The most striking observation is that the LNF and Pr-GDC related elements are not confined to the CCL and FL layers, respectively, as would be expected based on the fabrication process. Instead, they are present in comparable quantities in both layers. For instance, in the FL of Pr-GDC$_{REF}$ sample approximately 40% of the detected elements correspond to LNF, a proportion that increases to 58% after electrolysis testing.

Furthermore, the CCL contains significant amounts of Praseodymium (Pr), up to 45%, despite the expectation that Pr should be limited in the FL. An exception to this trend is GDC, which appears to be primarily confined to the FL, as its concentration in the CCL is near the detection limit of the method. The surface concentration of Ce slightly increases after electrolysis, suggesting a possible reconstruction that results in a greater exposure of GDC on the surface. When comparing the surface composition of Pr-GDC$_{REF}$ and Pr-GDC$_{3.6k}$, i.e., the O_2-electrode before and after electrolysis, the CCL composition remains practically unchanged within experimental error. However, in the FL, the concentration of LNF-related elements increases at the expense of Pr.

a) AP-XPS (surface)

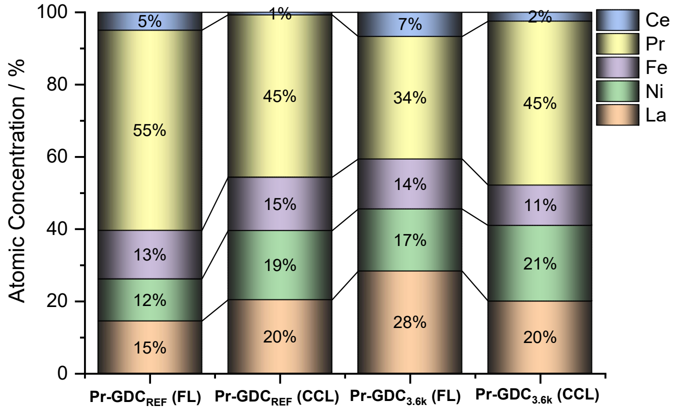

b) EDS (bulk)

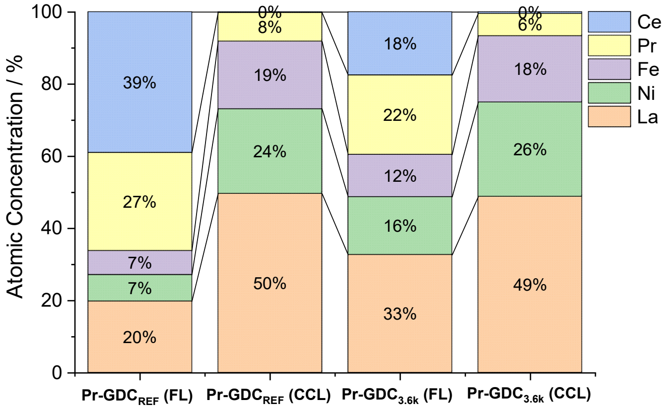

Figure 6.5. Stacked column plots showing the atomic concentrations of the surface elements (at. %) in the FL and CCL of Pr-GDC$_{REF}$ and Pr-GDC$_{3.6k}$ electrodes, based on a) NAP-XPS and b) EDS spectra. Note that the analysis depths of the two methods differ significantly, with NAP-XPS probing approximately 2 nm (surface composition) and EDS probing around 2 µm (bulk composition), enabling a correlation between surface and bulk measurements of the electrodes.

To confirm the preferential surface segregation of Pr, as suggested by the quantitative analysis of the electrode, we conducted non-destructive, depth-dependent photoemission measurements. As discussed in previous chapters, in these measurements the energy of the incident photons is varied, allowing us to probe different depths within the material [487]. Figure 6.6 illustrates the atomic concentrations of Pr, Ce, and La across an analysis depth ranging from 2.3 to 6.5 nm. The depth-dependent concentration profiles reveal that Pr is more concentrated at the surface, while La (representing the LNF particles) shows an inverse trend, being more prevalent at greater depths. Meanwhile, Ce maintains a relatively constant concentration throughout the analyzed depth, with no significant variation observed. These results suggest a surface arrangement where Pr preferentially migrates and covers the LNF particles, while the GDC particles remain largely unaffected. This surface configuration appears to form after reduction pretreatment and is preserved, despite the noticeable decrease in Pr concentration following electrolysis. The reduction in Pr amount could be attributed to either a partial withdrawal from the surface of LNF particles or a thinning of the surface layer. However, when comparing the element concentrations in Figure 6.6a and Figure 6.5b, it is evident that Pr concentration drops significantly after operation (i.e., Pr-GDC$_{3.6k}$), while Ce concentration increases, consistent with the quantitative analysis presented in Figure 6.5a.

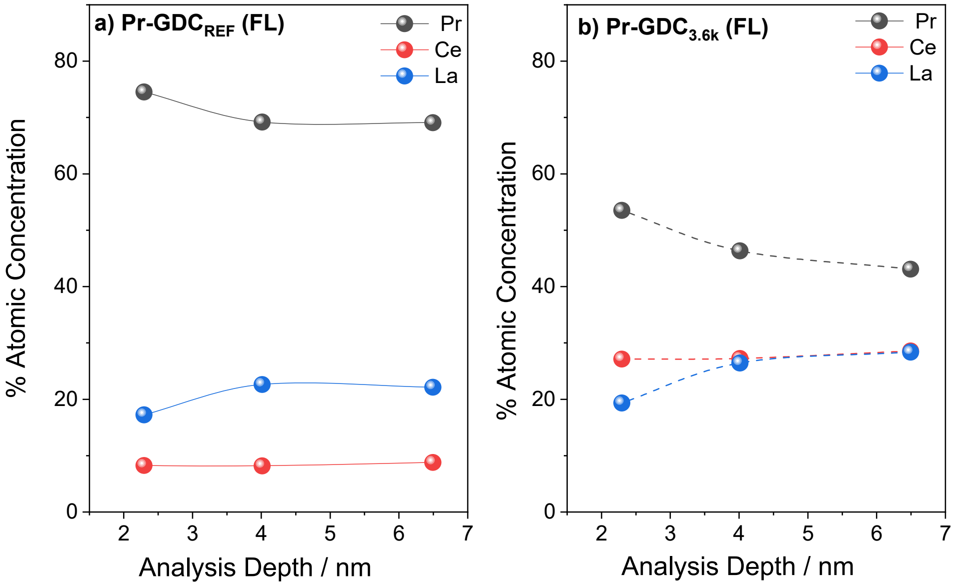

Figure 6.6. Percentage atomic concentration (% at.) of Pr, Ce, and La as a function of analysis depth, calculated from the Pr 3d, Ce 3d, and La 3d NAP-XPS spectra. Measurements were conducted in the Functional Layer (FL) area for **(a)** Pr-GDC$_{REF}$ and **(b)** Pr-GDC$_{3.6k}$ electrodes.

6.3.1.3 Quantification of the bulk composition by Energy-dispersive X-ray spectroscopy

Driven by the unexpected surface composition highlighted in the NAP-XPS analysis and with the goal of verifying the elemental composition within the bulk of the electrodes, Energy-dispersive X-ray spectroscopy (EDS or EDX) was employed. In this technique, a focused electron beam is directed at the sample, causing the atoms to emit characteristic X-rays. Each element produces X-rays at distinct energy levels unique to that element, enabling EDS to detect the presence and relative abundance of elements in the sample. However, a limitation of the method is that some elements have overlapping X-ray emission peaks, which can complicate the analysis. This technique is typically used in conjunction with scanning electron microscopy (SEM).

The probing depth of EDS, or its information depth, depends on both the applied voltage and the density of the element being analyzed. In our case, a voltage of 15 kV was used, which corresponds to an analysis depth of approximately 1-2 µm—about 1000 times more than NAP-XPS. Therefore, EDS-based quantification provides the bulk composition of the sample, whereas NAP-XPS reflects the surface composition. In this study, EDS analysis was performed on the same samples and at the same locations as the NAP-XPS measurements, with the aim of comparing the bulk and surface composition of the electrode areas. Figure 6.7 presents low-magnification SEM micrographs of both electrodes, with EDS measurement points indicated and CCL and FL regions highlighted. A direct comparison of the SEM images with the optical photographs of the two samples can be found in Figure 6.3c.

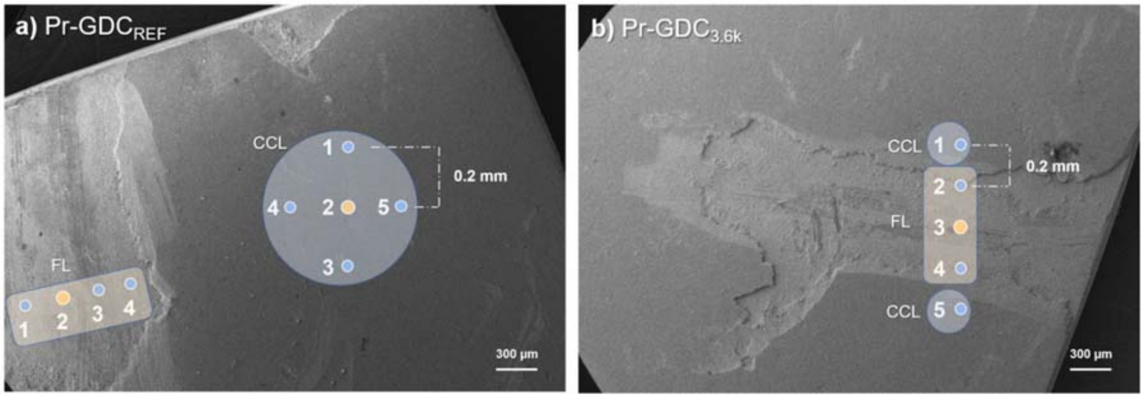

Figure 6.7. SEM micrographs of **(a)** Pr-GDC$_{REF}$ and (b) Pr-GDC$_{3.6k}$ electrodes, with EDS measurement points indicated. The CCL and FL regions are highlighted. The measurement areas correspond to those analyzed by NAP-XPS, as shown in the optical images of Figure 6.3b.

The atomic concentration calculated on the basis of EDS spectra for each sample averaging several measurement spots at the CCL and FL electrode areas are shown in Figure 6.5b. These quantification results present some similarities and some differences as compared to the quantification provided by the NAP-XPS measurements shown in Figure 6.5a. In particular the data confirm the presence of LNF in the FL region and show a significant increase in LNF concentration after electrolysis. Interestingly, the LNF concentrations measured by both EDS and NAP-XPS are in reasonable agreement— with approximately 40% and 60% LNF for Pr-GDC_{REF} and Pr-$GDC_{3.6k}$ respectively—demonstrating the consistency of the measurements. This also suggests that LNF likely forms separate aggregates in contact with Pr-GDC, rather than spreading across its surface. In contrast, the relative amount of Pr is found to be significantly higher in the NAP-XPS measurements compared to EDS in the expense of Ce signal. This can be explained by the tendency of Pr to migrate to the surface of GDC and LNF particles, which has a greater impact in NAP-XPS, as these measurements primarily analyse the outermost surface layers. Furthermore, EDS confirms the presence of Pr in the CCL, although its concentration is significantly lower than that measured by NAP-XPS for the reasons explained above. Both methods confirm the reduction in Pr concentration in the FL after electrolysis.

6.3.1.4 Surface chemical state analysis using NAP-XPS

We now turn our attention to the chemical state of the O_2-electrode through the analysis of high-resolution NAP-XPS spectra. Figure 6.8 shows the Pr 3d, La 3d (including part of Ni $2p_{3/2}$ peak), Ce 3d and Fe 2p spectra corresponding to the FL of the Pr-$GDC_{3.6k}$ sample. The excitation photon energy used in each spectrum was carefully selected to yield photoelectrons with a kinetic energy of approximately 180 eV, corresponding to an analysis depth of around 2 nm. It is important to note that the NAP-XPS spectra exhibit nearly identical peak shapes for both electrodes (Pr-GDC_{REF} and Pr-$GDC_{3.6k}$) regardless of the location where the spectra were collected (FL or CCL). Therefore, for the sake of brevity, only a representative spectrum for each element is discussed, except for the Pr 3d and La 3d spectra, which exhibit differences between the FL before and after electrolysis.

The Pr 3d spectrum shown in Figure 6.8a has a complicate shape due to the presence of intense satellite features. It is composed by the Pr $3d_{5/2}$ and Pr $3d_{3/2}$ doublet, with a spin-orbit splitting of 20.4 ± 0.1 eV, with a binding energy of the main Pr $3d_{5/2}$ peak at 932.5 eV. The two satellite features observed at the lower binding energy side of the main Pr 3d peaks are attributed to final-state photoemission effects, resulting from the strong covalent interaction between Pr and

O ions [488]. Additionally, an extra structure (*mult. sat.*), present exclusively in the $3d_{3/2}$ component, is caused by multiplet effects [488–490].

The complexity of the Pr 3d spectrum makes it challenging to acuratelly determine the Pr oxidation state. However, based on literature, there are two characteristic differences between the spectra of trivalent and tetravalent Pr oxides, such as Pr_2O_3 and PrO_2, which can be used to identify the Pr oxidation state. In particular, although both Pr^{3+} and Pr^{4+} oxidation states display the characteristic satelite peaks, Pr^{4+} exhibits a relatively higher intensity of this satelite for both the $3d_{5/2}$ and $3d_{3/2}$ doublet peaks compared to Pr^{3+} [488–490]. Additionally, the presence of Pr^{4+} is also indicated by an extra satellite component, attributed to $3d4f^1$ final state, appearing at 945 eV, just before the Pr $3d_{3/2}$ peak satellite [488–490]. This feature is observed exclusively in PrO_2 and is absent in the spectra of pure metallic Pr or Pr_2O_3.

To better illustrate the different spectral features, the Pr 3d peaks measured at the FL of the Pr-GDC_{REF} and Pr-$GDC_{3.6k}$ electrodes, the spectra were fitted using a previously established approach for Pr-containing oxides [491]. As shown in Figure 6.8a, in the case of Pr-GDC_{REF}, apart of the Pr 3d main and satellite peaks, a distinct component at 945.6 eV can be observed, which is absent in Pr-$GDC_{3.6k}$. The absence of the 945.6 eV satellite and the slightly lower main-to-satellite peak area ratio in the Pr-$GDC_{3.6k}$ sample suggest that nearly all Pr is in the Pr^{3+} state in this sample, likely as Pr_2O_3. In contrast, the presence of the $3d4f^1$ feature in Pr-GDC_{REF} indicates the presence of Pr^{4+}.

The La 3d spectra measured at the FL and CCL regions of the Pr-$GDC_{3.6k}$ electrode are shown in Figure 6.8b. Similar to the Pr 3d spectrum, the La 3d peak exhibit a complex shape due to multiple satellite and plasmon loss features [492]. Additionally, the Ni $2p_{3/2}$ peak partially overlaps with the La $3d_{3/2}$ component, further complicating the spectral profile analysis. To highlight subtle differences in curve shape between the spectra from the FL and CCL areas, the overall spectrum is fitted using a linear combination of six components related to La 3d and Ni $2p_{3/2}$ spectral features, as shown in Figure 6.8b.

Comparison of the spectra from the FL and CCL regions reveals two key differences. First, there is a notably lower contribution of the Ni $2p_{3/2}$ peak in the FL compared to CCL. Since both Ni and La originate from LNF, which, according to the fabrication procedure, should not be present in the FL, it is likely that the LNF particles mixed within the FL are non-stoichiometric, but deficient in Ni. This assumption is further supported by the quantitative analysis in Figure 6.5a, which shows a relatively higher La/Ni ratio in the FL (La/Ni ~ 0.95) compared to the CCL (La/Ni ~ 0.65).

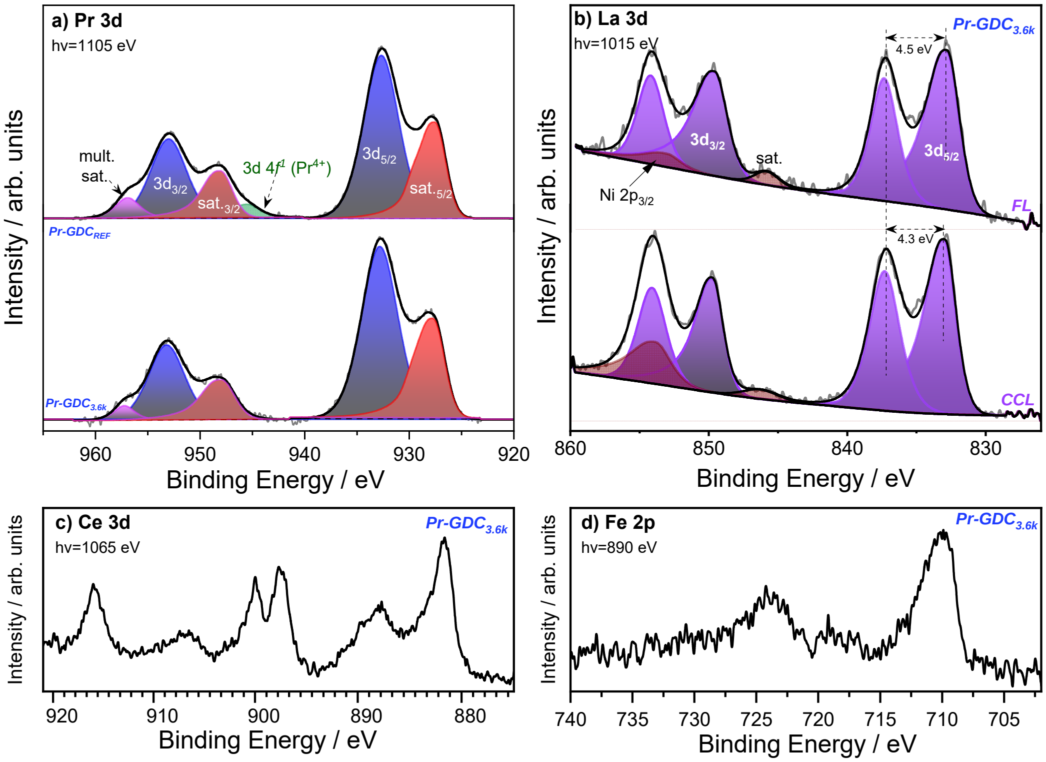

Figure 6.8. NAP-XPS specta collected at 350 °C in in 2mbar O_2 for **(a)** Pr 3d, **(b)** La 3d, **(c)** Ce 3d and **(d)** Fe 2p. The Pr 3d and La 3d spectra are fitted, with main peaks and the satellite features indicated in the figure. These figures are representative of both electrodes and layers. The Pr 3d spectra in (a) exhibit differences between the two electrodes at the FL.

The second difference between the two layers, is the binding energy (BE) splitting between the main and satellite peaks of the La 3d spectra. This split, referred to here as ΔLa3d, is highly sensitive to the chemical state of lanthanum and is commonly used to differentiate between various lanthanum compounds (see Table 6.2). The peak-fitting procedure shown in Figure 6.8b indicates a small but consistent difference in ΔLa3d between the FL and CCL regions. In the CCL, ΔLa3d is measured at 4.5 eV, consistent with previous reports for $LaNi_{0.6}Fe_{0.4}O_3$ perovskites [493]. However, in the FL, this value decreases to 4.3 eV, providing independent evidence that the LNF found in the FL has undergone a chemical modification compared to its stoichiometric perovskite state. Accurately describing the chemical state of La in the FL is challenging based solely on ΔLa3d measurements, as this change likely results from a convolution of La 3d spectra involving two or more lanthanum oxidation states.

Table 6.2. The La $3d_{5/2}$ component splitting (ΔLa3d) for various lanthanum compounds. The standard deviation of the values collected from the cited literature is included in parenthesis.

Name	ΔLa3d (STD) (eV)	Reference
Lanthanum oxide (lanthana)	4.6(±0.3)	[492,494–496]
$LaNi_{0.6}Fe_{0.4}O_3$	4.5	[493]
Lanthanum oxycarbonate	4.3(±0.2)	[494,496,497]
Lanthanum hydroxide $La(OH)_3$	3.7(±0.3)	[492,494–496,498,499]
Lanthanum carbonate	3.5(±0.1)	[498–500]
$LaNiO_3$	3.8	[501]

The Ce 3d spectrum in Figure 6.8c displays six distinct peak features, including an intense, almost symmetric satellite peak around 916 eV, characteristic of the Ce^{4+} oxidation state. The close resemblance of this Ce 3d spectrum to previously published spectra of samples calcined at atmospheric pressure [502] suggests that ceria is fully oxidized in the tetravalent oxidation state. Additionally, the identical Ce 3d peak shape observed across both samples and analysis areas confirms that ceria remains consistently in the Ce^{4+} oxidation state.

The Fe 2p spectrum for the Pr-$GDC_{3.6k}$ sample shown in Figure 6.8d, reveals the characteristic Fe $2p_{3/2}$ and Fe $2p_{1/2}$ spin-orbit splitting states, along with a weak satellite peak approximately 8 eV higher in binding energy than the Fe $2p_{3/2}$. A comparison with previously reported Fe 2p spectra for metallic iron, Fe^{2+}, and Fe^{3+} oxidation states [503,504] suggests that iron predominantly exists in the Fe^{3+} oxidation state.

Overall, the above displayed results indicate that the surface chemical state remains consistent across different electrode layers and is not significantly affected during electrolysis mode operation.

6.3.2 Analysis of LSCF based O_2 electrodes.

6.3.2.1 Sample preparation and mounting

A second set of electrodes, containing $La_{0.6}Sr_{0.4}Co_{0.2}Fe_{0.8}O_{3-\delta}$ perovskite (abbreviated as LSCF) as the main O_2-electrode constituent, was analyzed using the same approach. The electrolyte, H_2-electrode and barrier layers were identical to those of the Pr-GDC cells, presented in Figure 6.2. However, the FL was a mixture of LSCF and GDC, while the CCL was composed solely of LSCF. The composition of the two cells, as revealed by SEM/EDS mapping analysis, is shown in Figure 6.9a. Similar to the Pr-GDC electrodes, these cells were analyzed both before and after electrolysis. In particular, two identical cells were analyzed: one after reduction pre-treatment ($LSCF_{REF}$) and another after 1000 hours electrolysis ($LSCF_{DRY}$) operation with dry air flow in the anode, as detailed in Table 6.1. As with the Pr-GDC electrodes, the upper section of the electrode was mechanically scraped off to expose both the FL area to the photoemission measurements.

Figure 6.9b presents an optical camera photograph of the $LSCF_{REF}$ and $LSCF_{DRY}$ electrodes mounted on the sample holder, using a top stainless-steel lead. In the image, the FL areas, which became exposed due to localized scraping of the top CLL, are clearly distinguishable by their darker grey colour. This contrasts with the lighter grey tone of the CCL, providing a clear visual distinction between the two layers. Multiple regions in both the FL and CCL of the electrodes were selected for analysis, with the measurement spots marked by circles in Figure 6.9b for clarity. This selection of several points ensures representative sampling from both the FL and CCL areas.

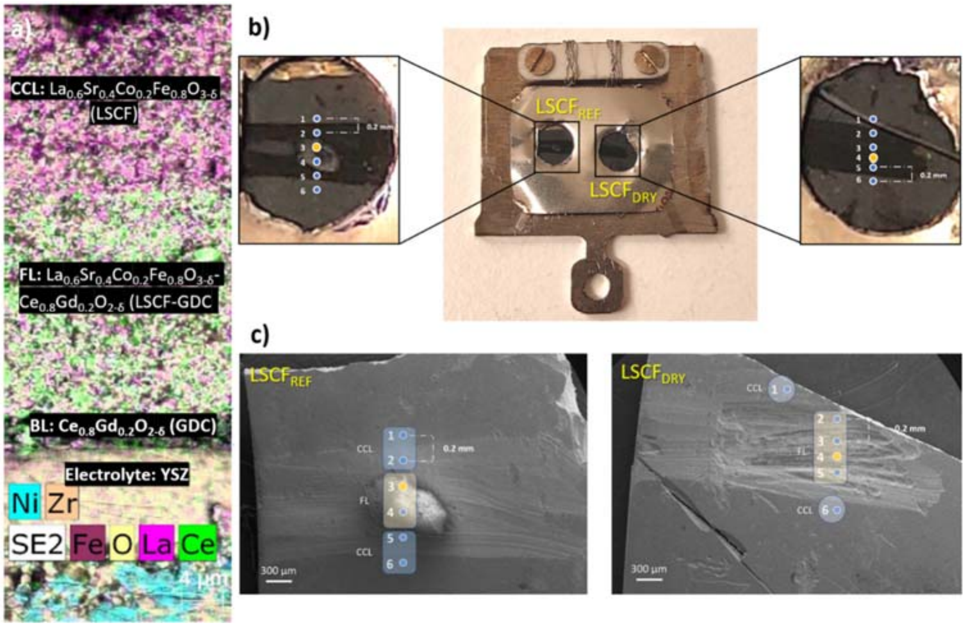

Figure 6.9. (a) Cross-sectional SEM/EDS micrographs with elemental mapping, illustrating the different layers of the LSCF/LSCF-GDC-based cell. The micrograph was provided by CEA, Liten **(b)** An optical camera photograph of the sample holder showing the two samples positioned on it, with the top lead used to fix the samples. At the left and right part of the image magnified optical images where the NAP-XPS measurements spots for each sample are indicated by cycles can be seen **(c)** SEM micrographs of the two electrodes, with EDS measurement points indicated. The CCL and FL regions are highlighted. The measurement areas correspond to those analyzed by NAP-XPS.

6.3.2.2 Quantification of the surface composition by NAP-XPS

Figure 6.10 shows characteristic survey spectra measured at the FL area of $LSCF_{REF}$ and $LSCF_{DRY}$ electrodes, in which the photoemission peaks corresponding to LSCF and GDC elements are highlighted. Additionally, the spectra contain other core-level peaks related to the electrodes' elements, along with Auger peaks, which are not marked to preserve the figure's clarity. According to this figure, common surface impurities, such as silicon, or other elements not native to the electrode composition, are not detected.

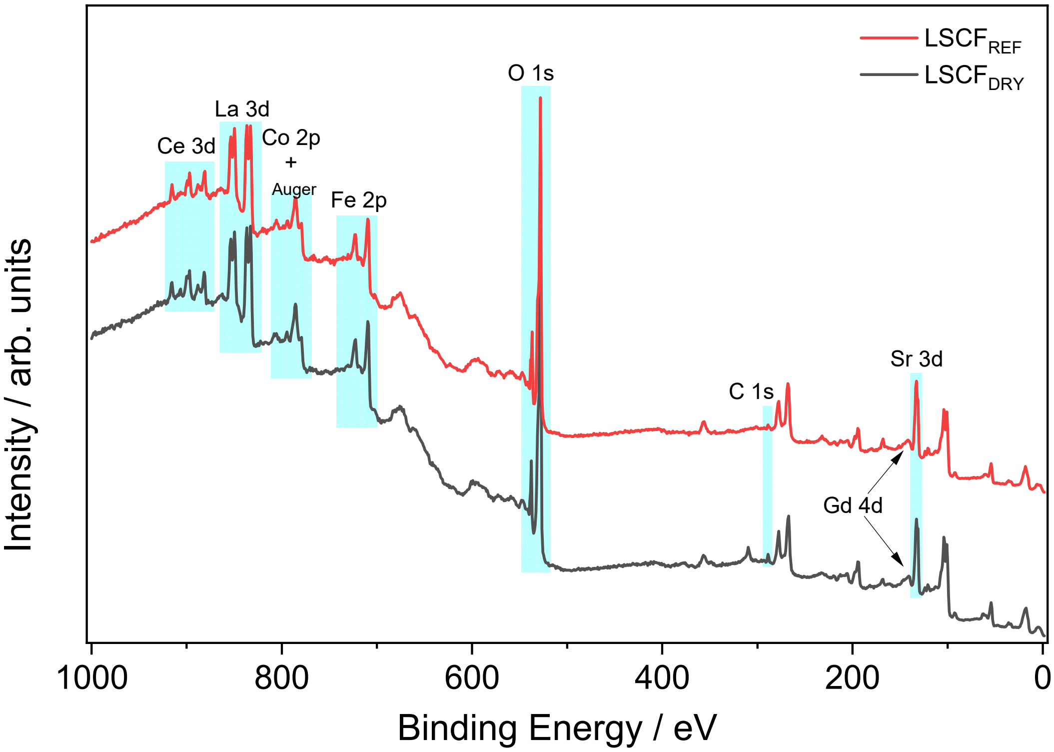

Figure 6.10. Survey spectra of the $LSCF_{REF}$ and $LSCF_{DRY}$ electrodes measured by 1300 eV photon energy in 2 mbar O_2 at 350 °C. The photoemission peaks associated with the main elements of the electrodes are identified in cyan background.

The surface composition of the two electrodes was calculated from survey NAP-XPS spectra similar to those shown in Figure 6.10. For clarity, the atomic concentrations are displayed in two graphs in Figure 6.11a: the graph on the left shows the surface composition of LSCF, while the graph on the right presents the distribution of LSCF and GDC across the electrode surface. The composition of both the FL and CCL areas is shown for the $LSCF_{REF}$ and $LSCF_{DRY}$ electrodes. It is important to note that the reported atomic concentrations represent average values derived from five measurement spots within each area, some of them are indicated in Figure 6.9b.

Several interesting observations can be drawn from Figure 6.11a. First, Sr is detected at significantly higher concentrations—ranging from 45% to 59%—compared to the expected bulk composition of the perovskite, which is approximately 20%. In contrast, La and Fe appear deficient, while Co exhibits a surface concentration close to its nominal value of 10%. This indicates substantial surface segregation of Sr, already occurring prior to electrochemical operation during H_2 electrode reduction pre-treatment.

A comparison of the atomic concentrations between the FL and CCL areas reveals a significantly higher Sr concentration in the FL area, at the expense of Fe, regardless of whether the electrode is subjected to electrolysis or just reduction. Interestingly, after 5000 hours of electrolysis ($LSCF_{DRY}$), there is a relative decrease in Sr concentration in both the FL and CCL areas of the electrode. These results suggest that while significant surface reorganization does not occur during electrolysis, Sr surface segregation is largely taking place and completed during the pre-treatment stage. Further electrochemical operation appears to have little to no effect on promoting additional Sr accumulation, and may even reverse some of the Sr segregation.

Another notable observation arises from the comparison of LSCF and GDC concentrations across different electrode layers, as shown in the right graph of Figure 6.11a. As expected from the fabrication process, GDC is absent in the CCL of $LSCF_{REF}$, while its relative concentration in the FL is approximately 40%. Interestingly, after electrolysis operation (i.e., $LSCF_{DRY}$), the GDC concentration decreases in the FL, while a small amount of GDC is detected in the CCL. These observations suggest a limited migration of GDC from the FL to the CCL during electrolysis, indicating a redistribution of material between the layers. Consequently, the FL area has reduced surface-accessible GDC after electrochemical operation.

Another remark, not immediately evident from the data in Figure 6.11a, is that the Gd/Ce peak ratio remains practically unchanged across all measurements. This indicates that the composition of the GDC does not undergo significant modification after electrolysis operation.

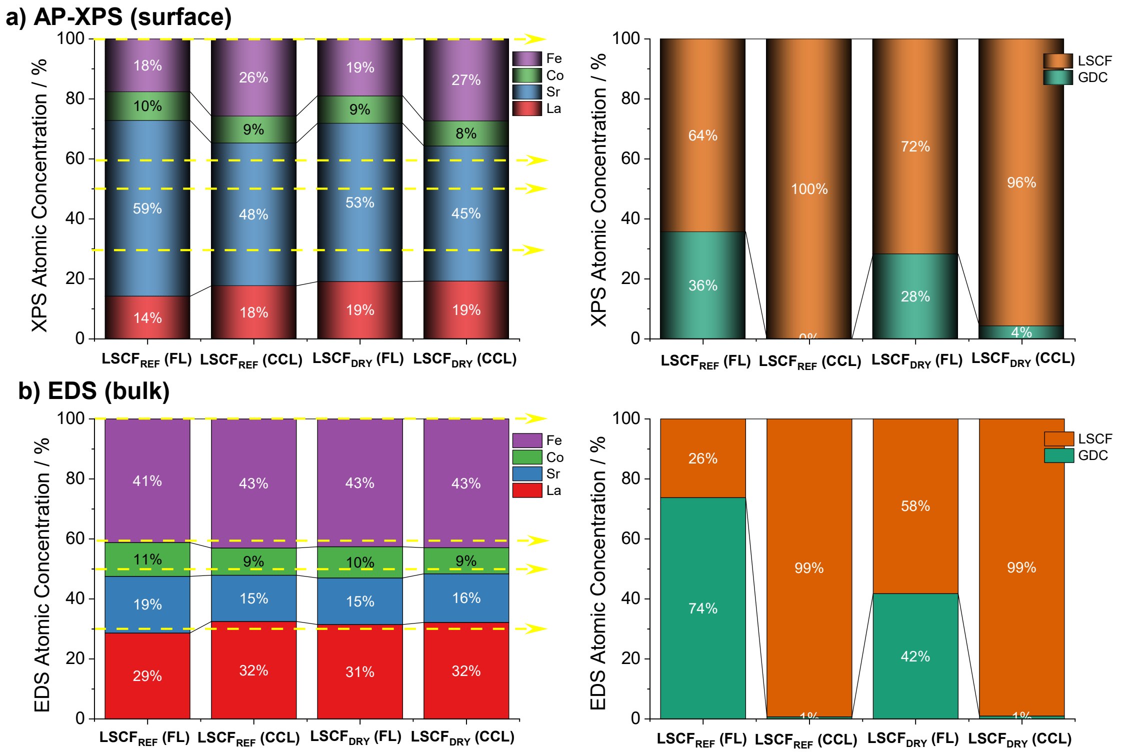

Figure 6.11. Stacked column plots of the atomic concentrations in the FL and CCL of LSCF$_{REF}$ and LSCF$_{DRY}$ electrodes, derived from **(a)** NAP-XPS and **(b)** EDS spectra. The graphs on the left show the composition of LSCF, while those on the right presents the distribution between LSCF and GDC. Note that the analysis depths of the two methods differ significantly, with NAP-XPS probing approximately 2 nm (surface composition) and EDS probing around 2 µm (bulk composition), enabling a correlation between surface and bulk measurements of the electrodes.

6.3.2.3 Quantification of the bulk composition by Energy-dispersive X-ray spectroscopy

Similar to the analysis performed on the Pr-GDC electrodes, EDS was conducted at the same sample locations where the NAP-XPS measurements were taken. This approach aimed to provide a comparative analysis of the bulk and surface composition of the LSCF electrode regions, enhancing our understanding of the elemental distribution between the surface and deeper layers. The low-magnification SEM micrographs of both electrodes, with the specific EDS measurement points indicated, are shown in Figure 6.9b. The corresponding atomic composition, representing the average of several measurement points in each area of the electrodes, is presented in Figure 6.11b. Focusing on the graph on the left, which displays the atomic concentrations of elements related to LSCF, it is evident that the bulk composition remains relatively stable for both electrodes and across the FL and CCL regions. Moreover, the calculated atomic concentrations closely match the expected LSCF stoichiometry. The enhancement of the Sr signal observed in the NAP-XPS measurements is not detected in the EDS analysis, confirming that Sr segregation is localized to the outermost surface layer and does not exists into the bulk.

In the case of the bulk LSCF relative to GDC composition, a trend similar to that seen in the NAP-XPS results is observed, as shown in the right graph of Figure 6.11b. Specifically, the relative concentration of GDC in the FL appears to decrease for $\mathrm{LSCF_{DRY}}$. This suggests that some redistribution of the components occurs during electrolysis operation. When comparing these findings with the NAP-XPS data, it becomes evident that the LSCF concentration is lower in the bulk than at the surface, indicating that the electrode does not consist of two distinct, physically mixed materials, but likely LSCF migrates over the GDC grains. This surface migration of LSCF likely plays a role in modifying the electrode's structural and electrochemical properties, and it implies that the interaction between LSCF and GDC is more complex than simple physical mixing, with possible implications for the electrode's long-term performance and stability.

EDS quantification did not confirm the presence of GDC in the CCL after electrolysis operation found by NAP-XPS, indicating that if GDC migration into the CCL does occur, it is very limited and predominantly confined to the surface.

6.3.2.4 Surface chemical state analysis using NAP-XPS

High-resolution NAP-XPS spectra were analyzed to detect potential differences in the oxidation states of the samples. Figure 6.12 presents the spectra of the primary electrode elements measured in the FL areas of the $\mathrm{LSCF_{REF}}$ and $\mathrm{LSCF_{DRY}}$ electrodes. Similar to the Pr-GDC electrode, the photon energies were selected to achieve an analysis depth of approximately 2 nm for each element. A direct comparison of the peak profiles reveals no significant differences between the two electrodes, with the exception of the Sr 3d peak, which will be discussed separately below. The splitting between the main and satellite La 3d peaks, denoted as ΔLa3d, is measured at 4.5 ± 0.1 eV, showing no evident differences between the two samples. This value is consistent with the expected ΔLa3d values for both lanthanum perovskites and oxides, making it impossible to distinguish between the two [492–496].

The Co 2p photoemission spectrum displays a prominent $2p_{3/2}$ peak at 780 eV, with a $2p_{1/2}$ doublet separation of 15 eV. As is typical for the photoemission spectra of transition metal oxides, the Co 2p peak exhibits a complex structure. Notably, the intensity of the satellite feature, which appears approximately 7.5 eV higher in energy, can be utilized to differentiate between Co^{3+} and Co^{2+} oxidation states. Specifically, the relative intensity of the satellite feature compared to the main photoemission peak is significantly higher for Co^{2+} than Co^{3+} [333,505,506]. The presence of the low-intensity satellite feature around 788 eV suggests the oxidation of cobalt to Co^{3+}. The Fe 2p spectra resemble those of the LNF perovskite, which, as discussed earlier, indicates the presence of Fe^{3+}. Finally, the Ce 3d peak is characteristic of Ce^{4+}.

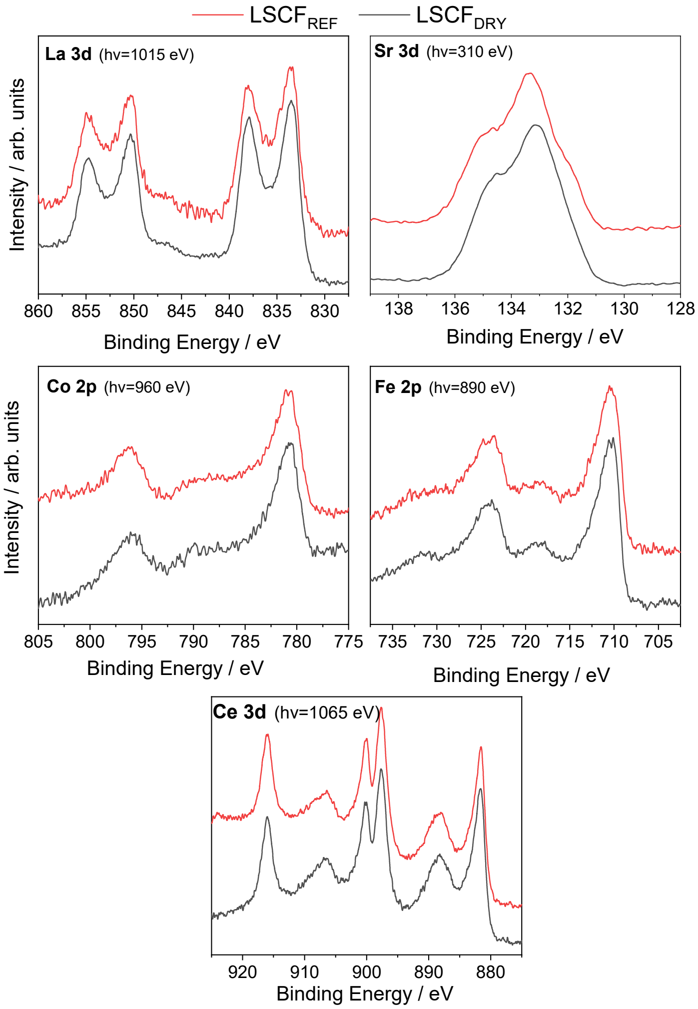

Figure 6.12. NAP-XPS spectra of La 3d, Sr 3d, Co 2p, Fe 2p, and Ce 3d (from top to bottom, left to right) measured in the functional layer (FL) areas of the $LSCF_{REF}$ and $LSCF_{DRY}$ electrodes. All spectra were collected at 350 °C under 2 mbar of O_2, using photon energies indicated in the parenthesis.

6.3.2.5 Chemical state and surface distribution of strontium cations

As previously mentioned, the Sr 3d spectra were the only ones to show noticeable differences between the two electrodes. Given that Sr segregation is widely recognized as one of the primary factors impacting the stability and performance of LSCF electrodes [507–509], we conducted a more detailed analysis of the Sr 3d region. To gain deeper insights, we applied a peak-fitting procedure to better resolve the spectral components and quantify any variations. For the Sr 3d peak fitting, two Sr 3d doublets were used, applying constraints on the width, area ratio, and spin-orbit splitting value of the peak components, following a previously reported method [510]. Figure 6.13a and b show the Sr 3d spectra for the FL area measurement points for both electrodes, recorded using three different photon energies. As previously mentioned, increasing the photon energy enhances the analysis depth, enabling the distinction between surface and subsurface Sr species. The analysis presented in Figure 6.13a and b shows a clear enchantment of the low-BE component with increasing analysis depth, manifesting that it corresponds to Sr species located in deeper layers. This observation aligns with literature reports [510–512], which typically attribute the low-BE component (Sr_{lat}) to Sr species from the perovskite lattice and the high-BE component (Sr_{surf}) to surface strontium oxide (SrO_x) species. The trend observed in the fitting of the Sr 3d spectra is quantified in the diagram shown in Figure 6.13c. It illustrates that the Sr_{surf}/Sr_{lat} peak area ratio decreases with increasing analysis depth, in a remarkably similar manner for both electrodes. The Sr_{surf}/Sr_{lat} ratio is also an indicator of Sr segregation, and the similarity of the values in Figure 6.13c indicates a comparable structural arrangement before and after electrolysis. However, as indicated by the results in Figure 6.11a, $LSCF_{REF}$ exhibits a higher overall Sr atomic percentage (%at). Since both Sr_{surf} and Sr_{lat} species are included in the quantitative calculations, the elevated Sr %at. in $LSCF_{REF}$ suggests that this sample contains a relatively greater amount of SrO_x on its surface compared to $LSCF_{DRY}$, despite their similar Sr_{surf}/Sr_{lat} ratios.

Interestingly, $LSCF_{REF}$ also exhibits a relatively lower La %at. (Figure 6.11a). The combination of higher Sr and lower La surface %at. may result from the partial substitution of La by Sr cations at the A-sites of the perovskite lattice. An alternative explanation could involve the substitution of La with Ce or Cd cations from GDC. This is consistent with the comparatively higher surface concentration of GDC at the $LSCF_{REF}$, as shown in both surface and bulk quantifications in Figure 6.11. Ce doping at the La-sites of the LSCF perovskite is plausible, given that both cations have similar sizes, and experimental studies indicate that such doping can lead to lattice expansion without altering the centrosymmetric cubic space group of LSCF

[513]. However, the aforementioned scenario should be viewed with caution, as the increased concentration of GDC in Figure 6.11 may also result from a higher exposure of GDC grains at the surface, as mentioned above in the text.

A close comparison of the spectra recorded in the FL area of the $LSCF_{REF}$ and $LSCF_{DRY}$ electrodes, shown in Figures 6.12a and b, reveals clear differences in the overall Sr 3d peak shape. The peak fitting procedure attributes this variation to differing shifts in the Sr_{surf} species relative to Sr_{lat}, referred to ΔSr_{surf} for brievity. In particular, the ΔSr_{surf} from 1.4±0.1 eV in the $LSCF_{REF}$ drops to 1.1±0.1 eV $LSCF_{DRY}$. Notably, this 0.3 eV shift is consistent across at least four measurement points and all three analysis depths, indicating a reliable and reproducible effect that reflects differences in the chemical environment of the surface Sr oxide. Crumlin and co-worker's [514,515], demonstrated that BE shifts in the Sr 3d peak are quantitative related to the abundance of oxygen vacancies ($V^{\cdot\cdot}_O$) in strontium oxides. Importantly, this shift should not be confused with classical chemical shifts in XPS spectra, which are typically induced by changes in the oxidation state of the cation.

It has been shown that the abundance of vacant oxygen sites can be probed by quantifying the magnitude of BE shifts in XPS [514,515]. Specifically, a higher population of oxygen vacancies results in a greater upshift in the Sr 3d binding energy. Referring back to the results in Figure 6.13, one could argue that the SrO_x formed over $LSCF_{REF}$ contains more oxygen vacancies compared to $LSCF_{DRY}$, given its larger ΔSr_{surf}. According to a previously proposed mechanism of SrO_x formation on Sr-containing perovskites [514], the driving force for Sr segregation from the perovskite lattice to the surface is the electrostatic interaction between $V^{\cdot\cdot}_O$ and Sr cations. Due to the appearance of $V^{\cdot\cdot}_O$ more Sr cations migrate from the LSCF lattice to the surface, creating a Sr-enriched surface layer. Apparently, a higher population of $V^{\cdot\cdot}_O$ results in the formation of increased SrO_x amounts at the surface.

This scenario aligns with the reduction in surface Sr observed after electrolysis (i.e. $LSCF_{DRY}$) indicated in Figure 6.11. Although the underlying mechanism behind the reduction of oxygen vacancies during electrolysis cannot be deduced from these post-mortem studies, the presented analysis highlights a clear correlation between the surface chemical state and composition.

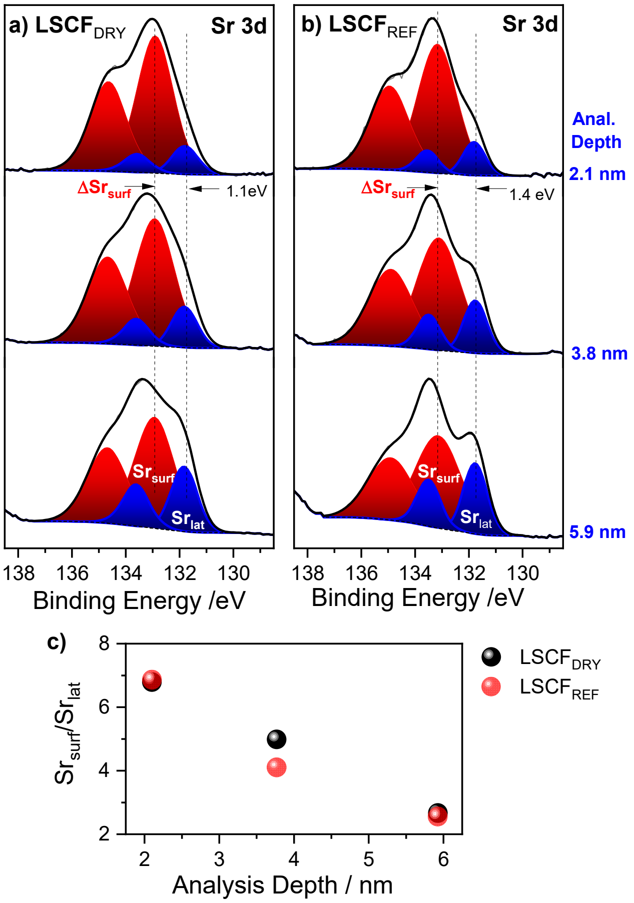

Figure 6.13. Sr 3d NAP-XPS specta collected at 350 °C in 2mbar O_2 using 3 diffefent photon enegries and thus information depths for **(a)** LSCF$_{DRY}$, **(b)** LSCF$_{REF}$.electrodes The spectra are fitted, with two sets of Sr 3d peaks as indicated in the figure. All spectra were recorded at the FL. **(c)** The peak area ratio of Sr$_{surf}$ and Sr$_{lat}$ components as a function of analysis depth, calculated from the spectra shown in **(a)** and **(b)**.

6.4 Conclusions

In this chapter, we conducted an in-depth investigation of PrO_x/GDC and LSCF/GDC oxygen electrodes combining NAP-XPS and SEM-EDS techniques. The results revealed minimal changes in both surface and bulk composition of the PrO_x electrodes before and after electrochemical testing, indicating excellent chemical stability. On the other hand, a key finding for the LSCF oxygen electrodes was the surface segregation of Sr, which became prominent during the pretreatment phase and persisted throughout long-term operation. The surface concentration of Sr was found less after extended electrochemical testing. These findings are crucial for the design and development of new high-performance oxygen electrode materials.

Chapter 7. General conclusions and perspectives

7.1. Summary and general conclusions of the thesis

Solid oxide cells (SOC) hold significant potential for hydrogen production through water electrolysis (in SOEC mode) and for power generation using hydrogen (in SOFC mode). Nickel/yttria-stabilized zirconia (Ni/YSZ) composites are the most commonly used fuel electrodes in solid oxide cells. These electrodes face degradation during operation, which can be categorized into two main types: (i) irreversible degradation, which is primarily related to the mechanical stability of SOEC devices (such as cracks, electrode delamination, and contamination), and these effects can easily be confirmed through post-operation analysis of the SOEC devices. (ii) Reversible degradation, particularly electrode oxidation, poses a greater challenge to study because it is dynamic and highly dependent on the operating conditions.

Although many studies have examined the microstructural changes of Ni/YSZ under operating conditions, the surface chemistry of Ni/YSZ under water electrolysis conditions remains less understood. *This thesis explored the surface chemistry of state-of-the-art fuel and oxygen electrodes during water electrolysis.* The unique capabilities of NAP-XPS technique, extensively used in this work, allow for the retrieval of chemical and compositional information from the electrode surface under reactive gas environments and operational conditions, offering insights into different surface layers (surface and sub-surface), which was indispensable for achieving the goals of this thesis.

The primary focus of this work is in state-of-the-art Ni/YSZ fuel electrodes and their surface modification by ceria-based nanoparticles, rather than developing new electrode materials. This is because current SOC technology still has significant room for improvement without the need to explore entirely new electrode materials with lower TRL (Technology Readiness Level). The research presented in this thesis predominantly utilizes commercial cermet electrodes with a standard multilayer configuration (buffer layer, catalytic layer, and conductive layer) prepared through traditional methods such as screen printing. Using functional materials, rather than developing model samples, represents a bold approach in electrochemical research, as the complexity of "real" cells far exceeds that of model systems. However, the advantages are clear since this approach yields more easily applicable and instructive results.

In Chapter 3, we investigate the interaction between Ni/YSZ electrodes and water vapor under both open circuit and polarization conditions using soft and hard X-rays NAP-XPS. Micro-cells featuring a conventional porous Ni/YSZ cermet cathode were used, allowing direct spectroscopic observation of the functional electrode region near the YSZ electrolyte interface.

The results reveal dynamic changes in the oxidation states and composition of Ni/YSZ under H_2 and H_2O atmospheres. A crucial aspect of the work in Chapter 3 is the study of electrode oxidation and its effect on the electrolysis performance. Through a carefully designed experiment and pre-treatment process, we were able to control the surface state of the electrodes, establishing a correlation between the oxidation state of the nickel surface during H_2O electroreduction and the electrochemical performance of the cell—something that is difficult to achieve in traditional electrolysis studies. It is evident that, during H_2O electrolysis, nickel oxidation tends to form NiO rather than $Ni(OH)_x$, providing key insights into the redistribution of Ni phases within the electrode during long-term operation.

In addition, surface-sensitive photoemission measurements combined with quantitative modeling revealed that during H_2O electrolysis, NiO and Ni were uniformly mixed on the surface. This observation deviates from the traditional expectation of the NiO shell/Ni core configuration commonly seen in gas-phase oxidation. Typically, oxidation of transition metals begins with the formation of a thin oxide layer on the surface, which serves as a protective barrier against further oxidation. The conventional NiO shell/Ni core model seems to only apply under non-polarized, static oxidation conditions. Under electrolysis conditions, however, the Ni surface demonstrates a certain "oxidation resistance."

In Chapter 4, we explore the surface modification of Ni/YSZ electrodes using Ce-based nanoparticles. This method builds on our group's previous work, including nanoparticle synthesis and infiltration techniques. Traditional infiltration methods for cermet electrodes face key challenges, such as multiple infiltration/calcination/reduction cycles and pore-blocking issues. Our method involves dispersing 5 nm-sized Ni-doped ($NiCeO_x$) and undoped (CeO_y) ceria nanoparticles in hexane, which are then directly applied to pre-fabricated Ni/YSZ cermet electrodes through a single or double infiltration/co-firing step. This contrasts with the literature where up to 10 steps are typically required, benefiting from the low surface tension of hexane to achieve high ceria catalyst loading efficiently.

Although the two types of nanoparticles tested showed different levels of agglomeration, dispersion sizes in the liquid phase, and slightly different particle sizes, both $NiCeO_x$ and CeO_y nanoparticles enhanced the electrolysis performance of Ni/YSZ electrodes when compared to untreated pristine samples. We sought to explore the effects of varying infiltration amounts and determined optimal performance for each type of nanoparticle. Specifically, $NiCeO_x$, which is smaller and less prone to agglomeration, exhibited better infiltration and significantly higher electrolysis performance than CeO_y. We hypothesize that $NiCeO_x$ nanoparticles uniformly decorate the Ni/YSZ scaffold's pores, reaching up to the electrolyte interface. In contrast, CeO_y nanoparticles, due to higher agglomeration in the liquid phase, primarily remain on the surface of Ni/YSZ and are less likely to penetrate the bulk. Consequently, $NiCeO_x$ nanoparticles form more 2PB (two-phase boundaries) and TPB (three-phase boundaries), providing more active sites, increasing mass transfer, and resulting in superior electrolysis performance.

The success of Ni-doped ceria to improve the performance of Ni/YSZ cathode electrode, lead us to synthesize and test ceria nanoparticles with other cation dopants, which is the subject of Chapter 5. We explored vanadium oxide nanoparticles, V-doped Ce nanoparticles, and Co-doped Ce nanoparticles. However, despite various synthesis methods, the experimental results for V were unsatisfactory, and Co-doped Ce nanoparticles only slightly improved electrolysis performance. The effect of nanoparticles reducibility and how they affect the surface properties of the Ni/YSZ electrode is discussed in the same chapter. Experiments conducted at the MAX IV synchrotron revealed that Ni-doping enchance the reduciblity of ceria nanoparticles, which is expected to influence the dynamic oxygen storage capacity of the modified Ni/YSZ electrodes. By using XAFS conducted at the ESRF synchrotron it was demonstrated that $NiCeO_x$ nanoparticles facilitate the reducibility of Ni/YSZ compared to the reference cell.

In Chapter 6, it was presented a detailed surface analysis study of LSCF-GDC and Pr-GDC oxygen electrode materials before and after long-term electrochemical testing. One major issue discussed in the context of oxygen electrodes is Sr segregation in LSCF electrodes. Additionally, we investigated the use of praseodymium oxide (Pr_6O_{11}) mixed with GDC as an alternative electrocatalyst for oxygen electrodes. It was shown that Pr is very mobile under pretreatment and electrolysis tests and can found in rather high quantities on the surface of both functional and conductive layers of the electrode.

7.2 Perspectives and proposed future work

In this study, was explored the electrolysis performance of both unmodified and modified Ni/YSZ electrodes using an infiltration method. While the results were highly encouraging, I must acknowledge that they are far from complete. For instance, in the comparative experiments between $NiCeO_x$ and CeO_y-modified electrodes, both types of nanoparticles were extracted using conventional methods. Specifically, after the thermal decomposition of Schiff base metal complexes in oleylamine, we used methanol for nanoparticle extraction. However, in results not included in this thesis, it was observed that varying the amount of methanol resulted in different nanoparticle properties. For example, adding 2.5 mL methanol to the 10 mL oleylamine solution produced larger nanoparticles with a higher Ce content, while adding 5 mL or 7.5 mL yielded smaller particles with a higher Ni content. Future experiments can be designed to further test these variations, and select the accordingly the nanoparticles for Ni/YSZ infiltration.

In terms of nanoparticle synthesis, we also explored vanadium nanoparticles. While the results were not particularly promising, this line of research should not be abandoned. More synthesis methods could be applied to control the size of V nanoparticles. In the synthesis of VCe, I used a 1:1 ratio of Schiff base ligands, but future work could experiment with different ratios, starting with smaller amounts and gradually increasing. Based on the performance of VCe nanoparticles shown in Figure 5.8, I remain optimistic about their potential. The same logic applies to CoCe nanoparticles. Additionally, cations such as Ru, Ti, Fe, and Mn possess unique catalytic properties, making them promising candidates for nanoparticle synthesis using Schiff base metal complexes. These nanoparticles could be used to improve Ni/YSZ electrode performance and durability through infiltration experiments.

The hexane-based nanoparticle infiltration method demonstrated high efficiency and potential. It could also be applied to perovskite-based LSFC electrodes. Perovskite-based cathode electrodes have garnered growing attention as promising cathode materials in SOECs due to their sufficient ionic and electronic conductivity and high thermal stability. However, relatively poor catalytic activity remains a significant challenge for most perovskite-related oxides. As demonstrated in this study, ceria nanoparticles can easily penetrate the entire electrode volume without significantly affecting macroscopic properties such as porosity. This method could also be used to regenerate deactivated electrode surfaces, offering exciting possibilities for future research.

One crucial point that cannot be overlooked is that despite the advanced and highly efficient characterization technique of synchrotron NAP-XPS, it has an inherent disadvantage when applied to SOFC and SOEC research—it operates within a single reaction chamber. To match this setup, we also utilized a single-chamber reaction setup in our lab-scale experiments. This leads to the mixing of fuel gas and air in SOFC experiments, as well as the mixing of product gases with the reactant gases in SOEC experiments. Such mixing can significantly impact the electrode surfaces, typically in a negative manner, causing deviations in the measured results compared to those from actual electrolysis devices. For example, the oxidation state evolution on the electrode surface can occur too rapidly, leading to accelerated cell degradation.

Mechanisms related to mass transport, as observed in EIS experiments, might also be inaccurately measured due to this setup.

Another issue is that to ensure rapid evacuation of gas products from the reaction chamber via the vacuum pump, the chamber pressure is usually much lower than the pressure found in real-world reactions. However, this limitation is still acceptable within the scope of our research.

For long-term performance tests of steam electrolysis, there are still areas that can be improved, such as addressing the water supply issue. Additionally, we discovered that long-term H_2O electrolysis experiments can proceed for considerable periods without adding H_2 as a reducing agent. In my trials, the cell's performance dropped to about 30% of its original level within the first 20 minutes but remained stable for nearly 20 hours afterward. This may be due to the effect of the produced H_2 on the surface of the Ni/YSZ electrode.

Last but not least, the co-electrolysis of CO_2 and H_2O is another important and intriguing topic. Co-electrolysis of H_2O and CO_2 is a more complex process due to the simultaneous occurrence of three reactions: H_2O electrolysis, CO_2 electrolysis, and the catalytic reverse water-gas shift reaction (RWGS).

In summary, in my opinion this work successfully elucidates the effects of nanoparticle modification on the performance of Ni/YSZ electrodes in steam electrolysis, demonstrating significant improvements in both efficiency and short-term stability. The combination of innovative material design and advanced characterization techniques has provided valuable insights, which not only contribute to academic discourse but also hold practical implications for the future of sustainable energy solutions.

References

[1] R. Łukajtis, I. Hołowacz, K. Kucharska, M. Glinka, P. Rybarczyk, A. Przyjazny, M. Kamiński, Hydrogen production from biomass using dark fermentation, Renewable and Sustainable Energy Reviews 91 (2018) 665–694. https://doi.org/10.1016/j.rser.2018.04.043.

[2] J.E. Zajic, N. Kosaric, J.D. Brosseau, Microbial production of hydrogen, in: Advances in Biochemical Engineering, Volume 9, Springer-Verlag, Berlin/Heidelberg, n.d.: pp. 57–109. https://doi.org/10.1007/BFb0048091.

[3] A. Nechache, M. Cassir, A. Ringuedé, Solid oxide electrolysis cell analysis by means of electrochemical impedance spectroscopy: A review, J Power Sources 258 (2014) 164–181. https://doi.org/10.1016/J.JPOWSOUR.2014.01.110.

[4] S.D. Ebbesen, S.H. Jensen, A. Hauch, M.B. Mogensen, High temperature electrolysis in alkaline cells, solid proton conducting cells, and solid oxide cells, Chem Rev 114 (2014) 10697–10734. https://doi.org/10.1021/CR5000865.

[5] L. Elikan, J.P. Morris, Solid electrolyte system for oxygen regeneration. NASA CR-1359., NASA Contract Rep NASA CR (1969) 1–166.

[6] M.J.P.W.C.K. Elikan L, Development of a solid electrolyte carbon dioxide and water reduction system for oxygen recovery, NASA Report CR (1972).

[7] Q. Jeangros, A. Faes, J.B. Wagner, T.W. Hansen, U. Aschauer, J. Van Herle, A. Hessler-Wyser, R.E. Dunin-Borkowski, In situ redox cycle of a nickel-YSZ fuel cell anode in an environmental transmission electron microscope, (2010). https://doi.org/10.1016/j.actamat.2010.04.019.

[8] C.-C. Cormos, Hydrogen production from fossil fuels with carbon capture and storage based on chemical looping systems, Int J Hydrogen Energy 36 (2011) 5960–5971. https://doi.org/10.1016/j.ijhydene.2011.01.170.

[9] T. Kåberger, Progress of renewable electricity replacing fossil fuels, Global Energy Interconnection 1 (2018) 48–52. https://doi.org/10.14171/j.2096-5117.gei.2018.01.006.

[10] J. Li, P. Qiu, M. Xia, L. Jia, B. Chi, J. Pu, J. Li, Microstructure optimization for high-performance PrBa0.5Sr0.5Co1.5Fe0.5O5+δ-La2NiO4+δ core-shell cathode of solid oxide fuel cells, J Power Sources 379 (2018) 206–211. https://doi.org/10.1016/J.JPOWSOUR.2018.01.055.

[11] J. Li, B. Liu, L. Jia, B. Chi, J. Pu, J. Li, S. Wang, Investigation on the oxygen reduction reaction mechanism of PrBa0.5Sr0.5Co1.5Fe0.5O5+δ@La2NiO4+δ core-shell structure cathode for solid oxide fuel cells, Int J Hydrogen Energy 44 (2019) 26489–26497. https://doi.org/10.1016/J.IJHYDENE.2019.08.064.

[12] S.P. Jiang, S.H. Chan, A review of anode materials development in solid oxide fuel cells, Journal of Materials Science 2004 39:14 39 (2004) 4405–4439. https://doi.org/10.1023/B:JMSC.0000034135.52164.6B.

[13] British Petroleum, Statistical Review of World Energy 2021, 2021. https://www.bp.com/content/dam/bp/business-sites/en/global/corporate/pdfs/energy-economics/statistical-review/bp-stats-review-2021-full-report.pdf.

[14] Energy Institute, Statistical Review of World Energy, 2024. https://www.energyinst.org/statistical-review.

[15] International Energy Agency, Global Hydrogen Review 2023, 2023. www.iea.org.

[16] British Petroleum, Energy Outlook 2023, 2023. https://www.bp.com/content/dam/bp/business-sites/en/global/corporate/pdfs/energy-economics/energy-outlook/bp-energy-outlook-2023.pdf.

[17] V. Papaefthimiou, D.K. Niakolas, F. Paloukis, D. Teschner, A. Knop-Gericke, M. Haevecker, S. Zafeiratos, Operando observation of nickel/ceria electrode surfaces during intermediate temperature steam electrolysis, J Catal 352 (2017) 305–313. https://doi.org/10.1016/j.jcat.2017.06.005.

[18] International Energy Agency, Grid-scale Storage, (2024). https://www.iea.org/energy-system/electricity/grid-scale-storage.

[19] M.S. Graboski, R.L. McCormick, Combustion of fat and vegetable oil derived fuels in diesel engines, Prog Energy Combust Sci 24 (1998) 125–164. https://doi.org/10.1016/S0360-1285(97)00034-8.

[20] L. Gradisher, B. Dutcher, M. Fan, Catalytic hydrogen production from fossil fuels via the water gas shift reaction, Appl Energy 139 (2015) 335–349. https://doi.org/10.1016/j.apenergy.2014.10.080.

[21] I. Dincer, C. Acar, Review and evaluation of hydrogen production methods for better sustainability, Int J Hydrogen Energy 40 (2015) 11094–11111. https://doi.org/10.1016/j.ijhydene.2014.12.035.

[22] I. Dincer, C. Zamfirescu, Sustainable hydrogen production options and the role of IAHE, Int J Hydrogen Energy 37 (2012) 16266–16286. https://doi.org/10.1016/j.ijhydene.2012.02.133.

[23] Y.E. Yuksel, M. Ozturk, I. Dincer, Development of a novel combined energy plant for multigeneration with hydrogen and ammonia production, Int J Hydrogen Energy 46 (2021) 28980–28994. https://doi.org/10.1016/j.ijhydene.2020.12.113.

[24] A.M.M.I. Qureshy, I. Dincer, A new integrated renewable energy system for clean electricity and hydrogen fuel production, Int J Hydrogen Energy 45 (2020) 20944–20955. https://doi.org/10.1016/j.ijhydene.2020.04.218.

[25] C. Acar, I. Dincer, Investigation of a new integrated system for multiple outputs with hydrogen and methanol, Int J Hydrogen Energy 46 (2021) 4699–4715. https://doi.org/10.1016/j.ijhydene.2020.02.167.

[26] H. Ishaq, O. Siddiqui, G. Chehade, I. Dincer, A solar and wind driven energy system for hydrogen and urea production with CO2 capturing, Int J Hydrogen Energy 46 (2021) 4749–4760. https://doi.org/10.1016/j.ijhydene.2020.01.208.

[27] A. Midilli, H. Kucuk, M.E. Topal, U. Akbulut, I. Dincer, A comprehensive review on hydrogen production from coal gasification: Challenges and Opportunities, Int J Hydrogen Energy 46 (2021) 25385–25412. https://doi.org/10.1016/j.ijhydene.2021.05.088.

[28] A.A. AlZahrani, I. Dincer, Exergoeconomic analysis of hydrogen production using a standalone high-temperature electrolyzer, Int J Hydrogen Energy 46 (2021) 13899–13907. https://doi.org/10.1016/j.ijhydene.2020.04.055.

[29] H. Jacobsen, "Heterogreeneous" Chemistry: Catalysts for Hydrogen Production from Biomass, Angewandte Chemie International Edition 43 (2004) 1912–1914. https://doi.org/10.1002/ANIE.200301700.

[30] P. Lv, J. Chang, Z. Xiong, H. Huang, C. Wu, Y. Chen, J. Zhu, Biomass Air−Steam Gasification in a Fluidized Bed to Produce Hydrogen-Rich Gas, Energy and Fuels 17 (2003) 677–682. https://doi.org/10.1021/EF020181L.

[31] J.A. Satrio, B.H. Shanks, T.D. Wheelock, Application of Combined Catalyst/Sorbent on Hydrogen Generation from Biomass Gasification, Iowa State University (2004).

[32] H.L. Chum, R.P. Overend, Biomass and renewable fuels, Fuel Processing Technology 71 (2001) 187–195. https://doi.org/10.1016/S0378-3820(01)00146-1.

[33] M. Steinberg, A Highly Efficient Combined Cycle Fossil and Biomass Fuel Cell Power Generation and Hydrogen Production Plant With Zero CO2 Emission, ASME 2004 2nd International Conference on Fuel Cell Science, Engineering and Technology, FUELCELL 2004 (2008) 401–408. https://doi.org/10.1115/FUELCELL2004-2498.

[34] O. Yamada, Generation of hydrogen gas by reforming biomass with superheated steam, Thin Solid Films 509 (2006) 207–211. https://doi.org/10.1016/J.TSF.2005.09.174.

[35] G. Chen, X. Lv, Q. Li, N. Deng, L. Jiao, Production of Hydrogen-Rich Gas Through Pyrolysis of Biomass in a Two-Stage Reactor, Proceedings of the ASME Turbo Expo 2004 7 (2008) 711–721. https://doi.org/10.1115/GT2004-53582.

[36] G. Weber, Q. Fu, H. Wu, Energy Efficiency of an Integrated Process Based on Gasification for Hydrogen Production from Biomass, Developments in Chemical Engineering and Mineral Processing 14 (2006) 33–48. https://doi.org/10.1002/APJ.5500140104.

[37] S. Vasileiadis, Z. Ziaka-Vasileiadou, Biomass reforming process for integrated solid oxide-fuel cell power generation, Chem Eng Sci 59 (2004) 4853–4859. https://doi.org/10.1016/J.CES.2004.07.071.

[38] D.B. Levin, H. Zhu, M. Beland, N. Cicek, B.E. Holbein, Potential for hydrogen and methane production from biomass residues in Canada, Bioresour Technol 98 (2007) 654–660. https://doi.org/10.1016/J.BIORTECH.2006.02.027.

[39] M. Asadullah, S.I. Ito, K. Kunimori, M. Yamada, K. Tomishige, Energy Efficient Production of Hydrogen and Syngas from Biomass: Development of Low-Temperature Catalytic Process for Cellulose Gasification, Environ Sci Technol 36 (2002) 4476–4481. https://doi.org/10.1021/ES020575R.

[40] M.F. Demirbas, Hydrogen from Various Biomass Species via Pyrolysis and Steam Gasification Processes, Energy Sources, Part A 28 (2006) 245–252. https://doi.org/10.1080/009083190890003.

[41] A. Demirbas, Combustion characteristics of different biomass fuels, Prog Energy Combust Sci 30 (2004) 219–230. https://doi.org/10.1016/J.PECS.2003.10.004.

[42] Y.S., F.W.J. and L.R.S. Guo, Coking-Inhibition of Pyrolysis-Cracking of Endothermic Hydrocarbon Fuel, Journal of Zhejiang University (Engineering Science) 39 (2005) 538–541.

[43] I.I. Salakhov, A.M. Ekimova, A.S. Eiyatdinov, I.N. Diyarov, K.K. Gil’manov, A.R. Shangareeva, Effect of feedstock hydrocarbon composition on the distribution of

products of initiated pyrolysis, Chemistry and Technology of Fuels and Oils 41 (2005) 386–394. https://doi.org/10.1007/S10553-005-0084-6.

[44] O. Yamada, Generation of hydrogen gas by reforming biomass with superheated steam, Thin Solid Films 509 (2006) 207–211. https://doi.org/10.1016/J.TSF.2005.09.174.

[45] M. Asadullah, S.I. Ito, K. Kunimori, M. Yamada, K. Tomishige, Energy Efficient Production of Hydrogen and Syngas from Biomass: Development of Low-Temperature Catalytic Process for Cellulose Gasification, Environ Sci Technol 36 (2002) 4476–4481. https://doi.org/10.1021/ES020575R.

[46] A. Demirbaş, M.F. Demirbaş, Biomass and Wastes: Upgrading Alternative Fuels, Energy Sources 25 (2003) 317–329. https://doi.org/10.1080/00908310390142352.

[47] H. Xiaohong, G. Liejin, A Review on investigation of Hydrogen Production by Biomass Catalytic Gasification in supercritical Water, Journal of Chemical Industry and Engineering(China) 53 (2002) 221–228.

[48] J Milliken, Hydrogen, Fuel Cells & Infrastructure Technologies Program Multi-Year Research, Development and Demonstration Plan, (2007). http://www.hydrogen.energy.gov.

[49] U.S. Department of Energy (DOE), 6.0 Program Management and Operations, Fuel Cell Technologies Office Multi-Year Research, Development and Demonstration Plan (2012) 1–11.

[50] S.Y. Wu, C.N. Lin, J.S. Chang, J.S. Chang, Biohydrogen production with anaerobic sludge immobilized by ethylene-vinyl acetate copolymer, Int J Hydrogen Energy 30 (2005) 1375–1381. https://doi.org/10.1016/J.IJHYDENE.2004.09.011.

[51] Y.T. Fan, Y.H. Zhang, S.F. Zhang, H.W. Hou, B.Z. Ren, Efficient conversion of wheat straw wastes into biohydrogen gas by cow dung compost, Bioresour Technol 97 (2006) 500–505. https://doi.org/10.1016/J.BIORTECH.2005.02.049.

[52] F.R. Hawkes, I. Hussy, G. Kyazze, R. Dinsdale, D.L. Hawkes, Continuous dark fermentative hydrogen production by mesophilic microflora: Principles and progress, Int J Hydrogen Energy 32 (2007) 172–184. https://doi.org/10.1016/J.IJHYDENE.2006.08.014.

[53] I.K. Kapdan, F. Kargi, Bio-hydrogen production from waste materials, Enzyme Microb Technol 38 (2006) 569–582. https://doi.org/10.1016/J.ENZMICTEC.2005.09.015.

[54] K. Nath, D. Das, Biohydrogen production as a potential energy resource – Present state-of-art, JSIR 63 (2004) 729–738.

[55] D.B. Levin, L. Pitt, M. Love, Biohydrogen production: prospects and limitations to practical application, Int J Hydrogen Energy 29 (2004) 173–185. https://doi.org/10.1016/S0360-3199(03)00094-6.

[56] R. Chaubey, S. Sahu, O.O. James, S. Maity, A review on development of industrial processes and emerging techniques for production of hydrogen from renewable and sustainable sources, Renewable and Sustainable Energy Reviews 23 (2013) 443–462. https://doi.org/10.1016/J.RSER.2013.02.019.

[57] J. Turner, G. Sverdrup, M.K. Mann, P.C. Maness, B. Kroposki, M. Ghirardi, R.J. Evans, D. Blake, Renewable hydrogen production, Int J Energy Res 32 (2008) 379–407. https://doi.org/10.1002/ER.1372.

[58] I. Dincer, C. Acar, A review on clean energy solutions for better sustainability, Int J Energy Res 39 (2015) 585–606. https://doi.org/10.1002/ER.3329.

[59] A.J. Guwy, R.M. Dinsdale, J.R. Kim, J. Massanet-Nicolau, G. Premier, Fermentative biohydrogen production systems integration, Bioresour Technol 102 (2011) 8534–8542. https://doi.org/10.1016/J.BIORTECH.2011.04.051.

[60] J.J. Bolívar Caballero, I.N. Zaini, W. Yang, Reforming processes for syngas production: A mini-review on the current status, challenges, and prospects for biomass conversion to fuels, Applications in Energy and Combustion Science 10 (2022). https://doi.org/10.1016/j.jaecs.2022.100064.

[61] J. Turner, G. Sverdrup, M.K. Mann, P.C. Maness, B. Kroposki, M. Ghirardi, R.J. Evans, D. Blake, Renewable hydrogen production, Int J Energy Res 32 (2008) 379–407. https://doi.org/10.1002/ER.1372.

[62] B. Sørensen, Hydrogen and Fuel Cells Emerging Technologies and Applications, Elsevier Academic Press, New York, 2011.

[63] R.D. Cortright, Hydrogen Generation from Biomass-Derived Carbohydrates via the Aqueous-Phase Reforming (APR) Process, 2005.

[64] H.L. Tsai, C.S. Wang, C.H. Lee, Hydrogen production in a thermal plasma hydrogen reformer using ethanol steam reforming, Journal of the Chinese Institute of Engineers 31 (2008) 417–425. https://doi.org/10.1080/02533839.2008.9671396.

[65] M. Balat, Possible methods for hydrogen production, Energy Sources, Part A: Recovery, Utilization and Environmental Effects 31 (2009) 39–50. https://doi.org/10.1080/15567030701468068.

[66] J.D. Holladay, J. Hu, D.L. King, Y. Wang, An overview of hydrogen production technologies, Catal Today 139 (2009) 244–260. https://doi.org/10.1016/J.CATTOD.2008.08.039.

[67] M. V Twigg, J. Mauhey PIc, Catalyst Handbook, Catalyst Handbook (2018). https://doi.org/10.1201/9781315138862.

[68] C. Song, Fuel processing for low-temperature and high-temperature fuel cells: Challenges, and opportunities for sustainable development in the 21st century, Catal Today 77 (2002) 17–49. https://doi.org/10.1016/S0920-5861(02)00231-6.

[69] M. El-Shafie, S. Kambara, Y. Hayakawa, Hydrogen Production Technologies Overview, (2019). https://doi.org/10.4236/JPEE.2019.71007.

[70] D.L. King, K. Brooks, C. Fischer, L. Pederson, G. Rawlings, V.S. Stenkamp, W. TeGrotenhuis, R. Wegeng, G. Whyatt, Fuel Reformation: Catalyst Requirements in Microchannel Architectures, (2005) 119–128. https://doi.org/10.1021/BK-2005-0914.CH007.

[71] R. Farrauto, S. Hwang, L. Shore, W. Ruettinger, J. Lampert, T. Giroux, Y. Liu, O. Ilinich, New Material Needs for Hydrocarbon Fuel Processing: Generating Hydrogen for the PEM Fuel Cell, Annu Rev Mater Res 33 (2003) 1–27. https://doi.org/10.1146/ANNUREV.MATSCI.33.022802.091348.

[72] G Hoogers, Fuel Cell Technology Handbook, (2002). https://doi.org/10.1201/9781420041552.

[73] P. Pietrogrande, M. Bezzeccheri, Fuel Processing, Fuel Cell Systems (1993) 121–156. https://doi.org/10.1007/978-1-4899-2424-7_5.

[74] M. Krumpelt, T.R. Krause, J.D. Carter, J.P. Kopasz, S. Ahmed, Fuel processing for fuel cell systems in transportation and portable power applications, Catal Today 77 (2002) 3–16. https://doi.org/10.1016/S0920-5861(02)00230-4.

[75] G. Kolb, R. Zapf, V. Hessel, H. Löwe, Propane steam reforming in micro-channels—results from catalyst screening and optimisation, Appl Catal A Gen 277 (2004) 155–166. https://doi.org/10.1016/J.APCATA.2004.09.007.

[76] A.M. Adris, B.B. Pruden, C.J. Lim, J.R. Grace, On the reported attempts to radically improve the performance of the steam methane reforming reactor, Can J Chem Eng 74 (1996) 177–186. https://doi.org/10.1002/CJCE.5450740202.

[77] K. Aasberg-Petersen, I. Dybkjær, C. V. Ovesen, N.C. Schjødt, J. Sehested, S.G. Thomsen, Natural gas to synthesis gas – Catalysts and catalytic processes, J Nat Gas Sci Eng 3 (2011) 423–459. https://doi.org/10.1016/J.JNGSE.2011.03.004.

[78] H. Song, L. Zhang, R.B. Watson, D. Braden, U.S. Ozkan, Investigation of bio-ethanol steam reforming over cobalt-based catalysts, Catal Today 129 (2007) 346–354. https://doi.org/10.1016/J.CATTOD.2006.11.028.

[79] H. Song, L. Zhang, U.S. Ozkan, Effect of synthesis parameters on the catalytic activity of Co–ZrO2 for bio-ethanol steam reforming, Green Chemistry 9 (2007) 686–694. https://doi.org/10.1039/B615087J.

[80] Y. Wang, Y.H. Chin, R.T. Rozmiarek, B.R. Johnson, Y. Gao, J. Watson, A.Y.L. Tonkovich, D.P. Vander Wiel, Highly active and stable Rh/MgOAl2O3 catalysts for methane steam reforming, Catal Today 98 (2004) 575–581. https://doi.org/10.1016/J.CATTOD.2004.09.011.

[81] JM Thomas, Surface and Defect Properties of Solids, The Chemical Society (1972). https://doi.org/10.1039/9781847556974.

[82] J. Wei, E. Iglesia, Mechanism and Site Requirements for Activation and Chemical Conversion of Methane on Supported Pt Clusters and Turnover Rate Comparisons among Noble Metals, Journal of Physical Chemistry B 108 (2004) 4094–4103. https://doi.org/10.1021/JP036985Z.

[83] J.R. Rostrup-Nielsen, Activity of nickel catalysts for steam reforming of hydrocarbons, J Catal 31 (1973) 173–199. https://doi.org/10.1016/0021-9517(73)90326-6.

[84] M. El-Shafie, S. Kambara, Y. Hayakawa, Hydrogen Production Technologies Overview, Journal of Power and Energy Engineering 07 (2019) 107–154. https://doi.org/10.4236/JPEE.2019.71007.

[85] S. Cavallaro, S. Freni, Ethanol steam reforming in a molten carbonate fuel cell. A preliminary kinetic investigation, Int J Hydrogen Energy 21 (1996) 465–469. https://doi.org/10.1016/0360-3199(95)00107-7.

[86] F. Haga, T. Nakajima, H. Miya, S. Mishima, Catalytic properties of supported cobalt catalysts for steam reforming of ethanol, Catal Letters 48 (1997) 223–227. https://doi.org/10.1023/A:1019039407126.

[87] N. Takezawa, N. Iwasa, Steam reforming and dehydrogenation of methanol: Difference in the catalytic functions of copper and group VIII metals, Catal Today 36 (1997) 45–56. https://doi.org/10.1016/S0920-5861(96)00195-2.

[88] V.M. Schmidt, P. Bröckerhoff, B. Höhlein, R. Menzer, U. Stimming, Utilization of methanol for polymer electrolyte fuel cells in mobile systems, J Power Sources 49 (1994) 299–313. https://doi.org/10.1016/0378-7753(93)01830-B.

[89] J.N. Armor, The multiple roles for catalysis in the production of H2, Appl Catal A Gen 176 (1999) 159–176. https://doi.org/10.1016/S0926-860X(98)00244-0.

[90] L.J. Pettersson, R. Westerholm, State of the art of multi-fuel reformers for fuel cell vehicles: problem identification and research needs, Int J Hydrogen Energy 26 (2001) 243–264. https://doi.org/10.1016/S0360-3199(00)00073-2.

[91] J.R. Rostrup-Nielsen, Conversion of hydrocarbons and alcohols for fuel cells, Physical Chemistry Chemical Physics 3 (2001) 283–288. https://doi.org/10.1039/B004660O.

[92] S.D. Angeli, G. Monteleone, A. Giaconia, A.A. Lemonidou, State-of-the-art catalysts for CH4 steam reforming at low temperature, Int J Hydrogen Energy 39 (2014) 1979–1997. https://doi.org/10.1016/J.IJHYDENE.2013.12.001.

[93] A. Czernichowski, Glidarc Assisted Preparation of the Synthesis Gas from Natural and Waste Hydrocarbons Gases, Oil & Gas Science and Technology 56 (2001) 181–198. https://doi.org/10.2516/OGST:2001018.

[94] D.L. Trimm, Z. Ilsen Önsan, Z. Ilsen, Ö. Nsan, ONBOARD FUEL CONVERSION FOR HYDROGEN-FUEL-CELL-DRIVEN VEHICLES, Catalysis Reviews 43 (2001) 31–84. https://doi.org/10.1081/CR-100104386.

[95] K.L. Hohn, L.D. Schmidt, Partial oxidation of methane to syngas at high space velocities over Rh-coated spheres, Appl Catal A Gen 211 (2001) 53–68. https://doi.org/10.1016/S0926-860X(00)00835-8.

[96] J.J. Krummenacher, K.N. West, L.D. Schmidt, Catalytic partial oxidation of higher hydrocarbons at millisecond contact times: decane, hexadecane, and diesel fuel, J Catal 215 (2003) 332–343. https://doi.org/10.1016/S0021-9517(03)00011-3.

[97] L. Pino, V. Recupero, S. Beninati, A.K. Shukla, M.S. Hegde, P. Bera, Catalytic partial-oxidation of methane on a ceria-supported platinum catalyst for application in fuel cell electric vehicles, Appl Catal A Gen 225 (2002) 63–75. https://doi.org/10.1016/S0926-860X(01)00734-7.

[98] H.E. Figen, S.Z. Baykara, Effect of ruthenium addition on molybdenum catalysts for syngas production via catalytic partial oxidation of methane in a monolithic reactor, Int J Hydrogen Energy 43 (2018) 1129–1138. https://doi.org/10.1016/J.IJHYDENE.2017.10.173.

[99] D.D. Nogare, N.J. Degenstein, R. Horn, P. Canu, L.D. Schmidt, Modeling spatially resolved data of methane catalytic partial oxidation on Rh foam catalyst at different inlet compositions and flowrates, J Catal 277 (2011) 134–148. https://doi.org/10.1016/J.JCAT.2010.10.020.

[100] D. Dalle Nogare, N.J. Degenstein, R. Horn, P. Canu, L.D. Schmidt, Modeling spatially resolved profiles of methane partial oxidation on a Rh foam catalyst with detailed chemistry, J Catal 258 (2008) 131–142. https://doi.org/10.1016/J.JCAT.2008.06.006.

[101] D.A. Hickman, L.D. Schmidt, Production of Syngas by Direct Catalytic Oxidation of Methane, Science (1979) 259 (1993) 343–346. https://doi.org/10.1126/SCIENCE.259.5093.343.

[102] D.A. Hickman, E.A. Haupfear, L.D. Schmidt, Synthesis gas formation by direct oxidation of methane over Rh monoliths, Catal Letters 17 (1993) 223–237. https://doi.org/10.1007/BF00766145.

[103] D.A. Hickman, L.D. Schmidt, Synthesis gas formation by direct oxidation of methane over Pt monoliths, J Catal 138 (1992) 267–282. https://doi.org/10.1016/0021-9517(92)90022-A.

[104] L. Basini, K. Aasberg-Petersen, A. Guarinoni, M. Østberg, Catalytic partial oxidation of natural gas at elevated pressure and low residence time, Catal Today 64 (2001) 9–20. https://doi.org/10.1016/S0920-5861(00)00504-6.

[105] Z. Ilsen Önsan, A.K. Avci, Reactor Design for Fuel Processing, Fuel Cells: Technologies for Fuel Processing (2011) 451–516. https://doi.org/10.1016/B978-0-444-53563-4.10014-8.

[106] C.Z. I Dincer, Sustainable energy systems and applications, Springer Science & Business Media (2011).

[107] F.M. Sapountzi, J.M. Gracia, C.J. (Kees J. Weststrate, H.O.A. Fredriksson, J.W. (Hans) Niemantsverdriet, Electrocatalysts for the generation of hydrogen, oxygen and synthesis gas, Prog Energy Combust Sci 58 (2017) 1–35. https://doi.org/10.1016/J.PECS.2016.09.001.

[108] R. Bhandari, C.A. Trudewind, P. Zapp, Life cycle assessment of hydrogen production via electrolysis – a review, J Clean Prod 85 (2014) 151–163. https://doi.org/10.1016/J.JCLEPRO.2013.07.048.

[109] M. Wietschel, M. Ball, The Hydrogen Economy: Opportunities and Challenges, The Hydrogen Economy: Opportunities and Challenges 9780521882163 (2009) 1–646. https://doi.org/10.1017/CBO9780511635359.

[110] A. Ursúa, L.M. Gandía, P. Sanchis, Hydrogen production from water electrolysis: Current status and future trends, Proceedings of the IEEE 100 (2012) 410–426. https://doi.org/10.1109/JPROC.2011.2156750.

[111] S.Y. Gómez, D. Hotza, Current developments in reversible solid oxide fuel cells, Renewable and Sustainable Energy Reviews 61 (2016) 155–174. https://doi.org/10.1016/J.RSER.2016.03.005.

[112] E.C. Shin, P.A. Ahn, H.H. Seo, J.M. Jo, S.D. Kim, S.K. Woo, J.H. Yu, J. Mizusaki, J.S. Lee, Polarization mechanism of high temperature electrolysis in a Ni–YSZ/YSZ/LSM solid oxide cell by parametric impedance analysis, Solid State Ion 232 (2013) 80–96. https://doi.org/10.1016/J.SSI.2012.10.028.

[113] T. Ishihara, N. Jirathiwathanakul, H. Zhong, Intermediate temperature solid oxide electrolysis cell using LaGaO3 based perovskite electrolyte, Energy Environ Sci 3 (2010) 665–672. https://doi.org/10.1039/B915927D.

[114] C. Zhang, M.E. Grass, A.H. McDaniel, S.C. Decaluwe, F. El Gabaly, Z. Liu, K.F. McCarty, R.L. Farrow, M.A. Linne, Z. Hussain, G.S. Jackson, H. Bluhm, B.W. Eichhorn, Measuring fundamental properties in operating solid oxide electrochemical cells by using in situ X-ray photoelectron spectroscopy, Nat Mater 9 (2010) 944–949. https://doi.org/10.1038/nmat2851.

[115] X.K. Gu, E. Nikolla, Fundamental Insights into High-Temperature Water Electrolysis Using Ni-Based Electrocatalysts, Journal of Physical Chemistry C 119 (2015) 26980–26988. https://doi.org/10.1021/ACS.JPCC.5B07814.

[116] S.Y. Gómez, D. Hotza, Current developments in reversible solid oxide fuel cells, Renewable and Sustainable Energy Reviews 61 (2016) 155–174. https://doi.org/10.1016/J.RSER.2016.03.005.

[117] Y. Zheng, J. Wang, B. Yu, W. Zhang, J. Chen, J. Qiao, J. Zhang, A review of high temperature co-electrolysis of H2O and CO2 to produce sustainable fuels using solid oxide electrolysis cells (SOECs): advanced materials and technology, Chem Soc Rev 46 (2017) 1427–1463. https://doi.org/10.1039/C6CS00403B.

[118] Y. Wang, W. Li, L. Ma, W. Li, X. Liu, Degradation of solid oxide electrolysis cells: Phenomena, mechanisms, and emerging mitigation strategies—A review, J Mater Sci Technol 55 (2020) 35–55. https://doi.org/10.1016/J.JMST.2019.07.026.

[119] W.H.S. J Weissbart, Study of electrolytic dissociation of CO2-H2O using a solid oxide electrolyte, NASA CR (1967).

[120] C. Graves, S.D. Ebbesen, M. Mogensen, Co-electrolysis of CO2 and H2O in solid oxide cells: Performance and durability, Solid State Ion 192 (2011) 398–403. https://doi.org/10.1016/J.SSI.2010.06.014.

[121] S.D. Ebbesen, J. Høgh, K.A. Nielsen, J.U. Nielsen, M. Mogensen, Durable SOC stacks for production of hydrogen and synthesis gas by high temperature electrolysis, Int J Hydrogen Energy 36 (2011) 7363–7373. https://doi.org/10.1016/J.IJHYDENE.2011.03.130.

[122] S.D. Ebbesen, C. Graves, M. Mogensen, Production of synthetic fuels by co-electrolysis of steam and carbon dioxide, Int J Green Energy 6 (2009) 646–660. https://doi.org/10.1080/15435070903372577.

[123] M. Shen, F. Ai, H. Ma, H. Xu, Y. Zhang, Progress and prospects of reversible solid oxide fuel cell materials, IScience 24 (2021) 103464. https://doi.org/10.1016/J.ISCI.2021.103464.

[124] Z. Zhan, W. Kobsiriphat, J.R. Wilson, M. Pillai, I. Kim, S.A. Barnett, Syngas Production By Coelectrolysis of CO2/H2O: The Basis for a Renewable Energy Cycle, Energy and Fuels 23 (2009) 3089–3096. https://doi.org/10.1021/EF900111F.

[125] S.D. Ebbesen, M. Mogensen, Electrolysis of carbon dioxide in Solid Oxide Electrolysis Cells, J Power Sources 193 (2009) 349–358. https://doi.org/10.1016/J.JPOWSOUR.2009.02.093.

[126] S.D. Ebbesen, R. Knibbe, M. Mogensen, Co-Electrolysis of Steam and Carbon Dioxide in Solid Oxide Cells, J Electrochem Soc 159 (2012) F482–F489. https://doi.org/10.1149/2.076208JES/XML.

[127] J.E. O'Brien, C.M. Stoots, J.S. Herring, M.G. McKellar, E.A. Harvego, M.S. Sohal, K.G. Condie, High Temperature Electrolysis for Hydrogen Production from Nuclear Energy – TechnologySummary, (2010). https://doi.org/10.2172/978368.

[128] Wenying Li, Study on the mechanism and performance of co-electrolysis of carbon dioxide and water in solid oxide electrolysis cell, Tsinghua University (2015).

[129] J. Mougin, A. Chatroux, K. Couturier, M. Petitjean, M. Reytier, G. Gousseau, F. Lefebvre-Joud, High Temperature Steam Electrolysis Stack with Enhanced Performance and Durability, Energy Procedia 29 (2012) 445–454. https://doi.org/10.1016/J.EGYPRO.2012.09.052.

[130] M. Ni, Computational fluid dynamics modeling of a solid oxide electrolyzer cell for hydrogen production, Int J Hydrogen Energy 34 (2009) 7795–7806. https://doi.org/10.1016/J.IJHYDENE.2009.07.080.

[131] M. Ni, Modeling of a solid oxide electrolysis cell for carbon dioxide electrolysis, Chemical Engineering Journal 164 (2010) 246–254. https://doi.org/10.1016/J.CEJ.2010.08.032.

[132] M. Ni, 2D thermal modeling of a solid oxide electrolyzer cell (SOEC) for syngas production by H2O/CO2 co-electrolysis, Int J Hydrogen Energy 37 (2012) 6389–6399. https://doi.org/10.1016/J.IJHYDENE.2012.01.072.

[133] Y.F. Bu, Q. Zhong, D.D. Xu, X.L. Zhao, W.Y. Tan, Performance of Y0.9Sr0.1Cr0.9Fe0.1O3−δ as a sulfur-tolerant anode material for intermediate temperate solid oxide fuel cells, J Power Sources 250 (2014) 143–151. https://doi.org/10.1016/J.JPOWSOUR.2013.11.005.

[134] F.W. Poulsen, J.J. Bentzen, T. Jacobsen, E. Skou, M.J.L. Oestergaard, High temperature electrochemical behaviour of fast ion and mixed conductors, Denmark: N. p. (1993) 311–318.

[135] K. Zhu, B. Luo, Z. Liu, X. Wen, Recent advances and prospects of symmetrical solid oxide fuel cells, Ceram Int 48 (2022) 8972–8986. https://doi.org/10.1016/J.CERAMINT.2022.01.258.

[136] S. He, M. Li, J. Hui, X. Yue, In-situ construction of ceria-metal/titanate heterostructure with controllable architectures for efficient fuel electrochemical conversion, Appl Catal B 298 (2021) 120588. https://doi.org/10.1016/J.APCATB.2021.120588.

[137] W. van Gool, P.H. Bottelberghs, Domain model for anomalously fast diffusion, J Solid State Chem 7 (1973) 59–65. https://doi.org/10.1016/0022-4596(73)90122-9.

[138] S.D. Ebbesen, M. Mogensen, Exceptional durability of solid oxide cells, Electrochemical and Solid-State Letters 13 (2010) B106. https://doi.org/10.1149/1.3455882.

[139] P. Blennow, A. Hagen, K.K. Hansen, L.R. Wallenberg, M. Mogensen, Defect and electrical transport properties of Nb-doped SrTiO3, Solid State Ion 179 (2008) 2047–2058. https://doi.org/10.1016/J.SSI.2008.06.023.

[140] O.A. Marina, L.R. Pederson, M.C. Williams, G.W. Coffey, K.D. Meinhardt, C.D. Nguyen, E.C. Thomsen, Electrode Performance in Reversible Solid Oxide Fuel Cells, J Electrochem Soc 154 (2007) B452. https://doi.org/10.1149/1.2710209/XML.

[141] S. Tao, J.T.S. Irvine, Synthesis and Characterization of (La0.75Sr0.25) Cr0.5Mn0.5 O 3 − δ , a Redox-Stable, Efficient Perovskite Anode for SOFCs, J Electrochem Soc 151 (2004) A252. https://doi.org/10.1149/1.1639161.

[142] Xingbao Zhu, Research on fuel cell anode composites based on manganese iron doped strontium lanthanum chromate, Harbin Institute of Technology (2008).

[143] S. Xu, S. Chen, M. Li, K. Xie, Y. Wang, Y. Wu, Composite cathode based on Fe-loaded LSCM for steam electrolysis in an oxide-ion-conducting solid oxide electrolyser, J Power Sources 239 (2013) 332–340. https://doi.org/10.1016/J.JPOWSOUR.2013.03.182.

[144] L.L. Zhang, S. Duan, X.L. Yang, G. Liang, Y.H. Huang, X.Z. Cao, J. Yang, M. Li, M.C. Croft, C. Lewis, Insight into cobalt-doping in Li2FeSiO4 cathode material for lithium-ion battery, J Power Sources 274 (2015) 194–202. https://doi.org/10.1016/J.JPOWSOUR.2014.10.048.

[145] C.D. Savaniu, J.T.S. Irvine, Reduction studies and evaluation of surface modified A-site deficient La-doped SrTiO3 as anode material for IT-SOFCs, J Mater Chem 19 (2009) 8119–8128. https://doi.org/10.1039/B912305A.

[146] M. Backhaus-Ricoult, K. Adib, T. St.Clair, B. Luerssen, L. Gregoratti, A. Barinov, In-situ study of operating SOFC LSM/YSZ cathodes under polarization by photoelectron microscopy, Solid State Ion 179 (2008) 891–895. https://doi.org/10.1016/J.SSI.2008.02.033.

[147] S.B. Adler, Factors governing oxygen reduction in solid oxide fuel cell cathodes, Chem Rev 104 (2004) 4791–4843. https://doi.org/10.1021/cr020724o.

[148] M. Sase, D. Ueno, K. Yashiro, A. Kaimai, T. Kawada, J. Mizusaki, Interfacial reaction and electrochemical properties of dense (La,Sr) CoO3−δ cathode on YSZ (1 0 0), Journal of Physics and Chemistry of Solids 66 (2005) 343–348. https://doi.org/10.1016/J.JPCS.2004.06.057.

[149] J. Song, D. Ning, B. Boukamp, J.M. Bassat, H.J.M. Bouwmeester, Structure, electrical conductivity and oxygen transport properties of Ruddlesden–Popper phases Ln n+1 Ni n O 3n+1 (Ln = La, Pr and Nd; n = 1, 2 and 3), J Mater Chem A Mater 8 (2020) 22206–22221. https://doi.org/10.1039/D0TA06731H.

[150] H. Li, X. Chen, S. Chen, Y. Wu, K. Xie, Composite manganate oxygen electrode enhanced with iron oxide nanocatalyst for high temperature steam electrolysis in a proton-conducting solid oxide electrolyzer, Int J Hydrogen Energy 40 (2015) 7920–7931. https://doi.org/10.1016/J.IJHYDENE.2015.04.067.

[151] I. Villarreal, C. Jacobson, A. Leming, Y. Matus, S. Visco, L. De Jonghe, Metal-supported solid oxide fuel cells, Electrochemical and Solid-State Letters 6 (2003) A178. https://doi.org/10.1149/1.1592372.

[152] W. Zhang, B. Yu, J. Xu, Investigation of single SOEC with BSCF anode and SDC barrier layer, Int J Hydrogen Energy 37 (2012) 837–842. https://doi.org/10.1016/J.IJHYDENE.2011.04.049.

[153] F. Chauveau, J. Mougin, J.M. Bassat, F. Mauvy, J.C. Grenier, A new anode material for solid oxide electrolyser: The neodymium nickelate Nd2NiO4+δ, J Power Sources 195 (2010) 744–749. https://doi.org/10.1016/J.JPOWSOUR.2009.08.003.

[154] T. Ogier, J.M. Bassat, F. Mauvy, S. Fourcade, J.C. Grenier, K. Couturier, M. Petitjean, J. Mougin, Enhanced Performances of Structured Oxygen Electrodes for High Temperature Steam Electrolysis, Fuel Cells 13 (2013) 536–541. https://doi.org/10.1002/FUCE.201200201.

[155] K. Chen, N. Ai, S.P. Jiang, Development of (Gd,Ce)O2-Impregnated (La,Sr)MnO3 Anodes of High Temperature Solid Oxide Electrolysis Cells, J Electrochem Soc 157 (2010) P89. https://doi.org/10.1149/1.3481436.

[156] C. Rossignol, J.M. Ralph, J.M. Bae, J.T. Vaughey, Ln1−xSrxCoO3 (Ln=Gd, Pr) as a cathode for intermediate-temperature solid oxide fuel cells, Solid State Ion 175 (2004) 59–61. https://doi.org/10.1016/J.SSI.2004.09.021.

[157] F. Tietz, D. Sebold, A. Brisse, J. Schefold, Degradation phenomena in a solid oxide electrolysis cell after 9000 h of operation, J Power Sources 223 (2013) 129–135. https://doi.org/10.1016/J.JPOWSOUR.2012.09.061.

[158] B. Wei, K. Chen, C.C. Wang, Z. Lü, S.P. Jiang, Cr deposition on porous La0.6Sr0.4Co0.2Fe0.8O3 − δ electrodes of solid oxide cells under open circuit condition, Solid State Ion 281 (2015) 29–37. https://doi.org/10.1016/J.SSI.2015.08.018.

[159] Z. Shao, S.M. Halle, A high-performance cathode for the next generation of solid-oxide fuel cells, Nature 2004 431:7005 431 (2004) 170–173. https://doi.org/10.1038/nature02863.

[160] Zhang W Q, Yu B, Zhang P, Xu J M, Solid oxide electrolysis cell, Scientia Sinica Chimica (2011) 6–9.

[161] J. Suntivich, K.J. May, H.A. Gasteiger, J.B. Goodenough, Y. Shao-Horn, A perovskite oxide optimized for oxygen evolution catalysis from molecular orbital principles, Science (1979) 334 (2011) 1383–1385. https://doi.org/10.1126/SCIENCE.1212858.

[162] M.A. Laguna-Bercero, N. Kinadjan, R. Sayers, H. El Shinawi, C. Greaves, S.J. Skinner, Performance of La2–xSrxCo0.5Ni0.5O4±δ as an Oxygen Electrode for Solid Oxide Reversible Cells, Fuel Cells 11 (2011) 102–107. https://doi.org/10.1002/FUCE.201000067.

[163] F. Chauveau, J. Mougin, J.M. Bassat, F. Mauvy, J.C. Grenier, A new anode material for solid oxide electrolyser: The neodymium nickelate Nd2NiO4+δ, J Power Sources 195 (2010) 744–749. https://doi.org/10.1016/J.JPOWSOUR.2009.08.003.

[164] A. Chroneos, D. Parfitt, J.A. Kilner, R.W. Grimes, Anisotropic oxygen diffusion in tetragonal La2NiO4+δ: molecular dynamics calculations, J Mater Chem 20 (2009) 266–270. https://doi.org/10.1039/B917118E.

[165] G. Tsekouras, J.T.S. Irvine, The role of defect chemistry in strontium titanates utilised for high temperature steam electrolysis, J Mater Chem 21 (2011) 9367–9376. https://doi.org/10.1039/C1JM11313E.

[166] A. Chroneos, D. Parfitt, J.A. Kilner, R.W. Grimes, Anisotropic oxygen diffusion in tetragonal La2NiO4+δ: molecular dynamics calculations, J Mater Chem 20 (2009) 266–270. https://doi.org/10.1039/B917118E.

[167] T. Chen, Y. Zhou, C. Yuan, M. Liu, X. Meng, Z. Zhan, C. Xia, S. Wang, Impregnated Nd2NiO4+δ- scandia stabilized zirconia composite cathode for intermediate-temperature solid oxide fuel cells, J Power Sources 269 (2014) 812–817. https://doi.org/10.1016/J.JPOWSOUR.2014.07.073.

[168] J. Li, C. Zhong, X. Meng, H. Wu, H. Nie, Z. Zhan, S. Wang, Sr2Fe1.5Mo0.5O6–δ – Zr0.84Y0.16O2–δ Materials as Oxygen Electrodes for Solid Oxide Electrolysis Cells, Fuel Cells 14 (2014) 1046–1049. https://doi.org/10.1002/FUCE.201400021.

[169] K. Yashiro, T. Nakamura, M. Sase, F. Hermes, K. Sato, T. Kawada, J. Mizusaki, Electrode Performance at Hetero-interface of Perovskite-related Oxides, (La, Sr)CoO3-δ / (La, Sr)2CoO4-δ, ECS Trans 7 (2007) 1287–1292. https://doi.org/10.1149/1.2729230.

[170] M. Sase, K. Yashiro, K. Sato, J. Mizusaki, T. Kawada, N. Sakai, K. Yamaji, T. Horita, H. Yokokawa, Enhancement of oxygen exchange at the hetero interface of (La,Sr)CoO3/(La,Sr)2CoO4 in composite ceramics, Solid State Ion 178 (2008) 1843–1852. https://doi.org/10.1016/J.SSI.2007.11.039.

[171] J.W. Han, B. Yildiz, Mechanism for enhanced oxygen reduction kinetics at the (La,Sr)CoO 3-δ/(La,Sr) 2CoO 4+δ hetero-interface, Energy Environ Sci 5 (2012) 8598–8607. https://doi.org/10.1039/C2EE03592H.

[172] C.S. Tedmon, H.S. Spacil, S.P. Mitoff, Cathode Materials and Performance in High-Temperature Zirconia Electrolyte Fuel Cells, J Electrochem Soc 116 (1969) 1170. https://doi.org/10.1149/1.2412271.

[173] High-temperature Solid Oxide Fuel Cells: Fundamentals, Design and Applications, Materials Today 5 (2002) 55. https://doi.org/10.1016/s1369-7021(02)01241-5.

[174] K. Eguchi, T. Hatagishi, H. Arai, Power generation and steam electrolysis characteristics of an electrochemical cell with a zirconia- or ceria-based electrolyte, Solid State Ion 86–88 (1996) 1245–1249. https://doi.org/10.1016/0167-2738(96)00295-0.

[175] K. Xie, Y. Zhang, G. Meng, J.T.S. Irvine, Direct synthesis of methane from CO2/H2O in an oxygen-ion conducting solid oxide electrolyser, Energy Environ Sci 4 (2011) 2218–2222. https://doi.org/10.1039/C1EE01035B.

[176] A. Hauch, S.D. Ebbesen, S.H. Jensen, M. Mogensen, Highly efficient high temperature electrolysis, J Mater Chem 18 (2008) 2331–2340. https://doi.org/10.1039/B718822F.

[177] S. Pandiyan, M. Bianco, A. El-Kharouf, R.I. Tomov, R. Steinberger-Wilckens, Evaluation of inkjet-printed spinel coatings on standard and surface nitrided ferritic stainless steels for interconnect application in solid oxide fuel cell devices, Ceram Int 48 (2022) 20456–20466. https://doi.org/10.1016/J.CERAMINT.2022.04.003.

[178] H.S. Spacil, C.S. Tedmon, Electrochemical Dissociation of Water Vapor in Solid Oxide Electrolyte Cells: I . Thermodynamics and Cell Characteristics, J Electrochem Soc 116 (1969) 1618. https://doi.org/10.1149/1.2411642.

[179] W. Dönitz, G. Dietrich, E. Erdle, Electrochemical high temperature technology for hydrogen production or direct electricity generation, Int J Hydrogen Energy (1988).

[180] J.E. O’Brien, C.M. Stoots, J.S. Herring, P.A. Lessing, J.J. Hartvigsen, S. Elangovan, Performance Measurements of Solid-Oxide Electrolysis Cells for Hydrogen Production, J Fuel Cell Sci Technol 2 (2005) 156–163. https://doi.org/10.1115/1.1895946.

[181] C. Stoots, J. O'Brien, J. Hartvigsen, Results of recent high temperature coelectrolysis studies at the Idaho National Laboratory, Int J Hydrogen Energy 34 (2009) 4208–4215. https://doi.org/10.1016/J.IJHYDENE.2008.08.029.

[182] J.E. O'Brien, M.G. McKellar, E.A. Harvego, C.M. Stoots, High-temperature electrolysis for large-scale hydrogen and syngas production from nuclear energy – summary of system simulation and economic analyses, Int J Hydrogen Energy 35 (2010) 4808–4819. https://doi.org/10.1016/J.IJHYDENE.2009.09.009.

[183] X. Zhang, J.E. O'Brien, G. Tao, C. Zhou, G.K. Housley, Experimental design, operation, and results of a 4 kW high temperature steam electrolysis experiment, J Power Sources 297 (2015) 90–97. https://doi.org/10.1016/J.JPOWSOUR.2015.07.098.

[184] X. Zhang, J.E. O'Brien, R.C. O'Brien, J.J. Hartvigsen, G. Tao, G.K. Housley, Improved durability of SOEC stacks for high temperature electrolysis, Int J Hydrogen Energy (2013). https://doi.org/10.1016/J.IJHYDENE.2012.09.176.

[185] J. Schefold, A. Brisse, F. Tietz, Nine Thousand Hours of Operation of a Solid Oxide Cell in Steam Electrolysis Mode, J Electrochem Soc 159 (2011) A137–A144. https://doi.org/10.1149/2.076202JES.

[186] V.N. Nguyen, Q. Fang, U. Packbier, L. Blum, Long-term tests of a Jülich planar short stack with reversible solid oxide cells in both fuel cell and electrolysis modes, Int J Hydrogen Energy 38 (2013) 4281–4290. https://doi.org/10.1016/J.IJHYDENE.2013.01.192.

[187] F. Petipas, A. Brisse, C. Bouallou, Model-based behaviour of a high temperature electrolyser system operated at various loads, J Power Sources 239 (2013) 584–595. https://doi.org/10.1016/J.JPOWSOUR.2013.03.027.

[188] L. Shao, S. Wang, J. Qian, X. Ye, T. Wen, Optimization of the electrode-supported tubular solid oxide cells for application on fuel cell and steam electrolysis, Int J Hydrogen Energy 38 (2013) 4272–4280. https://doi.org/10.1016/J.IJHYDENE.2012.12.144.

[189] J.S. Herring, J.E. O'Brien, C.M. Stoots, G.L. Hawkes, J.J. Hartvigsen, M. Shahnam, Progress in high-temperature electrolysis for hydrogen production using planar SOFC technology, Int J Hydrogen Energy 32 (2007) 440–450. https://doi.org/10.1016/J.IJHYDENE.2006.06.061.

[190] W. Wang, Y. Huang, S. Jung, J.M. Vohs, R.J. Gorte, A Comparison of LSM, LSF, and LSCo for Solid Oxide Electrolyzer Anodes, J Electrochem Soc 153 (2006) A2066. https://doi.org/10.1149/1.2345583.

[191] A. Hauch, S.H. Jensen, J.B. Bilde-Sørensen, M. Mogensen, Silica Segregation in the Ni/YSZ Electrode, J Electrochem Soc 154 (2007) A619. https://doi.org/10.1149/1.2733861.

[192] Y. Matsuzaki, I. Yasuda, Dependence of SOFC Cathode Degradation by Chromium-Containing Alloy on Compositions of Electrodes and Electrolytes, J Electrochem Soc 148 (2001) A126. https://doi.org/10.1149/1.1339869.

[193] H. Dulli, E.W. Plummer, P.A. Dowben, J. Choi, S.H. Liou, Surface electronic phase transition in colossal magnetoresistive manganese perovskites: La0.65Sr0.35MnO3, Appl Phys Lett 77 (2000) 570–572. https://doi.org/10.1063/1.127047.

[194] C.N. Borca, B. Xu, T. Komesu, H.K. Jeong, M.T. Liu, S.H. Liou, P.A. Dowben, The surface phases of the La0.65Pb0.35MnO3 manganese perovskite surface, Surf Sci 512 (2002) L346–L352. https://doi.org/10.1016/S0039-6028(02)01494-2.

[195] B. Borglum, E. Tang, M. Pastula, Development of Solid Oxide Fuel Cells at Versa Power Systems, ECS Trans 35 (2011) 63. https://doi.org/10.1149/1.3569979.

[196] E. Lay-Grindler, J. Laurencin, J. Villanova, P. Cloetens, P. Bleuet, A. Mansuy, J. Mougin, G. Delette, Degradation study by 3D reconstruction of a nickel–yttria stabilized zirconia cathode after high temperature steam electrolysis operation, J Power Sources 269 (2014) 927–936. https://doi.org/10.1016/J.JPOWSOUR.2014.07.066.

[197] A. Hauch, S.D. Ebbesen, S.H. Jensen, M. Mogensen, Solid Oxide Electrolysis Cells: Microstructure and Degradation of the Ni/Yttria-Stabilized Zirconia Electrode, J Electrochem Soc 155 (2008) B1184. https://doi.org/10.1149/1.2967331.

[198] D.A. Osinkin, B.L. Kuzin, N.M. Bogdanovich, Effect of oxygen activity and water partial pressure to degradation rate of Ni cermet electrode contacting Zr0.84Y0.16O 1.92 electrolyte, Russian Journal of Electrochemistry 46 (2010) 41–48. https://doi.org/10.1134/S1023193510010052.

[199] M.S. Sohal, J.E. O’Brien, C.M. Stoots, J.J. Hartvigsen, D. Larsen, S. Elangovan, J.S. Herring, J.D. Carter, V.I. Sharma, B. Yildiz, Critical Causes of Degradation in Integrated Laboratory Scale Cells during High Temperature Electrolysis, (2009). https://doi.org/10.2172/961923.

[200] J.W. Fergus, Effect of cathode and electrolyte transport properties on chromium poisoning in solid oxide fuel cells, Int J Hydrogen Energy 32 (2007) 3664–3671. https://doi.org/10.1016/J.IJHYDENE.2006.08.005.

[201] M. Stanislowski, J. Froitzheim, L. Niewolak, W.J. Quadakkers, K. Hilpert, T. Markus, L. Singheiser, Reduction of chromium vaporization from SOFC interconnectors by highly effective coatings, J Power Sources 164 (2007) 578–589. https://doi.org/10.1016/J.JPOWSOUR.2006.08.013.

[202] Y. Zhen, A.I.Y. Tok, F.Y.C. Boey, S.P. Jiang, Development of Cr-tolerant cathodes of solid oxide fuel cells, Electrochemical and Solid-State Letters 11 (2008) B42. https://doi.org/10.1149/1.2828212.

[203] J.E. O'brien, C.M. Stoots, High Temperature Electrolysis Using Electrode-Supported Cells European Fuel Cell Forum 2010 High Temperature Electrolysis using Electrode-Supported Cells, (2010).

[204] A. V. Virkar, Mechanism of oxygen electrode delamination in solid oxide electrolyzer cells, Int J Hydrogen Energy 35 (2010) 9527–9543. https://doi.org/10.1016/J.IJHYDENE.2010.06.058.

[205] J. Fleig, Solid Oxide Fuel Cell Cathodes: Polarization Mechanisms and Modeling of the Electrochemical Performance, Annu Rev Mater Res 33 (2003) 361–382. https://doi.org/10.1146/ANNUREV.MATSCI.33.022802.093258.

[206] T. Jacobsen, M. Mogensen, The Course of Oxygen Partial Pressure and Electric Potentials across an Oxide Electrolyte Cell, ECS Trans 13 (2008) 259–273. https://doi.org/10.1149/1.3050398.

[207] S.N. Rashkeev, M. V. Glazoff, Atomic-scale mechanisms of oxygen electrode delamination in solid oxide electrolyzer cells, Int J Hydrogen Energy 37 (2012) 1280–1291. https://doi.org/10.1016/J.IJHYDENE.2011.09.117.

[208] M. Liang, B. Yu, M. Wen, J. Chen, J. Xu, Y. Zhai, Preparation of LSM–YSZ composite powder for anode of solid oxide electrolysis cell and its activation mechanism, J Power Sources 190 (2009) 341–345. https://doi.org/10.1016/J.JPOWSOUR.2008.12.132.

[209] M. Backhaus-Ricoult, K. Adib, T. St.Clair, B. Luerssen, L. Gregoratti, A. Barinov, In-situ study of operating SOFC LSM/YSZ cathodes under polarization by photoelectron microscopy, Solid State Ion 179 (2008) 891–895. https://doi.org/10.1016/J.SSI.2008.02.033.

[210] M. Keane, M.K. Mahapatra, A. Verma, P. Singh, LSM–YSZ interactions and anode delamination in solid oxide electrolysis cells, Int J Hydrogen Energy 37 (2012) 16776–16785. https://doi.org/10.1016/J.IJHYDENE.2012.08.104.

[211] Y. Zheng, Q. Li, T. Chen, W. Wu, C. Xu, W.G. Wang, Comparison of performance and degradation of large-scale solid oxide electrolysis cells in stack with different composite air electrodes, Int J Hydrogen Energy 40 (2015) 2460–2472. https://doi.org/10.1016/J.IJHYDENE.2014.12.101.

[212] P. Hjalmarsson, X. Sun, Y.L. Liu, M. Chen, Influence of the oxygen electrode and inter-diffusion barrier on the degradation of solid oxide electrolysis cells, J Power Sources 223 (2013) 349–357. https://doi.org/10.1016/J.JPOWSOUR.2012.08.063.

[213] R. Knibbe, M.L. Traulsen, A. Hauch, S.D. Ebbesen, M. Mogensen, Solid Oxide Electrolysis Cells: Degradation at High Current Densities, J Electrochem Soc 157 (2010) B1209. https://doi.org/10.1149/1.3447752.

[214] M.A. Peña, J.L.G. Fierro, Chemical structures and performance of perovskite oxides, Chem Rev 101 (2001) 1981–2017. https://doi.org/10.1021/CR980129F.

[215] X. Xu, Y. Zhong, Z. Shao, Double Perovskites in Catalysis, Electrocatalysis, and Photo(electro)catalysis, Trends Chem 1 (2019) 410–424. https://doi.org/10.1016/J.TRECHM.2019.05.006.

[216] B. Delgado-Galicia, A. López-García, A.J. Carrillo, J.M. Serra, Effects of lanthanide doping on the electrode properties and exsolution behavior of A-site deficient Sr1.9Fe1.3Ni0.2Mo0.5O6-δ double perovskites, Solid State Ion 410 (2024) 116532. https://doi.org/10.1016/J.SSI.2024.116532.

[217] Y. Hou, L. Wang, L. Bian, Q. Zhang, L. Chen, K. chih Chou, Effect of high-valence elements doping at B site of La0.5Sr0.5FeO3-δ, Ceram Int 48 (2022) 4223–4229. https://doi.org/10.1016/J.CERAMINT.2021.10.214.

[218] S. Park, H. Han, W. Yoon, J. Choi, Y. Kim, H. Kim, W.B. Kim, Improving a Sulfur-Tolerant Ruddlesden–Popper Catalyst by Fluorine Doping for CO 2 Electrolysis Reaction, ACS Sustain Chem Eng 8 (2020) 6564–6571. https://doi.org/10.1021/ACSSUSCHEMENG.0C01774.

[219] T. Yajima, F. Takeiri, K. Aidzu, H. Akamatsu, K. Fujita, W. Yoshimune, M. Ohkura, S. Lei, V. Gopalan, K. Tanaka, C.M. Brown, M.A. Green, T. Yamamoto, Y. Kobayashi, H. Kageyama, A labile hydride strategy for the synthesis of heavily nitridized BaTiO3, Nat Chem 7 (2015) 1017–1023. https://doi.org/10.1038/NCHEM.2370.

[220] F. Su, C. Xia, R. Peng, Novel fluoride-doped barium cerate applied as stable electrolyte in proton conducting solid oxide fuel cells, J Eur Ceram Soc 35 (2015) 3553–3558. https://doi.org/10.1016/J.JEURCERAMSOC.2015.05.016.

[221] Z. Zhang, Y. Zhu, Y. Zhong, W. Zhou, Z. Shao, Anion Doping: A New Strategy for Developing High-Performance Perovskite-Type Cathode Materials of Solid Oxide Fuel Cells, Adv Energy Mater 7 (2017). https://doi.org/10.1002/AENM.201700242.

[222] T. Wei, L. Jia, J.L. Luo, B. Chi, J. Pu, J. Li, CO2 dry reforming of CH4 with Sr and Ni co-doped LaCrO3 perovskite catalysts, Appl Surf Sci 506 (2020). https://doi.org/10.1016/J.APSUSC.2019.144699.

[223] T. Wei, L. Jia, H. Zheng, B. Chi, J. Pu, J. Li, LaMnO3-based perovskite with in-situ exsolved Ni nanoparticles: a highly active, performance stable and coking resistant catalyst for CO2 dry reforming of CH4, Appl Catal A Gen 564 (2018) 199–207. https://doi.org/10.1016/J.APCATA.2018.07.031.

[224] D. Neagu, T.S. Oh, D.N. Miller, H. Ménard, S.M. Bukhari, S.R. Gamble, R.J. Gorte, J.M. Vohs, J.T.S. Irvine, Nano-socketed nickel particles with enhanced coking resistance grown in situ by redox exsolution, Nature Communications 2015 6:1 6 (2015) 1–8. https://doi.org/10.1038/ncomms9120.

[225] T. Wei, P. Qiu, L. Jia, Y. Tan, X. Yang, S. Sun, F. Chen, J. Li, Power and carbon monoxide co-production by a proton-conducting solid oxide fuel cell with La0.6Sr0.2Cr0.85Ni0.15O3−δ for on-cell dry reforming of CH4 by CO2, J Mater Chem A Mater 8 (2020) 9806–9812. https://doi.org/10.1039/D0TA03458D.

[226] C. Li, Y. Deng, L. Yang, B. Liu, D. Yan, L. Fan, J. Li, L. Jia, An active and stable hydrogen electrode of solid oxide cells with exsolved Fe-Co-Ni nanoparticles from Sr 2 FeCo 0.2 Ni 0.2 Mo 0.6 O 6-δ double-perovskite, (2023). https://doi.org/10.1016/j.apmate.2023.100133.

[227] S. Park, Y. Kim, H. Han, Y.S. Chung, W. Yoon, J. Choi, W.B. Kim, In situ exsolved Co nanoparticles on Ruddlesden-Popper material as highly active catalyst for CO2 electrolysis to CO, Appl Catal B 248 (2019) 147–156. https://doi.org/10.1016/J.APCATB.2019.02.013.

[228] A. Cho, J. Ko, B.K. Kim, J.W. Han, Electrocatalysts with Increased Activity for Coelectrolysis of Steam and Carbon Dioxide in Solid Oxide Electrolyzer Cells, ACS Catal 9 (2019) 967–976. https://doi.org/10.1021/ACSCATAL.8B02679.

[229] A.R. Hanifi, M.A. Laguna-Bercero, T.H. Etsell, P. Sarkar, The effect of electrode infiltration on the performance of tubular solid oxide fuel cells under electrolysis and fuel cell modes, Int J Hydrogen Energy 39 (2014) 8002–8008. https://doi.org/10.1016/J.IJHYDENE.2014.03.071.

[230] L. Spiridigliozzi, E. Di Bartolomeo, G. Dell'Agli, F. Zurlo, GDC-Based Infiltrated Electrodes for Solid Oxide Electrolyzer Cells (SOECs), Applied Sciences 2020, Vol. 10, Page 3882 10 (2020) 3882. https://doi.org/10.3390/APP10113882.

[231] H. Fan, M. Keane, N. Li, D. Tang, P. Singh, M. Han, Electrochemical stability of La0.6Sr0.4Co0.2Fe0.8O3−δ-infiltrated YSZ oxygen electrode for reversible solid oxide fuel cells, Int J Hydrogen Energy 39 (2014) 14071–14078. https://doi.org/10.1016/J.IJHYDENE.2014.05.149.

[232] A. Torabi, A.R. Hanifi, T.H. Etsell, P. Sarkar, Effects of Porous Support Microstructure on Performance of Infiltrated Electrodes in Solid Oxide Fuel Cells, J Electrochem Soc 159 (2011) B201–B210. https://doi.org/10.1149/2.068202JES.

[233] J. Yang, A.F.S. Molouk, T. Okanishi, H. Muroyama, T. Matsui, K. Eguchi, A Stability Study of Ni/Yttria-Stabilized Zirconia Anode for Direct Ammonia Solid Oxide Fuel Cells, ACS Appl Mater Interfaces 7 (2015) 28701–28707. https://doi.org/10.1021/ACSAMI.5B11122.

[234] T.Z. Sholklapper, H. Kurokawa, C.P. Jacobson, S.J. Visco, L.C. De Jonghe, Nanostructured solid oxide fuel cell electrodes, Nano Lett 7 (2007) 2136–2141. https://doi.org/10.1021/NL071007I.

[235] V. Sarıboğa, M.A. Faruk Öksüzömer, Cu-CeO2anodes for solid oxide fuel cells: Determination of infiltration characteristics, J Alloys Compd 688 (2016) 323–331. https://doi.org/10.1016/J.JALLCOM.2016.07.217.

[236] S. Park, R.J. Gorte, J.M. Vohs, Applications of heterogeneous catalysis in the direct oxidation of hydrocarbons in a solid-oxide fuel cell, Appl Catal A Gen 200 (2000) 55–61. https://doi.org/10.1016/S0926-860X(00)00650-5.

[237] J.R. Wilson, S.A. Barnett, Solid oxide fuel cell Ni-YSZ anodes: Effect of composition on microstructure and performance, Electrochemical and Solid-State Letters 11 (2008) B181–B185. https://doi.org/10.1149/1.2960528.

[238] M.C. Tucker, G.Y. Lau, C.P. Jacobson, L.C. DeJonghe, S.J. Visco, Performance of metal-supported SOFCs with infiltrated electrodes, J Power Sources 171 (2007) 477–482. https://doi.org/10.1016/J.JPOWSOUR.2007.06.076.

[239] R.M.C. Clemmer, S.F. Corbin, The influence of pore and Ni morphology on the electrical conductivity of porous Ni/YSZ composite anodes for use in solid oxide fuel cell applications, Solid State Ion 180 (2009) 721–730. https://doi.org/10.1016/J.SSI.2009.02.030.

[240] S.F. Corbin, X. Qiao, Development of Solid Oxide Fuel Cell Anodes Using Metal-Coated Pore-Forming Agents, Journal of the American Ceramic Society 86 (2003) 401–406. https://doi.org/10.1111/J.1151-2916.2003.TB03312.X.

[241] S. Vafaeenezhad, A.R. Hanifi, M.A. Laguna-Bercero, T.H. Etsell, P. Sarkar, Microstructure and long-term stability of Ni–YSZ anode supported fuel cells: a review, Materials Futures 1 (2022) 042101. https://doi.org/10.1088/2752-5724/AC88E7.

[242] K.S. Howe, A.R. Hanifi, K. Kendall, M. Zazulak, T.H. Etsell, P. Sarkar, Performance of microtubular SOFCs with infiltrated electrodes under thermal cycling, Int J Hydrogen Energy 38 (2013) 1058–1067. https://doi.org/10.1016/J.IJHYDENE.2012.10.098.

[243] A. Buyukaksoy, S.P. Kammampata, V.I. Birss, Effect of porous YSZ scaffold microstructure on the long-term performance of infiltrated Ni-YSZ anodes, J Power Sources 287 (2015) 349–358. https://doi.org/10.1016/J.JPOWSOUR.2015.04.072.

[244] A.R. Hanifi, A. Torabi, X. Chen, S. Hill, P. Sarkar, T.H. Etsell, Development of Redox Resistant Fully Infiltrated Tubular SOFCs, J Electrochem Soc 161 (2014) F391–F397. https://doi.org/10.1149/2.022404JES.

[245] P. Keyvanfar, A.R. Hanifi, P. Sarkar, T.H. Etsell, V. Birss, Enhancing the Stability of Infiltrated Ni/YSZ Anodes, ECS Trans 68 (2015) 1255–1263. https://doi.org/10.1149/06801.1255ECST.

[246] X. Li, H.Y. Wang, H. Yang, W. Cai, S. Liu, B. Liu, In Situ/Operando Characterization Techniques to Probe the Electrochemical Reactions for Energy Conversion, Small Methods 2 (2018) 1700395. https://doi.org/10.1002/SMTD.201700395.

[247] Q. Meyer, Y. Zeng, C. Zhao, In Situ and Operando Characterization of Proton Exchange Membrane Fuel Cells, Advanced Materials 31 (2019) 1901900. https://doi.org/10.1002/ADMA.201901900.

[248] S.J. Skinner, Recent Advances in the Understanding of the Evolution of Surfaces and Interfaces in Solid Oxide Cells, Adv Mater Interfaces 6 (2019) 1900580. https://doi.org/10.1002/ADMI.201900580.

[249] Z. Fan, L. Zhang, D. Baumann, L. Mei, Y. Yao, X. Duan, Y. Shi, J. Huang, Y. Huang, X. Duan, In Situ Transmission Electron Microscopy for Energy Materials and Devices, Advanced Materials 31 (2019) 1900608. https://doi.org/10.1002/ADMA.201900608.

[250] S. Hwang, X. Chen, G. Zhou, D. Su, In Situ Transmission Electron Microscopy on Energy-Related Catalysis, Adv Energy Mater 10 (2020) 1902105. https://doi.org/10.1002/AENM.201902105.

[251] J.G. Swallow, J.K. Lee, T. Defferriere, G.M. Hughes, S.N. Raja, H.L. Tuller, J.H. Warner, K.J. Van Vliet, Atomic Resolution Imaging of Nanoscale Chemical Expansion in PrxCe1-xO2-δ during in Situ Heating, ACS Nano 12 (2018) 1359–1372. https://doi.org/10.1021/ACSNANO.7B07732.

[252] M. Niania, R. Podor, T. Ben Britton, C. Li, S.J. Cooper, N. Svetkov, S. Skinner, J. Kilner, In situ study of strontium segregation in La0.6Sr0.4Co0.2Fe0.8O3−δ in ambient atmospheres using high-temperature environmental scanning electron microscopy, J Mater Chem A Mater 6 (2018) 14120–14135. https://doi.org/10.1039/C8TA01341A.

[253] F. Zaera, New advances in the use of infrared absorption spectroscopy for the characterization of heterogeneous catalytic reactions, Chem Soc Rev 43 (2014) 7624–7663. https://doi.org/10.1039/C3CS60374A.

[254] D.J. Cumming, C. Tumilson, S.F.R. Taylor, S. Chansai, A. V. Call, J. Jacquemin, C. Hardacre, R.H. Elder, Development of a diffuse reflectance infrared fourier transform spectroscopy (DRIFTS) cell for the in situ analysis of co-electrolysis in a solid oxide cell, Faraday Discuss 182 (2015) 97–111. https://doi.org/10.1039/C5FD00030K.

[255] T. Murai, K. Yashiro, A. Kaimai, T. Otake, H. Matsumoto, T. Kawada, J. Mizusaki, Application of FT-IR for in situ investigation of high temperature electrode reactions, Solid State Ion 176 (2005) 2399–2403. https://doi.org/10.1016/J.SSI.2005.06.029.

[256] J.D. Kirtley, D.A. Steinhurst, J.C. Owrutsky, M.B. Pomfret, R.A. Walker, In situ optical studies of methane and simulated biogas oxidation on high temperature solid oxide fuel cell anodes, Physical Chemistry Chemical Physics 16 (2013) 227–236. https://doi.org/10.1039/C3CP53278J.

[257] M. Liu, M.E. Lynch, K. Blinn, F.M. Alamgir, Y. Choi, Rational SOFC material design: new advances and tools, Materials Today 14 (2011) 534–546. https://doi.org/10.1016/S1369-7021(11)70279-6.

[258] X. Li, J.P. Lee, K.S. Blinn, D. Chen, S. Yoo, B. Kang, L.A. Bottomley, M.A. El-Sayed, S. Park, M. Liu, High-temperature surface enhanced Raman spectroscopy for in situ

study of solid oxide fuel cell materials, Energy Environ Sci 7 (2013) 306–310. https://doi.org/10.1039/C3EE42462F.

[259] H. Bluhm, M. Hävecker, A. Knop-Gericke, M. Kiskinova, R. Schlögl, M. Salmeron, In Situ X-Ray Photoelectron Spectroscopy Studies of Gas-Solid Interfaces at Near-Ambient Conditions, MRS Bull 32 (2007) 1022–1030. https://doi.org/10.1557/MRS2007.211.

[260] F. Paloukis, K.M. Papazisi, T. Dintzer, V. Papaefthimiou, V.A. Saveleva, S.P. Balomenou, D. Tsiplakides, F. Bournel, J.J. Gallet, S. Zafeiratos, Insights into the Surface Reactivity of Cermet and Perovskite Electrodes in Oxidizing, Reducing, and Humid Environments, ACS Appl Mater Interfaces 9 (2017) 25265–25277. https://doi.org/10.1021/ACSAMI.7B05721.

[261] Z. Liu, T. Duchoň, H. Wang, D.C. Grinter, I. Waluyo, J. Zhou, Q. Liu, B. Jeong, E.J. Crumlin, V. Matolín, D.J. Stacchiola, J.A. Rodriguez, S.D. Senanayake, Ambient pressure XPS and IRRAS investigation of ethanol steam reforming on Ni–CeO2(111) catalysts: an in situ study of C–C and O–H bond scission, Physical Chemistry Chemical Physics 18 (2016) 16621–16628. https://doi.org/10.1039/C6CP01212D.

[262] A. Nenning, A.K. Opitz, C. Rameshan, R. Rameshan, R. Blume, M. Hävecker, A. Knop-Gericke, G. Rupprechter, B. Klötzer, J. Fleig, Ambient pressure XPS study of mixed conducting perovskite-type SOFC cathode and anode materials under well-defined electrochemical polarization, Journal of Physical Chemistry C 120 (2016) 1461–1471. https://doi.org/10.1021/acs.jpcc.5b08596.

[263] A.K. Opitz, A. Nenning, C. Rameshan, R. Rameshan, R. Blume, M. Hävecker, A. Knop-Gericke, G. Rupprechter, J. Fleig, B. Klötzer, Enhancing electrochemical water-splitting kinetics by polarization-driven formation of near-surface iron(0): An in situ XPS study on perovskite-type electrodes, Angewandte Chemie - International Edition 54 (2015) 2628–2632. https://doi.org/10.1002/anie.201409527.

[264] Y. Wen, T. Yang, D. Lee, H.N. Lee, E.J. Crumlin, K. Huang, Temporal and thermal evolutions of surface Sr-segregation in pristine and atomic layer deposition modified La0.6Sr0.4CoO3−δ epitaxial films, J Mater Chem A Mater 6 (2018) 24378–24388. https://doi.org/10.1039/C8TA08355J.

[265] A.K. Opitz, C. Rameshan, M. Kubicek, G.M. Rupp, A. Nenning, T. Götsch, R. Blume, M. Hävecker, A. Knop-Gericke, G. Rupprechter, B. Klötzer, J. Fleig, The Chemical Evolution of the La0.6Sr0.4CoO3−Δ Surface Under SOFC Operating Conditions and Its

Implications for Electrochemical Oxygen Exchange Activity, Top Catal 61 (2018) 2129–2141. https://doi.org/10.1007/S11244-018-1068-1/FIGURES/10.

[266] S. Kumar, S. Gautam, T.K. Song, K.H. Chae, K.W. Jang, S.S. Kim, Electronic structure study of Co doped CeO2 nanoparticles using X-ray absorption fine structure spectroscopy, J Alloys Compd 611 (2014) 329–334. https://doi.org/10.1016/J.JALLCOM.2014.05.025.

[267] Y. Chen, Y. Chen, D. Ding, Y. Ding, Y.M. Choi, L. Zhang, S. Yoo, D. Chen, B. DeGlee, H. Xu, Q. Lu, B. Zhao, G. Vardar, J. Wang, H. Bluhm, E.J. Crumlin, C. Yang, J. Liu, B. Yildiz, M. Liu, A robust and active hybrid catalyst for facile oxygen reduction in solid oxide fuel cells, Energy Environ Sci 10 (2017) 964–971. https://doi.org/10.1039/C6EE03656B.

[268] P. Kim-Lohsoontorn, Y.M. Kim, N. Laosiripojana, J. Bae, Gadolinium doped ceria-impregnated nickel–yttria stabilised zirconia cathode for solid oxide electrolysis cell, Int J Hydrogen Energy 36 (2011) 9420–9427. https://doi.org/10.1016/J.IJHYDENE.2011.04.199.

[269] W. Luo, S. Zafeiratos, Tuning Morphology and Redox Properties of Cobalt Particles Supported on Oxides by an in between Graphene Layer, Journal of Physical Chemistry C 120 (2016) 14130–14139. https://doi.org/10.1021/ACS.JPCC.6B03595.

[270] D.E. Starr, Z. Liu, M. Hävecker, A. Knop-Gericke, H. Bluhm, Investigation of solid/vapor interfaces using ambient pressure X-ray photoelectron spectroscopy, Chem Soc Rev 42 (2013) 5833–5857. https://doi.org/10.1039/C3CS60057B.

[271] X. Liu, W. Yang, Z. Liu, Recent progress on synchrotron-based in-situ soft X-ray spectroscopy for energy materials, Advanced Materials 26 (2014) 7710–7729. https://doi.org/10.1002/adma.201304676.

[272] D.E. Starr, Z. Liu, M. Hävecker, A. Knop-Gericke, H. Bluhm, Investigation of solid/vapor interfaces using ambient pressure X-ray photoelectron spectroscopy, Chem Soc Rev 42 (2013) 5833–5857. https://doi.org/10.1039/c3cs60057b.

[273] A. Knop-Gericke, E. Kleimenov, M. Hävecker, R. Blume, D. Teschner, S. Zafeiratos, R. Schlögl, V.I. Bukhtiyarov, V. V. Kaichev, I.P. Prosvirin, A.I. Nizovskii, H. Bluhm, A. Barinov, P. Dudin, M. Kiskinova, Chapter 4 X-Ray Photoelectron Spectroscopy for Investigation of Heterogeneous Catalytic Processes, Advances in Catalysis 52 (2009) 213–272. https://doi.org/10.1016/S0360-0564(08)00004-7.

[274] W.J. F., An introduction to surface analysis by XPS and AES, Chapter 5 (2003) 149–156.

[275] L. Zhong, D. Chen, S. Zafeiratos, A mini review of in situ near-ambient pressure XPS studies on non-noble, late transition metal catalysts, Catal Sci Technol 9 (2019) 3851–3867. https://doi.org/10.1039/c9cy00632j.

[276] A. Katsaounis, D. Teschner, S. Zafeiratos, The Effect of Polarization and Reaction Mixture on the Rh/YSZ Oxidation State During Ethylene Oxidation Studied by Near Ambient Pressure XPS, Top Catal 61 (2018) 2142–2151. https://doi.org/10.1007/S11244-018-1073-4.

[277] W. Derafa, F. Paloukis, B. Mewafy, W. Baaziz, O. Ersen, C. Petit, G. Corbel, S. Zafeiratos, Synthesis and characterization of nickel-doped ceria nanoparticles with improved surface reducibility, RSC Adv 8 (2018) 40712–40719. https://doi.org/10.1039/C8RA07995A.

[278] S. Zhu, M. Scardamaglia, J. Kundsen, R. Sankari, H. Tarawneh, R. Temperton, L. Pickworth, F. Cavalca, C. Wang, H. Tissot, J. Weissenrieder, B. Hagman, J. Gustafson, S. Kaya, F. Lindgren, I. Kallquist, J. Maibach, M. Hahlin, V. Boix, T. Gallo, F. Rehman, G. D'Acunto, J. Schnadta, A. Shavorskiy, HIPPIE: A new platform for ambient-pressure X-ray photoelectron spectroscopy at the MAX IV Laboratory, J Synchrotron Radiat 28 (2021) 624–636. https://doi.org/10.1107/S160057752100103X.

[279] M.C. Biesinger, B.P. Payne, A.P. Grosvenor, L.W.M. Lau, A.R. Gerson, R.S.C. Smart, Resolving surface chemical states in XPS analysis of first row transition metals, oxides and hydroxides: Cr, Mn, Fe, Co and Ni, Appl Surf Sci 257 (2011) 2717–2730. https://doi.org/10.1016/J.APSUSC.2010.10.051.

[280] E. Bêche, P. Charvin, D. Perarnau, S. Abanades, G. Flamant, Ce 3d XPS investigation of cerium oxides and mixed cerium oxide (CexTiyOz), Surface and Interface Analysis 40 (2008) 264–267. https://doi.org/10.1002/SIA.2686.

[281] S. Kato, M. Ammann, T. Huthwelker, C. Paun, M. Lampimäki, M.T. Lee, M. Rothensteiner, J.A. Van Bokhoven, Quantitative depth profiling of Ce3+ in Pt/CeO2 by in situ high-energy XPS in a hydrogen atmosphere, Physical Chemistry Chemical Physics 17 (2015) 5078–5083. https://doi.org/10.1039/C4CP05643D.

[282] R.C. Maher, G. Kerherve, D.J. Payne, X. Yue, P.A. Connor, J. Irvine, L.F. Cohen, The Reduction Properties of M–Doped (M=Zr, Gd) CeO2/YSZ Scaffolds Co–Infiltrated with

Nickel, Energy Technology 6 (2018) 2045–2052. https://doi.org/10.1002/ENTE.201800146.

[283] L. Pasquali, B.P. Doyle, F. Borgatti, A. Giglia, N. Mahne, M. Pedio, S. Nannarone, A.K. Kaveev, A.S. Balanev, B.B. Krichevtsov, S.M. Suturin, N.S. Sokolov, Cobalt on calcium fluoride: Initial stages of growth and magnetic properties, Surf Sci 600 (2006) 4170–4175. https://doi.org/10.1016/J.SUSC.2006.01.141.

[284] D. Channei, B. Inceesungvorn, N. Wetchakun, S. Ukritnukun, A. Nattestad, J. Chen, S. Phanichphant, Photocatalytic Degradation of Methyl Orange by CeO2 and Fe–doped CeO2 Films under Visible Light Irradiation, Scientific Reports 2014 4:1 4 (2014) 1–7. https://doi.org/10.1038/srep05757.

[285] V. Papaefthimiou, M. Shishkin, D.K. Niakolas, M. Athanasiou, Y.T. Law, R. Arrigo, D. Teschner, M. Hävecker, A. Knop-Gericke, R. Schlögl, T. Ziegler, S.G. Neophytides, S. Zafeiratos, On the Active Surface State of Nickel-Ceria Solid Oxide Fuel Cell Anodes During Methane Electrooxidation, Adv Energy Mater 3 (2013) 762–769. https://doi.org/10.1002/AENM.201200727.

[286] B. Mewafy, F. Paloukis, K.M. Papazisi, S.P. Balomenou, W. Luo, D. Teschner, O. Joubert, A. Le Gal La Salle, D.K. Niakolas, S. Zafeiratos, Influence of Surface State on the Electrochemical Performance of Nickel-Based Cermet Electrodes during Steam Electrolysis, ACS Appl Energy Mater 2 (2019) 7045–7055. https://doi.org/10.1021/acsaem.9b00779.

[287] V. Papaefthimiou, D.K. Niakolas, F. Paloukis, T. Dintzer, S. Zafeiratos, Is Steam an Oxidant or a Reductant for Nickel/Doped-Ceria Cermets?, ChemPhysChem 18 (2017) 164–170. https://doi.org/10.1002/cphc.201600948.

[288] B.P. Payne, M.C. Biesinger, N.S. McIntyre, The study of polycrystalline nickel metal oxidation by water vapour, J Electron Spectros Relat Phenomena 175 (2009) 55–65. https://doi.org/10.1016/J.ELSPEC.2009.07.006.

[289] S. Zafeiratos, S. Kennou, The interaction of oxygen with ultrathin Ni deposits on yttria-stabilized ZrO2(1 0 0), Surf Sci 482–485 (2001) 266–271. https://doi.org/10.1016/S0039-6028(01)00929-3.

[290] R. Barfod, M. Mogensen, T. Klemenso, A. Hagen, Y.-L. Liu, P. Vang Hendriksen, Detailed Characterization of Anode-Supported SOFCs by Impedance Spectroscopy, J Electrochem Soc 154 (2007) B371. https://doi.org/10.1149/1.2433311.

[291] M.J. Jørgensen, S. Primdahl, M. Mogensen, Characterisation of composite SOFC cathodes using electrochemical impedance spectroscopy, Electrochim Acta 44 (1999) 4195–4201. https://doi.org/10.1016/S0013-4686(99)00134-6.

[292] X.-Z. Yuan, C. Song, H. Wang, J. Zhang, Impedance and its Corresponding Electrochemical Processes, Electrochemical Impedance Spectroscopy in PEM Fuel Cells (2010) 95–138. https://doi.org/10.1007/978-1-84882-846-9_3.

[293] M. Grossi, B. Riccò, Electrical impedance spectroscopy (EIS) for biological analysis and food characterization: A review, Journal of Sensors and Sensor Systems 6 (2017) 303–325. https://doi.org/10.5194/JSSS-6-303-2017.

[294] P.S. Shah, J.D. Holmes, K.P. Johnston, B.A. Korgel, Size-selective dispersion of dodecanethiol-coated nanocrystals in liquid and supercritical ethane by density tuning, Journal of Physical Chemistry B 106 (2002) 2545–2551. https://doi.org/10.1021/JP013931L.

[295] T. Arita, J. Yoo, Y. Ueda, T. Adschiri, Size and size distribution balance the dispersion of colloidal CeO 2 nanoparticles in organic solvents, Nanoscale 2 (2010) 689–693. https://doi.org/10.1039/B9NR00395A.

[296] S. Usune, M. Ando, M. Kubo, T. Tsukada, K.I. Sugioka, O. Koike, R. Tatsumi, M. Fujita, S. Takami, T. Adschiri, Numerical simulation of dispersion and aggregation behavior of surface-modified nanoparticles in organic solvents, Journal of Chemical Engineering of Japan 51 (2018) 492–500. https://doi.org/10.1252/JCEJ.17WE197.

[297] B. Faure, G. Salazar-Alvarez, A. Ahniyaz, I. Villaluenga, G. Berriozabal, Y.R. De Miguel, L. Bergström, Dispersion and surface functionalization of oxide nanoparticles for transparent photocatalytic and UV-protecting coatings and sunscreens, Sci Technol Adv Mater 14 (2013) 023001. https://doi.org/10.1088/1468-6996/14/2/023001.

[298] B. Vincent, J. Edwards, S. Emmett, A. Jones, Depletion flocculation in dispersions of sterically-stabilised particles ("soft spheres"), Colloids and Surfaces 18 (1986) 261–281. https://doi.org/10.1016/0166-6622(86)80317-1.

[299] S. Aslam, S. Rani, K. Lal, M. Fatima, T. Hardwick, B. Shirinfar, N. Ahmed, Electrochemical hydrogen production: sustainable hydrogen economy, Green Chemistry (2023). https://doi.org/10.1039/D3GC02849F.

[300] A. Hauch, R. Küngas, P. Blennow, A.B. Hansen, J.B. Hansen, B. V Mathiesen, M.B. Mogensen, Recent advances in solid oxide cell technology for electrolysis, Science (1979) 370 (2020) eaba6118. https://doi.org/10.1126/science.aba6118.

[301] W. Zhang, M. Liu, X. Gu, Y. Shi, Z. Deng, N. Cai, Water Electrolysis toward Elevated Temperature: Advances, Challenges and Frontiers, Chem Rev 123 (2023) 7119–7192. https://doi.org/10.1021/ACS.CHEMREV.2C00573.

[302] S.E. Wolf, F.E. Winterhalder, V. Vibhu, L.G.J. de Haart, O. Guillon, R.A. Eichel, N.H. Menzler, Solid oxide electrolysis cells – current material development and industrial application, J Mater Chem A Mater 11 (2023) 17977–18028. https://doi.org/10.1039/D3TA02161K.

[303] L.A. Jolaoso, I.T. Bello, O.A. Ojelade, A. Yousuf, C. Duan, P. Kazempoor, Operational and scaling-up barriers of SOEC and mitigation strategies to boost H2 production- a comprehensive review, Int J Hydrogen Energy 48 (2023) 33017–33041. https://doi.org/10.1016/J.IJHYDENE.2023.05.077.

[304] J. Zhou, L. Xu, C. Ding, C. Wei, Z. Tao, Layered perovskite (PrBa)0.95(Fe0.9Mo0.1)2O5+δ as electrode materials for high-performing symmetrical solid oxide electrolysis cells, Mater Lett 257 (2019) 126758. https://doi.org/10.1016/J.MATLET.2019.126758.

[305] J. Cao, Y. Li, Y. Zheng, S. Wang, W. Zhang, X. Qin, G. Geng, B. Yu, J. Cao, Y. Zheng, S. Wang, W. Zhang, X. Qin, G. Geng, B. Yu, Y. Li, A Novel Solid Oxide Electrolysis Cell with Micro-/Nano Channel Anode for Electrolysis at Ultra-High Current Density over 5 A cm−2, Adv Energy Mater 12 (2022) 2200899. https://doi.org/10.1002/AENM.202200899.

[306] B. Königshofer, G. Pongratz, G. Nusev, P. Boškoski, M. Höber, Đ. Juričić, M. Kusnezoff, N. Trofimenko, H. Schröttner, C. Hochenauer, V. Subotić, Development of test protocols for solid oxide electrolysis cells operated under accelerated degradation conditions, J Power Sources 497 (2021) 229875. https://doi.org/10.1016/J.JPOWSOUR.2021.229875.

[307] X. Chen, Y. Ning, J. Pei, G. Zhang, Q. Fu, External Voltage-Induced Restructuring of the Solid-State Electrode/Electrolyte Interface Revealed by X-ray Photoelectron Spectroscopy Depth Profiling Analysis, ACS Appl Mater Interfaces 16 (2024) 10908–10915. https://doi.org/10.1021/acsami.3c16478.

[308] F.R. Bianchi, A.K. Padinjarethil, A. Hagen, B. Bosio, Multiscale analysis of Ni-YSZ and Ni-CGO anode based SOFC degradation: From local microstructural variation to cell electrochemical performance, Electrochim Acta 460 (2023) 142589. https://doi.org/10.1016/J.ELECTACTA.2023.142589.

[309] S.D. Kim, D.W. Seo, A.K. Dorai, S.K. Woo, The effect of gas compositions on the performance and durability of solid oxide electrolysis cells, Int J Hydrogen Energy 38 (2013) 6569–6576. https://doi.org/10.1016/J.IJHYDENE.2013.03.115.

[310] V. Subotić, S. Futamura, G.F. Harrington, J. Matsuda, K. Natsukoshi, K. Sasaki, Towards understanding of oxygen electrode processes during solid oxide electrolysis operation to improve simultaneous fuel and oxygen generation, J Power Sources 492 (2021) 229600. https://doi.org/10.1016/J.JPOWSOUR.2021.229600.

[311] A. Hauch, K. Brodersen, M. Chen, M.B. Mogensen, Ni/YSZ electrodes structures optimized for increased electrolysis performance and durability, Solid State Ion 293 (2016) 27–36. https://doi.org/10.1016/J.SSI.2016.06.003.

[312] A. Hauch, J.R. Bowen, L.T. Kuhn, M. Mogensen, Nanoscale chemical analysis and imaging of solid oxide cells, Electrochemical and Solid-State Letters 11 (2008). https://doi.org/10.1149/1.2828845.

[313] K.A. Stoerzinger, W.T. Hong, E.J. Crumlin, H. Bluhm, Y. Shao-Horn, Insights into Electrochemical Reactions from Ambient Pressure Photoelectron Spectroscopy, Acc Chem Res 48 (2015) 2976–2983. https://doi.org/10.1021/acs.accounts.5b00275.

[314] Q. Jeangros, M. Bugnet, T. Epicier, C. Frantz, S. Diethelm, D. Montinaro, E. Tyukalova, Y. Pivak, J. Van herle, A. Hessler-Wyser, M. Duchamp, Operando analysis of a solid oxide fuel cell by environmental transmission electron microscopy, Nature Communications 2023 14:1 14 (2023) 1–10. https://doi.org/10.1038/s41467-023-43683-4.

[315] K.V. Hansen, T. Jacobsen, K. Thyden, Y. Wu, M.B. Mogensen, In situ surface reduction of a NiO-YSZ-alumina composite using scanning probe microscopy, Journal of Solid State Electrochemistry 18 (2014) 1869–1878. https://doi.org/10.1007/s10008-014-2428-9.

[316] Q. Jeangros, A. Faes, J.B. Wagner, T.W. Hansen, U. Aschauer, J. Van herle, A. Hessler-Wyser, R.E. Dunin-Borkowski, In situ redox cycle of a nickel{â} YSZ fuel cell anode in an environmental transmission electron microscope, Acta Mater. 58 (2010) 4578–4589. https://doi.org/10.1016/j.actamat.2010.04.019.

[317] J. Matsuda, T. Kawasaki, S. Futamura, T. Kawabata, S. Taniguchi, K. Sasaki, In situ transmission electron microscopic observations of redox cycling of a Ni–ScSZ cermet fuel cell anode, Microscopy 67 (2018) 251–258. https://doi.org/10.1093/JMICRO/DFY025.

[318] Q. Jeangros, T.W. Hansen, J.B. Wagner, R.E. Dunin-Borkowski, C. Hébert, J. Van herle, A. Hessler-Wyser, Energy-filtered environmental transmission electron microscopy for the assessment of solid–gas reactions at elevated temperature: NiO/YSZ–H2 as a case study, Ultramicroscopy 169 (2016) 11–21. https://doi.org/10.1016/J.ULTRAMIC.2016.06.005.

[319] Q. Jeangros, T.W. Hansen, J.B. Wagner, R.E. Dunin-Borkowski, C. Hébert, J. Van Herle, A. Hessler-Wyser, Measurements of local chemistry and structure in Ni(O)–YSZ composites during reduction using energy-filtered environmental TEM, Chemical Communications 50 (2014) 1808–1810. https://doi.org/10.1039/C3CC46682E.

[320] S.B. Simonsen, K. Agersted, K.V. Hansen, T. Jacobsen, J.B. Wagner, T.W. Hansen, L.T. Kuhn, Environmental TEM study of the dynamic nanoscaled morphology of NiO/YSZ during reduction, Appl Catal A Gen 489 (2015) 147–154. https://doi.org/10.1016/J.APCATA.2014.10.045.

[321] Z. Liu, H. Shimada, Visualization of the structural transformation of NiO/YSZ/BZY nanocomposite particles using in situ gas environmental transmission electron microscopy, Nanoscale 16 (2024) 1890–1896. https://doi.org/10.1039/D3NR04525K.

[322] S.W. Chee, T. Lunkenbein, R. Schlögl, B. Roldán Cuenya, Operando Electron Microscopy of Catalysts: The Missing Cornerstone in Heterogeneous Catalysis Research?, Chem Rev 123 (2023) 13374–13418. https://doi.org/10.1021/acs.chemrev.3c00352.

[323] Y. Han, H. Zhang, Y. Yu, Z. Liu, In Situ Characterization of Catalysis and Electrocatalysis Using APXPS, ACS Catal 11 (2021) 1464–1484. https://doi.org/10.1021/ACSCATAL.0C04251.

[324] F. El Gabaly, K.F. McCarty, H. Bluhm, A.H. McDaniel, Oxidation stages of Ni electrodes in solid oxide fuel cell environments , Physical Chemistry Chemical Physics 15 (2013) 8334–8341. https://doi.org/10.1039/c3cp50366f.

[325] B. Mewafy, F. Paloukis, K.M. Papazisi, S.P. Balomenou, W. Luo, D. Teschner, O. Joubert, A. Le Gal La Salle, D.K. Niakolas, S. Zafeiratos, Influence of Surface State on the Electrochemical Performance of Nickel-Based Cermet Electrodes during Steam Electrolysis, ACS Appl Energy Mater 2 (2019) 7045–7055. https://doi.org/10.1021/acsaem.9b00779.

[326] C.W. Thurner, L. Haug, D. Winkler, V. Zarth, J. Glätzle, K. Ploner, J. Schäfer, S. Penner, B. Klötzer, Preparation of Ni and NiCu/Yttria-Stabilized Zirconia Model Electrodes with

Optimized Triple-Phase Boundary Geometry for Fundamental Operando Spectroscopic Studies, Small Struct (2023) 2300414. https://doi.org/10.1002/SSTR.202300414.

[327] C.M. Goodwin, P. Lömker, D. Degerman, B. Davies, M. Shipilin, F. Garcia-Martinez, S. Koroidov, J. Katja Mathiesen, R. Rameshan, G.L.S. Rodrigues, C. Schlueter, P. Amann, A. Nilsson, Operando probing of the surface chemistry during the Haber–Bosch process, Nature 2024 625:7994 625 (2024) 282–286. https://doi.org/10.1038/s41586-023-06844-5.

[328] M. Favaro, P.C.J. Clark, M.J. Sear, M. Johansson, S. Maehl, R. van de Krol, D.E. Starr, Spectroscopic analysis with tender X-rays: SpAnTeX, a new AP-HAXPES end-station at BESSY II, Surf Sci 713 (2021) 121903. https://doi.org/10.1016/J.SUSC.2021.121903.

[329] Y. Takagi, T. Uruga, M. Tada, Y. Iwasawa, T. Yokoyama, Ambient Pressure Hard X-ray Photoelectron Spectroscopy for Functional Material Systems as Fuel Cells under Working Conditions, Acc Chem Res 51 (2018) 719–727. https://doi.org/10.1021/acs.accounts.7b00563.

[330] A. Ishihara, T. Nagai, K. Ukita, M. Arao, M. Matsumoto, L. Yu, T. Nakamura, O. Sekizawa, Y. Takagi, K. Matsuzawa, T.W. Napporn, S. Mitsushima, T. Uruga, T. Yokoyama, Y. Iwasawa, H. Imai, K.I. Ota, Emergence of Oxygen Reduction Activity in Zirconium Oxide-Based Compounds in Acidic Media: Creation of Active Sites for the Oxygen Reduction Reaction, Journal of Physical Chemistry C 123 (2019) 18150–18159. https://doi.org/10.1021/ACS.JPCC.9B02393.

[331] S. Hendel, F. Schäfers, M. Hävecker, G. Reichardt, M. Scheer, J. Bahrdt, K. Lips, The EMIL project at BESSY II: Beamline design and performance, in: AIP Conference Proceedings 1741, 2016: p. 030038. https://doi.org/10.1063/1.4952861.

[332] D. Salusso, C. Scarfiello, A. Efimenko, D.P. Minh, P. Serp, K. Soulantica, S. Zafeiratos, Direct Evidence of Dynamic Metal Support Interactions in Co/TiO2 Catalysts by Near-Ambient Pressure X-ray Photoelectron Spectroscopy, Nanomaterials 13 (2023) 2672. https://doi.org/10.3390/NANO13192672.

[333] V. Papaefthimiou, T. Dintzer, M. Lebedeva, D. Teschner, M. Hävecker, A. Knop-Gericke, R. Schlögl, V. Pierron-Bohnes, E. Savinova, S. Zafeiratos, Probing metal-support interaction in reactive environments: An in situ study of PtCo bimetallic nanoparticles supported on TiO 2, Journal of Physical Chemistry C 116 (2012) 14342–14349. https://doi.org/10.1021.

[334] H. Li, Z. Lyu, M. Han, Robust and fast estimation of equivalent circuit model from noisy electrochemical impedance spectra, Electrochim Acta 422 (2022) 140474. https://doi.org/10.1016/J.ELECTACTA.2022.140474.

[335] S. Dierickx, A. Weber, E. Ivers-Tiffée, How the distribution of relaxation times enhances complex equivalent circuit models for fuel cells, Electrochim Acta 355 (2020) 136764. https://doi.org/10.1016/J.ELECTACTA.2020.136764.

[336] D. Chen, J. Zhang, M. Barreau, S. Turczyniak-Surdacka, O. Joubert, A.L.G. La Salle, S. Zafeiratos, Ni-doped CeO2 nanoparticles to promote and restore the performance of Ni/YSZ cathodes for CO2 electroreduction, Appl Surf Sci 611 (2023) 155767. https://doi.org/10.1016/J.APSUSC.2022.155767.

[337] S. Zafeiratos, S. Kennou, The interaction of oxygen with ultrathin Ni deposits on yttria-stabilized ZrO2(1 0 0), Surf Sci 482–485 (2001) 266–271. https://doi.org/10.1016/S0039-6028(01)00929-3.

[338] V. Papaefthimiou, D.K. Niakolas, F. Paloukis, T. Dintzer, S. Zafeiratos, Is Steam an Oxidant or a Reductant for Nickel/Doped-Ceria Cermets?, ChemPhysChem 18 (2017) 164–170. https://doi.org/10.1002/cphc.201600948.

[339] Q. Jeangros, T.W. Hansen, J.B. Wagner, C.D. Damsgaard, R.E. Dunin-Borkowski, C. H??bert, J. Van Herle, A. Hessler-Wyser, Reduction of nickel oxide particles by hydrogen studied in an environmental TEM, J Mater Sci 48 (2013) 2893–2907. https://doi.org/10.1007/s10853-012-7001-2.

[340] Z. Jiao, Y. Su, W. Yang, J. Zhou, J. Zhang, X. Tong, Y. Shang, M. Chen, Integrated 3D modeling unravels the measures to mitigate nickel migration in solid oxide fuel/electrolysis cells, J Mater Chem A Mater 12 (2023) 162–173. https://doi.org/10.1039/D3TA06563D.

[341] T. Le Cheng, Y. Lei, Y. Chen, Y. Fan, H. Abernathy, X. Song, Y.H. Wen, Oxidation of nickel in solid oxide cells during electrochemical operation: Experimental evidence, theoretical analysis, and an alternative hypothesis on the nickel migration, J Power Sources 569 (2023) 232991. https://doi.org/10.1016/J.JPOWSOUR.2023.232991.

[342] W. Smekal, W.S.M. Werner, C.J. Powell, Simulation of electron spectra for surface analysis (SESSA): A novel software tool for quantitative Auger-electron spectroscopy and X-ray photoelectron spectroscopy, Surface and Interface Analysis 37 (2005) 1059–1067. https://doi.org/10.1002/sia.2097.

[343] S. Chenna, R. Banerjee, P.A. Crozier, Atomic-Scale Observation of the Ni Activation Process for Partial Oxidation of Methane Using In Situ Environmental TEM, ChemCatChem 3 (2011) 1051–1059. https://doi.org/10.1002/CCTC.201000238.

[344] G. Greczynski, L. Hultman, Impact of sample storage type on adventitious carbon and native oxide growth: X-ray photoelectron spectroscopy study, Vacuum 205 (2022) 111463. https://doi.org/10.1016/J.VACUUM.2022.111463.

[345] T.C.R. Rocha, A. Oestereich, D.V. Demidov, M. Hävecker, S. Zafeiratos, G. Weinberg, V.I. Bukhtiyarov, A. Knop-Gericke, R. Schlögl, The silver-oxygen system in catalysis: New insights by near ambient pressure X-ray photoelectron spectroscopy, Physical Chemistry Chemical Physics 14 (2012). https://doi.org/10.1039/c2cp22472k.

[346] Z.A. Feng, F. El Gabaly, X. Ye, Z.X. Shen, W.C. Chueh, Fast vacancy-mediated oxygen ion incorporation across the ceria-gas electrochemical interface, Nat Commun 5 (2014) 4374. https://doi.org/10.1038/ncomms5374.

[347] M.R. Pillai, Y. Jiang, N. Mansourian, al -, H. Sumi, R. Kishida, J.-Y. Kim, S. Vafaeenezhad, A. Reza Hanifi, M.A. Laguna-Bercero, T.H. Etsell, P. Sarkar, Microstructure and long-term stability of Ni–YSZ anode supported fuel cells: a review, Materials Futures 1 (2022) 042101. https://doi.org/10.1088/2752-5724/AC88E7.

[348] I. Spanos, M.F. Tesch, M. Yu, H. Tüysüz, J. Zhang, X. Feng, K. Müllen, R. Schlögl, A.K. Mechler, Facile Protocol for Alkaline Electrolyte Purification and Its Influence on a Ni-Co Oxide Catalyst for the Oxygen Evolution Reaction, ACS Catal 9 (2019) 8165–8170. https://doi.org/10.1021/ACSCATAL.9B01940.

[349] S. Volkov, V. Vonk, N. Khorshidi, D. Franz, M. Kubicek, V. Kilic, R. Felici, T.M. Huber, E. Navickas, G.M. Rupp, J. Fleig, A. Stierle, Operando X-ray Investigation of Electrode/Electrolyte Interfaces in Model Solid Oxide Fuel Cells, Chemistry of Materials 28 (2016) 3727–3733. https://doi.org/10.1021/ACS.CHEMMATER.6B00351.

[350] T. Nagasawa, K. Hanamura, Prediction of overpotential and effective thickness of Ni/YSZ anode for solid oxide fuel cell by improved species territory adsorption model, J Power Sources 353 (2017) 115–122. https://doi.org/10.1016/j.jpowsour.2017.03.154.

[351] W.G. Bessler, S. Gewies, M. Vogler, A new framework for physically based modeling of solid oxide fuel cells, Electrochim Acta 53 (2007) 1782–1800. https://doi.org/10.1016/J.ELECTACTA.2007.08.030.

[352] F. El Gabaly, M. Grass, A.H. McDaniel, R.L. Farrow, M.A. Linne, Z. Hussain, H. Bluhm, Z. Liu, K.F. McCarty, Measuring individual overpotentials in an operating solid-

oxide electrochemical cell, Physical Chemistry Chemical Physics 12 (2010) 12138–12145. https://doi.org/10.1039/c003581e.

[353] M.P. Hoerlein, M. Riegraf, R. Costa, G. Schiller, K.A. Friedrich, A parameter study of solid oxide electrolysis cell degradation: Microstructural changes of the fuel electrode, Electrochim Acta 276 (2018) 162–175. https://doi.org/10.1016/J.ELECTACTA.2018.04.170.

[354] M.B. Mogensen, M. Chen, H.L. Frandsen, C. Graves, A. Hauch, P.V. Hendriksen, T. Jacobsen, S.H. Jensen, T.L. Skafte, X. Sun, Ni migration in solid oxide cell electrodes: Review and revised hypothesis, Fuel Cells 21 (2021) 415–429. https://doi.org/https://doi.org/10.1002/fuce.202100072.

[355] Z. Jiao, N. Shikazono, In operando optical study of active three phase boundary of nickel-yttria stabilized zirconia solid-oxide fuel cell anode under polarization, J Power Sources 396 (2018) 119–123. https://doi.org/10.1016/J.JPOWSOUR.2018.06.001.

[356] B.P. Payne, M.C. Biesinger, N.S. McIntyre, The study of polycrystalline nickel metal oxidation by water vapour, J Electron Spectros Relat Phenomena 175 (2009) 55–65. https://doi.org/10.1016/j.elspec.2009.07.006.

[357] V. Papaefthimiou, D.K.D.K. Niakolas, F. Paloukis, D. Teschner, A. Knop-Gericke, M. Haevecker, S. Zafeiratos, Operando observation of nickel/ceria electrode surfaces during intermediate temperature steam electrolysis, J Catal 352 (2017) 305–313. https://doi.org/10.1016/j.jcat.2017.06.005.

[358] M. Al Samarai, A.W. Hahn, A. Beheshti Askari, Y.T. Cui, K. Yamazoe, J. Miyawaki, Y. Harada, O. Rüdiger, S. Debeer, Elucidation of Structure-Activity Correlations in a Nickel Manganese Oxide Oxygen Evolution Reaction Catalyst by Operando Ni L-edge X-ray Absorption Spectroscopy and 2p3d Resonant Inelastic X-ray Scattering, ACS Appl Mater Interfaces 11 (2019) 38595–38605. https://doi.org/10.1021/ACSAMI.9B06752/.

[359] S. Zafeiratos, T. Dintzer, D. Teschner, R. Blume, M. Hävecker, A. Knop-Gericke, R. Schlögl, Methanol oxidation over model cobalt catalysts: Influence of the cobalt oxidation state on the reactivity, J Catal 269 (2010) 309–317. https://doi.org/10.1016/j.jcat.2009.11.013.

[360] Trevor Letcher, Future Energy: Improved, Sustainable, and Clean Options for Our Planet, Chemistry International -- Newsmagazine for IUPAC 30 (2008) 20–21. https://doi.org/10.1515/CI.2008.30.2.20.

[361] S.E. Hosseini, M.A. Wahid, Hydrogen production from renewable and sustainable energy resources: Promising green energy carrier for clean development, Renewable and Sustainable Energy Reviews 57 (2016) 850–866. https://doi.org/10.1016/J.RSER.2015.12.112.

[362] N.S. Hassan, A.A. Jalil, S. Rajendran, N.F. Khusnun, M.B. Bahari, A. Johari, M.J. Kamaruddin, M. Ismail, Recent review and evaluation of green hydrogen production via water electrolysis for a sustainable and clean energy society, Int J Hydrogen Energy 52 (2024) 420–441. https://doi.org/10.1016/J.IJHYDENE.2023.09.068.

[363] Y. Zhang, J. Liu, S.L. Li, Z.M. Su, Y.Q. Lan, Polyoxometalate-based materials for sustainable and clean energy conversion and storage, EnergyChem 1 (2019) 100021. https://doi.org/10.1016/J.ENCHEM.2019.100021.

[364] S.E. Hosseini, M.A. Wahid, Hydrogen from solar energy, a clean energy carrier from a sustainable source of energy, Int J Energy Res 44 (2020) 4110–4131. https://doi.org/10.1002/ER.4930.

[365] A. Pandiyan, A. Uthayakumar, R. Subrayan, S.W. Cha, S.B.K. Moorthy, Review of solid oxide electrolysis cells: a clean energy strategy for hydrogen generation, ICE 8 (2019). https://doi.org/10.1680/JNAEN.18.00009.

[366] E. Zoulias, E. Varkaraki, N. Lymberopoulos, C.N. Christodoulou, G.N. Karagiorgis, A review on water electrolysis, Tcjst 4 (2004) 41–71.

[367] E. Pomerantseva, C. Resini, K. Kovnir, Y. V. Kolen'ko, Emerging nanostructured electrode materials for water electrolysis and rechargeable beyond Li-ion batteries, Adv Phys X 2 (2017) 211–253. https://doi.org/10.1080/23746149.2016.1273796.

[368] A.N. Colli, H.H. Girault, A. Battistel, Non-Precious Electrodes for Practical Alkaline Water Electrolysis, Materials 2019, Vol. 12, Page 1336 12 (2019) 1336. https://doi.org/10.3390/MA12081336.

[369] A.J. Shih, M.C.O. Monteiro, F. Dattila, D. Pavesi, M. Philips, A.H.M. da Silva, R.E. Vos, K. Ojha, S. Park, O. van der Heijden, G. Marcandalli, A. Goyal, M. Villalba, X. Chen, G.T.K.K. Gunasooriya, I. McCrum, R. Mom, N. López, M.T.M. Koper, Water electrolysis, Nature Reviews Methods Primers 2022 2:1 2 (2022) 1–19. https://doi.org/10.1038/s43586-022-00164-0.

[370] H.B. Suffredini, J.L. Cerne, F.C. Crnkovic, S.A.S. MacHado, L.A. Avaca, Recent developments in electrode materials for water electrolysis, Int J Hydrogen Energy 25 (2000) 415–423. https://doi.org/10.1016/S0360-3199(99)00049-X.

[371] S. Singh, T. Dosani, A.S. Karakoti, A. Kumar, S. Seal, W.T. Self, A phosphate-dependent shift in redox state of cerium oxide nanoparticles and its effects on catalytic properties, Biomaterials 32 (2011) 6745–6753. https://doi.org/10.1016/J.BIOMATERIALS.2011.05.073.

[372] A. Trovarelli, Catalytic Properties of Ceria and CeO2-Containing Materials, Catalysis Reviews 38 (1996) 439–520. https://doi.org/10.1080/01614949608006464.

[373] J.C. Bear, P.D. McNaughter, P. Southern, P. O'Brien, C.W. Dunnill, Nickel-Doped Ceria Nanoparticles: The Effect of Annealing on Room Temperature Ferromagnetism, Crystals 2015, Vol. 5, Pages 312-326 5 (2015) 312–326. https://doi.org/10.3390/CRYST5030312.

[374] W. Qi, K. Xie, M. Liu, G. Wu, Y. Wang, Y. Zhang, Y. Wu, Single-phase nickel-doped ceria cathode with in situ grown nickel nanocatalyst for direct high-temperature carbon dioxide electrolysis, RSC Adv 4 (2014) 40494–40504. https://doi.org/10.1039/C4RA06712F.

[375] J. Zhao, W. Fan, W. Liu, L. Sun, Y. Wang, H. Liu, P. Chen, Q. Liang, Y. Cheng, X. Wang, Effect of Nickel-doped cerium dioxide on electrochemical hydrogen storage properties of Co0.9Cu0.1Si alloy, Journal of Physics and Chemistry of Solids 195 (2024) 112223. https://doi.org/10.1016/J.JPCS.2024.112223.

[376] A. Miri, M. Sarani, M. Khatami, Nickel-doped cerium oxide nanoparticles: biosynthesis, cytotoxicity and UV protection studies, RSC Adv 10 (2020) 3967–3977. https://doi.org/10.1039/C9RA09076B.

[377] A.S. Yu, R. Küngas, J.M. Vohs, R.J. Gorte, Modification of SOFC Cathodes by Atomic Layer Deposition, J Electrochem Soc 160 (2013) F1225–F1231. https://doi.org/10.1149/2.045311JES.

[378] I.A. Robinson, Y.L. Huang, S.A. Horlick, A.M. Hussain, A. Pesaran, E.D. Wachsman, Enhancement of low-temperature solid oxide fuel cell performance and durability via surface chemistry modification, Electrochim Acta 442 (2023) 141881. https://doi.org/10.1016/J.ELECTACTA.2023.141881.

[379] H. Chen, Z. Guo, L.A. Zhang, Y. Li, F. Li, Y. Zhang, Y. Chen, X. Wang, B. Yu, J.M. Shi, J. Liu, C. Yang, S. Cheng, Y. Chen, M. Liu, Improving the Electrocatalytic Activity and Durability of the La0.6Sr0.4Co0.2Fe0.8O3-δ Cathode by Surface Modification, ACS Appl Mater Interfaces 10 (2018) 39785–39793. https://doi.org/10.1021/ACSAMI.8B14693.

[380] S. Saher, C.Y. Tan, S. Ramesh, B.K. Yap, B.H. Ong, M.S.H. Al-Furjan, Enhancing oxygen exchange kinetics of solid oxide fuel cell cathode: Unleashing the potential of higher order Ruddlesden-Popper phase surface modification, J Power Sources 584 (2023) 233607. https://doi.org/10.1016/J.JPOWSOUR.2023.233607.

[381] D. Ding, X. Li, S.Y. Lai, K. Gerdes, M. Liu, Enhancing SOFC cathode performance by surface modification through infiltration, Energy Environ Sci 7 (2014) 552–575. https://doi.org/10.1039/C3EE42926A.

[382] B. Jackson, Engineering the Solid Oxide Fuel Cell Through Infiltrating the Porous Electrodes, (2018).

[383] S. Omar, Infiltration technique to fabricate nanostructured electrodes for high-performance solid oxide fuel cells, Chemical Solution Synthesis for Materials Design and Thin Film Device Applications (2021) 545–559. https://doi.org/10.1016/B978-0-12-819718-9.00022-4.

[384] M. Kishimoto, M. Lomberg, E. Ruiz-Trejo, N.P. Brandon, Enhanced triple-phase boundary density in infiltrated electrodes for solid oxide fuel cells demonstrated by high-resolution tomography, J Power Sources 266 (2014) 291–295. https://doi.org/10.1016/J.JPOWSOUR.2014.05.038.

[385] S.P. Jiang, Nanoscale and nano-structured electrodes of solid oxide fuel cells by infiltration: Advances and challenges, Int J Hydrogen Energy 37 (2013) 449–470. https://doi.org/10.1016/J.IJHYDENE.2011.09.067.

[386] D. Chen, M. Barreau, S. Turczyniak-Surdacka, K. Sobczak, M. Strawski, A.L.G. La Salle, A. Efimenko, D. Teschner, C. Petit, S. Zafeiratos, Ceria nanoparticles as promoters of CO2 electroreduction on Ni/YSZ: An efficient preparation strategy and insights into the catalytic promotion mechanism, Nano Energy 101 (2022). https://doi.org/10.1016/j.nanoen.2022.107564.

[387] S. He, Y. Zou, K. Chen, S.P. Jiang, C.P. San Jiang, A critical review of key materials and issues in solid oxide cells, Interdisciplinary Materials 2 (2023) 111–136. https://doi.org/10.1002/IDM2.12068.

[388] S. Kim, G. Kim, A. Manthiram, A review on infiltration techniques for energy conversion and storage devices: from fundamentals to applications, Sustain Energy Fuels 5 (2021) 5024–5037. https://doi.org/10.1039/D1SE00878A.

[389] M. Barreau, D. Salusso, J. Li, J. Zhang, E. Borfecchia, K. Sobczak, L. Braglia, J.J. Gallet, P. Torelli, H. Guo, S. Lin, S. Zafeiratos, Ionic Nickel Embedded in Ceria with High

Specific CO2 Methanation Activity, Angewandte Chemie International Edition 62 (2023) e202302087. https://doi.org/10.1002/ANIE.202302087.

[390] F. Lan, J. Bai, H. Wang, The preparation of oleylamine modified micro-size sphere silver particles and its application in crystalline silicon solar cells, RSC Adv 8 (2018) 16866–16872. https://doi.org/10.1039/C8RA02620C.

[391] A.P. Ramos, Dynamic Light Scattering Applied to Nanoparticle Characterization, Nanocharacterization Techniques (2017) 99–110. https://doi.org/10.1016/B978-0-323-49778-7.00004-7.

[392] J.S. Elias, M. Risch, L. Giordano, A.N. Mansour, Y. Shao-Horn, Structure, bonding, and catalytic activity of monodisperse, transition-metal-substituted CeO2 nanoparticles, J Am Chem Soc 136 (2014) 17193–17200. https://doi.org/10.1021/JA509214D.

[393] R.L. Zahradnik, Diffusional Processes in Solid Electrolyte Fuel Cell Electrodes, J Electrochem Soc 117 (1970) 1443. https://doi.org/10.1149/1.2407341.

[394] D.A. Osinkin, Boosting electrochemical performance of Ni/YSZ electrode through simultaneous injection of nickel and ceria, Int J Hydrogen Energy 82 (2024) 1222–1229. https://doi.org/10.1016/J.IJHYDENE.2024.08.083.

[395] Z. Tan, J.T. Song, A. Takagaki, T. Ishihara, Infiltration of cerium into a NiO–YSZ tubular substrate for solid oxide reversible cells using a LSGM electrolyte film, J Mater Chem A Mater 9 (2021) 1530–1540. https://doi.org/10.1039/D0TA08564B.

[396] D. Chen, J. Zhang, M. Barreau, S. Turczyniak-Surdacka, O. Joubert, A.L.G. La Salle, S. Zafeiratos, Ni-doped CeO2 nanoparticles to promote and restore the performance of Ni/YSZ cathodes for CO2 electroreduction, Appl Surf Sci 611 (2023) 155767. https://doi.org/10.1016/J.APSUSC.2022.155767.

[397] S. Sharma, R. Stanley, P. Tiwari, S. Basu, N. Kumari, In situ exsolution of ceria nanoparticles in perovskite cathode for elevating CO2 reduction performance of solid oxide electrolysis cells (SOECs), Journal of Electroanalytical Chemistry 962 (2024) 118254. https://doi.org/10.1016/J.JELECHEM.2024.118254.

[398] P. Li, R. Dong, X. Jiang, S. Zhang, T. Liu, R. Wang, F. Yan, D. Fu, The effect of CeO2 morphology on the electrochemical performance of the reversible solid oxide cells, Journal of Electroanalytical Chemistry 873 (2020) 114513. https://doi.org/10.1016/J.JELECHEM.2020.114513.

[399] L. Zhang, S. Hu, W. Li, Z. Cao, H. Liu, X. Zhu, W. Yang, Nano-CeO2-Modified Cathodes for Direct Electrochemical CO2 Reduction in Solid Oxide Electrolysis Cells,

ACS Sustain Chem Eng 7 (2019) 9629–9636. https://doi.org/10.1021/ACSSUSCHEMENG.9B01183.

[400] P. Błaszczak, A. Mizera, B. Bochentyn, S.F. Wang, P. Jasiński, Preparation of methanation catalysts for high temperature SOEC by β-cyclodextrin-assisted impregnation of nano-CeO2 with transition metal oxides, Int J Hydrogen Energy 47 (2022) 1901–1916. https://doi.org/10.1016/j.ijhydene.2021.10.144.

[401] S. Sharma, P. Tiwari, S. Basu, N. Kumari, Highly Efficient Perovskite Cathode with In-Situ Exsolved CE Nanoparticles for Co2 Reduction in Solid Oxide Electrolysis Cell (Soec), Elsevier BV (2023).

[402] T. Chen, G. Zheng, K. Liu, G. Zhang, Z. Huang, M. Liu, J. Zhou, S. Wang, Application of CuNi–CeO2 fuel electrode in oxygen electrode supported reversible solid oxide cell, Int J Hydrogen Energy 48 (2023) 9565–9573. https://doi.org/10.1016/J.IJHYDENE.2022.11.236.

[403] L. Lu, D. He, R. Fang, C. Ni, J.T.S. Irvine, Co nanoparticles decorated with in-situ exsolved oxygen-storage CeO2 for an efficient and stable electrolysis of pure CO2, J Power Sources 580 (2023) 233424. https://doi.org/10.1016/J.JPOWSOUR.2023.233424.

[404] J. Carrasco, D. Lõpez-Durán, Z. Liu, T. Duchoň, J. Evans, S.D. Senanayake, E.J. Crumlin, V. Matolín, J.A. Rodríguez, M.V. Ganduglia-Pirovano, In situ and theoretical studies for the dissociation of water on an active Ni/CeO2 Catalyst: Importance of strong metal-support interactions for the cleavage of O-H bonds, Angewandte Chemie - International Edition 54 (2015) 3917–3921. https://doi.org/10.1002/ANIE.201410697.

[405] R.C. Maher, P.R. Shearing, E. Brightman, D.J.L. Brett, N.P. Brandon, L.F. Cohen, Reduction Dynamics of Doped Ceria, Nickel Oxide, and Cermet Composites Probed Using In Situ Raman Spectroscopy, Advanced Science 3 (2016) 1500146. https://doi.org/10.1002/ADVS.201500146.

[406] S. Ovtar, X. Tong, J.J. Bentzen, K.T.S. Thydén, S.B. Simonsen, M. Chen, Boosting the performance and durability of Ni/YSZ cathode for hydrogen production at high current densities: Via decoration with nano-sized electrocatalysts, Nanoscale 11 (2019) 4394–4406. https://doi.org/10.1039/c8nr07678b.

[407] Q. Liu, Y. Song, R. Li, H. Lv, W. Feng, Y. Shen, X. Zhang, G. Wang, X. Bao, A vanadium-doped BSCF perovskite for CO2 electrolysis in solid oxide electrolysis cells,

Int J Hydrogen Energy 46 (2021) 19814–19821. https://doi.org/10.1016/j.ijhydene.2021.03.134.

[408] T. Miruszewski, B. Kamecki, M. Łapiński, J. Karczewski, Fabrication, structural and electrical properties of Sr(V,Nb)O3-δ perovskite materials, Mater Chem Phys 212 (2018) 446–452. https://doi.org/10.1016/j.matchemphys.2018.03.070.

[409] Y. Zhu, N. Zhang, W. Zhang, L. Zhao, Y. Gong, R. Wang, H. Wang, J. Jin, B. He, Realizing Efficient Activity and High Conductivity of Perovskite Symmetrical Electrode by Vanadium Doping for CO2 Electrolysis, ACS Applied Materials and Interfaces 16 (2024) 36343–36353. https://doi.org/10.1021/ACSAMI.4C05465.

[410] A.E. Kisa, O. Demircan, Fabrication and performance analysis of A-site metal-promoted La0.595V0.005Sr0.4CoO3−∂ perovskite oxides as cathodes for intermediate temperature solid oxide fuel cells, Journal of Solid State Electrochemistry 28 (2024) 1785–1798. https://doi.org/10.1007/S10008-024-05851-4.

[411] P.A. Connor, X. Yue, C.D. Savaniu, R. Price, G. Triantafyllou, M. Cassidy, G. Kerherve, D.J. Payne, R.C. Maher, L.F. Cohen, R.I. Tomov, B.A. Glowacki, R.V. Kumar, J.T.S. Irvine, Tailoring SOFC Electrode Microstructures for Improved Performance, Adv Energy Mater 8 (2018) 1800120. https://doi.org/10.1002/AENM.201800120.

[412] B.F. Serôdio Costa, B.I. Arias-Serrano, A.A. Yaremchenko, Development of ni-sr(V,ti)o3-δ fuel electrodes for solid oxide fuel cells, Materials 15 (2022) 278. https://doi.org/10.3390/MA15010278/S1.

[413] C.Y. Liu, S.Y. Tsai, C.T. Ni, K.Z. Fung, Effect of Strontium-Doped Lanthanum Vanadate on Crystal Structure, Conductivity and Vanadium Valence State of a La1−xSrxVO3Anode in a Reducing Environment, J Electron Mater 46 (2017) 2301–2308. https://doi.org/10.1007/s11664-016-5268-9.

[414] D.G. Barceloux, Dr.D. Barceloux, Vanadium, J Toxicol Clin Toxicol 37 (1999) 265–278. https://doi.org/10.1081/CLT-100102425.

[415] J. Costa Pessoa, Thirty years through vanadium chemistry, J Inorg Biochem 147 (2015) 4–24. https://doi.org/10.1016/J.JINORGBIO.2015.03.004.

[416] Y. Jiang, Z. Liu, Y. Lv, A. Tang, L. Dai, L. Wang, Z. He, Perovskite enables high performance vanadium redox flow battery, Chemical Engineering Journal 443 (2022) 136341. https://doi.org/10.1016/J.CEJ.2022.136341.

[417] G. Qu, J. Wang, G. Liu, B. Tian, C. Su, Z. Chen, J.P. Rueff, Z. Wang, Vanadium Doping Enhanced Electrochemical Performance of Molybdenum Oxide in Lithium-Ion

Batteries, Adv Funct Mater 29 (2019) 1805227. https://doi.org/10.1002/ADFM.201805227.

[418] X. Xu, F. Xiong, J. Meng, X. Wang, C. Niu, Q. An, L. Mai, Vanadium-Based Nanomaterials: A Promising Family for Emerging Metal-Ion Batteries, Adv Funct Mater 30 (2020) 1904398. https://doi.org/10.1002/ADFM.201904398.

[419] T.K. Pietrzak, M. Wasiucionek, I. Gorzkowska, J.L. Nowiński, J.E. Garbarczyk, Novel vanadium-doped olivine-like nanomaterials with high electronic conductivity, Solid State Ion 251 (2013) 40–46. https://doi.org/10.1016/J.SSI.2013.02.012.

[420] J. Zhu, X. Chen, A.Q. Thang, F.L. Li, D. Chen, H. Geng, X. Rui, Q. Yan, Vanadium-based metal-organic frameworks and their derivatives for electrochemical energy conversion and storage, SmartMat 3 (2022) 384–416. https://doi.org/10.1002/SMM2.1091.

[421] J.S. Park, I.D. Hasson, M.D. Gross, C. Chen, J.M. Vohs, R.J. Gorte, A high-performance solid oxide fuel cell anode based on lanthanum strontium vanadate, J Power Sources 196 (2011) 7488–7494. https://doi.org/10.1016/J.JPOWSOUR.2011.05.028.

[422] Y. Zhou, Z. Zhou, Y. Song, X. Zhang, F. Guan, H. Lv, Q. Liu, S. Miao, G. Wang, X. Bao, Enhancing CO2 electrolysis performance with vanadium-doped perovskite cathode in solid oxide electrolysis cell, Nano Energy 50 (2018) 43–51. https://doi.org/10.1016/j.nanoen.2018.04.054.

[423] A. Eslem Kisa, O. Demircan, Synthesis and characterization of La0.595V0.005Sr0.4CoO3−δ as a novel cathode material for solid oxide fuel cells (SOFC), J Solgel Sci Technol 82 (2017) 352–362. https://doi.org/10.1007/s10971-017-4334-y.

[424] N.M. Vo, M.D. Gross, The Effect of Vanadium Deficiency on the Stability of Pd and Pt Catalysts in Lanthanum Strontium Vanadate Solid Oxide Fuel Cell Anodes, J Electrochem Soc 159 (2012) B641–B646. https://doi.org/10.1149/2.092205jes.

[425] T. Matsuura, J. Tabuchi, J. Mizusaki, S. Yamauchi, K. Fueki, Electrical properties of La2−xSrxCoO4—II: Models and analysis of the relationship between cobalt 3d electron state and structural, electrical and magnetic properties, Journal of Physics and Chemistry of Solids 49 (1988) 1409–1418. https://doi.org/10.1016/0022-3697(88)90113-8.

[426] V.S. Stashchuk, O.P. Polyans'ka, S.Y. Stashenko, Optical and electronic properties of metallic cobalt in the different structural states;Optichnyi ta elektronnyi vlastivostyi

metalyichnogo kobal'tu v ryiznikh strukturnyikh stanakh, Ukrayins'kij Fyizichnij Zhurnal (Kyiv) 55 (2010).

[427] B. Alrafei, I. Polaert, A. Ledoux, F. Azzolina-Jury, Remarkably stable and efficient Ni and Ni-Co catalysts for CO2 methanation, Catal Today 346 (2020) 23–33. https://doi.org/10.1016/j.cattod.2019.03.026.

[428] L.W. Tai, M.M. Nasrallah, H.U. Anderson, D.M. Sparlin, S.R. Sehlin, Structure and electrical properties of La1−xSrxCo1−yFeyO3. Part 1. The system La0.8Sr0.2Co1−yFeyO3, Solid State Ion 76 (1995) 259–271. https://doi.org/10.1016/0167-2738(94)00244-M.

[429] C. Sındıraç, S. Çakırlar, A. Büyükaksoy, S. Akkurt, Lowering the sintering temperature of solid oxide fuel cell electrolytes by infiltration, J Eur Ceram Soc 39 (2019) 409–417. https://doi.org/10.1016/J.JEURCERAMSOC.2018.09.029.

[430] P. Błaszczak, M. Zając, A. Ducka, K. Matlak, B. Wolanin, S.F. Wang, A. Mandziak, B. Bochentyn, P. Jasiński, High-temperature Co-electrolysis of CO2/H2O and direct methanation over Co-impregnated SOEC. Bimetallic synergy between Co and Ni, Int J Hydrogen Energy 47 (2022) 35017–35037. https://doi.org/10.1016/j.ijhydene.2022.08.057.

[431] B. Hou, M. Lin, Y. Wei, X. Lu, S. Mi, C. Bao, First-Principles Study on Exsolution of Ni and Ni-M (M = Fe, Co, Cr, Cu) Alloy Nanoparticles in the SrTiO3 Model as the Perovskite Cathode of Solid Oxide Electrolysis Cells, Journal of Physical Chemistry C 128 (2024) 2867–2875. https://doi.org/10.1021/ACS.JPCC.3C07287/.

[432] C. Gaudillere, L. Navarrete, J.M. Serra, Syngas production at intermediate temperature through H2O and CO2 electrolysis with a Cu-based solid oxide electrolyzer cell, Int J Hydrogen Energy 39 (2014) 3047–3054. https://doi.org/10.1016/J.IJHYDENE.2013.12.045.

[433] K. Zhao, Q. Bkour, X. Hou, S.W. Kang, J.C. Park, M.G. Norton, J. Il Yang, S. Ha, Reverse water gas shift reaction over CuFe/Al2O3 catalyst in solid oxide electrolysis cell, Chemical Engineering Journal 336 (2018) 20–27. https://doi.org/10.1016/J.CEJ.2017.11.028.

[434] J. Huang, H. Wei, T. Wei, Y. Lee, CO2 conversion improvement of solid-oxide electrolysis cells by inserting buffer layers between MFe2O4 (M = Ni, Cu, Co, Fe) cathode and electrolyte, Journal of CO2 Utilization 77 (2023) 102618. https://doi.org/10.1016/J.JCOU.2023.102618.

[435] U. Draz, E. Di Bartolomeo, A.P. Panunzi, U.P. Laverdura, N. Lisi, R. Chierchia, L. Duranti, Copper-Enhanced CO2 Electroreduction in SOECs, ACS Appl Mater Interfaces 16 (2024) 8842–8852. https://doi.org/10.1021/ACSAMI.3C17766/.

[436] Y. Du, L. Zhao, Y. Xiao, J. Kong, P. Liu, X. Yang, T. Zhou, High electrolysis performance of the SOEC cathode by creating oxygen vacancies to regulate the adsorption energy, J Mater Chem A Mater (2024). https://doi.org/10.1039/D4TA04915B.

[437] B. Bozzini, M. Amati, C. Mele, A. Knop-Gericke, E. Vesselli, An in situ near-ambient pressure X-ray photoelectron spectroscopy study of CO2 reduction at Cu in a SOE cell, Journal of Electroanalytical Chemistry 799 (2017) 17–25. https://doi.org/10.1016/j.jelechem.2017.05.011.

[438] S. Wang, B. Qian, Z. Wang, B. Yin, Y. Zheng, L. Ge, H. Chen, H. Yang, High catalytic activity of Fe-based perovskite fuel electrode for direct CO2 electroreduction in SOECs, J Alloys Compd 888 (2021). https://doi.org/10.1016/j.jallcom.2021.161573.

[439] A. Bergerud, R. Buonsanti, J.L. Jordan-Sweet, D.J. Milliron, Synthesis and phase stability of metastable bixbyite V2O 3 colloidal nanocrystals, Chemistry of Materials 25 (2013) 3172–3179. https://doi.org/10.1021/cm401530t.

[440] N. V. Skorodumova, S.I. Simak, B.I. Lundqvist, I.A. Abrikosov, B. Johansson, Quantum origin of the oxygen storage capability of ceria, Phys Rev Lett 89 (2002) 166601/1-166601/4. https://doi.org/10.1103/PHYSREVLETT.89.166601.

[441] K. Dewangan, D. Singh, S.K.S. Patel, K. Shrivas, Temperature-programmed nitridation of monodispersed VOx nanoparticles into nanocrystalline superconducting oxygen-doped vanadium nitride, New Journal of Chemistry 45 (2021) 6129–6135. https://doi.org/10.1039/d1nj00244a.

[442] W. Zhang, H. Li, M. Al-Hussein, A.Y. Elezzabi, Electrochromic Battery Displays with Energy Retrieval Functions Using Solution-Processable Colloidal Vanadium Oxide Nanoparticles, Adv Opt Mater 8 (2020). https://doi.org/10.1002/adom.201901224.

[443] T. Paik, S.H. Hong, E.A. Gaulding, H. Caglayan, T.R. Gordon, N. Engheta, C.R. Kagan, C.B. Murray, Solution-processed phase-change VO2 metamaterials from colloidal vanadium oxide (VOx) nanocrystals, ACS Nano 8 (2014) 797–806. https://doi.org/10.1021/nn4054446.

[444] O. Mathon, A. Beteva, J. Borrel, D. Bugnazet, S. Gatla, R. Hino, I. Kantor, T. Mairs, M. Munoz, S. Pasternak, F. Perrin, S. Pascarelli, The time-resolved and extreme conditions

XAS (TEXAS) facility at the European Synchrotron Radiation Facility: the general-purpose EXAFS bending-magnet beamline BM23, J Synchrotron Radiat 22 (2015) 1548–1554. https://doi.org/10.1107/S1600577515017786.

[445] S. Durmus, A. Dalmaz, M. Ozdincer, S. Sivrikaya, Preparation of cerium oxide nanoparticles: an efficient catalyst to the synthesis of dimeric disulphide Schiff bases, J. of Sci 13 (2017) 25–30. https://doi.org/10.18466/cbujos.282116.

[446] S. Ghamari Arbati, M. Ranjbar, Synthesis of nickel oxide/gadulinium doped ceria nanostructures by new methods as anode material for solid oxide fuel cells: Ni(II) complexes as new precursors, Nanochemistry Research 6 (2021) 104–116. https://doi.org/10.22036/NCR.2021.01.010.

[447] D. Kilinc, O. Sahin, Highly active and stable CeO2 supported nickel-complex catalyst in hydrogen generation, Int J Hydrogen Energy 46 (2021) 499–507. https://doi.org/10.1016/J.IJHYDENE.2020.09.201.

[448] S.G. Arbati, M. Ranjbar, A. Babaei, Nickel oxide-gadolinium doped ceria synthesized by new methods as anodes material for solid oxide fuel cells Article Information, Iranian Journal of Hydrogen & Fuel Cell 9 (2022) 133–147. https://doi.org/10.22104/IJHFC.2022.5797.1242.

[449] M. V. Martínez-Huerta, J.M. Coronado, M. Fernández-García, A. Iglesias-Juez, G. Deo, J.L.G. Fierro, M.A. Bañares, Nature of the vanadia-ceria interface in V5+/CeO2 catalysts and its relevance for the solid-state reaction toward CeVO4 and catalytic properties, J Catal 225 (2004) 240–248. https://doi.org/10.1016/j.jcat.2004.04.005.

[450] M. Rahimi-Nasrabadi, F. Ahmadi, A. Fosooni, Influence of capping agents additives on morphology of CeVO4 nanoparticles and study of their photocatalytic properties, Journal of Materials Science: Materials in Electronics 28 (2017) 537–542. https://doi.org/10.1007/S10854-016-5556-4.

[451] G. Lu, B. Song, Z. Li, H. Liang, X. Zou, Photocatalytic degradation of naphthalene on CeVO4 nanoparticles under visible light, Chemical Engineering Journal 402 (2020) 125645. https://doi.org/10.1016/J.CEJ.2020.125645.

[452] A. Zonarsaghar, M. Mousavi-Kamazani, S. Zinatloo-Ajabshir, Sonochemical synthesis of CeVO4 nanoparticles for electrochemical hydrogen storage, Int J Hydrogen Energy 47 (2022) 5403–5417. https://doi.org/10.1016/J.IJHYDENE.2021.11.183.

[453] P. Intaphong, P. Pookmanee, S. Artkla, P. Intaphong, S. Jonjana, A. Phuruangrat, P. Pookmanee, S. Artkla, S. Thongtem, T. Thongtem, Synthesis and photocatalytic

properties of CeVO4 nanoparticles under UV irradiation, Dig J Nanomater Biostruct 10 (2015) 1281–1287.

[454] S. Ghotekar, S. Pansambal, K.Y.A. Lin, D. Pore, R. Oza, Recent Advances in Synthesis of CeVO4 Nanoparticles and Their Potential Scaffold for Photocatalytic Applications, Top Catal 66 (2023) 89–103. https://doi.org/10.1007/S11244-022-01630-5.

[455] D.R. Kamble, S.V. Bangale, S.K. Ghotekar, S.R. Bamane, Efficient Synthesis of CeVO4 Nanoparticles Using Combustion Route and Their Antibacterial Activity, Journal of Nanostructures 8 (2018) 144–151. https://doi.org/10.22052/JNS.2018.02.004.

[456] J.E. Penner-Hahn, X-ray Absorption Spectroscopy, 2005. https://doi.org/10.1038/npg.els.0002984.

[457] J.K. Kesavan, I. Luisetto, S. Tuti, C. Meneghini, C. Battocchio, G. Iucci, Ni supported on YSZ: XAS and XPS characterization and catalytic activity for CO2 methanation, J Mater Sci 52 (2017) 10331–10340. https://doi.org/10.1007/S10853-017-1179-2.

[458] M. V. Alekseeva, O.A. Bulavchenko, A.A. Saraev, A.M. Kremneva, M. V. Shashkov, O.O. Zaikina, Y.K. Gulyaeva, A.N. Grachev, O. Kikhtyanin, D. Kubička, V.A. Yakovlev, Effect of Temperature on the Hydrotreatment of Sewage Sludge-Derived Pyrolysis Oil and Behavior of Ni-Based Catalyst, Catalysts 2020, Vol. 10, Page 1273 10 (2020) 1273. https://doi.org/10.3390/CATAL10111273.

[459] N.B. Duc, V.Q. Tho, T.S. Tien, D.Q. Khoa, H.K. Hieu, Pressure and temperature dependence of EXAFS Debye-Waller factor of platinum, Radiation Physics and Chemistry 149 (2018) 61–64. https://doi.org/10.1016/J.RADPHYSCHEM.2018.03.017.

[460] F.D. Vila, J.J. Rehr, H.H. Rossner, H.J. Krappe, Theoretical x-ray absorption Debye-Waller factors, Phys Rev B Condens Matter Mater Phys 76 (2007). https://doi.org/10.1103/PHYSREVB.76.014301.

[461] Z. Gao, L. V. Mogni, E.C. Miller, J.G. Railsback, S.A. Barnett, A perspective on low-temperature solid oxide fuel cells, Energy Environ Sci 9 (2016) 1602–1644. https://doi.org/10.1039/C5EE03858H.

[462] A. Mineshige, J. Izutsu, M. Nakamura, K. Nigaki, J. Abe, M. Kobune, S. Fujii, T. Yazawa, Introduction of A-site deficiency into La0.6Sr0.4Co0.2Fe0.8O3–δ and its effect on structure and conductivity, Solid State Ion 176 (2005) 1145–1149. https://doi.org/10.1016/J.SSI.2004.11.021.

[463] S. He, M. Saunders, K. Chen, H. Gao, A. Suvorova, W.D.A. Rickard, Z. Quadir, C.Q. Cui, S.P. Jiang, A FIB-STEM Study of Strontium Segregation and Interface Formation

of Directly Assembled La 0.6 Sr 0.4 Co 0.2 Fe 0.8 O 3-δ Cathode on Y 2 O 3 -ZrO 2 Electrolyte of Solid Oxide Fuel Cells, J Electrochem Soc 165 (2018) F417–F429. https://doi.org/10.1149/2.0151807jes.

[464] L. Ma, P. Priya, N.R. Aluru, A Multiscale Model for Electrochemical Reactions in LSCF Based Solid Oxide Cells, J Electrochem Soc 165 (2018) F1232–F1241. https://doi.org/10.1149/2.0921814jes.

[465] F. Qiang, K.N. Sun, N.Q. Zhang, X.D. Zhu, S.R. Le, D.R. Zhou, Characterization of electrical properties of GDC doped A-site deficient LSCF based composite cathode using impedance spectroscopy, J Power Sources 168 (2007) 338–345. https://doi.org/10.1016/J.JPOWSOUR.2007.03.040.

[466] C. Fu, K. Sun, N. Zhang, X. Chen, D. Zhou, Electrochemical characteristics of LSCF–SDC composite cathode for intermediate temperature SOFC, Electrochim Acta 52 (2007) 4589–4594. https://doi.org/10.1016/J.ELECTACTA.2007.01.001.

[467] Q. Zhou, F. Wang, Y. Shen, T. He, Performances of LnBaCo2O5+x–Ce0.8Sm0.2O1.9 composite cathodes for intermediate-temperature solid oxide fuel cells, J Power Sources 195 (2010) 2174–2181. https://doi.org/10.1016/J.JPOWSOUR.2009.10.062.

[468] P. Qiu, J. Li, L. Jia, B. Chi, J. Pu, J. Li, F. Chen, LaCoO3-δ coated Ba0.5Sr0.5Co0.8Fe0.2O3-δ cathode for intermediate temperature solid oxide fuel cells, Electrochim Acta 319 (2019) 981–989. https://doi.org/10.1016/J.ELECTACTA.2019.07.054.

[469] P. Qiu, X. Yang, T. Zhu, S. Sun, L. Jia, J. Li, Review on core-shell structured cathode for intermediate temperature solid oxide fuel cells, Int J Hydrogen Energy 45 (2020) 23160–23173. https://doi.org/10.1016/J.IJHYDENE.2020.06.034.

[470] Z. Zhang, J. Wang, Y. Chen, S. Tan, Z. Shao, D. Chen, In situ formation of a 3D core-shell and triple-conducting oxygen reduction reaction electrode for proton-conducting SOFCs, J Power Sources 385 (2018) 76–83. https://doi.org/10.1016/J.JPOWSOUR.2018.03.029.

[471] P. Qiu, A. Wang, J. Li, Z. Li, L. Jia, B. Chi, J. Pu, J. Li, Promoted CO2-poisoning resistance of La0.8Sr0.2MnO3−δ-coated Ba0.5Sr0.5Co0.8Fe0.2O3−δ cathode for intermediate temperature solid oxide fuel cells, J Power Sources 327 (2016) 408–413. https://doi.org/10.1016/J.JPOWSOUR.2016.07.074.

[472] H.J. Hwang, J.W. Moon, S. Lee, E.A. Lee, Electrochemical performance of LSCF-based composite cathodes for intermediate temperature SOFCs, J Power Sources 145 (2005) 243–248. https://doi.org/10.1016/J.JPOWSOUR.2005.02.063.

[473] F. Wang, M. Nishi, M.E. Brito, H. Kishimoto, K. Yamaji, H. Yokokawa, T. Horita, Sr and Zr diffusion in LSCF/10GDC/8YSZ triplets for solid oxide fuel cells (SOFCs), J Power Sources 258 (2014) 281–289. https://doi.org/10.1016/J.JPOWSOUR.2014.02.046.

[474] S.P. Simner, J.P. Shelton, M.D. Anderson, J.W. Stevenson, Interaction between La(Sr)FeO3 SOFC cathode and YSZ electrolyte, Solid State Ion 161 (2003) 11–18. https://doi.org/10.1016/S0167-2738(03)00158-9.

[475] P. Qiu, A. Wang, H. Zheng, L. Jia, B. Chi, J. Pu, J. Li, LaCoO3-δ-coated Ba0.5Sr0.5Co0.8Fe0.2O3-δ: A promising cathode material with remarkable performance and CO2 resistance for intermediate temperature solid oxide fuel cells, Int J Hydrogen Energy 43 (2018) 20696–20703. https://doi.org/10.1016/J.IJHYDENE.2018.09.154.

[476] F. Wang, M.E. Brito, K. Yamaji, D.H. Cho, M. Nishi, H. Kishimoto, T. Horita, H. Yokokawa, Effect of polarization on Sr and Zr diffusion behavior in LSCF/GDC/YSZ system, Solid State Ion 262 (2014) 454–459. https://doi.org/10.1016/J.SSI.2014.04.002.

[477] A. Jun, J. Kim, J. Shin, G. Kim, Perovskite as a Cathode Material: A Review of its Role in Solid-Oxide Fuel Cell Technology, ChemElectroChem 3 (2016) 511–530. https://doi.org/10.1002/CELC.201500382.

[478] K. Chen, N. Ai, S.P. Jiang, Reasons for the high stability of nano-structured (La,Sr)MnO3 infiltrated Y2O3–ZrO2 composite oxygen electrodes of solid oxide electrolysis cells, Electrochem Commun 19 (2012) 119–122. https://doi.org/10.1016/J.ELECOM.2012.03.033.

[479] H. Ibrahim, A. Ilinca, J. Perron, Energy storage systems—Characteristics and comparisons, Renewable and Sustainable Energy Reviews 12 (2008) 1221–1250. https://doi.org/10.1016/J.RSER.2007.01.023.

[480] V.N. Nguyen, Q. Fang, U. Packbier, L. Blum, Long-term tests of a Jülich planar short stack with reversible solid oxide cells in both fuel cell and electrolysis modes, Int J Hydrogen Energy 38 (2013) 4281–4290. https://doi.org/10.1016/J.IJHYDENE.2013.01.192.

[481] C. Nicollet, A. Flura, V. Vibhu, A. Rougier, J.-M. Bassat, J.-C. Grenier, An innovative efficient oxygen electrode for SOFC: Pr 6 O 11 infiltrated into Gd-doped ceria backbone, Int J Hydrogen Energy 41 (2016) 15538–15544. https://doi.org/10.1016/j.ijhydene.2016.04.024.

[482] S. Nam, J. Kim, H. Kim, S. Ahn, S. Jeon, Y. Choi, B. Park, W. Jung, Revitalizing Oxygen Reduction Reactivity of Composite Oxide Electrodes via Electrochemically Deposited PrO $_x$ Nanocatalysts, Advanced Materials 36 (2024). https://doi.org/10.1002/adma.202307286.

[483] Y. Li, Y. Tian, Z. Li, X. Wu, L. Wang, T. Bian, Boosting the performance of La0.5Sr0.5Fe0.9Mo0.1O3-δ oxygen electrode via surface-decoration with Pr6O11 nano-catalysts, Int J Hydrogen Energy 84 (2024) 305–312. https://doi.org/10.1016/j.ijhydene.2024.08.223.

[484] G. Sassone, Degradation Mechanisms of the Lanthanum Strontium Cobalt Ferrite Used as Oxygen Electrode in Solid Oxide Cells, Université Grenoble Alpes (2024).

[485] G. Sassone, O. Celikbilek, M. Hubert, K.D. Bagarinao, T. David, L. Guetaz, I. Martin, J. Villanova, L. Rorato, B. Morel, A. Léon, J. Laurencin, Advanced Nanoscale Characterizations of Solid Oxide Cell Electrodes, ECS Trans 111 (2023) 885. https://doi.org/10.1149/11106.0885ECST.

[486] G. Sassone, O. Celikbilek, M. Hubert, K. Develos-Bagarinao, T. David, L. Guetaz, I. Martin, J. Villanova, A. Benayad, L. Rorato, J. Vulliet, B. Morel, A. Léon, J. Laurencin, Effect of the operating temperature on the degradation of solid oxide electrolysis cells, J Power Sources 605 (2024) 234541. https://doi.org/10.1016/J.JPOWSOUR.2024.234541.

[487] W.H. Doh, V. Papaefthimiou, T. Dintzer, V.V. Dupuis, S. Zafeiratos, Synchrotron radiation X-ray photoelectron spectroscopy as a tool to resolve the dimensions of spherical core/shell nanoparticles, Journal of Physical Chemistry C 118 (2014) 26621–26628. https://doi.org/10.1021/jp508895u.

[488] M. Nagoshi, Y. Fukuda, N. Yamada, Z. Guo, T. Iri, K. Gondaira, H. Iwasaki, Y. Syono, M. Tachiki, Valence states of praseodymium in Y-Ba-Cu oxides studied by x-ray-photoelectron spectroscopy, Phys Rev B 46 (1992) 8635. https://doi.org/10.1103/PhysRevB.46.8635.

[489] S. Lütkehoff, M. Neumann, A. Ślebarski, 3d and 4d x-ray-photoelectron spectra of Pr under gradual oxidation, Phys Rev B 52 (1995) 13808. https://doi.org/10.1103/PhysRevB.52.13808.

[490] A.X. Bin Yong, L.O. Anderson, N.H. Perry, E. Ertekin, Effects of state filling and localization on chemical expansion in praseodymium-oxide perovskites, J Mater Chem A Mater 11 (2023) 4045–4056. https://doi.org/10.1039/D2TA06756K.

[491] M. Szubka, E. Talik, A. Molak, S. Turczyński, D.A. Pawlak, Electronic structure of Prx La1-xAlO3 solid solution, Crystal Research and Technology 45 (2010) 1309–1315. https://doi.org/10.1002/CRAT.201000371.

[492] M.F. Sunding, K. Hadidi, S. Diplas, O.M. Løvvik, T.E. Norby, A.E. Gunnæs, XPS characterisation of in situ treated lanthanum oxide and hydroxide using tailored charge referencing and peak fitting procedures, J Electron Spectros Relat Phenomena 184 (2011) 399–400. https://doi.org/10.1016/j.elspec.2011.04.002.

[493] N. Soltani, R. Martínez-Bautista, A. Bahrami, L. Huerta Arcos, M. Cassir, J. Chávez Carvayar, Fabrication of aligned porous LaNi0.6Fe0.4O3 perovskite by water based freeze casting, Chem Phys Lett 700 (2018) 138–144. https://doi.org/10.1016/J.CPLETT.2018.04.026.

[494] Y. Pang, X. Zhou, E.I. Vovk, C. Guan, S. Li, A.P. van Bavel, Y. Yang, Understanding lanthanum oxide surface structure by DFT simulation of oxygen 1s calibrated binding energy in XPS after in situ treatment, Appl Surf Sci 548 (2021) 149214. https://doi.org/10.1016/J.APSUSC.2021.149214.

[495] S. Mickevičius, S. Grebinskij, V. Bondarenka, B. Vengalis, K. Šliužiene, B.A. Orlowski, V. Osinniy, W. Drube, Investigation of epitaxial LaNiO3−x thin films by high-energy XPS, J Alloys Compd 423 (2006) 107–111. https://doi.org/10.1016/J.JALLCOM.2005.12.038.

[496] J.P.H. Li, X. Zhou, Y. Pang, L. Zhu, E.I. Vovk, L. Cong, A.P. Van Bavel, S. Li, Y. Yang, Understanding of binding energy calibration in XPS of lanthanum oxide by in situ treatment, Physical Chemistry Chemical Physics 21 (2019) 22351–22358. https://doi.org/10.1039/C9CP04187G.

[497] W. Gu, J. Liu, M. Hu, F. Wang, Y. Song, La2O2CO3 encapsulated La2O3 nanoparticles supported on carbon as superior electrocatalysts for oxygen reduction reaction, ACS Appl Mater Interfaces 7 (2015) 26914–26922. https://doi.org/10.1021/acsami.5b06100.

[498] D.R. Inns, X. Pei, Z. Zhou, D.J.M. Irving, S.A. Kondrat, The influence of phase purity on the stability of Pt/LaAlO3 catalysts in the aqueous phase reforming of glycerol, Mater Today Chem 26 (2022) 101230. https://doi.org/10.1016/J.MTCHEM.2022.101230.

[499] D.R. Inns, A.J. Mayer, V. Skukauskas, T.E. Davies, J. Callison, S.A. Kondrat, Evaluating the Activity and Stability of Perovskite LaMO3-Based Pt Catalysts in the Aqueous Phase Reforming of Glycerol, Top Catal 64 (2021) 992–1009. https://doi.org/10.1007/s11244-021-01449-6.

[500] X. Zhou, Y. Pang, Z. Liu, E.I. Vovk, A.P. van Bavel, S. Li, Y. Yang, Active oxygen center in oxidative coupling of methane on La2O3 catalyst, Journal of Energy Chemistry 60 (2021) 649–659. https://doi.org/10.1016/J.JECHEM.2021.01.008.

[501] M. Barreau, D. Salusso, J. Zhang, M. Haevecker, D. Teschner, A. Efimenko, F. Bournel, J.J. Gallet, E. Borfecchia, K. Sobczak, C. Petit, S. Zafeiratos, Uncovering the critical function of lanthanum in CH4 production from CO2 using exsolved LaNiO3 perovskite catalysts, J Mater Chem A Mater 12 (2024) 7605–7621. https://doi.org/10.1039/D3TA07391B.

[502] W. Derafa, F. Paloukis, B. Mewafy, W. Baaziz, O. Ersen, C. Petit, G. Corbel, S. Zafeiratos, Synthesis and characterization of nickel-doped ceria nanoparticles with improved surface reducibility, RSC Adv 8 (2018) 40712–40719. https://doi.org/10.1039/C8RA07995A.

[503] S.J.J. Kay, N. Chidhambaram, A. Thirumurugan, Synthesis of Lanthanum Ferrite Perovskite Nanoparticles: An Alternative Bio-Approach Versus a Conventional Chemical Approach, ChemistrySelect 9 (2024) e202304329. https://doi.org/10.1002/SLCT.202304329.

[504] P.C.J. Graat, M.A.J. Somers, Simultaneous determination of composition and thickness of thin iron-oxide films from XPS Fe 2p spectra, Appl Surf Sci 100–101 (1996) 36–40. https://doi.org/10.1016/0169-4332(96)00252-8.

[505] W. Luo, S. Zafeiratos, Tuning Morphology and Redox Properties of Cobalt Particles Supported on Oxides by an in between Graphene Layer, The Journal of Physical Chemistry C 120 (2016) 14130–14139. https://doi.org/10.1021/acs.jpcc.6b03595.

[506] S. Turczyniak, W. Luo, V. Papaefthimiou, N.S.S. Ramgir, M. Haevecker, A. MacHocki, S. Zafeiratos, A Comparative Ambient Pressure X-ray Photoelectron and Absorption Spectroscopy Study of Various Cobalt-Based Catalysts in Reactive Atmospheres, Top Catal 59 (2016) 532–542. https://doi.org/10.1007/s11244-015-0531-5.

[507] S.S. Liu, K. Develos-Bagarinao, R.A. Budiman, T. Ishiyama, H. Kishimoto, K. Yamaji, Towards an atomic scale understanding of the early-stage deterioration mechanism of LSCF, J Mater Chem A Mater 11 (2023) 21983–22000. https://doi.org/10.1039/D3TA04585D.

[508] S.P. Jiang, Development of lanthanum strontium cobalt ferrite perovskite electrodes of solid oxide fuel cells – A review, Int J Hydrogen Energy 44 (2019) 7448–7493. https://doi.org/10.1016/J.IJHYDENE.2019.01.212.

[509] Y. Sun, S. He, M. Saunders, K. Chen, Z. Shao, S.P. Jiang, A comparative study of surface segregation and interface of La0·6Sr0·4Co0·2Fe0·8O3-δ electrode on GDC and YSZ electrolytes of solid oxide fuel cells, Int J Hydrogen Energy 46 (2021) 2606–2616. https://doi.org/10.1016/J.IJHYDENE.2020.10.113.

[510] D. Chen, B. Mewafy, F. Paloukis, L. Zhong, V. Papaefthimiou, T. Dintzer, K. Papazisi, S. Balomenou, D. Tsiplakides, D. Teschner, V. Pérez-Dieste, C. Escudero, S. Zafeiratos, Revising the role of chromium on the surface of perovskite electrodes: Poison or promoter for the solid oxide electrolysis cell performance?, J Catal 381 (2020) 520–529. https://doi.org/10.1016/j.jcat.2019.11.032.

[511] J. Kuyyalil, Jr. Newby D., J. Laverock, Y. Yu, D. Cetin, S.N. Basu, K. Ludwig, K.E. Smith, Vacancy assisted SrO formation on La0.8Sr0.2Co0.2Fe0.8O3−δ surfaces—A synchrotron photoemission study, Surf Sci 642 (2015) 33–38. https://doi.org/10.1016/j.susc.2015.08.001.

[512] M. Pagliari, M. Marasi, A. Donazzi, Electrocatalytic and operando characterization of state-of-the-art SOFC cathodes for applications at high CO2 concentration in novel clean power production cycles, Electrochim Acta 501 (2024) 144779. https://doi.org/10.1016/J.ELECTACTA.2024.144779.

[513] F. Zhou, Y. Liu, X. Zhao, W. Tang, S. Yang, S. Zhong, M. Wei, Effects of cerium doping on the performance of LSCF cathodes for intermediate temperature solid oxide fuel cells, Int J Hydrogen Energy 43 (2018) 18946–18954. https://doi.org/10.1016/J.IJHYDENE.2018.08.041.

[514] E.J. Crumlin, E. Mutoro, Z. Liu, M.E. Grass, M.D. Biegalski, Y.L. Lee, D. Morgan, H.M. Christen, H. Bluhm, Y. Shao-Horn, Surface strontium enrichment on highly active perovskites for oxygen electrocatalysis in solid oxide fuel cells, Energy Environ Sci 5 (2012) 6081–6088. https://doi.org/10.1039/C2EE03397F.

[515] J. Wang, D.N. Mueller, E.J. Crumlin, Recommended strategies for quantifying oxygen vacancies with X-ray photoelectron spectroscopy, J Eur Ceram Soc 44 (2024) 116709. https://doi.org/10.1016/J.JEURCERAMSOC.2024.116709.

This page intentionally left blank

Curriculum Vitae

Jinming ZHAHG

Nationality: Chinese Gender: Male Date of birth: 12/09/1992
Address: 54 Rue du Ban de la Roche 67000, Strasbourg, France
Phone: +33 695638835 Email: jinming.zhang@etu.unistra.fr & jinmingworks@qq.com

Educational Background

2021.09-present University of Strasbourg Strasbourg, FRANCE

PhD student: Major in Physical Chemistry

2017.04-2017.08 CHOU University Tokyo, Japan

International Exchange Student: Major in Spectrochemical

2014.09-2017.12 Kunming University of Science and Technology Kunming, CHINA

Master of Engineering: Major in Environmental Engineering

2010.09-2014.06 Xi'an Technological University Xi'an, CHINA

Bachelor of Engineering: Major in Environmental Engineering

Relevant Research Experiences

2021.09-present Institut de chimie et procédés pour l'énergie, l'environnement et la santé (ICPEES) UMR 7515 du CNRS National Center of Scientific Research (CNRS) & University of Strasbourg (UDS)

Supervisor: Dr. Spyridon Zafeiratos (HdR)

2014.09-2017.12 Research Group on Industrial Flue Gas Desulfurization, Kunming University of Science and Technology

Supervisor: Professor Dongdong ZHANG

Present Research Activity

- Investigation of the surface chemistry of SOEC cermet electrodes during high-temperature H_2O Electrolysis via evaluation of surface characteristics by means of advanced characterization techniques (Synchrotron XPS, etc.) to establish a structure-performance relationship.

Journal Papers

- **J. Zhang**, M. Barreau, T. Dintzer, S. Zafeiratos*, et al. Unveiling Key Interface Characteristics of Ni/Yttria-Stabilized Zirconia Solid Oxide Cell Electrodes in H_2O Electroreduction Using Operando X-ray Photoelectron Spectroscopy. ACS Appl. Mater. Interfaces. (2024), 16(29), 37915-37926.

- **Zhang, J.**, Wei, A., Zhang, D.*, et al. Photocatalytic degradation of Br-trihalomethanes by nanosized TiO_2/diatomite hybrid photocatalyst. Kinet. Catal+, (2016), 57(4), 429-433.
- Ping N., **Jinming Z.**, Dongdong Z.*, et al. Liquid-Phase Catalytic Oxidation of SO_2 by Phosphate Ore Slurry, Oxid. Commun., (2018), 41, No 1, 45–52.
- **J. Zhang**, Q. Wu, D. Zhang*, et al., Effect of metal ions on the formation of trihalomethanes by humic acids with different molecular weights, Guangzhou Chemistry, 2016, 41(05):28-32.
- **J. Zhang**, S. Li, D. Zhang*, et al., Preparation of Al/Fe polynuclear hydroxyl cation-pillared bentonite and its adsorption of Cr(VI), Guangzhou Chemistry, 2016, 41(06):46-49.
- M. Barreau, D. Chen, **J. Zhang**, Papaefthimiou, V., Petit, C., Salusso, D., Zafeiratos, S.* Synthesis of Ni-doped ceria nanoparticles and their unusual surface reduction in hydrogen, Mater. Today Chem. (2022), 26, 101011.
- D. Chen, **J. Zhang**, M. Barreau, S. Turczyniak-Surdacka, O. Joubert, ALG. La Salle, S. Zafeiratos*. Ni-doped CeO_2 nanoparticles to promote and restore the performance of Ni/YSZ cathodes for CO_2 electroreduction, Appl. Surf. Sci., (2023) 611, 155767
- Mathias Barreau, Davide Salusso, Juan Li, **Jinming Zhang**, Borfecchia, E., Sobczak, K., Zafeiratos, S.*. Ionic Nickel Embedded in Ceria with High Specific CO_2 Methanation Activity, Angew. Chem. Int. Edit., (2023) 62, 25.
- Barreau M., Salusso D., **Zhang J.**, Haevecker M., Teschner D., Efimenko,A. Zafeiratos S*. Uncovering the critical function of lanthanum in CH_4 production from CO_2 using exsolved $LaNiO_3$ perovskite catalysts, J. Mater. Chem. A, (2024), 12, 7605-7621